Universidad de Oviedo

PhD Thesis

Development of techniques for the analysis and synthesis of spatially-fed arrays for emerging applications in near-field

Author

Álvaro Fernández Vaquero

M.Sc. Ingeniero de Telecomunicación

Supervisors

Dr. Manuel Arrebola Baena

Dr. Marcos Rodríguez Pino

September, 2021

Programa de Doctorado en Tecnologías de la Información y Comunicaciones en Redes Móviles

Justificación

El trabajo realizado por el autor de la tesis tiene gran calidad técnica y es altamente innovador, lo que está refrendado por diferentes publicaciones científicas tanto en revistas como en congresos de ámbito internacional, así como proyectos/contratos, estancias y premios:

Publicaciones

1. D. R. Prado, A. F. Vaquero, M. Arrebola, M. R. Pino, F. Las-Heras. "General Near Field Synthesis of reflectarray antennas for their use as probes in CATR", PIER Progress in Electromagnetics Research, vol. 160, pp. 9-17, 2017.
2. D. R. Prado, A. F. Vaquero, M. Arrebola, M. R. Pino, F. Las-Heras, "Acceleration of Gradient-Based Algorithm for Near and Far Field Array Antennas Optimization Based on Finite Differences", IEEE Transactions on Antennas and Propagation, vol. 66, no. 10, pp. 5239-5248, Oct. 2018.
3. A. F. Vaquero, M. R. Pino, M. Arrebola, S. A. Matos, J. R. Costa, C. A. Fernandes, "Bessel Beam Generation Using Dielectric Planar Lenses at Millimeter Frequencies", IEEE Access, vol. 8, pp. 216185-216196, 2020.
4. A. F. Vaquero, M. R. Pino, M. Arrebola,S. A. Matos, J. R. Costa, C. A. Fernandes, "Evaluation of a Dielectric-Only Transmitarray for Generating Multi-Focusing Near-Field Spots Using a Cluster of Feeds in the Ka-band", Sensors, vol. 21, no. 2, Jan. 2021.
5. A. F. Vaquero, M. Arrebola, M. R. Pino, R. Florencio, J. A. Encinar, "Demonstration of a Reflectarray with Near-_eld Amplitude and Phase Constraints as Compact Antenna Test Range Probe for 5G New Radio Devices", IEEE Transactions on Antennas and Propagation, vol. 69, no. 5, pp. 2715-2726, May 2021.
6. A. Rebollo, A. F. Vaquero, M. Arrebola, and M. R. Pino, "3D-Printed Dual-Reflector Antenna With Self-Supported Dielectric Subreflector", IEEE Access, vol. 8, pp. 209091-209100, 2020.
7. A. F. Vaquero, M. R. Pino, M. Arrebola, "Dual-Polarized Shaped-Beam Transmitarray to Improve wide-angular 5G femtocell", IEEE Antennas Wireless Propagation Letters, (under review).
8. B. Imaz-Lueje, A. F. Vaquero, D. R. Prado, M. R. Pino, M. Arrebola, "Shaped-Pattern Reflectarray Antennas for mm-wave Networks Using a Simple Cell Topology", IEEE Access, (under review).

Congresos internacionales

1. A. F. Vaquero, D. R. Prado, M. Arrebola, M. R. Pino and F. Las-Heras, "Near Field synthesis of reectarray antennas based on Intersection Approach", 11th European Conference on Antennas and Propagation (EuCAP), Paris, (France), 19-24/03/2017. (Convened Session).
2. A. F. Vaquero, M. Arrebola, M. R. Pino, J. R. Costa, S. Matos, and C. A. Fernandes, "Low-Cost Dielectric Flat Lens for Near-Field Focusing", Proc. Of the 2018 IEEE International Symposium on Antennas and Propagation (APS) & USNC/URSI National Radio Science Meeting, Boston, (USA), 08-13/07/2018.
3. A. F. Vaquero, D. R. Prado, M. Arrebola, and M. R. Pino, "Reflectarray Antenna for 5-G Indoor Coverage", Proc. of the 13th European Conference on Antennas and Propagation (EuCAP), Krakow, (Poland), 31/03-05/04/2019. (Convened Session).
4. A. F. Vaquero, M. Arrebola, and M. R. Pino, "Spatially-fed arrays for near-field multiple-spot coverage", Proc. of the International Conference on Electromagnetic in Advanced Applications and Topical Conference on Antennas and Propagation in Wireless Communications (ICEAA), Granada (Spain), 9-13/09/2019. (Special session).
5. A. F. Vaquero, M. Arrebola, and M. R. Pino, "Near-field multi-focusing transmit-array optimization for multi-position feed", Proc. of the 41st Annual Meeting & Symposium of the Antenna Measurement Techniques Association (AMTA), San Diego, California (USA), 6-11/10/2019.
6. A. F. Vaquero, M. Arrebola, and M. R. Pino, "Bandwidth response of a reflectarray antenna working as a Compact Antenna Test Range probe", Proc. of the 41st Annual Meeting & Symposium of the Antenna Measurement Techniques Association (AMTA), San Diego, California (USA), 6-11/10/2019.
7. A. F. Vaquero, M. Arrebola, M. R. Pino, R. Florencio, and J. A. Encinar, "Performance evaluation of near-field plane wave generated by a reflectarray for 5G testing", Proc. of the 2020 IEEE International Symposium on Antennas and Propagation (APS) & USNC/URSI National Radio Science Meeting, Boston, (USA), 05-10/07/2020. (Special Session).

8. A. F. Vaquero, M. Arrebola, M. R. Pino, J. A. Encinar, "Evaluation of a Ka-Band reflectarray Capability to Generate a Uniform Plane Wave in Near Field Region", Proc. of the 15th European Conference on Antennas and Propagation (EuCAP), Düsseldorf (Germany), 22-26/03/2021.
9. E. Martinez-de-Rioja, A. F. Vaquero, M. Arrebola, E. Carrasco, J. A. Encinar, and M. Achour, "Passive Dual-Polarized Shaped-Beam Reflectarrays to Improve Coverage in Millimeter-Wave 5G Networks", 15th European Conference on Antennas and Propagation (EuCAP), D□usseldorf (Germany), 22-26/03/2021.
10. A. F. Vaquero, M. Arrebola, and M. R. Pino, "Reflectarray as plane wave generator for Compact Antenna Test Range in millimeter frequency band", XXXIV Simposium Nacional de la Unión Científica Internacional de Radio (URSI), Málaga (Spain), 04-06/09/2020. Accessit to the best Young Researcher Paper Award.
11. A. F. Vaquero, M. R. Pino, and M. Arrebola, "Multi-feed shaped-beam perforated dielectric transmitarray in millimeter-band", XXXVI Simposium Nacional de la Unión Científica Internacional de Radio (URSI), Vigo (Spain), 20-24/09/2021 (Special session).

Estancias internacionales

1. Instituto de Telecomunicações, Lisboa, Portugal. (Supervisor: Prof. Jorge R. Costa.). 6/09/2017 - 06/11/2017. (2 meses).
2. Instituto de Telecomunicações, Lisboa, Portugal. (Supervisor: Prof. Jorge R. Costa.). 01/01/2021 – 31/03/2021. (3 meses).

Proyectos y financiación

1. "Development of a European-based Collaborative Network to Accelerate Technological, Clinical and Commercialisation Progress in the Area of Medical Microwave Imaging" , Code: TD1301, Funding: ESF/COST, Term: 01/11/2013 - 01/11/2017. Main researcher: Jorge Manuel Lopes Leal Rodrigues da Costa.
2. "Reflectarray Antennas with Improved Performances And Design Techniques (RAIPAD)" , Code: 1-7064/12/NL/MH, Funding: European Space Agency (ESA), Term: 01/09/2012{31/03/2014. Main researcher: Manuel Arrebola.
3. "Antenas Reconfigurables para Transferencia Eficiente de Información y Energía a múltiples usuarios en femtoceldas/Reconfigurable Antennas for a Multi-User Efficient Information and Energy Transfer in femtocells (ARTEINE)", Code: MINECO-18-TEC2017-R, Funding: Ministerio de Economía y Competitividad (Spanish Goverment), Term: 01/01/2018 - 31/12/2020. Main researcher: Marcos Rodríguez Pino and Germán León.
4. "Ayudas a organismos públicos de investigación para apoyar la actividad que desarrollen sus grupos de investigación en el Principado de Asturias en el periodo 2018-2020", Code: FC-GRUPIN-IDI/2018/000191, Funding: Principado de Asturias, Term: 01/01/2018{31/12/2020. Main researcher: Fernando Las-Heras Andrés.
5. "RFID shoplifting Gateway in UHF band", Code: FUO-20-124, Funding: University of Pisa, Term: 01/04/2020{30/04/2020. Main researcher: Marcos Rodríguez Pino.
6. "Synthesis and design of reflectarrays for improving coverage of 5G base station antennas at mm-waves", Code: FUO-221-20, Funding: METAWAVE CORPORATION., Term: 01/09/2020 - 01/08/2021. Main researcher: Manuel Arrebola.

Premios y reconocimientos

1. TICRA grant to attend the 15th European Conference on Antennas and Propagation (EuCAP). TICRA, March 2021.
2. Accessit to the Best Young Researcher Paper Award. XXXIV Simposium Nacional de la Unión Científica Internacional de Radio (URSI), Málaga (Spain), 04-06/09/2020.

Universidad de Oviedo
Universidá d'Uviéu
University of Oviedo

RESUMEN DEL CONTENIDO DE TESIS DOCTORAL

1.- Título de la Tesis	
Español/Otro Idioma: Desarrollo de técnicas de análisis y síntesis de arrays alimentados espacialmente para aplicaciones emergentes de campo cercano	Inglés: Development of techniques for the analysis and synthesis of spatially-fed arrays for emerging applications in near-field

2.- Autor	
Nombre: Álvaro Fernández Vaquero	DNI/Pasaporte/NIE: . .
Programa de Doctorado: Tecnologías de la Información, Comunicaciones en Redes Móviles	
Órgano responsable: Centro Internacional de Postgrado	

RESUMEN (en español)

La evolución de las tecnologías inalámbricas ha requerido evolucionar sus diferentes subsistemas, en particular, las antenas. Se busca que las antenas satisfagan especificaciones más exigentes que, mejoren la capacidad y calidad de los sistemas inalámbricos. Por otro lado, las aplicaciones de campo cercano han incrementado su interés a lo largo de los últimos años, siendo de alto interés en la comunidad científica. Clásicamente, las antenas de campo cercano se utilizaban para concentrar la potencia en un punto o área. Sin embargo, nuevas aplicaciones demandan antenas que mejoren sus prestaciones de campo cercano, como por ejemplo generar haces no difractados o haces conformados similares a campo lejano.

Las comunicaciones inalámbricas 5G han establecido como parámetro clave la eficiencia energética, siendo las antenas un subsistema elemental para poder lograr este objetivo. El nuevo paradigma que se origina con las comunicaciones 5G y, más concretamente, en las comunicaciones en interiores, ha generado un especial interés en antenas que sean capaces de controlar su diagrama en la zona de Fresnel para poder mejorar las capacidades de estos sistemas, siendo especialmente importante en el despliegue de comunicaciones en bandas milimétricas. Tomando como referencia diferentes tipos de comunicaciones ya existentes, terrestres o espaciales, las antenas de apertura parecen ser una alternativa muy interesante para estas nuevas comunicaciones y, más concretamente, los arrays alimentados espacialmente.

La principal motivación de esta tesis es el desarrollo de técnicas de análisis y síntesis de este tipo de antenas, con el objetivo de evaluar sus prestaciones en aplicaciones emergentes de campo cercano, tales como comunicaciones interiores y sistemas de caracterización de dispositivos. Ambas enfocadas en comunicaciones 5G en banda milimétrica. De acuerdo con esta línea, la tesis presenta dos bloques. Primero, se presenta un modelo de cálculo del campo cercano de un array alimentado espacialmente. Este modelo se utiliza para desarrollar una técnica de síntesis solo fase (*phase-only)* para estas antenas. Esta técnica permite imponer condiciones en la amplitud del campo cercano radiado y, por primera vez, sobre la fase. Segundo, se analizan, fabrican y testean diferentes antenas, especialmente transmitarrays y reflectarrays, para evaluar sus características aplicaciones de campo cercano que requieren conformado de amplitud o, incluso de fase.

Los resultados presentados en esta tesis demuestran que la técnica propuesta de análisis y síntesis son válidas para el diseño de estas antenas. A través de los prototipos desarrollados, se puede observar que este tipo de antena tiene capacidades suficientes para aplicaciones de campo cercano, destacando su uso como estaciones base y, haciendo una mención especial a su capacidad de poder controlar tanto la amplitud, como la fase del campo cercano radiado.

Universidad de Oviedo
Universidá d'Uviéu
University of Oviedo

RESUMEN (en inglés)

The evolution of wireless technologies has sparked a need to evolve different subsystems, particularly, the antennas' subsystem to satisfy tighter requirements and improve the capacity and quality of wireless systems. Conversely, near-field applications have increased their popularity throughout the last years, becoming a current topic in research activity. The classical use of a near-field antenna is to concentrate the power within a certain spot or area. However, intensive research is done on designing near-field antennas with different performances within their near-field region, such as the generation of non-diffractive beams or radiating shaped beams similar to the ones used in far-field applications.

Conversely, the new generation of communications (5G) and wireless communications have established energy efficiency as a key factor. Hence, the antenna plays an important role to achieve this goal. The new challenges of 5G and the use of indoor communications have arisen a special interest in the design of antenna whose near-field pattern can be controlled to enhance the performances of these communication systems. Especially, the communications deployed at millimeter frequencies. Like terrestrial and space communications, aperture antennas are a potential candidate for these wireless communications. Moreover, spatially-fed arrays are s suitable solution to address the new challenges.

The main motivation of this thesis is the development of techniques to analyze and synthesize spatially-fed array antennas to use them in near-field applications. Particularly, spatially-fed array antennas are suitable for emerging applications such as indoor communications and antenna measuring systems. Both applications focus on the future 5G communications at the millimeter band. In this line, the thesis is divided into two blocks. First, a novel approach to compute the radiation of a spatially-fed array within its Fresnel region is presented. This model Is used to develop a phase-only synthesis technique for spatially-fed array antennas. This approach allows imposing specifications in the amplitude of the radiated near-field, as well as in the phase for the first time. Second, several spatially-fed array antennas are analyzed, manufactured, and tested to evaluate their performances in novel applications that demand shaped-beam patterns, or even shaped-phase patterns within the Fresnel region. Mainly, two types of spatially-fed arrays are analyzed: transmitarray and reflectarray antennas.

The results presented in this thesis have validated the analysis and synthesis technique proposed. In addition, the capability of spatially-fed array antennas has been demonstrated for emerging applications that require shaped patterns in the near-field. It is important to highlight the use of these antennas as base stations in indoor communications and make a special emphasis on the possibility of controlling both amplitude and phase of the radiated field.

SR. PRESIDENTE DE LA COMISIÓN ACADÉMICA DEL PROGRAMA DE DOCTORADO EN TECNOLOGÍAS DE LA INFORMACIÓN Y COMUNICACIONES EN REDES MÓVILES

Corred
insensatos.

Resumen

La constante evolución de las tecnologías inalámbricas ha propiciado la necesidad de evolucionar los subsistemas formados por las antenas, de manera que, estos satisfagan especificaciones más exigentes, mejorando la capacidad y calidad de los sistemas inalámbricos. Por otro lado, las aplicaciones de campo cercano han incrementado su interés a lo largo de los últimos años, generando un alto impacto en la actividad investigadora. Clásicamente, las antenas de campo cercano han sido utilizadas para enfocar, o concentrar, la potencia radiada en un determinado punto o volumen. En esta línea y, más recientemente, ha crecido el interés por desarrollar antenas de campo cercano que sean capaces de radiar haces no difractados. Este tipo de haces, idealmente, se definen como haces capaces de eliminar el fenómeno de difracción en su propagación, obteniendo haces perfectamente colimados. Sin embargo, aplicaciones emergentes de campo cercano también requieren antenas con nuevas capacidades, tales como, haces conformados similares a los utilizados en campo lejano, pero dentro de la región de Fresnel de la antena.

En las nuevas comunicaciones de 5G y, en especial, las comunicaciones inalámbricas, se ha establecido como un parámetro clave la eficiencia energética a la hora de desplegar este tipo de comunicaciones. Respecto a las antenas, estas tienen que lidiar con un número masivo de usuarios que, no solo estarán interconectados entre ellos, sino que, también estarán conectados con diferentes dispositivos, tales como sensores o diferentes tipos de dispositivos electrónicos. Por otro lado, un reto importante de las comunicaciones de 5G o, generaciones futuras, *beyond* 5G o 6G, es el despliegue eficiente de comunicaciones en frecuencias milimétricas, especialmente, en las bandas centradas en 28, 39 o 60 GHz. Por lo tanto, con la llegada de estas comunicaciones, aparecen nuevos escenarios y retos. Tomando como referencia las comunicaciones interiores, la proximidad entre los diferentes elementos que conforman la red 5G y que, por tanto, cada dispositivo estará ubicado dentro de la región de Fresnel de las demás antenas, se establece como un punto clave el desarrollo eficiente de comunicaciones interiores para poder dar soporte a este tipo de comunicaciones. Por lo tanto, el diseño de antenas con la capacidad de mejorar sus capacidades dentro de la región de Fresnel, permitirá mejorar la calidad de este tipo de sistemas. De manera similar a

las comunicaciones espaciales, el uso de antenas con la capacidad de radiar haces conformados, permitirá mejorar la calidad de las comunicaciones. Además, siguiendo este mismo ejemplo, una alternativa muy interesante para lograr este objetivo es hacer uso de las antenas de apertura, en especial, los arrays alimentados espacialmente. Este tipo de antenas ha demostrado ampliamente obtener características especialmente buenas tanto en comunicaciones terrestres como espaciales.

La principal motivación de esta tesis es el desarrollo de técnicas de análisis y síntesis de arrays alimentados espacialmente, con el objetivo de utilizar este tipo de antenas en aplicaciones de campo cercano y, en particular, en aplicaciones emergentes: comunicaciones y sistemas de medidas de antenas. Siguiendo esta línea, la tesis se divide en dos bloques principales. Primero, se presenta un modelo novedoso de análisis que permite calcular el campo cercano radiado por un array alimentado espacialmente. Este modelo es utilizado para desarrollar una técnica de síntesis solo fase (*phase-only synthesis*) para arrays alimentados espacialmente, la cual permite imponer restricciones en la amplitud como la fase del campo cercano radiado. En segundo lugar, diferentes tipos de arrays alimentados espacialmente son analizados, fabricados y testeados para evaluar sus prestaciones en diferentes aplicaciones novedosas de campo cercano, que requieran de diagramas conformados e, incluso, impongan condiciones sobre la fase del campo radiado. Estas aplicaciones están principalmente centradas en sistemas 5G que operan en la banda de frecuencias milimétricas.

El primer bloque de la tesis se centra en el desarrollo del análisis y la técnica de síntesis que se utiliza a lo largo de la tesis. Primero, se presenta un modelo de cálculo del campo cercano basado en el Principio de Huygens y el Principio de Superposición. Este modelo considera el array alimentado espacialmente como una antena de apertura, cuyos campos en la apertura son muestreados. Cada una de las muestras será considerada como una fuente puntual e isotrópica de manera que, el campo cercano radiado por el array alimentado espacialmente en un punto del espacio será la superposición de la radiación de cada una de las muestras o, elementos, en ese punto del espacio. Este modelo será mejorado, considerando que los elementos o muestras son pequeñas aperturas radiantes, en lugar de fuentes puntuales e isotrópicas. En este caso, el campo cercano será obtenido mediante la superposición de las contribuciones de campo lejano da cada uno de los elementos en ese punto del espacio. Esta última consideración permite tener en cuenta la potencia radiada por los elementos. Por lo tanto, es posible definir un análisis de potencia del campo cercano radiado por este tipo de antenas. En este análisis de potencia se definirán diferentes parámetros tales como: la potencia radiada, la intensidad de radiación, o la ganancia en campo cercano. Por otro lado, el cálculo de la contribución de campo lejano de cada uno de

los elementos, modelados como pequeñas aperturas radiantes, se obtiene mediante la aplicación de los Principios de Equivalencia, de manera similar al caso general de una antena de apertura. Este modelo permite obtener una formulación relativamente sencilla que mejora la precisión de modelos existentes, únicamente basados en modelar los elementos como fuentes puntuales e isotrópicas.

Este modelo se emplea para el desarrollo de una técnica de síntesis solo fase basada en el *Intersection Approach*. Esta técnica permite realizar la síntesis de arrays alimentados espacialmente con especificaciones o, restricciones, sobre el campo cercano radiado. El *Intersection Approach*, a diferencia de otros algoritmos de optimización, busca la mínima distancia entre dos conjuntos en lugar de minimizar una función de coste. Este algoritmo ha sido ampliamente utilizado en la síntesis de diagramas de radiación de antenas de tipo reflectarray, obteniendo resultados muy satisfactorios incluso imponiendo requisitos muy estrictos. El *Intersection Approach* requiere definir dos proyectores: el proyector *forward* y el proyector *backward*. En la implementación clásica del *Intersection Approach* se utiliza la *Fast Fourier Transform* (FFT) para calcular el campo radiado (proyector *forward*) mientras que, se utiliza la FFT inversa (IFFT) para recuperar los campos en la apertura (proyector *backward*), obteniendo un algoritmo altamente eficiente. Cuando el *Intersection Approach* se aplica a problemas de campo cercano, la implementación basada en la FFT puede utilizarse. Sin embargo, implementación limita de manera severa el número de problemas que es posible abordar con el *Intersection Approach*. Si se utiliza la FFT para implementar los proyectores, únicamente será posible imponer restricciones de campo en planos paralelos a la apertura de la antena, limitando el número de aplicaciones de campo cercano donde pueden utilizarse este tipo de antenas. En esta tesis se propone una alternativa basada en el *Intersection Approach* generalizado para campo cercano, el cual permite superar esta limitación. El campo radiado será calculado con el modelo propuesto anteriormente para obtener el proyector *forward*, mientras que, el proyector *backward* será implementado con un segundo algoritmo de optimización, el *Levenberg-Marquardt*. A pesar de que esta versión generalizada del algoritmo reduce su eficiencia, permite imponer condiciones en cualquier punto del espacio, lo que es especialmente útil en muchas aplicaciones emergentes de campo cercano.

El segundo bloque se dedica al diseño y validación experimental de diferentes diseños prácticos de arrays alimentados espacialmente, principalmente antenas de tipo reflectarray y transmitarray. La validación de estos diseños tiene como objetivo validar las técnicas desarrolladas junto a evaluar la capacidad de este tipo de antenas en diferentes aplicaciones de campo cercano. Tales como, el clásico enfoque en campo cercano, comunicaciones interiores, o sistemas que permitan caracterizar antenas.

Para las aplicaciones de enfoque de campo cercano se han utilizado tres antenas de tipo transmitarray, las cuales son diseñadas para concentrar la potencia radiada en un punto o, en un cierto volumen o área. El primer diseño es un transmitarray que genera un haz no difractado en banda Ka, empleando una antena con una apertura relativamente pequeña. Además, este transmitarray está basado en elemento solo dieléctrico (*dielectric-only*), lo cual permite su fabricación mediante técnicas de fabricación aditivas. Las dos antenas restantes también se basan en este mismo tipo de elementos, pero con la capacidad de realizar un enfoque del campo radiado, en configuraciones de un solo spot o múltiples. Ambas antenas operan en banda Ka.

Estos diseños son realizados mediante el uso de técnicas analíticas, basadas únicamente en consideraciones de fase. Aunque los resultados obtenidos validan este tipo de técnicas, no es posible utilizar técnicas analíticas para la obtención de diagramas conformados complejos. Por lo tanto, es necesario utilizar técnicas de síntesis de antenas para poder diseñar arrays alimentados espacialmente con especificaciones en su campo cercano radiado.

El *Intersection Approach* generalizado para campo cercano es usado para diseñar diferentes arrays alimentados espacialmente, permitiendo obtener haces conformados en su campo cercano. Primero, esta técnica se aplicará para obtener haces conformados con condiciones en la amplitud del campo cercano radiado. Las antenas diseñadas y validadas experimentalmente están desarrolladas para su uso como estaciones base en comunicaciones 5G interiores en banda Ka. El objetivo de estas síntesis es obtener zonas uniformes de potencia radiada que actúen como coberturas uniformes en un cierto rango.

Finalmente, se aborda la síntesis de una antena de tipo reflectarray, imponiendo tanto condiciones en la amplitud del campo cercano radiado, como en su fase. Hasta este momento, la síntesis de antenas de tipo array o array alimentado espacialmente se había realizado únicamente para obtener diagramas conformados con restricciones de amplitud, sin restricciones sobre la fase del campo radiado. Sin embargo, el *Intersection Approach* generalizado para campo cercano permite controlar simultáneamente la amplitud y la fase. En este caso, un reflectarray ha sido diseñado, fabricado y testeado con el objetivo de generar una onda uniformemente plana en las proximidades de la apertura de la antena, siendo la primera vez que se imponen condiciones simultaneas en amplitud y fase. El objetivo es obtener una antena de tipo reflectarray que actúe como sonda de medida en un sistema de rango compacto para caracterizar los futuros dispositivos 5G o, antenas que operan en frecuencias milimétricas de manera rápida. En particular, se ha evaluado la capacidad de este reflectarray como sonda de medida en un pequeño sistema de rango compacto desarrollado para este propósito. Esta va-

lidación ha permitido demostrar por primera vez que, es posible medir diagramas de radiación, empleando antenas de tipo reflectarray que generen una onda uniformemente plana. Después, este diseño se ha repetido para obtener un reflectarray que genere una onda uniformemente plana en doble polarización lineal.

Los resultados presentados en esta tesis demuestran que la técnica propuesta de análisis y síntesis son válidas, al igual que la capacidad de las antenas de tipo array alimentado espacialmente para aplicaciones de campo cercano emergente, haciendo una mención especial a la capacidad de poder controlar tanto la amplitud, como la fase del campo cercano radiado.

Conclusiones

Esta tesis está dedicada al desarrollo de técnicas de análisis y síntesis de antenas de tipo array alimentados espacialmente (SFA), para su uso en aplicaciones dentro de la región de Fresnel. Se presenta un modelo de cálculo de campo cercano de este tipo de antenas, el cual está basado en el Principio de Huygens y, utiliza el principio de superposición para obtener los campos radiados por un SFA. En particular, la apertura del SFA es muestreada, asegurando que se cumple el teorema de Nyquist, de manera que cada muestra es considerada como un elemento, el cual es modelado como una fuente puntual e isotrópica, de manera similar a los modelos utilizados en teoría de arrays. El campo cercano en un punto del espacio se obtendrá mediante la superposición de la radiación de cada uno de los elementos en ese punto. Además, se presenta una evolución de este modelo que permite incrementar su precisión, considerando cada elemento como una pequeña apertura radiante, en lugar de una fuente puntual e isotrópica. Esta nueva aproximación permite tener en cuenta la potencia radiada por el elemento. La contribución de cada uno de los elementos sobre un punto del espacio se calculará utilizando la teoría de aperturas, la cual permite analizar cada elemento con los Principios de Equivalencia, calculando el campo lejano radiado por una apertura a partir de sus campos tangenciales. Aunque es posible aplicar indistintamente cada uno de los tres Principios de Equivalencia, es común utilizar el Segundo Principio de Equivalencia, ya que únicamente requiere conocer el campo tangencial eléctrico. En caso de aplicar el Primer Principio de Equivalencia, se debe de calcular el campo magnético, el cual se puede obtener mediante aproximar la onda incidente sobre un elemento como una onda incidente localmente plana. El modelo presentado permite obtener el campo cercano de un SFA en cualquier punto del espacio, siempre y cuando se encuentre en la región de campo lejano del elemento. Junto a este modelo se han definido una serie de parámetros análogos a un análisis de potencia de campo lejano. En particular, se define la potencia radiada, la intensidad de radiación o la ganancia de una antena de tipo SFA, todos ellos particularizados para la región de Fresnel.

Respecto a la síntesis de antenas SFA, se introduce una técnica de síntesis que permite obtener diagramas de campo cercano conformados. El *Intersection Approach* es particularizado para campo cercano, obteniendo un algoritmo para síntesis solo fase.

Este algoritmo es altamente eficiente y ha obtenido resultados muy satisfactorios en la síntesis de antenas de tipo reflectarray. Parte de esta eficiencia se debe a la implementación de sus proyectores con la FFT. Sin embargo, cuando se particulariza para campo cercano, esta implementación basada en la FFT no puede ser aplicada, teniendo que redefinir los proyectores utilizados, más concretamente el proyector backward. En este caso, se ha utilizado el algoritmo Levenberg-Marquardt para implementar dicho proyector. Mediante esta nueva definición de proyectores se obtiene una versión generalizada del *Intersection Approach*. A pesar de que esta versión generalizada reduce su eficiencia respecto a la versión clásica, permite sintetizar antenas SFA con restricciones de amplitud y fase en cualquier punto del espacio. Por otro lado, también se presenta una técnica basada en diferencias finitas para acelerar el cálculo de la matriz Jacobiana y, por tanto, incrementar la eficiencia del algoritmo.

El resto de la tesis se dedica al análisis de diferentes antenas SFA para su uso en diferentes aplicaciones de campo cercano. Algunas de estas aplicaciones requieren diagramas de campo cercano conformado y se aplicará el *Intersection Approach* generalizado para lograrlo.

Se diseña una lente plana con variación gradual de su índice de refracción, la cual se utiliza para general un haz de Bessel en banda milimétrica, en particular, en banda Ka. La antena está compuesta de elementos solo dieléctrico, presentando dos topologías nuevas en este tipo de elementos. El desfase que introducen estos elementos se controla mediante la inserción de agujeros de aire contenidos dentro de cada uno de los elementos. Estas inserciones permiten controlar la cantidad de material dieléctrico de la celda y, por tanto, la constante dieléctrica de la celda, la cual está relacionada con el desfase de la celda. Se presentan dos topologías distintas, pero como se demuestra, la geometría de la celda no afecta a la respuesta de la celda siempre y cuando se mantenga la ratio aire-dieléctrico de esta. La lente plana se diseña para obtener un haz de Bessel en un rango de 650 mm y se valida experimentalmente mediante dos prototipos, uno por cada tipo de celda. Ambos prototipos se fabrican mediante técnicas de fabricación aditiva. Los dos prototipos son evaluados, obteniendo resultados satisfactorios en la generación de haces de Bessel en el rango de frecuencias de 26 a 30 GHz. Cabe destacar el potencial de las antenas de tipo SFA en la generación de este tipo de haces en banda milimétrica. Una segunda lente plana es diseñada para comparar su capacidad de enfoque con una lente hiperbólica doble. Ambas antenas consiguen enfocar el campo cercano con prestaciones similares y únicamente se obtienen dos principales diferencias. Primero, la lente plana no concentra la potencia sobre el punto de enfoque teórico sino que, se produce una compresión de la posición del máximo del campo. Segundo, la respuesta en banda de la lente plana está limitado por la respuesta de los

elementos mientras que, en el caso de la lente hiperbólica, únicamente está limitado por el alimentador, siendo idealmente infinito el ancho de banda de la propia lente. Por lo tanto, el uso de lentes planas puede ser una alternativa interesante cuando se requieren antenas ligeras y compactas frente a soluciones que requieren anchos de banda mayores. Esta misma lente plana de enfoque se combina con una técnica que permite obtener una configuración de múltiples spots enfocados. Esta técnica se basa en incrementar el número de alimentadores de manera que, cada uno de ellos produce un spot enfocado diferente. Esto implica tener que alimentar la lente plana con un clúster de bocinas. Para que esta técnica funcione correctamente se debe colocar cada una de las bocinas que conforman el clúster siguiendo un arco circular, el cual es definido por la distancia focal del SFA. Esta distribución permite obtener campos incidentes similares para cada una de las bocinas. De esta manera, si el elemento del SFA tiene una buena respuesta ante variaciones del ángulo de incidencia, el desplazamiento de cada uno de los alimentadores determinará la posición del spot enfocado que genera. Este método se ha evaluado para obtener una distribución angular de $\pm 20^{\circ}$ en un ancho de banda de 4 GHz. El uso de elementos dieléctricos permite obtener anchos de banda mayores que utilizando elementos resonantes. En la validación experimental se han obtenidos buenos resultados para el rango evaluado. Sin embargo, para las posiciones más abiertas se pueden observar diferentes efectos que introducen cierta distorsión en el enfoque obtenido. Principalmente, estas distorsiones se deben a la estabilidad angular de la celda, el efecto conocido como *spatial phase delay* y el posicionamiento de alimentadores fuera del foco de la antena. Esta técnica podría combinarse con otras técnicas para minimizar estos efectos y mejorar las características de la antena para una configuración con una distribución de alimentadores muy amplia.

A pesar de que el enfoque de campo cercano ha sido la aplicación más popular dentro de las antenas de campo cercano, han surgido nuevas aplicaciones que requieren extender el uso de estas antenas. Alguna de estas aplicaciones requiere de haces conformados de manera similar a como ocurre en campo lejano. Por lo tanto, es necesario utilizar el *Intersection Approach* generalizado para campo cercano para obtener antenas de tipo SFA con requerimientos sobre la amplitud del campo cercano radiado. En este caso, se sintetizan dos tipos de antenas, reflectarrays y transmitarray, en las cuales se evaluará su capacidad para actuar como estaciones base para comunicaciones 5G en entornos interiores. Primero, se sintetiza un reflectarray para obtener un diagrama rectangular sobre un plano ubicado en una estación de trabajo a la que se dará cobertura a una frecuencia central de 28 GHz. El reflectarray se diseña utilizando elementos tipo parche impresos sobre una sola capa de material dieléctrico, lo cual permite obtener una solución de bajo perfil. La principal limitación de este tipo de elementos reside en

no poder implementar un ciclo de fase completo, limitando el rango de desfases que es posible alcanzar a 260°. Esta limitación se incluye dentro del proceso de síntesis. Por otro lado, como estos elementos permiten trabajar en doble polarización lineal, el reflectarray generará el diagrama en dos polarizaciones, obteniendo una cobertura con prestaciones similares para cada una de ellas. Se fabrica y evalúa un prototipo, obteniendo una buena concordancia con los resultados basados en simulaciones. Además, se obtiene un alto grado de cumplimiento de los requisitos establecidos sobre el diagrama de campo cercano. Estos resultados permiten validar tanto la técnica de análisis y síntesis presentada en los capítulos anteriores, como el potencial de las antenas de tipo reflectarray para obtener diagramas conformados complejos dentro de la región de Fresnel. La segunda antena sintetizada es un transmitarray. El objetivo de la síntesis es generar una cobertura uniforme sobre un área extensa a 28 GHz. Para obtener un área de cobertura mayor, el transmitarray sintetizado se combina con la técnica utilizada para obtener múltiples spots enfocados. En este caso, el transmitarray se alimenta con un clúster formado por 5 antenas de tipo bocina, las cuales operan a 28 GHz, pero utilizan polarizaciones ortogonales para evitar interferencias. Se pretende evaluar si es posible obtener configuraciones de haces conformados múltiples, de manera similar a la obtención de configuraciones múltiples de spots enfocados. En el proceso de síntesis únicamente se considera el spot central, el cual incrementa notablemente su tamaño mediante el uso del *Intersection Approach* generalizado. Debido a la distribución de los alimentadores, los spots adyacentes que se generen también se verán mejorados. Después del proceso de síntesis el spot central ha incrementado su tamaño un 457 %. A pesar de que los spots adyacentes también ven incrementado su tamaño, aparece cierta distorsión en estos. Esto se debe a que el desplazamiento de los alimentadores genera una fase progresiva en la superficie del transmitarray, la cual produce la variación en la dirección de apuntamiento de haz. Sin embargo, los alimentadores también radian un frente de onda esférico, el cual modifica la fase progresiva y, por tanto, el campo transmitido y radiado. Este efecto no se observó en los spots enfocados porque este tipo de haces son más robustos frente a este tipo de efectos. A pesar de obtener estas distorsiones en los spots adyacentes, se obtiene una cobertura que alcanza los 1,4 metros en sus planos principales. La validación experimental muestra una alta concordancia con las simulaciones, obteniendo resultados similares e incluyendo las distorsiones. Las pequeñas diferencias existentes entre ambas se deben a la respuesta en amplitud de la celda, la cual no se tiene en cuenta en el proceso de síntesis ya que los elementos se modelan como desfasadores ideales. En la línea de síntesis de antenas SFA con condiciones en la amplitud del campo cercano radiado, también se presenta un nuevo método para obtener este tipo de diagramas en zonas de coberturas

muy extensas. Un punto importante de esta síntesis es demostrar que el *Intersection Approach* generalizado permite sintetizar un SFA con condiciones impuestas sobre un plano definido en la dirección de propagación del campo cercano. Esta técnica se basa en definir máscaras durante el proceso de síntesis que se adapten a la forma del campo cercano radiado, lo cual permite mejorar la convergencia en este tipo de síntesis. El método presentado junto con el *Intersection Approach* generalizado ha permitido obtener una distribución de potencia radiada en un rango de más de 14 metros con una distribución geométrica compleja. De mamera general, se puede extraer de la síntesis de antenas de tipo SFA con condiciones sobre la amplitud del campo cercano que, el *Intersection Approach* generalizado es un algoritmo potente que permite obtener diagramas de campo cercano complejos, definidos en diferentes planos del espacio y, obteniendo una solución genérica en la síntesis de este tipo de antenas.

Finalmente, el *Intersection Approach* generalizado es utilizado para sintetizar una antena de tipo reflectarray con condiciones sobre la amplitud y la fase del campo cercano radiado. Con esta síntesis se obtiene un reflectarray que genera una onda uniformemente plana que pueda ser usada como sonda de medida en un sistema CATR. En este caso, la síntesis solo fase realizada debe tener en cuenta y, de manera simultánea, las condiciones impuestas sobre la amplitud y la fase. La onda uniformemente plana se genera a una distancia de 46λ a una frecuencia de 28 GHz. Para poder considerar que el campo cercano se comporta como una onda uniformemente plana, se debe obtener un rizado máximo de 1 dB en amplitud y 10° en fase. La distribución de fases obtenida tras la síntesis es implementada con un elemento basado en tres dipolos paralelos que operan en polarización lineal. Las medidas del prototipo muestran muy buena concordancia con las simulaciones, obteniendo un alto grado de cumplimiento de las especificaciones en un volumen total de 100 mm $\times$ 100 mm $\times$ 150 mm. Prácticamente el 90 % del campo cercano, en los planos principales y, a lo largo del volumen, presenta un rizado comprendido entre 1-1,5 dB (evaluando el rizado pico a pico), y un táper inferior a 1 dB. La fase presenta un comportamiento muy plano a lo largo de todo el volumen, obteniendo que casi el 90 % de esta presenta un rizado de 10° y, el 100 % un rizado inferior a 15°. Se realiza una segunda síntesis para obtener una onda uniformemente plana en doble polarización lineal. En este caso el reflectarray se diseña usando un elemento basado en dos conjuntos de dipolos, cada uno de ellos compuesto por tres dipolos paralelos, permitiendo controlar ambas polarizaciones de manera independiente mediante una topología de bajo perfil. El diseño es evaluado con simulaciones MoM, obteniendo incluso mejores resultado que en el caso del reflectarray anterior. Dado que el objetivo principal de este capítulo es evaluar la capacidad de las antenas de tipo reflectarray para ser usadas como sondas de medidas, se presenta un

sistema CATR basado en un reflectarray como sonda de medida a 28 GHz. En particular, el reflectarray que opera en una única polarización lineal es integrado dentro de un pequeño sistema CATR, construido para este propósito. En particular, se ha evaluado el diagrama de radiación de una antena de tipo bocina y de un array de bocinas 2×1, ambas antenas a 28 GHz. Los diagramas de radiación medidos obtienen una concordancia total con las simulaciones *full-wave*. Por lo tanto, las antenas reflectarray son una solución con mucho potencial en la generación de ondas uniformemente planas en bandas milimétricas, siendo una alternativa de bajo coste y perfil para ser usada en sistemas compactos de medida. Por otro lado, el *Intersection Approach* generalizado para campo cercano ha demostrado ser un algoritmo realmente potente en la síntesis de SFA. En especial, cabe destacar los resultados obtenidos en diagramas con restricciones de amplitud pero, sobre todo, destacar las síntesis realizadas con requerimientos simultáneos de amplitud y fase.

Abstract

The constant evolution of wireless technologies has sparked a need to evolve antennas' subsystems to satisfy tighter requirements and improve the capacity and quality of wireless systems. Conversely, near-field applications have increased their popularity throughout the last years, becoming a current topic in research activity. The most common use of near-field antennas is focusing the power radiated in a certain spot or volume. Recently, there is intensive research on the design of near-field antennas to radiate non-diffraction beams, which ideally suppresses the diffraction along the propagation direction and results in well-collimated beams. However, emerging applications demand near-field antennas with new capabilities within the Fresnel region, such as shaped beams similar to far-field applications.

For the recent 5G communications and, especially wireless communications, high energy efficiency is a key factor. The antennas must lead with a massive number of users, which are interconnected, and also with a myriad of different devices, sensors, or electronic appliances. Moreover, an important challenge of 5G or, even beyond 5G, is the deployment of efficient communications in millimeter bands, particularly 28, 39, or 60 GHz. Hence, new scenarios and requirements would appear. Regarding indoor communications, the proximity among the different 5G elements, mainly within the Fresnel region of their antennas, makes the development of efficient indoor communications an indispensable chance to support 5G communications. Therefore, the design of antennas with the capability of improving their near-field performances would enhance these systems. In this line and similar to terrestrial and space communications, the use of antennas with shaped-beam radiation patterns would improve the quality of the communications. In addition, some potential candidates are aperture antennas and, especially spatially-fed arrays, since they have extensively demonstrated significantly good performances in communication systems, both terrestrial and space communications.

The main motivation of this thesis is the development of techniques that analyze and synthesize spatially-fed arrays which are used in near-field applications, making a special emphasis on emerging applications, such as communications and antenna measuring systems. In this way, the thesis is divided into two main blocks. First, a

novel approach to compute the radiation within the Fresnel region of a spatially-fed antenna is presented. Then, this model is used to develop a phase-only synthesis of spatially-fed arrays with constraints on the amplitude and phase of the radiated near-field. Second, several spatially-fed array antennas are analyzed, manufactured, and tested to evaluate their performances on novel applications that demand shaped-beam patterns, or even shaped-phase patterns within the Fresnel region, which are mainly focused on 5G systems at millimeter frequencies.

The first block concerns the analysis and the synthesis technique used throughout the thesis. First, the presented near-field model is based on Huygens' Principle and the Principle of Superposition. This model considers the spatially-fed array as an aperture antenna whose fields at the aperture are sampled. Each sample is considered as a punctual isotropic source, and the near-field radiated by the spatially-fed array at a certain point of the space is the superposition of the radiation of all the samples at this point. Then, the accuracy of the model is improved by considering the elements or samples as a small radiating aperture, instead of a punctual isotropic source. In this case, the near-field is obtained by the superposition of the far-field contribution of all the elements. This assumption allows taking the radiated power of the elements into account. Hence, it is feasible to define a proper power analysis of the antenna. In this sense, it is proposed the definition of different parameters, such as the power radiated, the radiation intensity, or the gain of a spatially-fed array in the near-field. Conversely, the far-field contribution of an element modeled as a small aperture can be derived from the Equivalent Principles, as in a general aperture antenna. The model provides a basic formulation that improves the accuracy of the models based on isotropic elements.

Then, this model is used to develop a phase-only synthesis technique based on the Intersection Approach. This approach enables the synthesis of spatially-fed arrays with requirements on the radiated near-field. The Intersection Approach seeks the minimum distance between two sets, instead of minimizing a cost function as other optimization algorithms. It has widely demonstrated very impressive results in the synthesis of copolar patterns of reflectarray antennas with tight specifications. However, the Intersection Approach defines two projectors: the forward and the backward projector. The classical implementation typically uses the Fast Fourier Transform (FFT) to compute the radiated field (forward projector) and the inverse FFT (IFFT) to retrieve the fields at the aperture (backward projector). This implementation results in a quite efficient algorithm. When dealing with a near-field synthesis, the FFT can also be applied. However, this solution severely restricts the problem to only impose conditions on planes parallels to the antenna aperture, which also limits the

range of applications of near-field antennas. In this thesis, a generalized Intersection Approach is proposed to overcome these limitations. The radiated field is computed with the proposed near-field model and the backward projector is implemented by an optimization algorithm, that is the Levenberg-Marquardt algorithm. Despite losing efficiency with this implementation, the proposed approach allows imposing conditions on any arbitrary point of the space, which is importantly useful for many emerging near-field applications.

The second block is devoted to the design and experimental validation of several and practical designs of spatially-fed arrays, mainly transmitarray and reflectarray antennas. The validation of these designs aims to validate the proposed techniques, as well as the capacity of spatially-fed array antennas in different near-field applications, such as classical near-field focusing, indoor communications, or antenna measurement systems.

Concerning near-field focusing, three transmitarray antennas are designed to concentrate the radiated power within a spot or a certain volume. The first design is a transmitarray to generate a non-diffractive beam in Ka-band using a relatively small aperture. Moreover, it is a dielectric-all transmitarray fabricated with an additive manufacturing technique. The other two designs are also based on dielectric solutions, and they radiate focused spots on single or multiple configurations in Ka-band.

These designs are obtained through analytical approaches based on sorely phase considerations. Although the obtained results validate these techniques, it is not feasible to apply an analytical approach to obtain a shaped-beam pattern. Therefore, it is needed to use a synthesis technique to design spatially-fed arrays with constraints on their near-field.

The generalized Intersection Approach for near-field is used to design different shaped-beam spatially-fed arrays. First, the phase-only synthesis technique is used with requirements imposed on the amplitude of the near-field. The antennas are designed and experimentally validated to be used as a base station in indoor 5G communications in Ka-band. The synthesis aim is to obtain a uniform distribution of the power radiated to reach a uniform coverage within a certain range.

Finally, it has been addressed the synthesis of a reflectarray antenna with constraints on its amplitude and phase of the radiated near-field. So far, the synthesis of arrays or spatially-fed array antennas was used to obtain shaped-beam patterns. However, the proposed generalized Intersection Approach is also able to deal with requirements on both amplitude and phase simultaneously. A reflectarray has been designed, manufactured, and tested to generate a uniform plane wave close to the antenna aperture for the first time. The aim is to obtain a reflectarray antenna probe

on a compact antenna measurement system to characterize the future 5G devices or antennas at millimeter band quickly. Particularly, the reflectarray has been evaluated in a homemade Compact Antenna Test Range of reduced dimensions, demonstrating that is possible to measure the radiation pattern of an antenna with a reflectarray-based Compact Antenna Test Range. Then, the design has been repeated to obtain a dual-polarized uniform plane wave.

The results presented in this thesis have demonstrated the analysis and synthesis technique proposed, as well as the capability of spatially-fed arrays for emerging near-field applications, making a special emphasis on the possibility of control both amplitude and phase of the radiated field.

Contents

List of Figures

List of Tables

List of Abbreviations

LMDS *Local Multipoint Distribution Service*, a broadband wireless access technology for provision of point-to-multipoint communication via microwaves.

WiMAX *Worldwide Interoperability for Microwave Access*, is a telecommunication technology aimed at providing wireless data over large distances in several ways, from point-to-point links to full mobile cellular type access. It is based on a family of broadband communication standards (IEEE 802.16).

DBS *Direct Broadcast satellite*, refers to the satellite television broadcast specific to home reception.

SFA *Spatially-fed array*, refers to array antennas fed by a primary feed.

PCB *Printed Circuit Board*, this term refers to an electronic circuit consisting of thin strips of a conducting material such as copper, which have been etched from a layer fixed to a flat insulating sheet called printed circuit board, and to which integrated circuits and other components are attached.

MEMS *MicroElectroMechanical Systems*, is a process technology used to create tiny integrated devices or systems that combine mechanical and electrical components.

MMIC *Monolithic Microwave Integrated Circuits*, is a type of integrated circuit device that operates at microwave frequencies.

SAR *Synthetic Aperture Radar*, a type of active data collection where a sensor produces its own energy and then records the amount of that energy reflected back after interacting with the Earth.

SATCOM *Satellite communications*, refers to satellite communications.

DR *Dielectric Resonator*, refers to a resonator makes up of dielectric material.

POS *Phase-Only Synthesis*, a technique for the synthesis of spatially-fed array radiation patterns based on the optimization of the direct reflection coefficient phases.

LMA *Levenberg-Marquardt Algorithm*, employed to solve non-linear least squares problems.

IA *Intersection Approach*, an algorithm for the synthesis of antennas.

BFGS *Broyden-Fletcher-Goldfarb-Shanno*, is an algorithm employed to solve unconstrained non-linear optimization problems.

IFFT *Inverse Fast Fourier Transform*, is an algorithm used to undoes the process of Fast Fourier Transform.

FFT *Fast Fourier Transform*, is an algorithm used to efficiently compute the Fourier transform in a regular grid, which reduces the time complexity of this computation.

GA *Genetic Algorithm*, is a class of numerical and combinational optimizers that are used to solve complex non-linear and non-convex problems.

PSO *Particle Swarm Optimization*, is a population-based optimization technique that optimizes a problem by iteratively trying to improve a candidate solution considering a given measure of quality.

FZP *Fresnel Zone Plane* lens, is a lens used to focus electromagnetic waves. It is based on a set of concentric rings to diffracted the incident wave.

GRIN *Graded-index* lens, refers to a lens whose electromagnetic effects are produced by a gradient of the refractive index of the material.

RLSA *Radial Line Slot Array*, is a type of cavity or waveguide antennas.

PSS *Phase-shifting surface*, consists of layers populated by conducting shapes of variable size, spaced by thin dielectric sheets used to add a delay on the incident field provided by a feed.

MWI *Microwave Imaging*, is an imaging technique that uses electromagnetic waves to evaluate hidden or embedded objects in a structure or media in microwave frequencies.

SNR *Signal Noise Ratio*, refers to the ratio of signal power to the noise power.

SLL *Secondary lobe level*, refers to the ratio of the amplitude at the peak of the main lobe to the amplitude at the peak of the secondary side lobe.

GPR *Ground Penetrating Radar*, is a non-intrusive radar that operates by transmitting high-frequency radio waves into the desired area to detect objects or singular elements hidden in a medium.

RFID *Radio Frequency Identification*, refers to a technology that uses radio waves to passively identify a tagged object.

WPT *Wireless Power Transfer*, is a transmission of electrical power without using wires.

CATR *Compact Antenna Test Range*, is an antenna measuring system that provides an efficient means of obtaining a plane wave illumination of an Antenna Under Test over a certain area, normally provided by a long far-field range, but in a relatively short distance in this case.

PWG *Plane Wave Generator*, refers to an antenna that can radiate a uniform plane wave in a certain area.

GO *Geometrical optics*, is a model that describes the electromagnetic wave propagation in terms of rays. The rays are computed considering their electrical paths.

MoM *Method of Moments*, is a numerical computational method of solving linear partial differential equations which have been formulated as integral equations. It is used to analyze the reflectarray element in order to characterize its behavior by means of the reflection coefficients matrix.

NUFFT *Non-Uniform Fast Fourier Transform*, is an algorithm used to efficiently compute the Fourier transform in a non-uniform grid.

CP *Conjugate Phase*, refers to the conjugate approach to design antennas.

DoF *Depth-of-field*, corresponds to the theoretical decay of 3 dB of the electric field in the propagation direction in a Bessel beam.

PLA *Polylactic acid*, refers to a thermoplastic material made from renewable resources used in additive manufacturing.

FDM *Fused Deposition Modeling*, is a type of additive manufacturing technology that enables the fabrication of three-dimensional objects.

SP *Square prism lens*, a lens made up of square prism elements.

HP *Square prism lens*, a lens made up of hexagon prism elements.

PVA *Polyvinyl alcohol*, is a water-soluble synthetic polymer used in additive manufacturing, commonly used to fabricate the supports of other pieces.

IoT *Internet of Things*, refers to the interconnection via the internet of computing devices embedded in different objects, enabling them to send and receive data.

B5G *beyond 5G*, refers to the next generation of 5G.

FR2 *Frequency Range 2*, gathers a set of millimeter frequencies reserved for 5G.

MoM-LP *Method of Moments based on local periodicity*, refers to the Method of Moments based considering local periodicity.

NF-NF *Near-field to near-field transformation*, is a transformation to obtain the near-field in the desired grid by using the near-field obtained in another grid.

OTA *On-the-Air measurement*, is a method used to predict the performance and reliability of wireless devices. The devices are placed in a free-space environment inside a test chamber, where different real-life tests are simulated.

FF-range *Far-field range*, is an antenna measuring system based on a far-field acquisition range.

NF-range *Near-field range*, is an antenna measuring system based on a near-field acquisition range.

AUT *Antenna Under Test*, refers to the antenna whose radiation pattern is measured in an antenna measuring system.

NF-FF *Near-field to far-field transformation*, refers to the transformation performed to obtain the far-field of an antenna through its measured or simulated near-field.

QZ *Quiet zone*, is the area or volume wherein the near-field of an antenna can be considered as a far-field since the near-field behaves like a uniform plane wave. It is commonly defined in compact antenna test range systems and is used to measure the radiation pattern of an antenna.

DUT *Device Under Test*, refers to the device whose radiation pattern is evaluated in a measuring system.

CHAPTER 1

Introduction

1.1. Motivation

The constant development of communications systems has arisen the need for systems that satisfy increasing tight requirements to enhance their quality. In particular, the popularity of wireless communications has required an inherent need of the development of the antenna's subsystems. Depending on the application, different parameters can be optimized, such as bandwidth, matching, radiation pattern, efficiency, etc.

When it comes to terrestrial and space communications, the radiation pattern synthesis is quite important to obtain non-canonical beam patterns to fulfill certain footprints or coverages. Some applications that demand shaped beams are base stations for cellular systems from 2G to 5G, Local Multipoint Distribution Service (LMDS), Worldwide Interoperability for Microwave Access (WiMAX), etc.; Direct Broadcast Satellite (DBS) requires a shaped beam to generate a given footprint on the Earth surface; or global Earth coverage applications, which demand isoflux patterns to provide constant energy flux on the surface of the Earth.

For the recent 5G communications and especially wireless communications, high energy efficiency is expected to be a key factor in scenarios with a massive number of users and high data rates. These scenarios consider the connection between users but also with a myriad of different devices such as sensors or electronic appliances. The proximity between the different 5G elements, mostly in the near-field region of their base station, makes the development of efficient indoor communication within the near-field an indispensable or even desired option to support 5G and beyond wireless communications. Similar to terrestrial or space communications, indoor communications require the use of antennas with shaped beam radiation patterns to improve the performances of these communications.

Traditionally, aperture antennas have been widely known in wireless communications, highlighting parabolic reflectors or lenses in space communications. However, both reflectors and lenses are bulky, complex, and expensive when dealing with shaped beam patterns. Conversely, array antennas are used on communications, both terrestrial and space communications, and near-field applications with focusing requirements. With the popularization of microstrip technology, array antennas have been a low-profile and low-cost solution when aperture antennas are needed. However, the current trend to increase the frequency in order to achieve a larger bandwidth, such as Ka-band on 5G or space communications, makes array antennas not feasible solutions because of the insertion losses of the feeding network at those frequencies.

A potential alternative to reflectors, lenses, or even microstrip arrays is spatially-fed array (SFA) antennas. These antennas can be physically implemented with microstrip technology but the replacement of the feeding network by another antenna makes SFAs an attractive solution for any kind of application in which the use of aperture antenna is common nowadays. SFA antennas are defined as an array antenna whose feeding network is replaced by a primary feed, such as in reflector antennas, which excites the array elements. Nowadays, this concept gathers reflectarray and transmitarray antennas and, the recent metasurfaces can be also considered in this classification.

Broadly speaking, an SFA antenna consists of a primary feed, typically a horn antenna, and an array of radiating elements, which add a certain phase-shift on either the transmitted or reflected wave. Figure 1.1 shows the typical structure of a reflectarray antenna based on a flat surface of printed elements illuminated by a horn antenna. In principle, the concept of spatially-fed array antenna is not associated with any particular technology. The phase-shifter elements of the first reflectarray proposed were short-ended waveguides of different lengths [1], resulting in a bulky and heavy antenna for practical applications [2]. Up to now, reflectarray and transmitarray phase-shifters have been mostly based on printed technology such as printed patches, dipoles, slots, split rings, etc. Newer solutions are based on printable materials to obtain antennas with additive manufacturing techniques or novel materials for metasurfaces. From now on, our interest is focused on both transmitarray and reflectarray antennas.

SFA antennas have some interesting characteristics that make them an attractive solution compared to reflectors, lenses, or printed arrays. First, the phase-shifter elements are based on printed or even additive technology, therefore SFA antennas are low-profile. For this reason, reflectarray and transmitarray antennas are lighter and more compact than reflector or lens antennas. Second, the losses depend on the quality of the substrate (loss tangent) and the elements, obtaining notably lower losses than classic printed arrays since the feeding network is not required. However, SFA

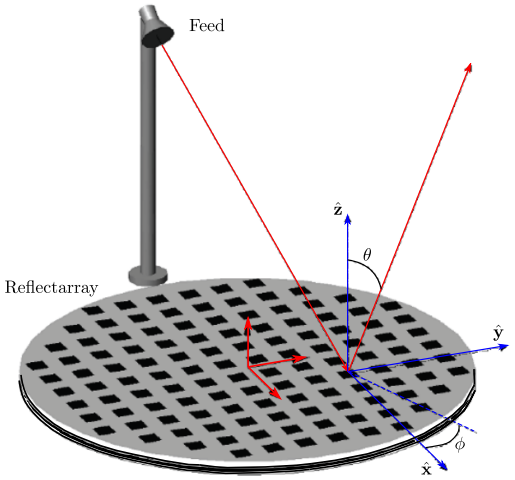

Figure 1.1: *Basic scheme of a reflectarray antenna.*

antennas require a larger volume structure (array plus feed) than planar printed arrays because of the primary feed. Third, the technology to manufacturing SFA antennas can be either photo-etching or additive manufacturing. The photo-etching process is the same as the one used in Printed Circuit Boards (PCBs), it is thus a well-known and mature technology that provides a precise and relatively cheap solution. Additive manufacturing is a current research topic focused on a reduction of the manufacturing costs while keeping the antenna performance. Also, SFA antennas are suitable to achieve beam reconfigurability or multi-beam solutions, reducing the costs of other alternatives such as phased arrays.

Unlike large reflectors or lenses, which have an inherent large bandwidth mainly limited by the feed, the bandwidth of SFA antennas is limited by two factors, namely the poor bandwidth of the narrow-band resonant elements, which is usually around $3\% - 5\%$ and the spatial phase delay [3, 4]. Despite reaching the reflector or lenses bandwidth is unattainable, it can be improved by using wideband printed elements which produce several resonances [5,6], or non-resonant elements [7]. The second issue can be solved by adjusting the geometry of the elements at several frequencies [5], increasing the f/D ratio (focal distance out of antenna aperture) [4], using true-time delay elements [8] or using more complex structures such as curved [9] or faceted surfaces [10, 11].

Previous works have demonstrated that both reflectarray and transmitarray are suitable technologies for applications that require shaped beam patterns, high gain, or

multiple beams as an alternative to reflectors, lenses, or classical printed arrays [12–15]. This thesis is focused on the development of new techniques for the analysis and synthesis of near-field patterns on SFA antennas. A special effort is made on transmitarray and reflectarray for novel near-field applications such as communications and measurement systems in the millimeter frequency (mm-wave) band.

Both reflectarray and transmitarray antennas are subjects of many research projects worldwide, which demonstrate their potential for many applications, with a combination of conformal performances and flexibility of microstrip technology. In particular, the research carried out during this thesis is framed within several projects ranging from several applications. The Ministerio de Economía y Competitividad, belonging to the Spanish Government, has funded three research projects: *"Múltiples fuentes de información para mejorar técnicas de EM inverso para aplicaciones de reflectometría e imaging (MIRIIEM)"*, with code TEC2014-54005-P; *"Antenas Reconfigurables para Transferencia Eficiente de Información y Energía a múltiples usuarios en femtoceldas/Reconfigurable Antennas for a Multi-User Efficient Information and Energy Transfer in femtocells (ARTEINE)"*, with code MINECO-18-TEC2017-R; and *"Enabling Antenna Technologies for Smart Connectivity in mm-Wave 5G and Beyond (ENHANCE-5G)"*, with code PID2020-114172RB-C21. The European Space Agency (ESA) has funded the project *"Reflectarray Antennas with Improved Performances And Design Techniques (RAIPAD)"*, with code 1-7064/12/NL/MH. Finally, the company METAWAVE Coorporation has funded the project *"Synthesis and design of reflect-arrays for improving coverage of 5G base station antennas at mm-waves"*, with code FUO-221-20.

1.2. State of the art of spatially-fed arrays for near-field applications

In this section, a review of the state of the art on spatially fed array antennas will be presented. The so-called spatially-fed array antenna gathers every antenna based on a combination of a primary feed and a phased array antenna, giving a non-close set of feasible alternatives that can belong to this classification. However, only those antennas directly related to the work developed in this thesis will be mentioned. First, an introduction to reflectarray and transmitarray antennas is presented together with a review of the different elements of which those antennas are made. Then, different techniques to analyze the field radiated by those antennas and different algorithms for synthesis are introduced. Finally, an overview of the state of the art of near-field

applications is presented.

1.2.1. Reflective spatially-fed arrays: Reflectarrays

The first reflectarray antenna was introduced by Berry, Malech, and Kennedy [1] in 1936. This reflectarray consisted of an array of shorted-ended waveguides of variable length which reradiate the field provided by the primary feed. The phase-shift of each element is adjusted by changing the length of the waveguide, which allows tilting of the beam. This prototype was bulky and heavy and, therefore not practical. In the 1970s a reflectarray was developed consisting of four spiral-shaped arms. This reflectarray was known as a spiralphase reflectarray [16] and it used to switch diodes to electronically scan the main beam. The spiraphase reflectarray was a bulky and heavy antenna. It was not until the 1980s and early 1990s when reflectarrays were investigated with more detail, occurring simultaneously with the popularization of the microstrip technology. This technology enables the development of lighter and smaller reflectarray antennas.

From that moment, reflectarray research activity has gradually increased for different applications that require large aperture antennas. Reflectarray antennas also present advantages in terms of manufacturing costs, beam reconfigurability, or mechanic characteristics. The manufacturing cost of a reflectarray antenna is independent of the beam characteristics, never mind whether is a pencil or a shaped beam. This fact is quite important for applications that use shaped reflectors since they are more expensive because of the cost of manufacturing molds and their impossibility to reuse them on different applications. Also, reflectarray antennas can provide an electronically reconfigurable beam by introducing control elements in the printed reflectarray elements, such as PIN diodes [17], MEMS (MicroElectroMechanical Systems) [18] or MMIC (Monolithic Microwave Integrated Circuits) devices [19]. In space applications, having a flat profile antenna is essential since the folding for the transportation in the spacecraft and deployment in space is easier than other geometries, such as parabolic reflectors [20]. Recently, reflectarray antennas were proposed as a suitable beam steerable alternative for CubeSat Internet of Space [21, 22].

Previous works have proposed different reflectarray antennas as an alternative to parabolic reflectors, or even phase array antennas in different applications because of their low-profile and low-loss features. Some of these reflectarrays were proposed for Synthetic Aperture Radar (SAR) [23] or DBS [12], generally in space communications [13, 24] or other communications such as LMDS [25]. The most relevant contributions have been developed for space antennas, showing that reflecatarray an-

tennas are able to generate contoured beams [26–28], with cross-polarization level reduction [29, 30] or bandwidth enhancements [31]. Also, a reflectarray antenna was proposed to be used as a sub-reflector of a principal reflector antenna to improve the overall performances [32], and a dual-offset reflectarray was introduced in [33] for the first time resulting in a reduction of the cross-polarization level together with an operational bandwidth of a 20%. Other works demonstrate the performances of reflectarray antennas operating as dual-band [34, 35] dual-polarized antennas, either on linear [36] or circular polarization [37, 38], being this last work the first reflectarray with independent dual-circular polarizations.

Throughout the last years, intensive research has been carried out for developing reflectarray antennas to generate multibeam configurations. Different approaches have been studied, such as single-fed reflectarrays to produce multiples beams per feed at the same frequency [24, 39], multi-feed reflectarray antennas that generate multiple beams by a single feed per beam [40] or dual multi-feed reflectarray to produce one beam per feed using phase aberration correction techniques to obtain bifocal reflectarray antennas [41, 42]. On the other hand, not only planar reflectarrays are from our interest in research activities, but also other geometries have also been presented such as parabolic or doubly-curved reflectarray to generate multiple spot beams in these communications [9, 43] as well as multi-faceted reflectarray for bandwidth improvements [44, 45].

A particular analysis of reflectarray antennas for near-field application will be presented in the next sections.

1.2.2. Transmissive spatially-fed arrays: Transmitarrays and planar lenses

A transmittary antenna is a classical name given to a periodic structure that can modify a radiation pattern of a second antenna source that behaves as a primary feed. Owing to their electromagnetic properties, a transmitarray antenna can modify the incident electromagnetic wave of the primary feed, and perform a focusing transmitted beam, beam steering, contoured beam, or even a polarization control. Generally speaking, a transmitarray antenna behaves similar to a lens, allowing it to pass through the incident wave of an electromagnetic source with an alteration or not of its radiation pattern.

Although research on transmitarray antennas has been closely related to reflectarray, there are fewer published works in the literature. There is a fundamental difference that increases the complexity when working with transmitarray antennas. In a

reflectarray if the elements are well matched to the frequency of operation, the incident wave is reradiated in the expected direction. However, if the elements are not matched to the desired frequency, the elements will have a small effect on the incident field while the ground plane will be responsible for the reflection, which will be produced in the specular direction (based on Snell's law) of the incident field, but the wave is always reradiated. On a transmitarray antenna, if the elements are not well matched to the free space or the frequency of operation, the incident wave will be partially reflected or, reflected in the worst case, resulting in no transmission through the antenna. Hence, on a transmitarray is necessary to have the control of both transmission and reflection of the elements while on a reflectarray is only needed on reflection. Broadly speaking, a transmitarray must be as *transparent* as possible, while a reflectarray must be a perfect reflecting surface.

The one that could be considered as the first transmitarray antenna is a microwave lens presented by McGrath in 1986 [46]. This lens achieved focusing and scanning capabilities by connecting two microstrip patch antennas using a bias on both sides of a planar structure. This configuration forms a spatial array whose elements are patches, similar to the current definition of a transmitarray. From that moment, transmitarray antennas have been widely used in space applications similar to reflectarray antennas. A contoured beam transmitarray to accomplish the contour beam pattern for a European coverage region is presented for both transmit and receive frequency bands in [47]. A transmitarray is synthesized to shape the beam according to a secant-squared power radiation pattern at 30 GHz in [48]. Also, transmitarray antennas have been proposed for reconfigurable beams using varactor diodes for a continuous phase range [49,50], or even liquid crystal [51] in the transmitarray elements. However, most of the research activity throughout the last years has been focused on the achievement of transmitarray antennas with beam steering or multiple beam generation capabilities for Satellite Communications (SATCOM). In [15] a polarizer is combined with a transmitarray antenna to generate dual-band dual-circularly polarized beams at 20 and 30 GHz with a feeding linear polarized horn antenna. Also, in [14] a transmitarray reaches a dual-band dual-polarized beam configuration at 20 and 30 GHz. In this case, the feeding antenna is a dual-band circularly polarized ridged cavity antenna, and the unit cell topology uses a dual-polarized structure. In [52] a wide beam scanning solution based on a dual-band transmitarray antenna is presented to cover both up-link and down-link at Ka-band. This transmitarray is composed of two subarrays, one for the up-link and the other for the downlink. Like reflectors and reflectarrays different bifocal techniques have been developed for transmitarrays, using either single [53] or dual transmitarray configurations [54]. Recently, a transmitarray antenna has been

suggested for inter-satellite links in CubeSat communications [55]

These works are only a few examples of the transmitarray antennas capabilities and their main research activity. In the next sections, some of the previous works developed on transmitarray for near-field applications will be discussed.

1.2.3. Phase-shift elements for reflectarrays and transmitarrays

The performances of SFA antennas such as bandwidth, cross-polarization, or dissipative losses among others, as well as the implementation of a phase-only synthesis solution, depending on the elements used to physically implement the phase-shift. The analysis and design of SFA elements are some of the most fruitful research topics nowadays. As a consequence, the result of a phase-only synthesis is the phase distribution, either on transmission or reflection, that should implement the SFA elements to radiate the desired beam. Therefore, different technologies can be applied to implement the required phase-shift. A revision of the state of the art of several phase-shift elements concerning different technologies is detailed in this part.

1.2.3.1. Printed elements

The most popular technology for both transmitarray and reflectarray is printed elements based on microstrip. There is a wide range of printed elements that can be used as phase-shifters, most of them implement their phase-shift by adjusting the geometry or some dimensions of the element. The classical geometry element is based on canonical shapes, mainly patches, slots, dipoles, or rings. A few examples are shown in Figure 1.2. A classical element used to produce a given phase-shift is microstrip patches connected to transmission line segments of different lengths [78]. The phase-shift can be controlled by the adjustment of the length of the stub. However, two important drawbacks are found. First, the cross-polar radiation produced is quite high since spurious radiation is produced because of the bent stubs. This effect can be compensated by changing the bending direction of the stubs [79]. Second, the stub is a microstrip line that inherently adds certain losses.

One of the most popular phase-shift concepts on both transmitarray and reflectarray antennas is the adjustment of resonant length dipoles when working in single linear polarization [80,81], crossed dipoles for dual-polarization [82] or the size of rectangular patches [12, 83–85]. These geometries produce lower dissipative losses and cross-polar radiation than the patches with stubs. Alternative configurations can be found in published works such as aperture coupled patches to delay lines [86], elements with rotation angles [87], rings [88], double square rings [89, 90], spiral-dipoles [91],

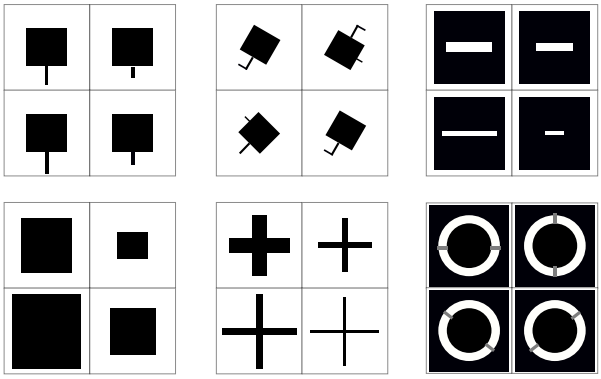

Figure 1.2: *Classical topologies of phase-shift elements: Squared patches with variable length stubs, sequential rotation patches, variable length slots, variable size rectangular patches, variable length crossed dipoles, resonators with reactive charges.*

stacked Jerusalem cross dipoles or doubly bent dipoles [92, 93], among other configurations. Some of these concepts, such as the elements with variable rotation angles or the rings, are only valid for circular polarization.

An important limitation of most of these concepts is the narrow band response of the element imposed by the bandwidth of the resonant elements. The concept of phase control by adjusting the resonant dimension of the element produces lower dissipative losses and cross-polarization levels than using patches connected to variably-length stubs. However, practical reflectarray and transmitarray designs require at least a full phase cycle of 360°, and the maximum phase-shift range achieved by those elements is in the order of 330° for substrates that are very thin [2]. Moreover, the strongly non-linear behavior of the phase limits the operation bandwidth of the antenna.

These drawbacks can be overcome by stacking two or three elements layers [5,24,94,95], or even more stacks are required for transmitarrays [96]. A high number of stacked layers, four or more in reflectarrays, is a not solution since the phase curve would be too steep and sensitive to manufacturing tolerance. A small error in the element dimension would produce a very large variation in the phase-shift. Smooth phase curves are obtained with two layers of patches [94] and stacking three layers a phase-shift range larger than 720° is obtained in [5]. Increasing the number of layers results in obtaining more degrees of freedom for optimizations in a frequency band.

Different alternatives have been proposed for broadband reflectarray elements as Figure 1.3 depicts. The aperture coupled reflectarray element is a broadband element based on a delay line that is adjusted to produce the required phase-shift [86, 97, 98]. Since the delay line can be very long, the broadband response of the element is in-

creased. However, two drawbacks are found in this configuration. First, the larger length of the delay line, the higher the dissipative losses. Moreover, a good design is more complicated, since apart from design the stub to produce the required phase-shift, it must be well matched to the impedance of the radiating patch element to obtain the maximum power transference from the stub [2]. A variation of this topology can be found in [99], it was presented a cut-ring patch coupled to a delay line. However, the performances are similar to the coupled patch, while the inconveniences are also the same.

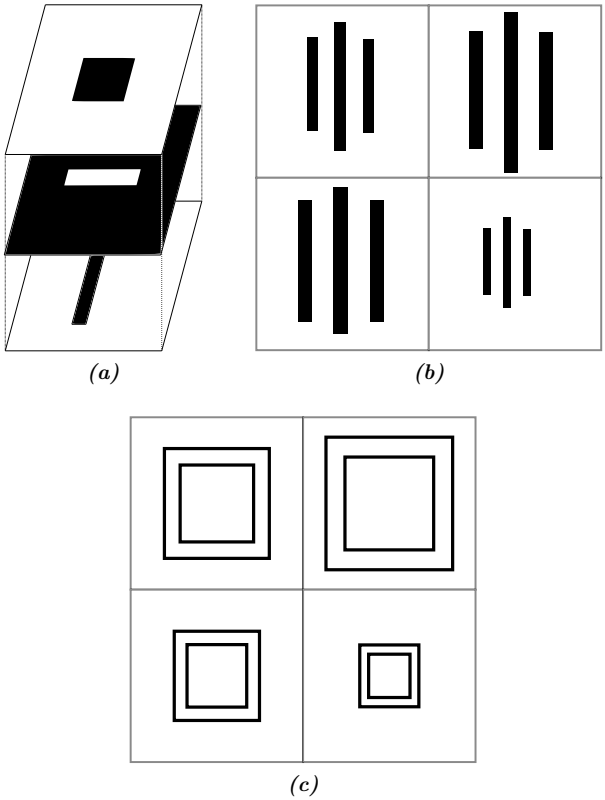

Figure 1.3: *Broadband reflectarray topologies: (a) Patch coupled to a delay line. (b) Parallel dipoles. (c) Concentric square rings.*

Recently published works are focused on modifications of the dipole element, using three [100] and five [101] dipoles to increase the phase-shift range combining different resonances to overcome the bandwidth limitation. This cell presents the major advantage of being printed on a single layer, along with the limitation of working in one polarization. The three-dipole cell was improved to work in dual-polarization in [102]

by using two orthogonal sets of three parallel dipoles, each set is printed in a different layer. It increased the complexity by adding an extra layer, but now it can work in dual-polarization. Comparing this two-layer dipole cell with the stacked patches topology, the dipole cell improved the coupling isolation between polarizations as well as a reduction of the cross-polarization.

Different improvements of this cell were studied in [103] to enhance the cell performances. First, the topology of [102] was extended to five dipoles in each layer instead of three. The result was a more complex topology with similar performances concerning the three-dipole configuration. To obtain more resonances and increase the phase-shift range, the number of layers was increased to finally obtain a four-layer reflectarray element, combining laterally coupled parallel dipoles with stacked dipoles. This configuration presents excellent results in phase range, polarization independence, and cross-polarization levels. The main drawback of this topology refers to the use of four levels of metallization, which significantly increases the complexity and thus the manufacturing cost increases too. The number of stacked layers of this topology was reduced from 4 to 2 by shifting half-a-period the set of dipoles associated to one polarization, and by printing on the same surface three parallel dipoles for one polarization and one dipole for the orthogonal polarization. The complexity of the cell was reduced while maintaining the performances with only two stacked layers. Different modifications of this two-layer cell based on stacked shifted sets of dipoles can be found in recently published works with quite good performances [104–106].

Concentric geometries have been presented as topologies that introduce several resonances increasing the phase range for operating in both a single frequency and dual-frequency [107–109]. These topologies can be found on single or stacked-layer configurations and the most popular ones are concentric split rings. These elements provide a phase control that can be adjusted independently for two separate frequencies. However, single layer split rings suffer from the narrow band limitation [107]. About parallel coplanar dipoles [100], concentric topologies present some disadvantages. The first one is that even though only one layer of metallization is used, the geometry of concentric topologies is more complex. Second, the coupling isolation between polarization is not as good as using dipole elements.

Particular attention should be given to the element known as Phoenix cell [110]. This element is presented as a broadband solution that is based on the cell topology rebirth capability. The geometry cycle is reset after almost achieving a phase cycle of 360°, as Figure 1.4 depicts. The rebirth of the geometry ensures a very smooth geometrical variation on the reflectarray design, therefore preserving the local periodic conditions between phase cycles. Some modifications of the original Phoenix cell were

studied to reduce the size and improve the phase response linearity [111, 112].

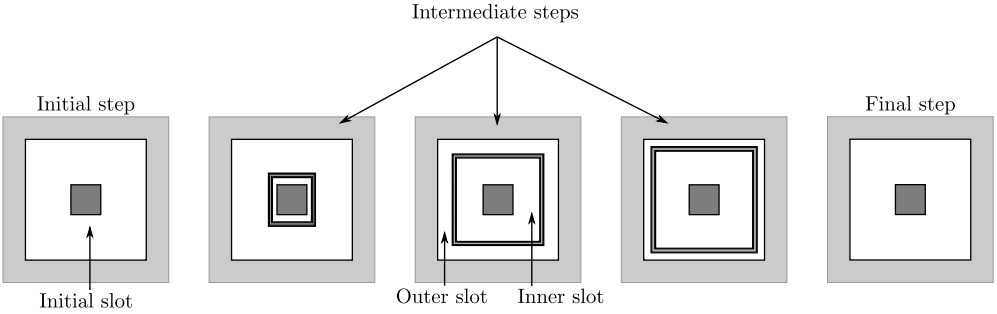

Figure 1.4: *Evolution of the original Phoenix cell geometry over a* 360° *phase cycle.*

Other single-layer elements include a quasi-spiral phase delay line with the capability of operating in linear or circular polarization depending on the polarization of the incident wavefront, producing around 1000° of phase delay [113]; double square rings and double-cross loops [114]; hexagonal rings [115]; circular patch with a curved stub which provides more than 1000° linear phase-shift range with low cross-polarization [116], among others.

1.2.3.2. Dielectric resonators and dielectric-only elements

Throughout the last decades, different alternatives have been proposed in the field of dielectric resonator (DR) antennas. The operational principle of a dielectric resonator is based on the use of a dielectric material of moderate to high refractive index, typically higher than $n > 3$, which generates a strong discontinuity at the dielectric boundary to free space. An originated wave inside the dielectric will be strongly reflected at this boundary, reflecting most of its energy to the dielectric. Hence, a part of this dielectric will behave as a resonant cavity since the reflected wave will be reflected internally forming a standing wave with a certain resonance frequency. Then, a given dielectric resonator will have several non-harmonic modes of resonance that are conjoined to enlarge the overall phase-shift of the DR up to more than 360° [117]. The main drawback of DR is the absence of control on the excitation of the different non-harmonic modes, thus on the phase-shift of the DR. Different topologies of DR behaving as elements of different SFA antennas can be found in published works. In [118] two different DR-based elements are proposed for a transmitarray antenna. The first element is based on a dielectric sheet of constant height with two rectangular dielectric resonators on either side of the substrate. The second element replaces the dielectric sheet to place the two rectangular resonators on either side of a ground plane coupled

with a rectangular slot. The cell is evaluated at 11 GHz obtaining a phase-shift close to 360° in both cases and a maximum transmission loss of 4 dB in the case of the first cell and 2 dB when the ground plane is used instead of the dielectric sheet. It is likely that at those frequencies DR does not provide a competitive advantage concerning printed technology. However, for broadband applications, DR-based elements could significantly improve the in-band response of the antenna. In a recently published work, [119], a transmitarray antenna based on a DR element similar to [118] has been presented, obtaining a large operational bandwidth with a 1 dB steady gain on a range from 14.5 to 20 GHz, up to a 29% of bandwidth. These results are not reachable with printed technology. At high frequencies such as terahertz frequencies or the upper band of millimeter band, it is not feasible to manufacture printed elements. Moreover, different alternatives such as metallic resonators are not an option since metals cease to behave as near-ideal conductors [120]. In [121] and [117] two DR-based elements are presented at terahertz frequencies for a transmitarray and a reflectarray, respectively.

Dielectric-only elements are characterized for not having any metallization, and they can be implemented in such different configurations. A wide technique is based on defining elements with dielectric perforations. This concept was applied in [122], in which a Fresnel lens antenna was perforated with circular holes whose dimension changes according to their position. The perforations allow to change the dielectric constant of the substrate, thus the phase compensation of the Fresnel lens, and different areas are defined with different phase compensations. This concept was applied for both transmitarray and reflectarray dielectric-only elements in [123]. The element was based on a dielectric layer with four circular holes of the same radius. The variation of the radius enables the adjustment of the phase-shift of the transmission coefficient or when the element is backed by a ground plane, the reflection coefficient. Although the numerical results for these elements show an enhancement of the in-band response, the results on reflection were not as good as expected. Similar to DR-based elements the phase-shift depends on the material but not on an element resonance. Hence, the in-band response can be improved with dielectric-only elements instead of printed elements. Moreover, these topologies are easier to manufacture than stacked topologies or multi-resonant printed elements [124]. In [125], a similar element was introduced for a reflectarray antenna. A single dielectric layer was drilled with a square hole which side allows to control the phase-shift. Then, the element is backed by a ground plane to reflect the incident wave.

This topology was improved to a multilayer configuration of 6 layers to enhance the in-band response of a transmitarray [126]. A different multilayer topology was evaluated in [127], which is based on three stacked layers. The middle layer is a

dielectric layer with a square hole with a variable side that enables the control of the phase-shift. Then, the two external layers placed on either side of the middle layer, are a dielectric layer with a different side square hole. These two external layers are designed to behave as a quarter-wave impedance transformer to minimize the reflection losses and improve the transmission response of the cell. The side of this cell is adjusted to match the impedance concerning the side of the middle layer hole.

A more recent alternative to control the dielectric-only element phase-shift consists of the variation of the element height instead of drilling the element. An example of this concept can be found in [128]. The element is based on a dielectric post, which at its maximum height, behaves as a fully dielectric cell, and as the height decreases the equivalent infill factor is reduced and the phase-shift is modified. Two drawbacks are found in this type of element. The first one is that one of the surfaces does not provide a planar profile and the different heights of the cells may cause some diffraction. The second, as [129] shows, the transmission coefficient is poor due to the dielectric losses and the reflection at the air-dielectric interfaces. An improvement is made in [129] by introducing an antireflection structure to reduce the impedance mismatch at the dielectric-air interfaces. The dielectric loss is inherent to the material used but this structure can suppress the strong reflection at the air-dielectric interface. In [7] a similar concept is applied to an element presented in [125] but on transmission (without the ground plane). The element is improved by adding two tapered matching layers that reduce the impedance mismatch on either side of the air-dielectric interface. Moreover, the tapered matching layers improve the angular stability ensuring that a change on the angle of incidence, no higher modes resonate, as occurs on other cells [130].

An additional advantage of dielectric-only elements is its design using 3D-printable materials, which allows manufacturing the antennas applying different 3D-printing techniques, reducing the fabrication costs, and providing lighter solutions.

1.2.3.3. Metal-only elements

Likewise dielectric-only elements there is an alternative based on metal-only elements. These elements do not use any dielectric but metallization. As occurs in printed elements the phase-shift can be controlled by modifying the geometrical parameters of the metal element. Most of these elements are based on slots made on a metallic layer or different stacked metallic layers. An important issue lies in finding a configuration to support the stacked metallic layers since there is not dielectric and the layers are separated by air gaps.

In Figure 1.5 different topologies of metal-only slot elements are shown. An inherent drawback of metal-slots concerning printed and dielectric-only elements is the need of using at least 3 layers to obtain a full phase cycle of 360° for a 3 dB transmission coefficient and a quaternary layer for 1 dB transmission coefficient [131]. This last quaternary-layer cross-slot element was used in [132], obtaining a full phase cycle with less than 1 dB losses on the transmission coefficient at 11.3 GHz. This topology provides good angular stability for angles of incidence lower than $\theta = 30°$. However, there is an inherent problem due to the slot element configuration. Each conductor layer blocks the following conductor layer producing a deep impact on the transmission coefficient of each element. This blockage depends on the angle of incidence and the feed polarization. However, better angular stabilities are obtained when using printed elements.

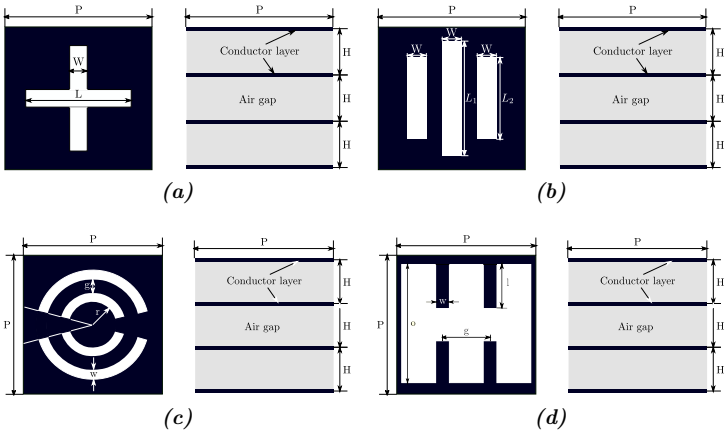

Figure 1.5: *Different elements based on metal-only topologies: (a) variable length crossed slots (b) variable length slots (c) concentric rings (d) variable length of slots and a crossed slot.*

A different topology based on a four-layer metal-only slot is used to operate on dual-band [133]. The element consists of four identical metallic layers and each layer is made up of three slots: two identical and shorter slots on the two sides of a middle longer slot. This topology is similar to the three printed parallel dipole elements of [100]. A major advantage of this element is that only by changing the dimensions of the slots, it is feasible to achieve a 360° and better losses than 3 dB on two separated frequencies. In addition, the cell provides quite good isolation between the two proposed frequencies.

A double-slit ring slot element is analyzed in [134]. This structure is based on four layers of two concentric split ring slot that controls the phase-shift by the variation

of the smaller ring radius. A full transmission phase range of 360° is reached with a linear phase curve, and the transmission loss is better than 1.5 dB. This cell has the advantages of low transmission losses and less sensitivity to the angle of incidence changes. The maximum phase deviation is 40° while most of the analyzed cells present a transmission loss better than 1.5 dB.

More complex topologies can be employed to obtain a circularly polarized element. In [135] a metal-only element has four identical layers of cross-slot elements that are connected by three identical waveguides instead of air gaps. The waveguide improves the isolation between elements and allows to manage higher power than air gap separations. The circular polarization is obtained by rotating the cross slots properly. Moreover, the polarization of the incident wave can be reversed with better conversion efficiencies than -0.75 dB within the simulated band.

Generally, metal-only elements present low transmission losses since they are based on a conductor or metal layer. A potential application is designing transmitarray antennas for high-power microwave applications or high frequencies where printed technology cannot be used. The main drawbacks are the number of layers required to reach a full phase cycle of 360°, the narrowband response of the elements and, their sensitivity to the angle of incidence regarding printed or even dielectric-only elements.

1.2.3.4. Elements for reconfigurability: graphene, liquid crystal and active elements

The rise of new materials and technological developments bring an opportunity to evolve cell topologies. For instance, in [136] it is evaluated for the first time the feasibility of fixed beam reflectarray at THz based on graphene. This material is proposed for an operational frequency of 1.3 THz, unattainable for none of the previous topologies discussed. The use of graphene improves the bandwidth response with a low cross-polarization level and low sensitivity to the angle of incidence compared with other elements such as gold patches. Another important advantage is that the number of elements does not increase the manufacturing complexity since the reflectarray is fabricated monolithically. The reflectarray proposed is comprised of 25448 electrically small elements. A long-term aim for graphene is to achieve an efficient dynamic reconfiguration reflectarray antenna at those frequencies. So far, only numerical simulations have been obtained for reconfigurable reflectarray [137, 138]. The reflectarray presented in [137] could be reconfigured with different biasing conditions to different modes of vortex radio waves at 1.6 THz. Although these results are only based on numerical simulations, graphene seems to be a promising material for future applications in THz communication systems. However, some drawbacks must be taken into

account. The graphene losses increase about other materials such as gold elements as well as the cost of the monolithic fabrication [136]. In addition, some theoretical limits on the efficiency of reconfigurable and non-reciprocal graphene antennas are presented in [139], mainly focused on graphene terahertz reflectarrays.

Liquid crystals are an alternative to implement reconfigurable reflectarray at high frequencies, especially at (sub)millimeter bands. At those frequencies, liquid crystal elements present better radio-frequency performances rather than at microwave or millimeter frequencies. Liquid crystal has been traditionally used in optical frequency applications and its use in lower frequencies decreases the liquid crystal performances obtaining a high loss element. In [140, 141] different liquid crystal elements were analyzed at a frequency of 77 GHz, obtaining losses from 6.7 dB to a maximum of 16 dB and a maximum phase-shift range lower than 300° depending on the topology used. Aiming for reaching a larger phase-shift range, in [142] the presented cell is based on three dipoles connected by a bias line perpendicular to the dipoles to polarize the liquid crystal layer. This element provides a phase-shift range larger than 550°. A similar element is used in [143] to design an electronically scanned reflectarray at 100 GHz. In [144] a nematic liquid crystal cell based on a patch radiating element is used to obtain a phase-shift range of 165° with a loss of 4.5-6.4 dB at 102 GHz and 130° with a loss variation of 4.3-7 dB at 130 GHz. A recent work [145] used a different nematic liquid crystal element that can achieve a phase-shift larger than 360° and a maximum loss of 7 dB. It should be noted that this element is presented to design broadband electronically scanned reflectarray at a central frequency of 24 GHz.

Different approaches can be used to obtain reconfigurable antennas, both reflectarray and transmitarray. The elements can be designed to provide a continuous phase control or a phase quantization to tune either the transmission or reflection phase and perform beam-forming functions. Some examples of continuous phase control elements can be found in [146], where two reconfigurable elements are proposed. The elements consist of a single and stacked patches configuration, based on proximity-coupled feeding and two balanced reconfigurable bridged-T phase shifters with varactor diodes. These topologies achieve a phase range larger than 400° with an average insertion loss of 3.6 dB. However, continuous phase control elements are quite complex structures and provide higher losses regarding phase quantization elements. The latest is mainly based on PIN diodes or MEMS to control the element state and its phase-shift. In [147] a linearly polarized electronically reconfigurable element for a transmitarray antenna is presented. The element provides a 2-bit phase resolution in Ka-band. The element consists of a dielectric stack-up of six metal layers, three dielectric substrates, and two bonding films. The radiating elements are center-fed O-slot rectangular patch antenna

printed on both external metallic layers and loaded by two PIN diodes that control the transmission phase. This element provides four different phase-shifts and the minimum insertion loss at the central frequency is 1.4 dB in the worst case. This cell was experimentally characterized in [148] obtaining similar results. In [149] a reflectarray based on patches aperture-coupled to delay lines is presented. The antenna switches the beam from $\pm 5^{\circ}$ using PIN diodes for the phase-shift control. The cell provides a very large phase range with an average loss in the order of 0.4 dB of insertion losses because of the PIN diode. Conversely, topologies based on MEMS typically provide lower power consumption, a better linear response, lower losses, and high isolation. Moreover, MEMS can be implemented with monolithic technology which decreases the complexity of the manufacturing process. A cell similar to [149] was analyzed in [18] but using MEMS instead of PIN diodes. In [150] a reflectarray antenna monolithically integrated was designed and manufactured to achieve switching the main beam at 34.8 GHz.

1.2.4. Synthesis techniques for spatially-fed arrays

The synthesis of antennas can be explained as a process to sought an antenna geometry so that it fulfills a set of field specifications. Although there are no restrictions on any aspect of the antenna that is suitable to be optimized in a synthesis process, and there are algorithms that can deal with this generalized problem [56], it is preferable to work with a simplified case, only focused on the optimization of one parameter such as the elements for a fixed and known antenna structure and feed system beforehand.

Likely, the most popular technique for the synthesis of shaped beam patterns is the Phase-Only Synthesis (POS), especially on reflectarray antennas. This technique is based on the fact that either the direct reflection or transmission coefficients, as well as the excitation on arrays, directly control the shape of the radiated pattern. Hence, the POS only needs to work with the phase of those coefficients, enormously simplifying the antenna analysis concerning a generalized problem. Despite this consideration, this technique has provided accurate results in the achievement of very complex shaped beam patterns. A phase-only synthesis is independent of the element topology, and the technique only provides the phase that the elements must implement subsequently. The main drawback is that during the synthesis process only the phase of the direct coefficient is considered, thus there is no control over the cross-polar component or different parameters related to the element topology such as the bandwidth or the influence of the angle of incidence on multi-feed configurations.

Different algorithms have been presented for carrying out a phase-only synthesis

and the achievement of complex radiation patterns. The most popular algorithms are: analytical [57,58], steepest descent [59], conjugate gradient [60], Levenberg-Marquardt Algorithm (LMA) [61,62], Intersection Approach (IA) [63,64], genetic algorithms [65], or particle swarm optimization [66–68]. However, each algorithm has its limitations. The analytical approaches are strongly limited to reach complex shaped-beam patterns, though they can be used to generate a good starting point for a more powerful algorithm [25]. The steepest descent has a very slow convergence rate [69, 70], thus it is an impractical solution when dealing with arrays of a large or moderate number of elements. To overcome this limitation the conjugate gradient methods can be adapted to solve non-linear optimization problems, offering a faster convergence than steepest descent algorithms [69]. Another approach that improves both solutions is the quasi-Newton methods, which improve the convergence as well as the efficiency and robustness of conjugate gradient algorithms [70]. Even though those methods have reached acceptable performances on the synthesis of arrays and reflectarray antennas, some of the solutions are difficult to implement into a design, because the resulting phase variation along the reflectarray surface is too high for a potential implementation [71] or, the excitations in array antennas are unreachable in a physical feeding network. Broadly speaking, an important drawback is the degree of freedom of the solutions and their hard implementation into a design along with a strong limitation on the number of variables that can be managed. An algorithm that overcomes these issues is the Intersection Approach, which also is a very efficient solution for dealing with a large number of optimization variables [72]. An inherent drawback of the IA is the traps, i.e., local minima, because of the non-convexity of the sets which deal with [56]. Although the trap problem can be minimized by working with the far-field squared amplitude instead of the amplitude or the complex field [56, 73], this modification causes that the projector which recovers the reflected field cannot be implemented with the Inverse Fast Fourier Transform (IFFT). An alternative is used a minimization algorithm based on optimization techniques, such as the Broyden-Fletcher-Goldfarb-Shanno (BFGS) algorithm [73] or the Levenberg-Marquardt algorithm [74], among others. This variation of the IA is the so-called generalized Intersection Approach and it is less efficient than the original IA but overcomes the trap problems. The majority of published works are related to the synthesis of the copolar component of the far-field radiated by different arrays or SFA antennas. However, some examples can be found on the synthesis of the near-field components such as [75], which proposes a theoretical approach and an alternate projection method, similar to the Intersection Approach, to derive the aperture field distribution aiming to control the sidelobe level and the beamwidth of the near-field radiated by a radial line slot array. Other works are [76]

or [77]. The first work proposes the integration of the plane wave spectrum theory with the Intersection Approach as an analytical near-field system transform function to characterize the forward and backward projector in the angular spectrum domain. This approach enables the use of the Fast Fourier Transform (FFT) and the IFFT. The second work proposes to model the transmitarray antenna and the spillover effect as a planar aperture from which the near-field is computed on a plane close to the planar aperture. Then, this near-field is trimmed according to given restrictions. The phase of the elements of the transmitarray is not obtained from the transmitarray but from the far-field corresponding to the trimmed near-field. Both works claim to use the FFT and provide a faster approach concerning the use of an optimization algorithm. However, both approaches are strongly limited to synthesize a single plane that must be parallel to the antenna aperture, which is an important drawback on the synthesis of the near-field when dealing with applications beyond focusing.

All the algorithms discussed above are local optimizers and strongly depend on the starting point to converge with success to a solution. On the other hand, there are global search algorithms that do not depend on the starting point. These global search algorithms are theoretically able to find the global maximum at the expense of taking many iterations. However, as the number of optimization variables increases, the search space grows exponentially, making it harder to find a suitable solution. Two common approaches for global search algorithms are genetic algorithms (GA) and particle swarm optimization (PSO) algorithms. Both have demonstrated their capability to synthesize phased array antennas, or even reflectarrays [66–68]. However, when dealing with moderate or large arrays the computing time would dramatically increase to achieve convergence.

1.2.5. Near-field antennas

The number of applications that require to operate electromagnetically within the Fresnel region of an antenna has increased their popularity throughout the last years. Most of these applications demand antennas capable of focusing their radiated electromagnetic field within the Fresnel region. This technique increases the electromagnetic power density in a spot of limited size close to the antenna aperture. Although this is not a novel technique, research activities in near-field focusing have proliferated significantly over the last decades, especially at microwave and millimeter bands and for array antennas [151]. Now, an overview of different near-field antennas will be introduced.

Starting from [152], where the properties of focused apertures within the Fresnel

region were defined, different types of aperture antennas have been appearing with this aim. Several planar and linear microstrip arrays have been designed for this purpose. These arrays require adjusting the microstrip feeding network to excite the radiating elements properly. Several examples can be found in literature such as [153], which introduce a 4×4 microstrip patch antenna to focus the near-field at a frequency of 10 GHz; similar to [154] which implemented an array based on broadband U-slotted microstrip patch-elements with an integrated microstrip feeding network at the same frequency or, [155], which uses a planar circular patch array of 2×6 elements at 2.4 GHz. An alternative based on a multi-panel configuration is proposed in [156]. Two different configurations have been studied. The first multi-panel structure is comprised of the same number of planar subarrays that are arranged on a cylindrical surface. Each subarray has its focal point at broadside direction. The cylindrical distribution of the subarrays allows getting a more symmetrical focal spot, comparing with conventional planar arrays. The second configuration consists of two symmetrical panels with their focal points out of the broadside direction. About the configuration of identical subarrays, this approach allows having flatter configurations while the focusing performances are similar. Moreover, the field peak position can be placed in a close position to the antenna surface.

Reflector antennas have been considered to implement near-field focused antennas [157, 158]. The first proposed a dome-shaped ellipsoidal reflector placing the feed at one of the two foci and creating the focused field distribution around the other focus. The second work presents a 3D-printed Cassegrain configuration at terahertz bands. Other alternatives are Fresnel zone plate (FZP) lenses as [159] shows. In this work, a dielectric FZP lens with a discontinuous profile was compared with a doubly-hyperbolic lens at 10 GHz. The focusing performances of the zone plate were shown to be qualitatively similar to the lens, despite delivering less power to its focal spot. Also, the lens obtains a better bandwidth since it is only limited by the feed bandwidth. The zone plate shifted the peak field position as well as the beam waist. In [160] a printed FZP lens is further detailed at Ka-band. Different parameters such as peak maximum positions and their displacement along the axial direction as a function of the focal length, the depth-of-focus, or the sidelobe levels are analyzed.

Other published works also include radial line slot arrays [161, 162] or leaky-wave antennas [163,164] at microwave frequencies. Both alternatives increase the complexity of the design concerning previous antennas. However, other benefits can be obtained such as a frequency scanning of the focal point on leaky-wave antenna due to their inherent dispersion feature of the leaky mode. Recent alternatives have been proposed for near-field-focused 2-D steering [165] and near-field focused multibeam [166, 167].

The first proposes a Rotman lens combined with a leaky-wave SIW slot antenna, scanning in one plane with different frequencies because of the leaky-wave antenna properties and scanning in the other plane by exciting different ports in the Rotman lens. The second work proposes a Luneburg lens to implement a two-dimensional beamforming network to excite a planar phased array of Vivaldi antennas obtaining a near-field focus multibeam radiation. The last work presents a modified Rotman lens to implement the beamforming network of a phased array of patch elements. This solution obtains a 1-D distribution of focused spots in a circular arc distribution. Two recent alternatives propose a dielectric transmitarray to radiate multiple beams [130, 168]. The first work proposes a single feed configuration with a mechanical rotation of the transmitarray to generate a different far-field focused beam in each position. The second introduced a multi-focus transmitarray to generate four focused spots simultaneously. The design is based on a subdivision of the antenna aperture into different areas that are associated with each different spot. Each area is designed according to the spot specifications. This approach is suitable for large aperture and the spots are far from the adjacent beam (broad angular deviation).

Other applications demand antennas whose radiated power is not focused on a limited-size spot but a finite area. This means having a constant power density within an area of the Fresnel region. An ideal approach for these applications is the radiation of beams without diffraction through the near-field region of the antenna. Thus, the transversal profile of the field along the propagation direction remains unaltered within a certain range. These type of beams is called non-diffraction beams, which are ideal solutions of scalar Helmholtz equation in cylindrical coordinates, that are theoretically exempted from the physical diffraction phenomenon. One of these non-diffraction solutions is Bessel beams, which are a well-known solution commonly used in optical frequencies [169–171]. However, non-diffraction beams have not become a research topic of interest at microwave and millimeter frequencies until a few years ago. The suppression of diffraction along the propagation direction results in well-collimated beams, which can have a deep impact on several near-field applications. However, Bessel beams are not achievable by finite radiating apertures. A non-diffraction beam inherently implies carrying infinity energy which is only valid for infinite aperture distributions. When using a finite radiating aperture a pseudo-Bessel beam is produced. The amplitude of these beams only remains constant at a certain distance before spreading and losing their collimating property.

A common approach to produce pseudo-Bessel beams at optical or high frequencies is axicons. An axicon is defined as a conical lens that can convert a Gaussian beam into a Bessel beam in a certain region close to the axicon [172,173]. In [174] a concentrically

corrugated near-field plate was presented to generate an evanescent Bessel beam [174]. Conversely, at millimeter and microwave wave frequencies resonant apertures such as leaky radial waveguides were proposed to radiate Bessel beams [175–177]. In [178] a gradient-index (GRIN) metamaterial lens was used as a broadband Bessel beam solution. Intensive research on Radial Line Slot Array (RLSA) antennas has been carried out over the last years as a planar and low-profile solution that can synthesize the required aperture distributions. RLSA was proposed in several works to obtain different types of Bessel beams at microwave frequencies [179–181] as well as millimeter band, at 30 GHz, for a right-handed circular polarized Bessel beam [182]. Also, at 30 GHz was proposed a radial waveguide loaded with metallic gratings to obtain a linear polarized Bessel beam [183].

Some of the antennas described above such as reflectors, FZP lens or GRIN lenses together with spatially-fed arrays are different alternatives to avoid the complexity and losses introduced by the feeding network of microstrip arrays. Particularly, spatially-fed arrays are low-profile planar antennas typically based on either printed or dielectric elements. Moreover, in SFA, the required phase-shift is obtained by properly adjusting the geometrical parameters of the elements which reduce the complexity of the design concerning RLSA or leaky radial waveguides. For these reasons, SFA antennas are attractive near-field antennas, always bearing in mind their inherent narrowband response.

Until recently, SFA research was mainly focused on far-field applications. However, some published work that introduces these antennas on near-field can be found. A reflectarray is proposed in [184] to focus the near-field at 2.4 GHz, and a dual-polarized reflectarray for near-field shaped focusing at 24.125 GHz is presented in [185]. An ultra-thin 2-bit transmitarray to focus the near-field was tested in [186] at X-band and another transmitarray was evaluated to generate a millimeter wave Gaussian Beam in [187]. A dual-polarized multi-focus near-field focusing reflective metasurface at X-band is proposed in [188]. Regarding Bessel beams, a Phase-Shifting Surface (PSS) was used to obtain a wideband quasi-non-diffraction large range at Ka-band in [189] and recently, a metasurface was designed to produce tilted Bessel beams [190].

1.2.6. Near-field applications

Most of these antennas are useful for several near-field applications, mainly on those which require concentrating the power density within a limited-size spot or a volume. A general overview of different near-field applications will be presented.

A classical near-field application is Microwave Imaging (MWI) for different fields.

The use of focused beams concentrates the radiation onto the object of interest reducing the sensitivity to other effects as undesired scatterers. Different antennas and beams can be used for that purpose. For instance, in [191] the influence of a focused beam generated by a passive near-field plate and the Bessel beam of a leaky radial waveguide on MWI was studied, resulting in a potential improvement of the imaging features. Also, it is commented that a major concentration of the field on the object of interest with a reduction of the undesired scatterers may lead to an enhancement of the Signal Noise Ratio (SNR) measured data. A different approach was proposed in [192], which introduces a near-field focused array antenna working as a receiver for two-dimensional MWI. The array scans its focus in the H-plane by changing the frequency, whereas the E-plane scanning is produced by feeding the array with different phases [193]. This approach enables high-quality imaging due to the low near-field secondary lobe levels (SLLs) of focused beams. A different alternative was presented in [17], a large electronically reconfigurable reflectarray based on PIN diodes for a millimeter-wave imaging system in the 60 GHz band. Near-field antennas can be also useful for medical microwave imaging since they operate at a close distance from the body. Hence, the near-field behavior of the antenna strongly determines the received signals, and the effectiveness of the imaging algorithm [194]. In this line, near-field antennas are applied on different medical applications such as hyperthermia [195,196], temperature sensors based on near-field focused microstrip array as a low-profile compact solution [197] or a focusing reflectarray microwave virus sanitizer [198].

Near-field radars can be used in industrial inspection for the detection or imaging of perforations or corroded areas in metal objects. The distance between the radar and the surface under exploration is critical for achieving success and effective detection of small anomalies [199]. Moreover, Ground Penetrating Radars (GPRs) can be improved by using Bessel beams because of the reduction of diffraction and better confinement of the field within the focusing area. An example is found in [200] where an RLSA has been proposed as a highly efficient and polarization purity solution for a GPR at microwave frequencies.

In other applications such as Radio Frequency Identification (RFID), near-field focused planar arrays have been suggested to operate as RFID readers [201, 202], or even a reflectarray at 2.4 GHz [184]. Also, planar arrays are a potential alternative for Wireless Power Transfer (WPT) applications [203] as well as near-field focusing reflective metasurfaces [188]. The transmitarray design in [187] to radiate s Gaussian-beam was used for a quasi-optical characterization of the S-parameters of transmitarray unit cells at V-band.

Throughout the last years, there has been intensive research activity on the de-

velopment of antenna measurement systems that operate within the Fresnel region of the probe at millimeter bands. In [204] the quiet zone performances of a reflectarray antenna were evaluated to act as a Compact Antenna Test Range (CATR) probe for the first time. Then, different works have demonstrated the viability of this concept by simulation [71, 205] and latter in [206]. For this concept, the near-field is not focused on a spot, it is necessary to generate a uniform plane wave. Hence, the design of the antennas must have control over the amplitude and phase of the radiated field. Newer published works suggest the use of array antennas for radiating uniform plane waves receiving the name of Plane Wave Generator (PWG) arrays [207, 208].

1.3. Thesis goals

This thesis is devoted to the analysis, synthesis, and design of shaped near-field patterns of SFA antennas, undertaking the study of these antennas in novel applications working within the Fresnel region of the SFA. The goals are divided into two main blocks: the development of a technique for the SFA analysis and its radiated near-field, as well as a technique for the synthesis of the near-field components with amplitude and/or phase control, similar to the synthesis of the copolar far-field component on reflectarray antennas. Then, this technique is applied to the design of SFAs, such as reflectarrays or transmitarrays, for novel near-field systems which require near-field patterns different from focused spots. Hence, the thesis has several goals divided into the two blocks that are detailed in the next lines.

1.3.1. Near-field analysis and synthesis on SFA antennas

The analysis of SFA antennas can be divided into different steps, including the analysis of the feed, the SFA element, and the computation of the radiated fields. With regard to the computation of radiation patterns, efficient techniques have been developed for periodic structures such as reflectarray antennas. This efficiency is based on the use of the FFT algorithm for the computation of the spectrum functions. However, these efficient techniques cannot be applied to the computation of the near-field of an SFA antenna. Hence, the first goal of the thesis is to develop an accurate technique for the analysis of the near-field radiated by SFA antennas.

From the incident field of the primary field, the analysis of the near-field is generalized to compute the tangential fields at the SFA elements working in either transmission or reflection. The characterization of the radiated near-field is based on Huygens' Principle. As it occurs on array near-field models each element is considered as a

punctual isotropic source. However, it is proposed the improvement of this model by modeling the SFA elements as a small aperture, as in the case of far-field analysis on reflectarray antennas. The near-field computation is based on the superposition of the far-field contribution of each element. Since the elements are modeled as antenna apertures either the First or Second equivalence principles can be used for computing the θ- and φ- components of each element. Then, the superposition of the different contributions of the elements gives the near-field components of the SFA.

An important goal derived from this block is to establish a power analysis on near-field, defining several parameters such as the spatial density power or the gain of an SFA within the Fresnel region, similar to a far-field analysis.

The second block is closely related since it comprises the development of techniques for the phase-only synthesis of SFA antennas. This block is aimed at the development of a technique for the synthesis of the near-field components by using the near-field model previously defined in the phase-only synthesis. The phase-only synthesis technique will be particularised for either transmitarrays or reflectarrays, and it will permit the control of both phase and amplitude of the radiated near-field.

1.3.2. Novel near-field applications

The analysis and synthesis technique developed are used to design several reflectarray and transmitarray antennas. Traditionally, near-field applications only require properly focusing the near-field within a certain spot. However, the goal of this second block is intended to show the potential applications which can be developed within the Fresnel region of the antenna as well as the necessity of shaping the near-field pattern using SFA antennas. Starting from the design of SFA antennas for focusing the near-field, including single and multi-feed configurations. Then, the phase-only technique is applied to a transmitarray to improve the focusing performance by imposing restrictions on the phase of the radiated near-field. It is important to underline that published works only imposed conditions in the amplitude of either near- or far-field. Hence, a secondary goal is to demonstrate that the control of the phase of the radiated field can lead to an enhancement of the field pattern performance. Then, the phase-only technique is applied to design different SFA antennas to be used as a base station for 5G indoor communications. In this case, the specifications are given for the near-field amplitude instead of the phase. However, the aim is not to focus the field but to shape it. Finally, it is addressed a complex synthesis with near-field amplitude and phase constraints. The synthesis with simultaneous constraints on the near-field amplitude and phase has the objective of reaching a uniform plane wave

which enables reflectarray antennas to behave as a probe on a measuring system. A recently published work based on the development of Plane Wave Generator arrays has addressed the control of both amplitude and phase of the near-field. Hence, an important point of the thesis is the addressed of near-field synthesis with near-field amplitude and phase constraints on SFA antennas, which add new contributions to this recently opened research line.

1.4. Thesis outline

The present thesis has been organized into six chapters, including this chapter for the introduction and the last one for summarizing the main ideas along with the novel contributions of the thesis. The remaining chapters describe the analysis and synthesis techniques developed as well as different examples to demonstrate and validate the presented contributions of the thesis.

Chapter 2 describes the analysis of SFA antennas and the computation of its radiated near-field. After the introduction, the SFA is geometrically characterized. Then, the analysis to obtain the tangential field on the surface of the SFA elements from the incident field is detailed. The feed is usually a horn antenna, which can be modeled as a mathematical function or full-wave simulated with dedicated software, and the SFA element is fully characterized with a full-wave method, typically based on local periodicity. The reflected tangential magnetic field on the SFA element is derived from the tangential electric field considering an incident plane wave on the element. Then, a technique to compute the near-field from the tangential field is described, which is based on Huygens' Principle and superposition. This model is used to describe the Intersection Approach for phase-only synthesis for near-field. This technique is presented for SFA antennas operating on both transmission and reflection.

Chapter 3, Chapter 4 and Chapter 5 comprehend the design and experimental validation of several transmitarray and reflectarray antennas which are design with the techniques described in Chapter 2. Despite being independent chapters, they are presented with a gradual increase in the complexity of the design addressed.

Chapter 3 is dedicated to the design of three different transmitarrays for focusing the near-field on a certain spot or area. The first case includes the design, manufacture, and test of a transmitarray to generate a Bessel beam using additive manufacturing. The second and third designs are the evaluation of single and multi-feed configurations to obtain a single focused spot or a multiple focused spot configuration. The three designs are based on an analytical expression.

Chapter 4 is devoted to the design, manufacture, and evaluation of a reflectarray and transmitarray antenna. In both cases, a near-field phase-only synthesis is carried out to achieve a phase distribution of the antenna elements which radiates a certain near-field pattern. The synthesis is carried out with only requirements on the near-field amplitude according to the shape of the desired specifications. The two SFA antennas are designed for indoor base station communications. The last section describes a novel technique to define the requirements on the phase-only synthesis when dealing with large coverage areas within the Fresnel region of the antenna.

Chapter 5 addressed the design, manufacture, and test of a reflectarray that controls the near-field amplitude and phase in order to obtain a uniform plane wave. This reflectarray works in linear polarization. The second case is the design of a similar reflectarray but working in dual-linear polarizations. Both reflectarrays are designed using the phase-only synthesis and then, each reflectarray uses a different element to work in single or dual-polarization. The last section is dedicated to the evaluation of the first reflectarray working as a probe on a measuring system and measuring different radiation patterns of other antennas.

Finally, Chapter 6 outlines the final conclusions of the work presented in the thesis, as well as the original contributions, several future lines of research opened during the development of this work, and a list of the published papers in international journals and conferences.

CHAPTER 2

Near-field for spatially-fed arrays: analysis and synthesis

2.1. Introduction

A spatially-fed array consists of a planar array of elements operating in transmission or reflection and illuminated by a primary feed. Despite combining the elements in such different geometries to improve the antenna performances, using different materials, or working in transmission or reflection, the operating principle is always the same for these antennas. The array of elements is illuminated by a primary feed, typically a horn antenna (though other types are possible), and the incident field is transmitted or reflected by the array elements adding a certain delay on the incident field. This phase-shift (delay) depends on the element geometry, which enables the control of the transmitted or reflected field by adjusting one or several parameters of the element. Depending on the phase introduced is it possible to generate collimated or shaped beams. Although different antennas can be classified as spatially-fed arrays, the most relevant are reflectarray and transmitarray antennas, as well as the recent metasurfaces.

The analysis of spatially-fed arrays and their radiation within the Fresnel region is discussed in different sections throughout this chapter. First, a common geometry for SFA is established as a baseline for all the antennas gathered on this classification. The starting point of this analysis is the tangential field at the antenna aperture, assuming that both the incident field and the response of the element are known beforehand. The incident field on the antenna surface can be computed with several methods. A common approach is based on considering that the radiation pattern of the primary feed is an ideal $\cos^q(\theta)$ function. Although this model only considers the main beam, it provides a useful approximation since the side lobes of a real feed typically fall at

the angles outside the antenna surface. Then, the phase onto the antenna surface can be easily computed using a geometrical optics (GO) approach, by computing the distance between the phase center of the feed and the elements. When dealing with ratios of f/D notably low this approximation is not accurate enough since the array is placed within the Fresnel region of the primary feed. Other alternatives to overcome this issue or improve the accuracy are based on considering an incident field obtained in a full-wave simulation of the feed, or even directly measuring the radiation of the feed at the SFA surface.

The relation between the incident and the tangential fields at the aperture of the antenna is given by the element response. In a primary approach, the element can be considered as an ideal phase-shifter, which behaves as a lossless element and only introduces a given phase-shift. However, this approximation does not take the cross-polar component of the field into account. Further analysis is to fully characterize the element. Typically, the different elements are analyzed assuming local periodic conditions. Under this assumption the analysis is carried out element by element, taking one element with a certain geometry and surrounding it with identical elements such as an infinite array comprised of the same element. This approach provides accurate results on the analysis of the entire spatial-feed array as long as the variation on the dimension of the element is smooth enough to ensure that each element is surrounded by similar elements like in the analysis. The most classical approaches to characterized elements are different implementation of the Method of Moments (MoM) in Spectral Domain and Floquet theorem, as well as different electromagnetic software such as CST Microwave Studio [209] or HFSS [210]. All these methods fully characterize the element response of a periodic structure. After this characterization, the tangential fields at the antenna aperture can be related to the incident field provided by the feed.

Once the tangential fields are obtained, they are used to compute the radiated field. In this case, the analysis is focused on the radiated near-field, though it can be easily extended to the far-field region by considering a large distance between the source (SFA) and the point of observation (wherein the field is computed). The present thesis proposes a near-field model bases on Huygens' Principle and superposition. Each element of the array is considered as a radiation unit, and it is modeled as a small aperture. The near-field radiated by the SFA on a certain point of the space is the sum of all the contribution of the array element, assuming that the point wherein the field is computed is in the far-field region of the element. Since the elements are modeled as small apertures, the far-field contribution can be derived from the application of the Equivalence Principle of finite aperture on an infinity ground plane. This approach can be extended to evaluate the near-field radiated by other planar arrays, not only

SFA since only depends on the tangential field on the array surface.

As it was pointed out above, the element response relates the incident with the tangential field, thus with the radiated field. If the incident field is fixed and the elements are considered ideal phase-shifters, the radiated field will depend on the phase-shift introduced by the array elements. Hence, it is feasible to obtain collimated or even shaped beams only controlling the phase of the elements. This approach is widely used when SFA antennas are designed to radiate focusing or pencil beam, both near- or far-field since the phase that should introduce the elements can be obtained analytically. However, when more complex field patterns are required, the use of synthesis algorithms is mandatory. Two different approaches can be used. On the one hand, a direct optimization of the geometry of the elements can be carried out. In this process, the geometry of the elements is adjusted to obtain the required field pattern using a full characterization of the elements. On the other hand, a widely used approach is the phase-only synthesis, which is based on modeling the elements as ideal phase-shifters and during this process, the phase-shift of the elements is adjusted to achieve the required field pattern. A POS is independent of the geometry of the element, and after the synthesis, the solution must be physically implemented by properly designing the element while the output of the direct optimization is the final layout. Despite having this limitation, Phase-Only synthesis is the most popular approach to synthesize the copolar component of both array and SFA antennas.

A common approach in this synthesis is the Intersection Approach, which has been widely used in the synthesis of reflectarray antennas because of its power and numerical efficiency. This algorithm offers a very fast approach in the synthesis of far-field shaped beams on reflectarray antennas since it takes the advantage of using the FFT on the analysis of the radiated field. However, when dealing with near-field beams the use of the FFT is not possible or, at least, to obtain a general solution. The last section of this chapter is devoted to extending the Intersection Approach to a newer version so-called generalized Intersection Approach for near-field. As a primary approach, the generalized IA is under the assumption of ideal phase-shifter, thus it is only feasible to optimize the copolar component of the field and there is no control over the cross-polar component or other parameters related to the element, such as the bandwidth.

2.2. Definition of spatially-fed arrays

This short section introduces the common geometry used in the analysis of the radiated field of spatially-fed arrays, as well as their main parameters that are used to support

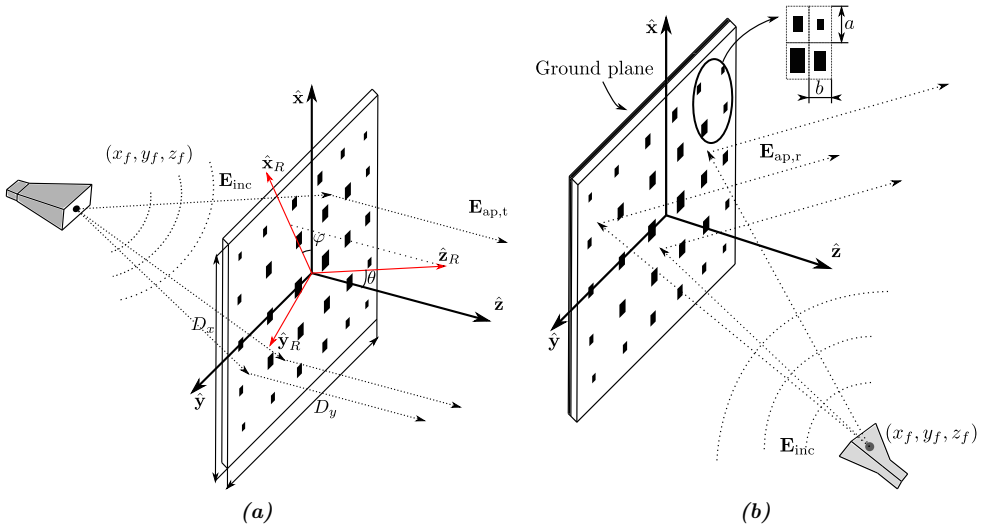

Figure 2.1: *Sketch of different configurations of spatially-fed array (a) centered-optic transmitarray or (b) offset-optic reflectarray.*

the formulation throughout this chapter. Although the most common configuration is single-offset and centered-feed configurations on reflectarray and transmitarray, respectively, there is no limitation. The formulation is generic and independent of the feed placement and the radiated field can be computed on any arbitrary point as long as $z > 0$ regarding the system shown in Figure 2.1.

This configuration sets the origin of the coordinate system $(\hat{\boldsymbol{x}}, \hat{\boldsymbol{y}}, \hat{\boldsymbol{z}})$ on the center of the array. Hence, the antenna parameters are referred to it. Considering that the feed is located at (x_f, y_f, z_f), the focal distance f is given by the coordinate z_f of the feed. Then, the element periodicity (a, b) is the periodicity in the $\hat{x}$ and $\hat{y}$, respectively, while the number of elements in each axis is given by

$$N_x = \left[\frac{\|\vec{x}_A\|}{a}\right] = \left[\frac{D_x}{a}\right], \tag{2.1}$$

where $[\circ]$ is the nearest integer function and D_x is the antenna aperture in the $\hat{x}_A$ axis. Likewise, the number of elements in $\hat{y}_A$ is given by

$$N_y = \left[\frac{\|\vec{y}_A\|}{b}\right] = \left[\frac{D_y}{b}\right], \tag{2.2}$$

Another parameter of interest is the pointing direction of the outgoing beam, which is defined by (θ_0, φ_0). These angles define the radiation systems $(\hat{\boldsymbol{x}}_R, \hat{\boldsymbol{y}}_R, \hat{\boldsymbol{z}}_R)$ and the

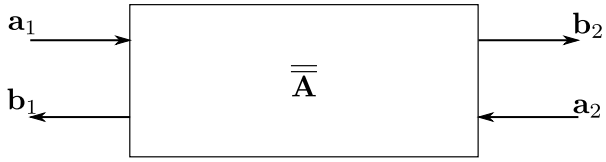

Figure 2.2: *Sketch of a cell modeled as a four port network.*

relation between both systems is [211]

$$\begin{pmatrix} \hat{\boldsymbol{x}}_R \\ \hat{\boldsymbol{y}}_R \\ \hat{\boldsymbol{z}}_R \end{pmatrix} = \begin{pmatrix} \cos\theta\cos^2\varphi + \sin^2\varphi & \cos\varphi\sin\varphi(\cos\theta - 1) & -\sin\theta\cos\varphi \\ \cos\varphi\sin\varphi(\cos\theta - 1) & \cos\theta\sin^2\varphi + \cos^2\varphi & -\sin\theta\sin\varphi \\ \sin\theta\cos\varphi & \sin\theta\sin\varphi & \cos\theta \end{pmatrix} \begin{pmatrix} \hat{\boldsymbol{x}} \\ \hat{\boldsymbol{y}} \\ \hat{\boldsymbol{z}} \end{pmatrix} \tag{2.3}$$

2.3. Near-field analysis on spatially-fed arrays

2.3.1. Electric field on the aperture

The computation of the radiated field by an SFA (transmitarray, reflectarray, metasurface, etc) requires knowing the tangential fields at the aperture. Spatially-fed arrays are considered aperture antennas and only the tangential field contributes to the radiation according to the Huygens' Principle [212].

Conversely, regardless the method used to compute the incident field on the SFA surface ($\cos^q\theta$ function, measurements, or full-wave simulations), it can be written for a $(x,\, y)$ point of the surface and both linear polarizations as

$$\boldsymbol{E}_{\text{inc}}^{X/Y}(x,\, y) = E_{\text{inc,x}}^{X/Y}(x,\, y)\,\hat{\boldsymbol{x}} + E_{\text{inc,y}}^{X/Y}(x,\, y)\,\hat{\boldsymbol{y}}, \tag{2.4}$$

where the superscripts denotes the polarization and the subscripts the field component projected over the array surface, for instance E_y^X would be the projection of the $\hat{y}$ component when the primary feed works in X polarization. Likewise, the tangential electric field on the radiating aperture can be written as

$$\boldsymbol{E}_{\text{ap}}^{X/Y}(x,\, y) = E_{\text{ap,x}}^{X/Y}(x,\, y)\,\hat{\boldsymbol{x}} + E_{\text{ap,y}}^{X/Y}(x,\, y)\,\hat{\boldsymbol{y}}, \tag{2.5}$$

where $\boldsymbol{E}_{\text{ap}}^{X/Y}$ is the tangential field at the antenna aperture and it is designated by either the reflected ($\boldsymbol{E}_{\text{ap,r}}$) or transmitted field ($\boldsymbol{E}_{\text{ap,t}}$).

The transmitted and reflected field at the element surface are related with the incident field by the response of the SFA element. In order to establish this relation, the SFA element would be modeled like a four port network as Figure 2.2 depicts. The inputs are $\boldsymbol{a}_1$ and $\boldsymbol{a}_2$ which are defined as

$$\boldsymbol{a}_1 = a_{x,1}\hat{\boldsymbol{x}} + a_{y,1}\hat{\boldsymbol{y}} \tag{2.6a}$$

$$\boldsymbol{a}_2 = a_{x,2}\hat{\boldsymbol{x}} + a_{y,2}\hat{\boldsymbol{y}}. \tag{2.6b}$$

and the outputs $\boldsymbol{b}_1$ and $\boldsymbol{b}_2$ as

$$\boldsymbol{b}_1 = b_{x,1}\hat{\boldsymbol{x}} + b_{y,1}\hat{\boldsymbol{y}} \tag{2.7a}$$

$$\boldsymbol{b}_2 = b_{x,2}\hat{\boldsymbol{x}} + b_{y,2}\hat{\boldsymbol{y}}. \tag{2.7b}$$

The relation between both inputs and outputs is given by the response of the network (element) which is characterized by the matrix $\overline{\overline{\boldsymbol{A}}}$. The elements of this matrix are the complex direct and cross components of the reflection ρ and transmission τ coefficients of the element. The relation between the inputs, outputs and the matrix $\overline{\overline{\boldsymbol{A}}}$ is

$$\begin{pmatrix} \boldsymbol{b}_1 \\ \boldsymbol{b}_2 \end{pmatrix} = \overline{\overline{\boldsymbol{A}}} \cdot \begin{pmatrix} \boldsymbol{a}_1 \\ \boldsymbol{a}_2 \end{pmatrix}. \tag{2.8}$$

where $\overline{\overline{\boldsymbol{A}}}$ is a combination of the reflection and transmission matrix defined as

$$\overline{\overline{\boldsymbol{A}}} = \begin{pmatrix} \boldsymbol{R} & \boldsymbol{T} \\ \boldsymbol{T} & \boldsymbol{R} \end{pmatrix} \tag{2.9}$$

Then, replacing (2.6) and (2.7) in (2.8) and expressing (2.9) regarding the direct coefficients (ρ_{xx}, ρ_{yy}, τ_{xx} and τ_{yy}) and the cross coefficients (ρ_{xy}, ρ_{yx}, τ_{xy} and τ_{yx}), (2.8) it is immediately written as

$$\begin{pmatrix} b_{x,1} \\ b_{y,1} \\ b_{x,2} \\ b_{y,2} \end{pmatrix} = \begin{pmatrix} \rho_{xx} & \rho_{xy} & \tau_{xx} & \tau_{xy} \\ \rho_{yx} & \rho_{yy} & \tau_{yx} & \tau_{yy} \\ \tau_{xx} & \tau_{xy} & \rho_{xx} & \rho_{xy} \\ \tau_{yx} & \tau_{yy} & \rho_{yx} & \rho_{yy} \end{pmatrix} \cdot \begin{pmatrix} a_{x,1} \\ a_{y,1} \\ a_{x,2} \\ a_{y,2} \end{pmatrix} \tag{2.10}$$

where the elements ρ_{xx}, ρ_{yy}, ρ_{xy} and ρ_{yx} are the reflection elements of $\boldsymbol{R}$ and τ_{xx}, τ_{yy}, τ_{xy} and τ_{yx} are the transmission coefficients of $\boldsymbol{T}$.

This equation fully characterizes the cell working in both transmission and reception. If the cell only works in transmission $\boldsymbol{a}_2$ is discarded ($\boldsymbol{a}_2 = 0$), while $\boldsymbol{a}_1 = 0$ when the antenna works in reception. From now on, it would be considered that the cell is working in transmission, thus (2.8) is simplified to

$$\begin{pmatrix} b_{x,1} \\ b_{y,1} \\ b_{x,2} \\ b_{y,2} \end{pmatrix} = \begin{pmatrix} \rho_{xx} & \rho_{xy} \\ \rho_{yx} & \rho_{yy} \\ \tau_{xx} & \tau_{xy} \\ \tau_{yx} & \tau_{yy} \end{pmatrix} \cdot \begin{pmatrix} a_{x,1} \\ a_{y,1} \end{pmatrix}. \tag{2.11}$$

Now, $\boldsymbol{a}_1$ as well as $\boldsymbol{b}_1$ and $\boldsymbol{b}_2$ can be related with the incident and tangential field at the cell, both reflected and transmitted tangential fields. Considering the following relations

$$\boldsymbol{a}_1 = \boldsymbol{E}_{\text{inc}} \tag{2.12a}$$

$$\boldsymbol{b}_1 = \boldsymbol{E}_{\text{ap,r}} \tag{2.12b}$$

$$\boldsymbol{b}_2 = \boldsymbol{E}_{\text{ap,t}}. \tag{2.12c}$$

Hence, the relation between the incident and tangential electric field regarding the $\overline{\overline{\boldsymbol{A}}}$ for a (m, n) element

$$\begin{pmatrix} E_{\text{ap,r},x} \\ E_{\text{ap,r},y} \\ E_{\text{ap,t},x} \\ E_{\text{ap,t},y} \end{pmatrix} = \begin{pmatrix} \rho_{xx} & \rho_{xy} \\ \rho_{yx} & \rho_{yy} \\ \tau_{xx} & \tau_{xy} \\ \tau_{yx} & \tau_{yy} \end{pmatrix} \cdot \begin{pmatrix} E_{\text{inc},x} \\ E_{\text{inc},y} \end{pmatrix}. \tag{2.13}$$

The elements ρ_{xx}, ρ_{yy}, τ_{xx} and τ_{yy} are the direct coefficients, which mainly affect the copolar component of the radiated fields; and the elements ρ_{xy}, ρ_{yx}, τ_{xy} and τ_{yx} are the cross coefficients and mostly affect to the crosspolar calculation.

2.3.2. Magnetic field on the aperture

The magnetic field can be also obtained for a (m, n) element of the array. In order to compute the magnetic field, it is assumed that the incident wave on the element coming from the feed is a locally uniform plane wave. Then, the magnetic field is

obtained using the following expression [213]

$$\boldsymbol{H}_{\mathrm{ap}}^{X/Y}(x_m,\, y_n) = \frac{1}{\omega\mu_0}\left[\boldsymbol{k} \times \boldsymbol{E}_{\mathrm{ap}}^{X/Y}(x_m,\, y_n)\right], \tag{2.14}$$

where $\boldsymbol{E}_{\mathrm{ap}}^{X/Y}(x_m,\, y_n)$ is either the reflected or transmitted field on the $(m,\, n)$ element; w is the angular frequency defined as $w = 2\pi f_0$ and $\boldsymbol{k}$ is the wave number vector, and it determines the direction of either reflected or transmitted wave in the absence of grating lobes. In this case, $\boldsymbol{k}$ is defined as

$$\boldsymbol{k} = -k_0 \sin\theta^{mn} \cos\varphi^{mn}\hat{x} - k_0 \sin\theta^{mn} \sin\varphi^{mn}\hat{y} + k_0 \cos\theta^{mn}\hat{z}, \tag{2.15}$$

where θ^{mn} and φ^{mn} are the incident angle of the plane wave coming from the feed on the $(m,\, n)$ element; and k_0 is the wave number in vacuum.

The resolution of the cross product (2.14) implies to know the three components of the electric field. Particularly, $E_{\mathrm{ap},x}$ and $E_{\mathrm{ap},y}$ are obtained from (2.13), and $E_{\mathrm{ap,\,z}}$ can be computed through the plane wave relation

$$\boldsymbol{k} \cdot \boldsymbol{E}_{\mathrm{ap}} = 0. \tag{2.16}$$

Solving this equation, it is immediately obtained that

$$E_{\mathrm{ap},z} = \frac{-k_x\, E_{\mathrm{ap},x} - k_y\, E_{\mathrm{ap},y}}{k_z}, \tag{2.17}$$

Now, (2.14) can be solved and the following expression is obtained for either the reflected or transmitted magnetic field on an element of the array

$$\begin{aligned}\boldsymbol{H}_{\mathrm{ap}}^{X/Y}(x_m, y_n) = \frac{1}{\omega\mu_0}\Big[&\big(k_y\, E_{\mathrm{ap},z}^{X/Y}(x_m, y_n) - k_z\, E_{\mathrm{ap},y}^{X/Y}(x_m, y_n)\big)\hat{x} \\ &- \big(k_x\, E_{\mathrm{ap},z}^{X/Y}(x_m, y_n) - k_z\, E_{\mathrm{ap},x}^{X/Y}(x_m, y_n)\big)\hat{y} \\ &+ \big(k_x\, E_{\mathrm{ap},y}^{X/Y}(x_m, y_n) - k_y\, E_{\mathrm{ap},x}^{X/Y}(x_m, y_n)\big)\hat{z}\Big].\end{aligned} \tag{2.18}$$

Note that, as it occurs with the electric field, only the tangential field is needed to compute the radiated fields. Hence, from (2.18) the following tangential components are obtained

$$H_{\mathrm{ap},x}^{X/Y} = \frac{k_y\, E_{\mathrm{ap},z}^{X/Y} - k_z\, E_{\mathrm{ap},y}^{X/Y}}{\omega\mu_0}, \tag{2.19a}$$

$$H_{\mathrm{ap},y}^{X/Y} = -\frac{k_x\, E_{\mathrm{ap},z}^{X/Y} - k_z\, E_{\mathrm{ap},x}^{X/Y}}{\omega\mu_0}. \tag{2.19b}$$

In order to alleviate notation, henceforth the polarization superscripts are dropped.

2.3.3. Huygens' Principle for near-field modeling

The final step on the analysis of a spatially-fed array is the computation of the radiated near-field. Previous works have developed different alternatives to compute the radiation pattern of transmitarray or reflectarray antennas, underling the reflectarray analysis presented in [214], which is based on the application of the field equivalence principles on an arbitrary surface. This approach takes the advantage of the antenna aperture condition of reflectarray antennas, and it computes the radiation pattern by applying the Equivalent Principles of aperture antennas. A major advantage of this approach is the use of the FFT to evaluate the spectrum function, or the non-uniform Fast Fourier transform (NUFFT) on aperiodic reflectarray antennas [215]. The FFT can be also applied to the computation of the near-field of an SFA, nonetheless, this approach is only valid to compute the near-field on planes parallel to the aperture which severely limits the number of addresses problems by this method. This thesis proposes a different alternative to compute the near-field radiated by an SFA. In this case, the near-field model is based on Huygens' Principle for aperture antennas [212] and the Principle of Superposition [212]. This approach enables the computation of the near-field in any arbitrary point of the space, with no limitation further than the physics of the problem.

Huygens' Principle was developed to explain the propagation and diffraction of light, stating that each point on a primary wavefront is a new source of a secondary spherical wave and, that secondary wavefront can be constructed as the envelope of these secondary spherical waves in the forward direction as Figure 2.3(a) depicts [212]. On this basis, Huygens' Principle can be used to explain the computation of the field radiated by an antenna aperture, especially to compute the near-field radiated by an SFA.

In this case, the primary wavefront would be the electric tangential field on the SFA aperture, sampling this field with the same periodicity of the SFA in both $\hat{\boldsymbol{x}}$- and $\hat{\boldsymbol{y}}$- direction, the wavefront is sampled at each element of the SFA providing that the Nyquist's Theorem is satisfied. By Huygens' Principle, each sample of the primary wavefront would be a source of a secondary spherical wave. Thus, each element of the SFA would be considered as a radiation source, having as many sources as elements on the SFA. The near-field radiated by the whole SFA at a certain point of the space

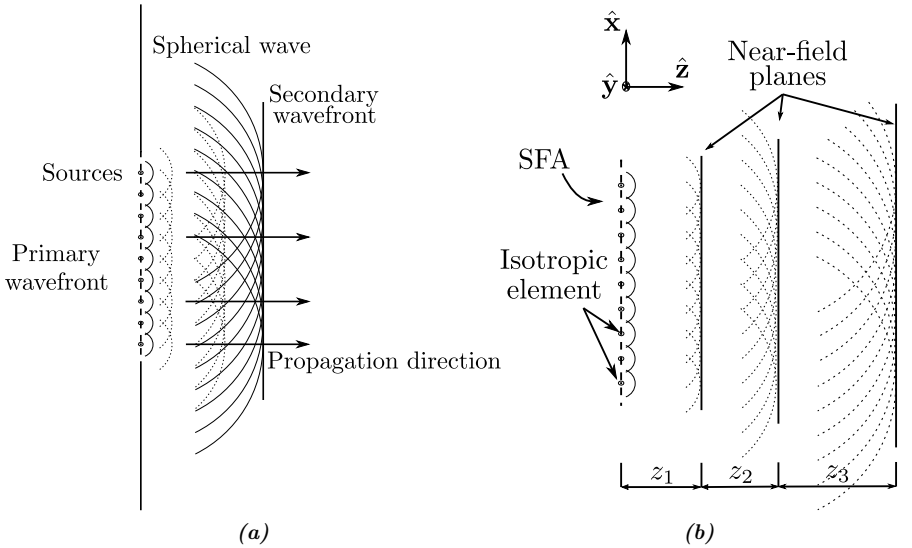

Figure 2.3: *Sketch of the (a) Huygens' Principle in an aperture and (b) the creation of wavefronts at different distances.*

would be a secondary wavefront, which is formed by the envelope of the different secondary spherical waves radiated by each SFA element, evaluated at the desired point. Hence, the near-field of an SFA on an arbitrary point defined by the position vector $\boldsymbol{r}$, using Huygens' Principle and the Principle of Superposition, and considering the SFA elements as isotropic sources, it can be expressed formally as

$$\mathbf{E}_{\mathrm{NF}}(\boldsymbol{r}) = \sum_{i}^{N} \mathbf{E}^{\mathrm{iso}}_{\mathrm{FF},i}(\boldsymbol{r}) = \sum_{i}^{N} \frac{e^{jk(\hat{\boldsymbol{r}}\cdot\boldsymbol{r}_i)}}{4\pi r_i} \tag{2.20}$$

where N is the total number of elements on the SFA given by $N_x \times N_y$ (see (2.1) and (2.2)) and r_i is the distance from the source to the near-field point.

To validate (2.20) in the computation of the near-field of an SFA, let us assume an SFA of 40×40 elements which field at the aperture is sampled on a regular grid of periodicity $\lambda/2 \times \lambda/2$ at 30 GHz. Nyquist's Theorem of sampling at $2f_s$ is satisfied with this periodicity. If it is assumed that the SFA is fed by a uniform plane wave and all the elements introduce the same phase-shift, the field at the aperture will be a plane wavefront. Moreover, if the elements are considered as lossless phase-shifters, the field at the aperture will be a uniform plane wave. According to Huygens' Principle, each sample of the uniform plane wave behaves as an isotropic source radiating spherical waves. Under these considerations, the near-field is evaluated using (2.20) at three

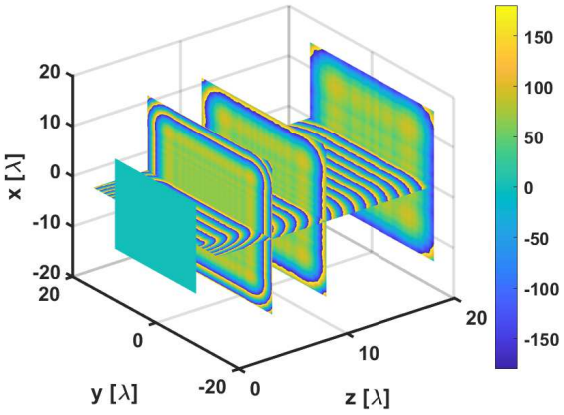

Figure 2.4: *Example of a SFA radiating a uniform plane wave (deg) within the near-field region to validate the near-field analysis.*

different planes parallel to the aperture: $5\lambda, 10\lambda$ and 20λ and the transversal plane yoz, considering $\hat{\mathbf{z}}$ the propagation direction as Figure 2.3(b) shows. The expected result would be a uniform plane wave propagating through $\hat{\mathbf{z}}$.

In Figure 2.4 the obtained near-field at the three different parallel planes and the transversal one are shown. From these results, it may be observed that, if the field at the SFA aperture is sampled in order to obtain the tangential fields on the SFA elements, it is feasible to compute the near-field at an arbitrary point of the space as the superposition of the radiation of each element on the desired point. As it was expected from Huygens' Principle, the computed near-field should be a uniform plane wave propagating through the $\hat{\mathbf{z}}$. As Figure 2.4 shows, in the transversal plane yoz a plane wave propagating through the $\hat{\mathbf{z}}$ is obtained, whilst the phase at the three different planes are almost constant. It should be noted that the constant phase is reached within an area equivalent to the antenna aperture D in the closest planes, for the further ones the angular aperture increases since the radius of the spherical waves radiated by the elements also increases. In light of these results, it is derived that Huygens' Principle together with the Principle of Superposition, thus (2.20), is a valid method for computing the near-field radiated by an SFA on an arbitrary point of the space.

2.3.4. Elements modeled as small radiating apertures

Although (2.20) allows the calculation of the near-field of an SFA, the consideration of using isotropic elements disables taking the radiated power of the elements into

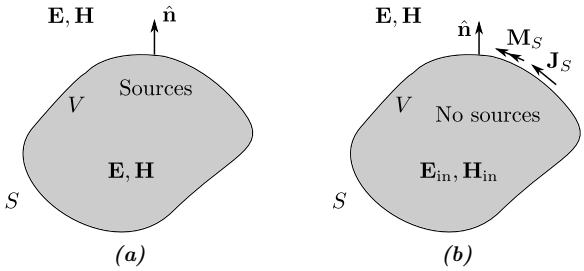

Figure 2.5: *Original (a) and equivalent (b) problems.*

account. To overcome this limitation, the element is modeled as a small antenna aperture. Now, the radiation of the element should be studied by applying the theory of antenna apertures. Particularly, the element is analyzed using the Equivalence Principle. This principle is deduced from Huygens' Principle and its mathematical form was developed by S. A. Schelkunoff [212]. This principle replaces an aperture antenna with equivalent currents that produce radiated fields equivalent to those from the antenna. The Equivalence Principle is derived from the mathematical uniqueness theorem, which states that *a field in a lossy region is uniquely specified by the sources within the region plus the tangential components of the electric field over the boundary, or the tangential component of the magnetic field over the boundary, or the former over part of the boundary and the latter over the rest of the boundary* [212]. Hence, a solution to Maxwell's equations and its boundary conditions is unique. This concept can be used to set up equivalent current relations for the analysis of aperture antennas.

In the original problem of Figure 2.5(a), the fields $\mathbf{E}$ and $\mathbf{H}$ accomplish Maxwell's equations in the external region of the volume V and satisfy the boundary conditions along the surface S, additionally those fields are unique. In the equivalent problem of Figure 2.5(b), the original sources have been removed and the fields within V have been altered, now denoted as $\mathbf{E}_{\text{in}}$ and $\mathbf{H}_{\text{in}}$. In order to keep the external fields as the original problem, equivalent currents must be introduced to fulfill the discontinuity of the fields across S. The equivalent currents denoted as $\mathbf{J}_S$ and $\mathbf{M}_S$, for the electric and magnetic current, must satisfy the following conditions,

$$\mathbf{J}_S = \hat{\mathbf{n}} \times (\mathbf{H} - \mathbf{H}_{\text{in}})\,|_s \ , \tag{2.21a}$$

$$\mathbf{M}_S = -\hat{\mathbf{n}} \times (\mathbf{E} - \mathbf{E}_{\text{in}})\,|_s \ . \tag{2.21b}$$

Since the fields $\mathbf{E}_{\text{in}}$ and $\mathbf{H}_{\text{in}}$ are arbitrary, they are chosen to be zero for simplicity,

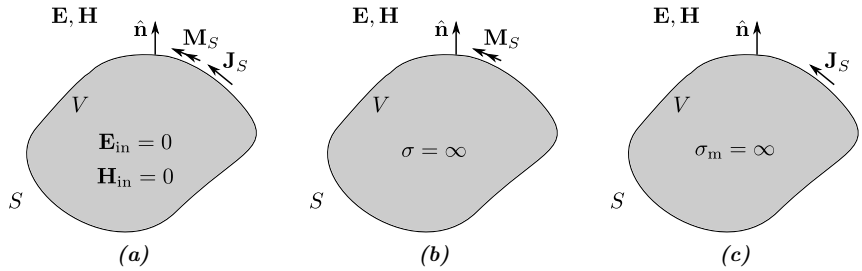

Figure 2.6: *Conditions to obtain the First (a), Second (b), and third (c) Principles of Equivalences.*

which is referred to as the *Love's Equivalence Principle* or *First Equivalence Principle* [216], see Figure 2.6(a). Then, the equivalent currents of (2.21) becomes

$$\mathbf{J}_S = \hat{\mathbf{n}} \times \mathbf{H}\,|_s \ , \tag{2.22a}$$

$$\mathbf{M}_S = -\hat{\mathbf{n}} \times \mathbf{E}\,|_s \ . \tag{2.22b}$$

Since the fields $\mathbf{E}_{\text{in}}$ and $\mathbf{H}_{\text{in}}$ are zero, the material inside S is freely chosen. Therefore, if a perfect electric conductor is placed along S, the electric current $\mathbf{J}_S$ is nullified and the magnetic current $\mathbf{M}_S$ is the unique responsible for the radiation, see Figure 2.6(b). The formulation of this problem is referred as the *Second Equivalence Principle* or the *Electric Conductor Equivalence Principle* [216]. In a dual case, a perfect magnetic conductor can be placed along S to eliminate $\mathbf{M}_S$, leaving $\mathbf{J}_S$ as the responsible of the radiated external fields, see Figure 2.6(c). This formulation leads to the *Third Equivalence Principle* or *Magnetic Conductor Equivalence Principle* [216]. Although three different principles are obtained, the three yield the correct fields external to S. These problems are difficult to solve as long S defines an arbitrary surface. However, if S and its curvature radius are large in terms of wavelength, the variation of the surface is smooth and S can be considered locally plane, simplifying the problem. Now, the *Image Theorem* can be applied, obtained the equivalent currents of Table 2.1.

Using the equivalent currents given by the equivalence principles, the electric and magnetic potential vector function on far-field conditions can be computed as,

$$\mathbf{A}(\boldsymbol{r}) = \frac{\mu}{4\pi r} e^{-jkr} \iint_S \mathbf{J}_S(\boldsymbol{r}') e^{jk\hat{\boldsymbol{r}}\cdot\boldsymbol{r}'} dS', \tag{2.23a}$$

$$\mathbf{F}(\boldsymbol{r}) = \frac{\epsilon}{4\pi r} e^{-jkr} \iint_S \mathbf{M}_S(\boldsymbol{r}') e^{jk\hat{\boldsymbol{r}}\cdot\boldsymbol{r}'} dS'. \tag{2.23b}$$

Table 2.1: *Equivalent currents for the three equivalence principles.*

	$\mathbf{V}$	$\mathbf{J}_S$	$\mathbf{M}_S$
First Equivalence Principle	-	$\hat{\boldsymbol{n}} \times \boldsymbol{H}\,\vert_S$	$\hat{\boldsymbol{n}} \times \boldsymbol{E}\,\vert_S$
Second Equivalence Principle	$\sigma = \infty$	0	$-2\hat{\boldsymbol{n}} \times \boldsymbol{E}\,\vert_S$
Third Equivalence Principle	$\sigma_m = \infty$	$2\hat{\boldsymbol{n}} \times \boldsymbol{H}\,\vert_S$	0

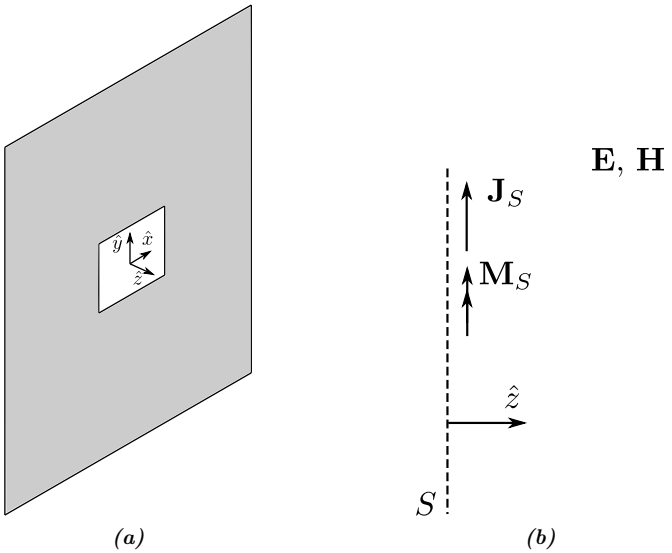

Figure 2.7: *Aperture in an infinite metal plane and its coordinate system (a) equivalent problem according to the First Equivalence Principle.*

where $\mathbf{A}$ and $\mathbf{F}$ are the magnetic anf electric vector potential, respectively. Then, the total electric far-field is obtained by summing the contributions from each potential vector function [212],

$$\begin{aligned}\mathbf{E} = \mathbf{E}_A + \mathbf{E}_F =& j\omega\left(\hat{\boldsymbol{r}} \times \left(\hat{\boldsymbol{r}} \times \mathbf{A}\right)\right) + j\omega\eta_0\left(\hat{\boldsymbol{r}} \times \mathbf{F}\right) = \\ & - j\omega\left(\left(A_\theta + \eta_0 F_\varphi\right)\hat{\boldsymbol{\theta}} + \left(A_\varphi - \eta_0 F_\varphi\right)\hat{\boldsymbol{\varphi}}\right). \end{aligned} \tag{2.24}$$

Since the SFA element is modeled as a planar aperture antenna, the previous formulation is particularized for this case, an aperture in an infinite ground plane, and the radiated fields will be deduced starting from the fields at the aperture of the element. The aperture is placed on a xy plane (see Figure 2.7(a)) and radiates in the hemisphere $z \geq 0$ with the propagation direction defined through $\hat{\boldsymbol{z}}$. The fields $\mathbf{E}_a$

and $\mathbf{H}_a$ at the aperture and tangential to S can be written as,

$$\mathbf{E}_a = E_{ax}(x', y')\hat{\boldsymbol{x}} + E_{ay}(x', y')\hat{\boldsymbol{y}}, \tag{2.25a}$$

$$\mathbf{H}_a = H_{ax}(x', y')\hat{\boldsymbol{x}} + H_{ay}(x', y')\hat{\boldsymbol{y}}, . \tag{2.25b}$$

This problem, according to the *First Equivalence Principle*, can be expressed as Figure 2.7(b). Considering that the normal vector to the surface $\hat{\mathbf{n}}$ is $\hat{\boldsymbol{z}}$, therefore the equivalent electric and magnetic printed currents can be obtained from (2.22) as,

$$\mathbf{J}_S = \hat{\boldsymbol{z}} \times \mathbf{H}_a, \tag{2.26a}$$

$$\mathbf{M}_S = -\hat{\boldsymbol{z}} \times \mathbf{E}_a. \tag{2.26b}$$

Solving (2.26), it immediately follows that the electric potential vector function is

$$\mathbf{A}(\boldsymbol{r}) = \frac{\mu}{4\pi r} e^{-jkr}\hat{\boldsymbol{z}} \times \iint_S \mathbf{H}_a(\boldsymbol{r}') e^{jk\hat{\boldsymbol{r}}\cdot\boldsymbol{r}'} dS' \tag{2.27}$$

and the magnetic potential vector is

$$\mathbf{F}(\boldsymbol{r}) = -\frac{\epsilon}{4\pi r} e^{-jkr}\hat{\boldsymbol{z}} \times \iint_S \mathbf{E}_a(\boldsymbol{r}') e^{jk\hat{\boldsymbol{r}}\cdot\boldsymbol{r}'} dS' \tag{2.28}$$

Without prejudice to the generality of the foregoing, the integrals can be computed separately, leading to the definition of $\mathbf{P}$ and $\mathbf{Q}$, which are called the spectrum functions and defined as,

$$\mathbf{P} = \iint_S \mathbf{E}_a(\boldsymbol{r}') e^{jk\hat{\boldsymbol{r}}\cdot\boldsymbol{r}'} dS' \tag{2.29}$$

$$\mathbf{Q} = \iint_S \mathbf{H}_a(\boldsymbol{r}') e^{jk\hat{\boldsymbol{r}}\cdot\boldsymbol{r}'} dS' \tag{2.30}$$

The aperture surface is in the XY-plane, $\mathbf{r}'$ is defined in (2.31) and $\hat{\mathbf{r}}$ is the unit vector in spherical coordinates defined in (2.32).

$$\mathbf{r}' = x'\hat{\mathbf{x}} + y'\hat{\mathbf{y}}. \tag{2.31}$$

$$\hat{\mathbf{r}} = \sin\theta\cos\varphi\hat{\mathbf{x}} + \sin\theta\cos\varphi\hat{\mathbf{y}} + \cos\theta\hat{\mathbf{z}}. \tag{2.32}$$

Then, applying (2.31) and (2.32) in (2.29) and (2.30) yield

$$P_x = \iint_S E_{ax}(x', y') e^{jk\left(x' \sin\theta\cos\varphi + y' \sin\theta\sin\varphi\right)} dx' dy', \tag{2.33a}$$

$$P_y = \iint_S E_{ay}(x', y') e^{jk\left(x' \sin\theta\cos\varphi + y' \sin\theta\sin\varphi\right)} dx' dy', \tag{2.33b}$$

$$Q_x = \iint_S H_{ax}(x', y') e^{jk\left(x' \sin\theta\cos\varphi + y' \sin\theta\sin\varphi\right)} dx' dy', \tag{2.33c}$$

$$Q_y = \iint_S H_{ay}(x', y') e^{jk\left(x' \sin\theta\cos\varphi + y' \sin\theta\sin\varphi\right)} dx' dy'. \tag{2.33d}$$

Now, the development of (2.24) for an aperture on a ground plane leads to the following θ- and φ-component of the radiated electric far-field, therefore to the far-field components radiated by an element of the SFA,

$$E_\theta = \frac{jk}{4\pi r} e^{-jkr} \left(P_x \cos\varphi + P_y \sin\varphi - \eta_0 \cos\theta \left(Q_x \sin\varphi - Q_y \cos\varphi\right)\right) \tag{2.34}$$

$$E_\varphi = -\frac{jk}{4\pi r} e^{-jkr} \left(\cos\theta \left(P_x \sin\varphi + P_y \cos\varphi\right) + \eta_0 \cos\theta \left(Q_x \cos\varphi - Q_y \sin\varphi\right)\right) \tag{2.35}$$

When the aperture is large in terms of the wavelength, the fields $\mathbf{E}_a$ and $\mathbf{H}_a$ are approximately related as a transverse electromagnetic TEM wave:

$$\mathbf{H}_a = \frac{1}{\eta_0} \left(\hat{\mathbf{z}} \times \mathbf{E}_a\right) \tag{2.36}$$

This implies the following relations between the spectrum functions

$$Q_x = -\frac{P_y}{\eta_0}, \tag{2.37a}$$

$$Q_y = \frac{P_x}{\eta_0}. \tag{2.37b}$$

Applying (2.37) in (2.34) and (2.35) leads to

$$E_\theta = \frac{jk}{2\pi r} e^{-jkr} \left(\frac{1 + \cos\theta}{2}\right) \left(P_x \cos\varphi + P_y \sin\varphi\right) \tag{2.38}$$

$$E_\phi = -\frac{jk}{2\pi r} e^{-jkr} \left(\frac{1 + \cos\theta}{2}\right) \left(P_x \sin\varphi - P_y \cos\varphi\right) \tag{2.39}$$

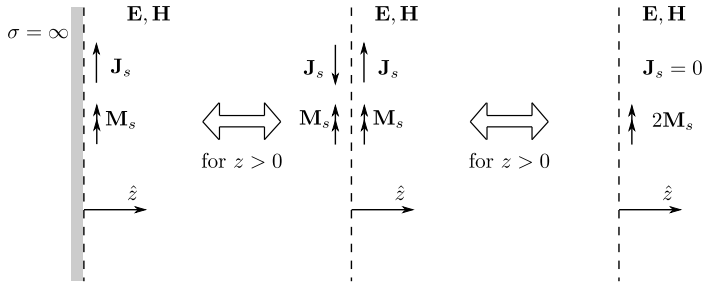

Figure 2.8: *Second Principle of Equivalence, considering perfect electric conductor, applied to a planar aperture.*

It should be underlined that (2.36) is an approximation for TEM waves and, the relation between the tangential fields, both electric and magnetic fields, on an array element is given by the TE and TM wave impedance for oblique incidence. Hence, (2.36) can be replaced by this relation to improve the accuracy of the computation of the fields.

Although the First and the Second Principle of Equivalence provide similar results when computing the copolar component, only the First Principle of Equivalence is suitable to accurately compute the cross-polar component of the radiated field. In Figure 2.8 the Second Principle of Equivalence is derived to solve this problem. Since only the magnetic currents are considered and the electric currents are discarded, only the magnetic potential vector $\mathbf{F}$ contributes to the radiation, and the θ- and φ-components of the electric field only depends on the $\mathbf{P}$ functions. Hence, (2.34) and (2.35) are now written as

$$E_\theta = \frac{jk}{2\pi r} e^{-jkr} \left(P_x \cos\varphi + P_y \sin\varphi\right) \tag{2.40}$$

$$E_\varphi = -\frac{jk}{2\pi r} e^{-jkr} \left(\cos\theta \left(P_x \sin\varphi + P_y \cos\varphi\right)\right) \tag{2.41}$$

2.3.5. Near-field radiated by the spatially-fed array

2.3.5.1. Electric near-field

Once the radiation of an element modeled as an antenna aperture has been obtained, it is feasible to compute the near-field on the basis of this consideration instead of using an isotropic source. In (2.20) the field radiated by an isotropic source is replaced with the radiation of an aperture antenna given by (2.24), which is expressed in terms of

its θ- and φ- component as

$$\boldsymbol{E}_{\mathrm{NF}}(\boldsymbol{r}) = \sum_{i}^{N} \boldsymbol{E}_{\mathrm{FF},i}(\boldsymbol{r}) = \sum_{i}^{N} \left(E_{\mathrm{FF},\theta,i}\hat{\boldsymbol{\theta}} + E_{\mathrm{FF},\varphi,i}\hat{\boldsymbol{\varphi}} \right) \tag{2.42}$$

The component $E_{\mathrm{FF},\theta}$ and $E_{\mathrm{FF},\varphi}$ are obtained from (2.34) and (2.35) and applying them to this expression, (2.42) is rewritten as

$$\begin{aligned}\boldsymbol{E}_{\mathrm{NF}}(\boldsymbol{r}) = {} & \frac{jk}{4\pi} \sum_{i}^{N} \frac{e^{-jk\boldsymbol{r}_i}}{r_i} \\ & \left[\left(P_{x,i}\cos\varphi_i + P_{y,i}\sin\varphi_i - \eta\cos\theta_i \left(Q_{x,i}\sin\varphi_i - Q_{y,i}\cos\varphi_i \right) \right) \hat{\boldsymbol{\theta}} \right. \\ & \left. - \left(\cos\theta_i \left(P_{x,i}\sin\varphi_i + P_{y,i}\cos\varphi_i \right) + \eta\cos\theta_i \left(Q_{x,i}\cos\varphi_i - Q_{y,i}\sin\varphi_i \right) \right) \hat{\boldsymbol{\varphi}} \right]\end{aligned} \tag{2.43}$$

Then, replacing (2.33) in (2.43) and considering the tangential field $\boldsymbol{E}_{\mathrm{ap}}$ of the SFA on a (x', y') point as the tangential field $\boldsymbol{E}_a$ of the element modeled as an aperture, the near-field is obtained as

$$\begin{aligned}\boldsymbol{E}_{\mathrm{NF}}(\boldsymbol{r}) = {} & \frac{jk}{4\pi} \sum_{i}^{N} \frac{e^{-jk\boldsymbol{r}_i}}{r_i} \\ & \left[\left(K_1 \iint_S E_{\mathrm{ap},x,i}(x',y') e^{jk\left(ux'+vy'\right)} dx'dy' + K_2 \iint_S E_{\mathrm{ap},y,i}(x',y') e^{jk\left(ux'+vy'\right)} dx'dy' - \right. \right. \\ & K_3 \left(K_2 \iint_S H_{\mathrm{ap},x,i}(x',y') e^{jk\left(ux'+vy'\right)} dx'dy' - K_1 \iint_S H_{\mathrm{ap},y,i}(x',y') e^{jk\left(ux'+vy'\right)} dx'dy' \right) \Bigg) \hat{\boldsymbol{\theta}} - \\ & \left(K_1 \left(K_2 \iint_S E_{\mathrm{ap},x,i}(x',y') e^{jk\left(ux'+vy'\right)} dx'dy' + K_1 \iint_S E_{\mathrm{ap},y,i}(x',y') e^{jk\left(ux'+vy'\right)} dx'dy' \right) + \right. \\ & \left. \left. K_3 \left(K_1 \iint_S H_{\mathrm{ap},x,i}(x',y') e^{jk\left(ux'+vy'\right)} dx'dy' - K_2 \iint_S H_{\mathrm{ap},y,i}(x',y') e^{jk\left(ux'+vy'\right)} dx'dy' \right) \right) \hat{\boldsymbol{\varphi}} \right]\end{aligned} \tag{2.44}$$

where $u = \sin\theta\cos\varphi$ and $v = \sin\theta\sin\varphi$. (θ, φ) are the outgoing angles from the source to the point of observation $\boldsymbol{r}$. K_1 is $\cos\varphi_i$; K_2 is $\sin\varphi_i$ and $K_3 = \eta_0\cos\theta_i$.

Both (2.43) and (2.44) are developed according to the First Principle of Equivalence. If the Second Principle of Equivalence is preferred, (2.40) and (2.41) should be applied in (2.42), obtaining the following expression

$$\begin{aligned}\boldsymbol{E}_{\mathrm{NF}}(\boldsymbol{r}) = {} & \frac{jk}{2\pi} \sum_{i}^{N} \frac{e^{-jk\boldsymbol{r}_i}}{r_i} \\ & \left[\left(P_{x,i}\cos\varphi_i + P_{y,i}\sin\varphi_i \right) \hat{\boldsymbol{\theta}} - \cos\theta \left(P_{x,i}\sin\varphi_i + P_{y,i}\cos\varphi_i \right) \hat{\boldsymbol{\varphi}} \right] \Big]\end{aligned} \tag{2.45}$$

Note that, since the SFA element is modeled as an aperture and its contribution to the radiated field is assuming far-field conditions, the minimum distance to compute the near-field radiated by the whole SFA is the beginning of the far-field region of the cell

$$|\boldsymbol{r}_{min}| = \frac{\sqrt{2}(a_{min} \cdot b_{min})}{\lambda} \tag{2.46}$$

As a result of the previous discussion, both (2.43) and (2.45) provide the near-field regarding its spherical $\hat{\boldsymbol{\theta}}$ and $\hat{\boldsymbol{\varphi}}$ components. However, when dealing with near-field applications there is an special interest on computing the near-field on a Cartesian grid. Therefore, it is highly desirable to operate with the Cartesian components of the near-field instead of the spherical ones. The relation between Cartesian and spherical coordinates is given by the classical matrix

$$\begin{pmatrix} E_x \\ E_y \\ E_z \end{pmatrix} = \begin{pmatrix} \sin\theta\cos\varphi & \cos\theta\cos\varphi & -\sin\varphi \\ \sin\theta\sin\varphi & \cos\theta\sin\varphi & \cos\varphi \\ \cos\theta & -\sin\theta & 0 \end{pmatrix} \cdot \begin{pmatrix} E_r \\ E_\theta \\ E_\varphi \end{pmatrix} \tag{2.47}$$

where E_r is ignored since the radial component of the field does not contribute to the radiated field.

Conversely, the change in the coordinate system should not be made for $\boldsymbol{E}_{\mathrm{NF}}$ but for the radiation element $\boldsymbol{E}_{\mathrm{FF},i}$ before adding all the contribution. Hence, (2.42) is written with regard to its Cartesian components as

$$\boldsymbol{E}_{\mathrm{NF}}(\boldsymbol{r}) = \sum_{i}^{N} (E_{\mathrm{FF},x,i}\hat{\boldsymbol{x}} + E_{\mathrm{FF},y,i}\hat{\boldsymbol{y}} + E_{\mathrm{FF},z,i}\hat{\boldsymbol{z}}) \tag{2.48}$$

2.3.5.2. Magnetic near-field

The computation of the near-field is based on the consideration that the element of the spatially-fed array is an antenna aperture, particularly based on the theory of an aperture on an infinity ground plane. Since the point of observation of the radiated field of the SFA is within its near-field region on the far-field of the element it is also possible to compute the magnetic field components of the far-field contribution of an element as [212]

$$H_{\mathrm{FF},r} = 0, \tag{2.49a}$$

$$H_{\mathrm{FF},\theta} = -\frac{E_{FF,\varphi}}{\eta_0}, \tag{2.49b}$$

$$H_{\mathrm{FF},\varphi} = \frac{E_{FF,\theta}}{\eta_0}. \tag{2.49c}$$

Then, the magnetic field radiated by the SFA will be the addition of all the elements on the point of observation, as the electric field computation. Hence, (2.42) is particularized as

$$\begin{aligned}\boldsymbol{H}_{\mathrm{NF}}(\boldsymbol{r}) = \sum_i^N \boldsymbol{H}_{\mathrm{FF},i}(\boldsymbol{r}) &= \sum_i^N \left(H_{\mathrm{FF},\theta,i}\hat{\boldsymbol{\theta}} + H_{\mathrm{FF},\varphi,i}\hat{\boldsymbol{\varphi}}\right) \\ &= \frac{-1}{\eta_0}\sum_i^N \left(E_{\mathrm{FF},\varphi,i}\hat{\boldsymbol{\theta}} - E_{\mathrm{FF},\theta,i}\hat{\boldsymbol{\varphi}}\right)\end{aligned} \tag{2.50}$$

2.3.6. Near-field computation considering unit cells with a physical displacement of phase-shifters in both polarizations

The unit cell is an important factor in the design of SFA antennas. Ideally, the unit cell should provide enough phase-shift to perform the layout design, moreover low losses, good angular stability, or a low cross-polarization level among others. Conversely, an SFA not only works in a single polarization but dual ones, either linear or circular. Therefore, the cell should behave with similar performances in both polarizations. Selecting an element with a decoupling between polarization would facilitate the SFA design since each polarization could be controlled independently. An adequate unit cell is based on dipoles elements oriented to the desired polarization, either stacking the different polarized elements on different layers or physically displacing those dipoles on the same layer. However, both configurations enable the control of each polarization independently.

Although the analysis of cells is not addressed in this work, the use of unit cells with a physical displacement of phase-shifters intrinsically affects the computation of the near-field. A physical displacement of the different polarized elements within the same unit cells can be seen as having different displaced polarized sources, thus the contribution of an element to the radiated near-field (2.42) would have a different origin of the source depending on the polarization.

Let us suppose a unit cell defined as Figure 2.9 depicts, where the X polarized element is oriented according to the $(\hat{\boldsymbol{x}}, \hat{\boldsymbol{y}})$ system and the Y polarized element to $(\hat{\boldsymbol{x}}', \hat{\boldsymbol{y}}')$. The phasing cell of the SFA element in the Y polarization is shifted $(\Delta x, \Delta y)$ with respect to the orthogonal polarization. Taking as reference the phase-shifter for polarization X, let $(\hat{\boldsymbol{x}}, \hat{\boldsymbol{y}})$ be the reference coordinates. Therefore, the relation between

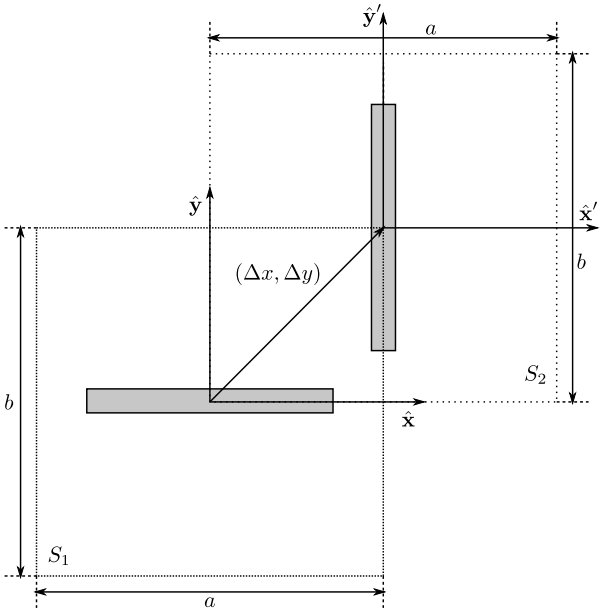

Figure 2.9: *Sketch of a cell with physical displacement between the phase-shifters in dual-linear polarization.*

the reference and the shifted system is

$$x' = x + \Delta x, \tag{2.51a}$$

$$y' = y + \Delta y. \tag{2.51b}$$

Hence, this shift has to be taken into account in the whole computation of the near-field. Starting from the illumination of the SFA, considering the spacial shift of the different polarized elements, (2.13) is modified as

$$\begin{pmatrix} E_{\mathrm{ap,r},x} \\ E_{\mathrm{ap,r},y} \\ E_{\mathrm{ap,t},x} \\ E_{\mathrm{ap,t},y} \end{pmatrix} = \boldsymbol{A} \cdot \begin{pmatrix} E_{\mathrm{inc},x}(x_m, y_n) \\ E_{\mathrm{inc},y}(x'_m, y'_n) \end{pmatrix}. \tag{2.52}$$

where (x_m, y_n) and (x'_m, y'_n) are the coordinates of the (m,n)th element considering the shift between the elements. Since the incident field is obtained at different spatial coordinates for each component, the tangential cannot be directly obtained. It should be noticed that the $\boldsymbol{A}$ matrix elements are the same for both reference coordinates

since they are computed assuming local periodicity.

Analysing the radiation of a single SFA element, the spectrum functions have to consider this shift. Thus, (2.33) is not integrated on a single surface S but on two different surfaces S_1 and S_2. In this case, the spectrum functions are written as

$$P_x^{X/Y} = \iint_{S_1} a_{xx} E_{inc,x}^{X/Y}(x,y) e^{jk\hat{\boldsymbol{r}}\cdot\boldsymbol{r}} dS_1 + \iint_{S2} a_{xy} E_{inc,y}^{X/Y}(x',y') e^{jk\hat{\boldsymbol{r}}\cdot\boldsymbol{r'}} dS_2, \quad (2.53a)$$

$$P_y^{X/Y} = \iint_{S_1} a_{yx} E_{inc,x}^{X/Y}(x,y) e^{jk\hat{\boldsymbol{r}}\cdot\boldsymbol{r}} dS_1 + \iint_{S2} a_{yy} E_{inc,y}^{X/Y}(x',y') e^{jk\hat{\boldsymbol{r}}\cdot\boldsymbol{r'}} dS_2. \quad (2.53b)$$

where a_{xx}, a_{xy}, a_{yx} and a_{yy} are either the transmission or reflection coefficients of the surface matrix $\boldsymbol{A}$; and $\boldsymbol{r}$ and $\boldsymbol{r'}$ are defined as

$$\mathbf{r} = x\hat{\mathbf{x}} + y\hat{\mathbf{y}}. \quad (2.54)$$

$$\mathbf{r'} = x'\hat{\mathbf{x}}' + y'\hat{\mathbf{y}}'. \quad (2.55)$$

Hence, replacing (2.54) and (2.55) in (2.53) and using (2.51) to relate both systems, the spectrum functions P_x and P_y can be expressed as

$$P_x^{X/Y} = \iint_{S_1} a_{xx} E_{inc,x}^{X/Y}(x,y) e^{jk(xu+yv)} dxdy + \iint_{S1} a_{xy} E_{inc,y}^{X/Y}(x',y') e^{jk(xu+yv)} e^{jk(\Delta x \sin\theta\cos\varphi + \Delta y \sin\theta\sin\varphi)} dxdy, \quad (2.56a)$$

$$P_y^{X/Y} = \iint_{S_1} a_{yx} E_{inc,x}^{X/Y}(x,y) e^{jk(xu+yv)} dxdy + \iint_{S1} a_{yy} E_{inc,y}^{X/Y}(x',y') e^{jk(xu+yv)} e^{jk(\Delta x \sin\theta\cos\varphi + \Delta y \sin\theta\sin\varphi)} dxdy. \quad (2.56b)$$

where $u = \sin\theta\cos\varphi$ and $v = \sin\theta\sin\varphi$.

Now, (2.56) are only integrated in the surface S_1, but the $\hat{y}$ component of the incident field is obtained in the $(\hat{\boldsymbol{x}}', \hat{\boldsymbol{y}}')$ system, related to $(\hat{\boldsymbol{x}}, \hat{\boldsymbol{y}})$ through (2.51).

2.3.7. Power balance in radiative near-field region

As it occurs on a far-field radiation pattern it is feasible to carry out a power analysis of the near-field. Throughout this section, it is discussed the power analysis of the near-field defining similar parameters as a far-field analysis. Note that, the radiating near-field is that region of the field of an antenna between the reactive near-field and

the far-field region wherein the radiation fields predominate, and the angular field distribution is dependent on the distance from the antenna, while the far-field only depends on the angular field distribution.

2.3.7.1. Radiated power density in near-field

The radiated power density associated to an electromagnetic field can be defined by the Poynting's theorem [212]. Hence, the spatial power density of a spatially-fed array on a point of its near-field can be computed as:

$$\boldsymbol{W}(\boldsymbol{r}) = \frac{1}{2}\,\mathrm{Re}\left[\boldsymbol{E}_{\mathrm{NF}}(\boldsymbol{r}) \times \boldsymbol{H}^{*}_{\mathrm{NF}}(\boldsymbol{r})\right] \tag{2.57}$$

where $\boldsymbol{E}_{\mathrm{NF}}(\boldsymbol{r})$ and $\boldsymbol{H}_{\mathrm{NF}}(\boldsymbol{r})$ are the electric and magnetic vector of the near-field on the point of observation $\boldsymbol{r}$.

Then, the radiated power can be computed as the integration of the flux of the Poynting's vector through the surface. Based on (2.57), the radiated power by a spatially-fed array is given by

$$P_{rad} = \oiint_{S} \boldsymbol{W} \cdot d\boldsymbol{S} = \oiint_{S} (\boldsymbol{W} \cdot \hat{\boldsymbol{n}})\, dS = \frac{1}{2} \oiint_{S} \mathrm{Re}\left[\boldsymbol{E}_{\mathrm{NF}}(\boldsymbol{r}) \times \boldsymbol{H}^{*}_{\mathrm{NF}}(\boldsymbol{r})\right] \cdot dS \tag{2.58}$$

If the point of observation $\boldsymbol{r}$ is considered on a large sphere of constant radius, the power radiated is extended into the far-field region. However, if the point of observation is considered on an area near to the antenna within the Fresnel range, the average Poynting's vector is obtained for the radiated near-field.

Now, the tangential field at the SFA surface ($\boldsymbol{E}_{ap}(x\,y)$ and $\boldsymbol{H}_{ap}(x\,y)$ are computed with (2.13) and (2.14), modeling the elements as ideal phase-shifters ($\tau_{xy} = \tau_{yx} = 0$ and $\rho_{xy} = \rho_{yx} = 0$). The radiated power of the SFA can be easily computed with (2.58), considering the tangential fields instead of the radiated field. Then, the tangential field are contained in the xy SFA surface which normal component is defined in $\hat{\boldsymbol{z}}$. Therefore, the radiated power by the SFA using (2.58) is given by

$$\begin{aligned} P_{rad,SFA} &= \frac{1}{2} \oiint_{xy} \mathrm{Re}\left(\left[\boldsymbol{E}_{\mathrm{ap}}(x\,y) \times \boldsymbol{H}^{*}_{\mathrm{ap}}(x\,y)\right] \cdot \hat{\boldsymbol{z}}\right) dxdy \\ &= \frac{1}{2} \oiint_{xy} \mathrm{Re}\left[E_{\mathrm{ap},x}(x\,y) H^{*}_{\mathrm{ap},y}(x\,y) - E_{\mathrm{ap},y}(x\,y) H^{*}_{\mathrm{ap},x}(x\,y)\right] dxdy \end{aligned} \tag{2.59}$$

If the SFA is comprised of $N_x \times N_y$ elements with a periodicity of $\Delta_x \times \Delta_y$ mm^2 and the tangential field is sampled at the center of each element of the SFA, (2.59)

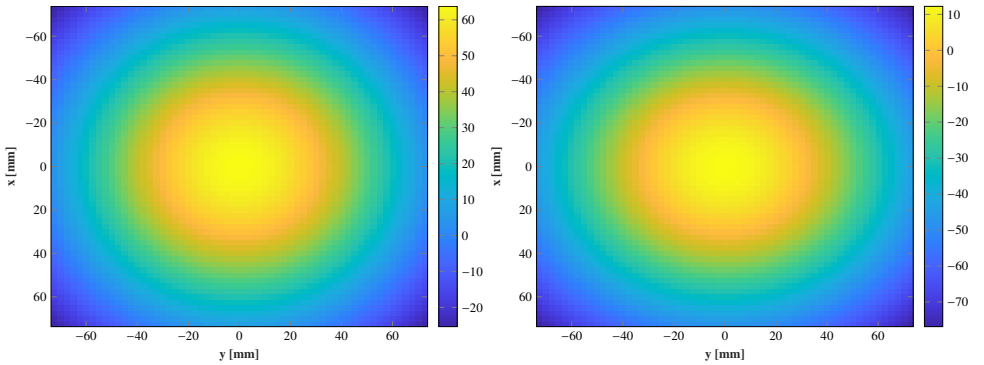

(a) *(b)*

Figure 2.10: *Amplitude (dB) of the tangential field at the transmitarray surface (a) Electric field $E_{ap,x}$ (b) Magnetic field $H_{ap,y}$.*

can be computed as

$$P_{rad,SFA} = \frac{1}{2}\sum_{i}^{N_y}\sum_{l}^{N_x} \mathrm{Re}\left[E_{\mathrm{ap},x}H^*_{\mathrm{ap},y} - E_{\mathrm{ap},y}H^*_{\mathrm{ap},x}\right](\Delta_x \cdot \Delta_y) \tag{2.60}$$

Conversely, the power radiated by the feed of the SFA can be obtained as [214]

$$P_{feed} = A_0 \frac{\pi}{\eta_0 \lambda^2 (2q+1)} \tag{2.61}$$

where A_0 is an amplitude factor to adjust the power radiated by the feed.

As an example, let us suppose a transmitarray antenna of 59×59 elements with a periodicity of 2.5 mm in both directions. The transmitarray antenna is fed by a horn antenna in a centered configuration at a distance of 65 mm and an outgoing pencil beam on $(\theta_0, \varphi_0) = (0^\circ, 0^\circ)$. The feed is modeled as a $\cos^q$ function with a q-factor of 15 at a central frequency of 30 GHz. Setting A_0 to 1 and applying (2.61), the power radiated by the feed is 2.69 W. Then, the electric and magnetic tangential fields at the transmitarray surfaces are the ones shown in Figure 2.10 for the copolar component. Applying (2.60) the resulting radiated power is 2.69 W.

From the tangential fields, the radiated near-field, both electric and magnetic field, using (2.48) and (2.49) can be computed. The near-field is computed in a parallel plane to the antenna aperture at a distance of 20λ (200 mm) in a regular xy grid large enough to capture most of the field at this distance. In Figure 2.11 the amplitude of the copolar component of the electric and magnetic near-field is shown. The power

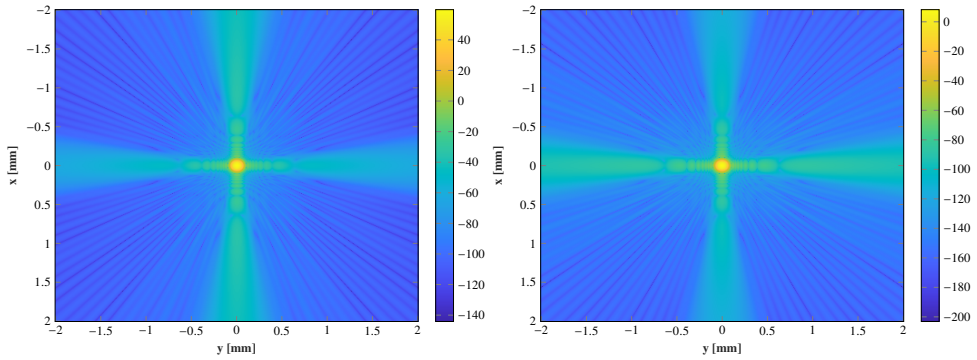

Figure 2.11: *Amplitude (dB) of the near-field at a distance of* 20λ *(a) Electric field* $E_{NF,x}$ *(b) Magnetic field* $H_{NF,y}$*. Considering a transmitarray antenna of* 59×59 *elements pointing in the direction* $(\theta_0, \varphi_0) = (0^\circ, 0^\circ)$ *and a feed modeled as a* $\cos^q$ *function with a q-factor of* 15 *at* 30 *GHz.*

radiated can be computed with (2.59) or (2.60) considering the whole plane as the integration domain. As it may be expected, the spatial density power is 2.69 W.

2.3.7.2. Radiation Intensity in near-field

Radiation intensity in a certain direction is defined as the power radiated from a source or antenna per unit solid angle. This concept is applied as a far-field parameter, which is obtained by multiplying the radiation density by the square of the distance. However, if the radiation density $\boldsymbol{W}$ can be computed as the average power density with (2.57), it is possible to obtain a radiation density in near-field as

$$U_{NF}(\boldsymbol{r}) = |\boldsymbol{r}|^2 |\boldsymbol{W}| = \frac{1}{2}|\boldsymbol{r}|^2 \left|\mathrm{Re}\left[\boldsymbol{E}_{NF}(\boldsymbol{r}) \times \boldsymbol{H}^*_{NF}(\boldsymbol{r})\right]\right| \tag{2.62}$$

where $\boldsymbol{r}$ is the observation point.

2.3.7.3. Definition of Gain in near-field

Once it is defined the radiation intensity on near-field, a gain on near-field can be defined too. Let us define P_{SFA} as the radiated power of a SFA antenna and U_{FF} as the radiation intensity in far-field. The gain in far-field in each direction (θ, φ) can be

defined as

$$g_{FF}(\theta,\varphi) = \frac{4\pi U_{FF}(\theta,\varphi)}{P_{SFA}} = \frac{U_{FF}(\theta,\varphi)}{\frac{P_{SFA}}{4\pi}} = \frac{U_{FF}(\theta,\varphi)}{U_{FF,iso}(\theta,\varphi)} \tag{2.63}$$

where $U_{FF,iso}(\theta,\varphi)$ is the radiation intensity of an equivalent isotropic source.

Similar to the definition of gain in far-field (2.63), the gain in near-field can be obtained too. The radiation intensity in near-field can be computed with (2.62) for both, SFA and equivalent isotropic source, considering $\boldsymbol{r}$ as the observation point defined from the SFA center to the point wherein the radiated near-field is computed. Therefore, starting from the relation of both radiation intensities the gain in near-field can be computed as

$$\frac{U_{NF}(\boldsymbol{r})}{U_{NF,iso}(\boldsymbol{r})} = \frac{U_{NF}(\boldsymbol{r})}{\frac{P_{SFA}}{4\pi}} = \frac{4\pi U_{NF}(\boldsymbol{r})}{P_{SFA}} = g_{NF}(\boldsymbol{r}) \tag{2.64}$$

Taking up again the previous transmitarray its near-field gain would be computed using (2.64). Considering that the electrical field $\boldsymbol{E}$ is defined in the $\hat{\boldsymbol{x}}$-axis and the propagation direction is defined along the $\hat{\boldsymbol{z}}$ direction (see Figure 2.1), the g_{NF} would be computed for different $\boldsymbol{r} = z\hat{\boldsymbol{z}}$ defined along $\hat{\boldsymbol{z}}$ and $x = y = 0$. The computed near-field gain as a function of the distance is shown in Figure 2.12. As the distance increases the value converges to the far-field gain, which is theoretically obtained when $\boldsymbol{r}$ tends to ∞.

2.3.7.4. Link budget in near-field

From the definition of radiated power density $\boldsymbol{W}$ it is possible to calculate the received power on an antenna. Using (2.57) the received power is given by

$$P_{RX} = \boldsymbol{W}(\boldsymbol{r}) \cdot A_{eff} = \frac{1}{2}\,\mathrm{Re}\left[\boldsymbol{E}_{\mathrm{NF}}(\boldsymbol{r}) \times \boldsymbol{H}^{*}_{\mathrm{NF}}(\boldsymbol{r})\right] \cdot A_{eff} \tag{2.65}$$

where A_{eff} is the effective area of the receiving antenna.

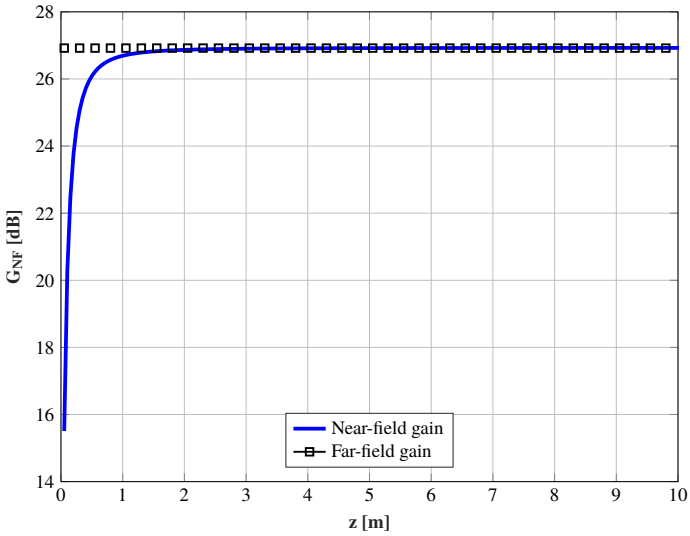

Figure 2.12: *Near-field gain of a transmitarray as a function of the distance according to the definition given in* (2.64)*. Considering a transmitarray antenna of* 59×59 *elements pointing in the direction* $(\theta_0, \varphi_0) = (0^\circ, 0^\circ)$ *and a feed modeled as a* $\cos^q$ *function with a q-factor of* 15 *at* 30 *GHz.*

2.4. Phase-only synthesis: shaping the near-field amplitude and phase

2.4.1. Classical Intersection Approach: Phase-only Synthesis

In direct optimization methods, a functional that is defined as an error cost function is optimized. However, there is an alternative method based on searching the intersection between two sets or, at least, the minor distance between them [56, 64]. In the literature, this approach is so-called the Intersection Approach and was first developed for the synthesis of arrays in which amplitude and phase could vary along the surface of the antenna [63]. However, the synthesis of spatially-fed arrays requires tighter restrictions, since the amplitude of the excitations is given by the illumination of the primary feed, therefore it is fixed beforehand. Still, the Intersection Approach has been used in the phase-only synthesis of the copolar component, as well as the generalized Intersection Approach, both obtaining successful results on complex radiation patterns. However, this approach has not been extended for the synthesis of near-field components. In this section, the generalized Intersection Approach is described for the synthesis of spatially-fed arrays with near-field constraints, taking the classical

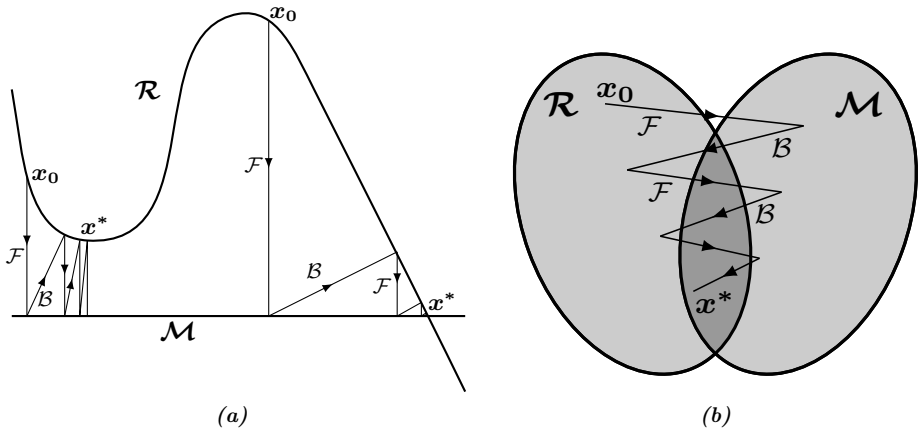

Figure 2.13: *Sketch of the Intersection Approach between two sets for (a) one dimension and (b) general case.*

Intersection Approach as the starting point to develop this approach.

The IA considers two sets: 1) the set of the radiated fields that comply with the requirements (set $\mathcal{M}$) and 2) the set of the radiated field that can be obtained with the SFA (set $\mathcal{R}$) [56, 64]. The search of the intersection between these two sets is an iterative process based on the method of Alternate Projections [64], performing the following two operations in each iteration

$$\boldsymbol{E}_{NF}^{i+1} = \mathcal{B}\left[\mathcal{F}\left(\boldsymbol{E}_{NF}^{i}\right)\right] \tag{2.66}$$

where $\mathcal{F}$ is the forward projector, which projects a point of $\mathcal{R}$ onto $\mathcal{M}$; $\mathcal{B}$ is the backward projector, and it retrieves one point of $\mathcal{M}$ onto $\mathcal{R}$. $\boldsymbol{E}_{NF}$ is the near-field radiated by the SFA at the i- iteration. The aim of the iterative sequence defined in (2.66) is to find a field that belongs simultaneously to both sets. Thus, a field that satisfies the specifications and is feasible to be radiated by the antenna geometry. If that is not possible because the intersection is not found, a near-field should be found whose distance to the set $\mathcal{M}$ is minimal [56]. Also, the IA is a local optimizer, and as such, the starting point is of sheer importance for the correct convergence of the algorithm.

A sketch of the IA applied to one-dimensional sets is depicted in Figure 2.13(a). There, x_0 denotes the starting point of the algorithm and x^* the solution reached. In this case, the projection operators are an orthogonal projection of one curve to the other. This example shows the utmost importance of the starting point, since depending on the x_0 used, the algorithm may reach non-desired local minima. Conversely,

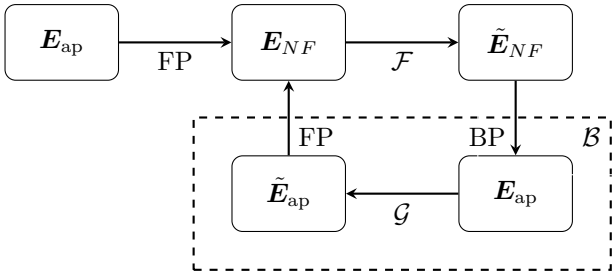

Figure 2.14: *Flowchart of the classical Intersection Approach.*

using a proper starting point, the algorithm after some iterations may find a solution that belongs to both sets or its distance to $\mathcal{M}$ is valid to consider x^* as a solution.

The Intersection Approach concept can be also explained in terms of the electric tangential field at the aperture ($\boldsymbol{E}_{\text{ap}}$) and its radiated field ($\boldsymbol{E}_{NF}$), following the flowchart of Figure 2.14. The field at the aperture $\boldsymbol{E}_{\text{ap}}$ is obtained with (2.13), and considering that the SFA only works in transmission or reflection, the matrix $\boldsymbol{A}$ (2.9) is simplified to a reflection matrix $\boldsymbol{R}$ or a transmission matrix $\boldsymbol{T}$. Hence, the tangential field will be the reflected or transmitted field given by the expresions

$$\boldsymbol{E}_{\text{ap},r}^{X/Y}(m,n) = \boldsymbol{R}^{mn} \cdot \boldsymbol{E}_{\text{inc}}^{X/Y}(m,n) = \begin{pmatrix} \rho_{xx}^{mn} & \rho_{xy}^{mn} \\ \rho_{yx}^{mn} & \rho_{yy}^{mn} \end{pmatrix} \cdot \begin{pmatrix} E_{\text{inc},x}^{X/Y} \\ E_{\text{inc},y}^{X/Y} \end{pmatrix}. \tag{2.67}$$

$$\boldsymbol{E}_{\text{ap},t}^{X/Y}(m,n) = \boldsymbol{T}^{mn} \cdot \boldsymbol{E}_{\text{inc}}^{X/Y}(m,n) = \begin{pmatrix} \tau_{xx}^{mn} & \tau_{xy}^{mn} \\ \tau_{yx}^{mn} & \tau_{yy}^{mn} \end{pmatrix} \cdot \begin{pmatrix} E_{\text{inc},x}^{X/Y} \\ E_{\text{inc},y}^{X/Y} \end{pmatrix}. \tag{2.68}$$

where $\boldsymbol{R}^{mn}$ and $\boldsymbol{T}^{mn}$ are the reflection and transmission matrix of the $(m\,n)$ element.

The phase-only synthesis is based on the consideration that the elements of the array are ideal phase-shifters, thus only the phase of the direct coefficients are needed in the synthesis. If the element is modeled as an ideal phase-shifter the module of the direct coefficients is 1 ($|\rho_{xx}^{mn}| = |\rho_{yy}^{mn}| = 1$ or $|\tau_{xx}^{mn}| = |\tau_{yy}^{mn}| = 1$). Furthermore, the cross coefficients are cancelled ($\rho_{xy}^{mn} = \rho_{yx}^{mn} = 0$ or $\tau_{xy}^{mn} = \tau_{yx}^{mn} = 0$) and the matrix $\boldsymbol{R}$ and $\boldsymbol{T}$ are simplified to

$$\boldsymbol{R}^{mn} = \begin{pmatrix} e^{j\phi_{xx}^{mn}} & 0 \\ 0 & e^{j\phi_{yy}^{mn}} \end{pmatrix} \tag{2.69}$$

$$\boldsymbol{T}^{mn} = \begin{pmatrix} e^{j\phi_{xx}^{mn}} & 0 \\ 0 & e^{j\phi_{yy}^{mn}} \end{pmatrix} \tag{2.70}$$

where ϕ_{xx}^{mn} and ϕ_{yy}^{mn} are the phase of the direct coefficients of the element (m, n) for reflection or transmission. These phases are the degrees of freedom in the synthesis of the radiated field by the SFA.

Once the field at the aperture is computed, the near-field $\boldsymbol{E}_{NF}$ can be obtained by the forward propagation (FP). In this case, the propagation model is given by (2.42), considering each element of the SFA as a small aperture antenna instead of a punctual isotropic source. Generally, the computed near-field $\boldsymbol{E}_{NF}$ does not satisfy the desired specifications, therefore the forward projector $\mathcal{F}$ projects $\boldsymbol{E}_{NF}$ onto a new radiated field $\tilde{\boldsymbol{E}}_{NF}$. This new field fulfills the specifications. However, having a radiated field that satisfies the specifications does not necessarily mean having a field that can be radiated by the antenna, since the constraints are only imposed in the radiated field but not in the antenna optics. The backward projector $\mathcal{B}$ definition is more complex than the forward projector, and it is divided into several steps. Firstly, the backward propagation (BP) permits the computation of the source of $\tilde{\boldsymbol{E}}_{NF}$, thus the field at the aperture $\boldsymbol{E}_{\text{ap}}$ is calculated. Reminding that the field at the aperture depends on the incident field and the cell response, (2.13), it is not guaranteed that $\boldsymbol{E}_{\text{ap}}$ can be a tangential field generated by the proposed antenna. To overcome this issue, new constraints ($\mathcal{G}$) have to be imposed on the antenna geometry, ensuring to obtain an achievable tangential field $\tilde{\boldsymbol{E}}_{\text{ap}}$ at the aperture. Once again, using the forward propagation a new radiated field is obtained. Despite not being this field $\tilde{\boldsymbol{E}}_{NF}$, it is closer to the requirements than the starting point and, it is guaranteed that is achievable by the antenna optics. By doing this process iteratively, a solution that satisfies both geometry restrictions and radiated field conditions may be found .

2.4.2. Generalized Intersection Approach for near-field

In the classic implementation, the hardest step to deal with is the backward projector, especially in the search of a proper backward propagation definition. In order to avoid this search, there is an alternative that proposes the use of an optimization algorithm instead [56]. In this case, the LMA has been chosen to be integrated inside the Intersection Approach as the flowchart of Figure 2.15 depicts.

The LMA is used to find $\boldsymbol{E}_{NF}^{i+1}$ in $\mathcal{R}$ closer to $\tilde{\boldsymbol{E}}_{NF}$ than $\boldsymbol{E}_{NF}$. Let us suppose a field at the aperture $\boldsymbol{E}_{\text{ap}}$ radiated by the antenna. Then, the forward propagation (FP) defined by (2.42) is applied to $\boldsymbol{E}_{\text{ap}}$ and a near-field $\boldsymbol{E}_{NF}$ is obtained (this field belongs to $\mathcal{R}$). It is likely that on the first iteration the field $\boldsymbol{E}_{NF}$ does not satisfy the requirements, therefore the forward projector $\mathcal{F}$ will project it onto a desired field

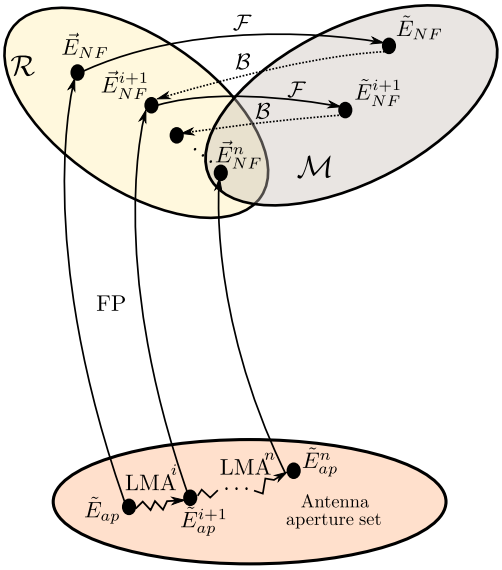

Figure 2.15: *Sketch of the generalized Intersection Approach integrating the LMA and its iterative process.*

$\tilde{\boldsymbol{E}}_{NF}$, which belongs to $\mathcal{M}$. This projector is defined to ensure that

$$T_{\text{lower}} \leq \tilde{\boldsymbol{E}}_{NF} \leq T_{\text{upper}} \tag{2.71}$$

where $\tilde{\boldsymbol{E}}_{NF}$ is the constrained field that belongs to $\mathcal{M}$; T_{lower} and T_{upper} are the lower and upper specification boundaries, respectively.

Ultimately, the projector $\mathcal{F}$ trims the radiated field $\boldsymbol{E}_{NF}$ according to a given specifications, which are generally expressed in form of templates. This process is shown in Figure 2.16 and the trimmed field $\tilde{\boldsymbol{E}}_{NF}$ is computed as

$$\tilde{\boldsymbol{E}}_{NF}(\boldsymbol{r}) = \begin{cases} T_{\text{upper}}(\boldsymbol{r}), & \text{if } \boldsymbol{E}_{NF}(\boldsymbol{r}) \geq T_{\text{upper}}(\boldsymbol{r}) \\ T_{\text{lower}}(\boldsymbol{r}), & \text{if } \boldsymbol{E}_{NF}(\boldsymbol{r}) \leq T_{\text{lower}}(\boldsymbol{r}) \\ \boldsymbol{E}_{NF}(\boldsymbol{r}), & \text{otherwise} \end{cases} \tag{2.72}$$

To apply the optimization algorithm LMA, the generalized Intersection Approach defines a functional d that evaluates the distances from one point on $\mathcal{R}$ to another on $\mathcal{M}$, therefore the distance from $\boldsymbol{E}_{NF}$ to $\tilde{\boldsymbol{E}}_{NF}$, see Figure 2.15. This functional is based on the Euclidean distance definition, noticing that each element of both sets has to be expressed in terms of magnitude and phase. Therefore, the functional should

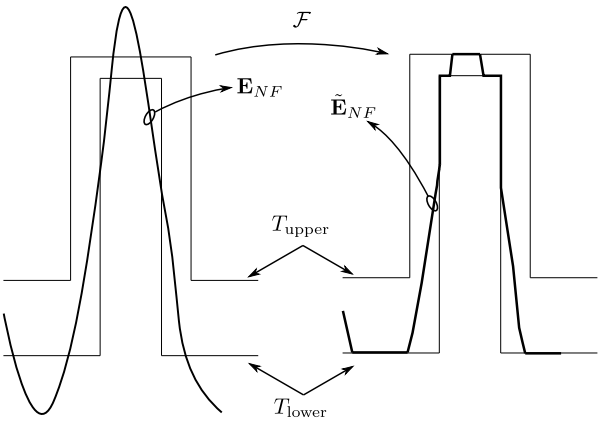

Figure 2.16: *Projection of the field $\boldsymbol{E}_{NF}$ (set $\mathcal{R}$) onto the set of valid near-fields $\mathcal{M}$, resulting on $\tilde{\boldsymbol{E}}_{NF}$.*

considered both terms independently.

$$\begin{aligned} d = d_M + d_P = \int_\Omega w_M \left(\left| |\tilde{\boldsymbol{E}}_{NF}|^2 - |\boldsymbol{E}_{NF}^{\text{LMA}}|^2 \right| \right) d\Omega + \\ \int_\Omega w_P \left(\left| \angle \tilde{\boldsymbol{E}}_{NF} - \angle \boldsymbol{E}_{NF}^{\text{LMA}} \right| \right) d\Omega \end{aligned} \tag{2.73}$$

where Ω is the volume where the near-field is computed, and w_M and w_P are the weighted functions. Now, if the volume Ω is discretized in N_z planes along $\hat{\boldsymbol{z}}$ and N_{xy} points in each plane, the functional d may be written as

$$\begin{aligned} d = d_M + d_P = \sum_l^{N_z} \Big[\sum_j^{N_{xy}} w_M \left(\left| |\tilde{\boldsymbol{E}}_{NF,j,l}|^2 - |\boldsymbol{E}_{NF,j,l}^{\text{LMA}}|^2 \right| \right) + \\ + \sum_j^{N_{xy}} w_P \left(\left| \angle \tilde{\boldsymbol{E}}_{NF,j,l} - \angle \boldsymbol{E}_{NF,j,l}^{\text{LMA}} \right| \right) \Big] \Delta_{x,j} \Delta_{y,j} \Delta_{z,l} \end{aligned} \tag{2.74}$$

where the subscript l indicates the plane that is evaluated and j the (x, y) point wherein the distance is computed. $\Delta_{x,j}$ and $\Delta_{y,j}$ are the steps of the plane discretization on the $\hat{\boldsymbol{x}}$ and $\hat{\boldsymbol{y}}$ direction, respectively. $\boldsymbol{E}_{NF}^{\text{LMA}}$ is the field used by the LMA to evaluate d, and it is related with the aperture by

$$\boldsymbol{E}_{NF}^{\text{LMA}} = \text{FP}\left(\boldsymbol{E}_{\text{ap}}^{\text{LMA}}\right) \tag{2.75}$$

On the other hand, the degrees of freedom of the LMA are the phase distribution

of the direct coefficients of the SFA elements given by ϕ_{xx}^{mn} and ϕ_{yy}^{mn}, depending on the polarization of the feed. The aim of the LMA is not to reach a minimum of d in each iteration of the generalized Intersection Approach but to reduce it. Hence, only a few iterations of the LMA are needed in each iteration of the generalized Intersection Approach [56]. The starting point of the LMA is the near-field of the iteration i of the generalized Intersection Approach $\boldsymbol{E}_{NF}^{i}$ and the LMA provides the near-field of the iteration $i+1$ ($\boldsymbol{E}_{NF}^{i+1}$), which is closer to $\tilde{\boldsymbol{E}}_{NF}$. After several iterations of the generalized Intersection Approach, an intersection between the two sets $\mathcal{M}$ and $\mathcal{R}$ may be found. Therefore, reaching a near-field within the constraints and feasible by the antenna optics. If the intersection is not found, at least a near-field $\boldsymbol{E}_{NF}$ whose distance to $\tilde{\boldsymbol{E}}_{NF}$ is minima.

2.4.3. Levenberg-Marquardt algorithm

The Levenberg-Marquardt algorithm is a modification of the Gauss-Newton algorithm, and uses and iterative process to solve non-linear least-square problems. The LMA has been used with sucess in the optimization of linear arrays or different planar arrays such as reflectarrays [61,62,217]. This algorithm minimizes a cost function of the form

$$F(\boldsymbol{\xi}) = \sum_{i=1}^{T} r_i(\boldsymbol{\xi})^2 \tag{2.76}$$

where $r(\boldsymbol{\xi})$ is known as the residual of the cost function and $\boldsymbol{\xi}$ is a vector of points where the cost function is evaluated, and it is discretized in T points. Since the generalized Intersection Approach integrates the LMA to minimize the functional d, this functional is the residual, and $\boldsymbol{\xi}$ should be a vector with the points of the discretized volume Ω, where the radiated field is computed according to (2.73) and (2.74). Hence, (2.76) can be expressed as

$$F(\boldsymbol{\Omega}) = \sum_{i=1}^{T} d_i(\boldsymbol{\Omega})^2 \tag{2.77}$$

where $\boldsymbol{\Omega}$ is the vector with the discretized point of Ω and its size is given by (2.74) as

$$T = N_z\,(2N_{xy}) \tag{2.78}$$

A flow chart of the algorithm is present in Figure 2.17. After the initialization, the cost function is computed, providing the error at the current iteration. If this error is lower than a reference error threshold, the algorithm finishes since a convergence solution has been reached. Otherwise, it continues with the computations. The LMA

belongs to the gradient-based algorithms, and such as, it computes a Jacobian matrix, which can be computed either analytically or by finite differences. After the Jacobian computations, a set of normal equations is formed, which involves a big matrix multiplication with the Jacobian and a matrix-vector. Then, the equation system is solved, obtaining the updating vector to the solution.

The LMA requires the computation of the Jacobian matrix (J), which is a $T \times P$ matrix, where P is the total number of variables to optimized. Thus, the phase of the direct reflection or transmitted coefficients of each element of the SFA (ϕ_{xx}^{mn} and ϕ_{yy}^{mn}). The gradient of a multidimensional scalar cost function uses to form the Jacobian matrix is

$$\nabla d(\mathbf{\Omega}, \bar{\phi}) = \left(\frac{\partial d(\mathbf{\Omega}, \bar{\phi})}{\partial \phi^1}, \cdots, \frac{\partial d(\mathbf{\Omega}, \bar{\phi})}{\partial \phi^i}, \cdots, \frac{\partial d(\mathbf{\Omega}, \bar{\phi})}{\partial \phi^m} \right) \tag{2.79}$$

where an element of $\mathbf{\Omega}$ is an observation point defined as $\mathbf{\Omega_t} = (x_t, y_t, z_t)$ and $\bar{\phi} \in (\phi^1, \cdots, \phi^i, \cdots, \phi^m)$ is a vector which elements are the optimization variables.

In the case where the analytical expression cannot be used, the derivatives can be computed using finite differences [69]. Considering the backward lateral difference, and dropping the dependence on $\mathbf{\Omega}$ in order to alleviate the notation, the derivative is expressed as

$$\frac{\partial d(\bar{\phi})}{\partial \phi^m} = \frac{d(\bar{\phi}) - d(\bar{\phi} - h\hat{e}_i)}{h} + \mathcal{O}(h) \tag{2.80}$$

where h is a small positive scalar and $\hat{e}_i$ is the ith unit vector such that

$$\bar{\phi} - h\hat{e}_i = (\phi^1, \cdots, \phi^i - h, \cdots, \phi^m) \tag{2.81}$$

Once the gradient and the Jacobian matrix have been computed, the LMA is applied iteratively as

$$\left[J_i^T \cdot J_i + \mu_i \cdot \mathrm{diag}\left(J_i^T \cdot J_i \right) \right] \cdot \delta_i = -J_i^T \cdot d_i \tag{2.82}$$

where the sub-index i represents the current iteration, J^T is the transpose Jacobian matrix, $\mathrm{diag}(\cdot)$ is the diagonal matrix, δ is the updating vector which satisfied the equality and μ is a real positive number. The choice of $\mathrm{diag}(J_i^T \cdot J_i)$ instead of other positive diagonal matrix, such as the identity, is to reduce the effects of poor scaling in the optimization variables by using and ellipsoidal trust region. This way, the algorithm is invariant under diagonal scaling of the components of $\bar{\phi}$ [69].

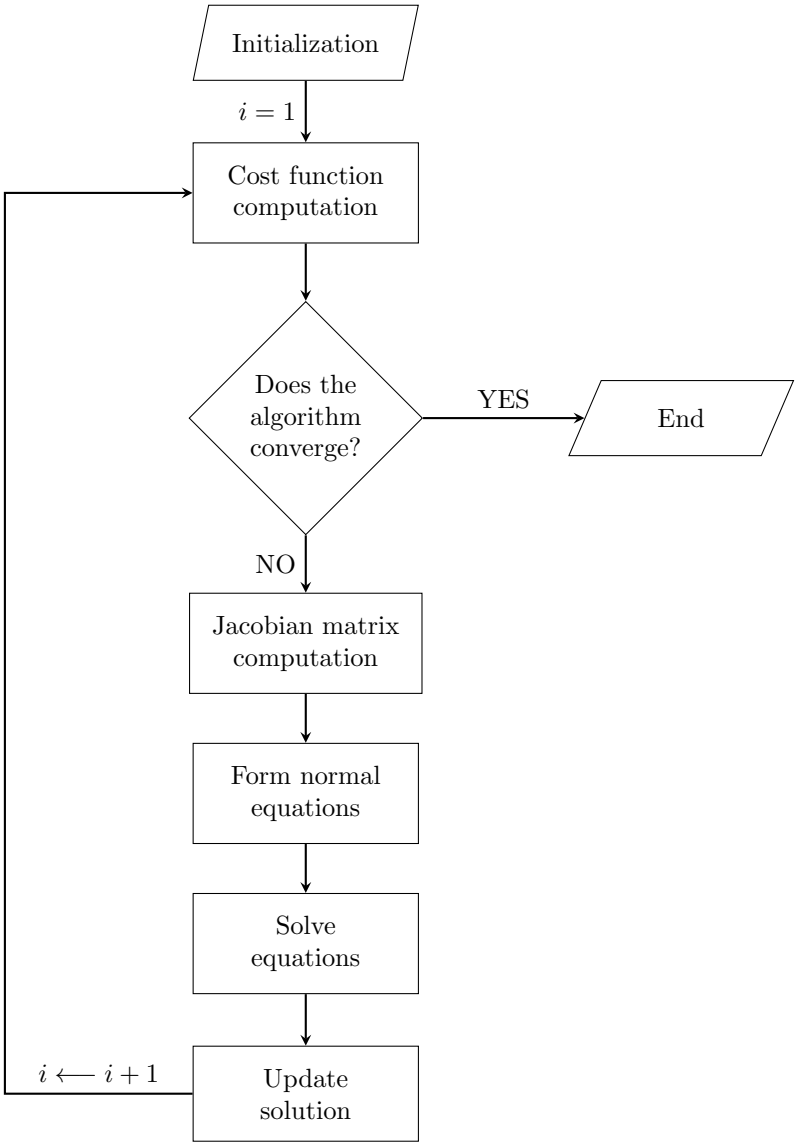

Figure 2.17: *Flow chart of the Levenberg-Marquardt algorithm for Phase-Only Synthesis.*

In order to solve (2.82), it can be compactly written as

$$A_i \cdot \delta_i = b_i \tag{2.83}$$

This compact equation can be solve using a Cholesky factorization [211]. The Cholesky decomposition is based on expressing A_i in the form

$$A_i = GG^T \tag{2.84}$$

where G is a lower triangular matrix. Then, (2.84) is solveb by solving the following equation system

$$G \cdot y = b_i \tag{2.85}$$

obtaining b_i from this equation and

$$G^T \cdot \delta_i = y \tag{2.86}$$

obtaining δ_i. Therefore,

$$b_i = G \cdot y = GG^T \cdot \delta_i = A_i \cdot \delta_i \tag{2.87}$$

After the matrix system is solved, the solution is updated as

$$\bar{\phi}_{i+1} = \bar{\phi}_i + \delta_i \tag{2.88}$$

2.4.4. Differential contributions on the gradient calculation

One of the most time-consuming operations on the LMA is the calculation of (2.79). An approach to speed up this process is the use of the technique of differential contributions. This approach requires two conditions that are met. First, the modification of a single variable does not affect other variables. Second, part of the process for the calculation of the cost function is linear.

The first condition is met when the analysis of each SFA element is independent of the rest, such as under the assumption of local periodicity. Despite this condition, the coupling between elements may be considered. In the case of a POS, the mutual coupling is considered in a further step, during the design process of the SFA element to match the phase distribution obtained in the synthesis stage [2].

The second condition states that the entire process for the calculation of the gradient or, at least, a part of it must be linear. Ideally, this linear relation would be

between the optimizing variable ϕ^m and the cost function $F(\mathbf{\Omega})$. In practice, this is not achievable for array antennas synthesis. Indeed, it is common the use of nonlinear cost function which breaks the linear relation. However, due to the linearity of Maxwell's equations, the relation between the tangential field and the radiated field is linear, and this can be exploited in array antennas synthesis to accelerate the computation of the gradient by applying the technique of differential contributions to the computation of the radiated field from the field at the aperture.

Bring (2.80) back, the residual $d(\bar{\phi})$ is common for all the derivatives in (2.79), and it can be computed once using (2.74). On the other hand, $d(\bar{\phi} - h\hat{e}_i)$ depends on the variable ϕ^m and it is computed in each derivative. Under local periodicity assumption, the modification of one element (variable) of the SFA does not affect the rest, so the perturbed field can be computed by extracting the original contribution of the unperturbed SFA element and adding the contribution of the perturbed element. Therefore, the residual $d(\bar{\phi} - h\hat{e}_i)$ is computed as

$$\begin{aligned} d(\bar{\phi} - h\hat{e}_i) = &\left[|\tilde{\boldsymbol{E}}_{NF}(\bar{\phi})|^2 - \left(|\boldsymbol{E}^{i+1}_{NF}(\bar{\phi}) + \Delta\boldsymbol{E}^{i+1}_{NF}(\phi^m)|^2\right)\right] + \\ &+ \left[\angle\tilde{\boldsymbol{E}}_{NF}(\bar{\phi}) - \angle\left(\boldsymbol{E}^{i+1}_{NF}(\bar{\phi}) + \Delta\boldsymbol{E}^{i+1}_{NF}(\phi^m)\right)\right] \end{aligned} \tag{2.89}$$

where $\Delta\boldsymbol{E}^{i+1}_{NF}(\bar{\phi})$ is the differential contribution of the near-field radiated by the element (variable) m of the SFA

$$\Delta\boldsymbol{E}^{i+1}_{NF}(\phi^m) = \boldsymbol{E}^{i+1}_{NF}(\phi^m - h) - \boldsymbol{E}^{i+1}_{NF}(\phi^m) \tag{2.90}$$

Hence, in the computation of one derivative is only necessary to compute the differential contribution of the perturbed element, accelerating the computing time of (2.79) in each iteration of the LMA.

CHAPTER 3

Dielectric graded-index planar lenses for focusing applications

3.1. Introduction

This chapter is devoted to the analysis of different techniques on the design of spatially-fed arrays to focus the near-field on either a spot or a non diffracted beam. As it was introduced in the first chapter, near-field applications have risen their popularity in different fields throughout the last years. Most of these applications demand antennas with the capability of focusing their radiated electromagnetic field within the Fresnel region to increase the electromagnetic power density in a spot close to the antenna aperture.

As it was detailed in Chapter 1, the generation of non-diffraction beams is a current research topic at microwave and millimeter frequencies because of its inherent suppression of diffraction through the propagation direction, resulting in well-collimated beams. This effect can improve the performance of many systems such as near-field radars obtaining a reduction of diffraction and better confinement of the field on the area of interest, reducing scattering from undesired areas. The most common non-diffraction solution is the Bessel beams, nonetheless, this solution is only valid for infinite apertures since non-diffraction beams require infinity energy. When using finite radiating apertures pseudo-Bessel beams are produced instead of Bessel beams. The amplitude of a pseudo-Bessel beam only remains constant through a certain range before losing its collimating property and spreading rapidly. As it was pointed out, different solutions were proposed to the generation of these pseudo-Bessel beams at microwave or millimeter frequencies such as leaky radial waveguides, GRIN metamaterial lenses or RLSA [175–181]. However, a spatially-fed array can be also considered

as a planar low-profile alternative to generate Bessel beam as the PSS antenna of [189] shows. Particularly, transmitarray antennas are a potential candidate, since they avoid the blockage losses of a reflectarray antenna, and they can be manufactured on PCB or, even 3D-printed elements, which provides a low-cost low-profile alternative.

In Section 3.2 the design of a transmitarray based on 3D printed elements is analyzed at Ka-band. In analogy with other near-field focusing antennas this approach is also so-called a graded-index planar lens. The working principle of these antennas is similar to a PSS or even a printed element transmitarray. However, the introduced phase-shift in the incoming wave is adjusted by the variation of the index media of the element. This solution takes the advantage of additive manufacturing techniques to obtain an easy-low-cost fabrication. This fabrication process has been applied on lenses [218, 219] or axicons [220] to generate Bessel beams or shaped near-field patterns [77] using transmitarray antennas. These elements are designed to obtain the index dielectric variation by the variation of the height of the element and produce the required phase-shift. However, these types of elements produce an important mismatch at the dielectric-air interface producing a low transmission coefficient, unless an anti-reflection structure is used in the element [129]. Moreover, one of the antenna surfaces has a stepped profile that may cause diffraction because of the edges of the cell of the non-planar surface. A novel element to overcome both issues, diffraction and mismatching, is presented in this section. These elements achieve the required phase-shift by a variation on the dimension of an air gap embedded in the cell. After a complete analysis of these cells and a detailed explanation of the generation of Bessel beams on graded-index planar lenses, two designs are carried out to evaluate the overall performances of this 3D printed solution on the generation of non-diffraction beams.

The following sections are devoted to analyzing the focusing capabilities of graded-index planar lenses. Similar to Bessel beams, the use of antennas with focusing capabilities can improve the performances of different applications. A few are MWI, RFID, or WPT whether a multiple near-field focusing antenna is used. What seems certain is that either near-field single or multiple focus techniques are needed to enhance the different performances of present and future applications.

Section 3.3 addresses the analysis and comparison of a graded-index planar lens with a doubly hyperbolic lens. The aim is to evaluate the focusing capability of spatially-fed arrays based on dielectric-only elements, which are manufactured on 3D-printed technology. The doubly hyperbolic lens is designed following the analytical equations of a converging lens. Then, the equivalent graded-index planar lens is designed using the Conjugate Phase (CP) technique. This approach is based on the

adjustment of the phase-shift elements so that the radiated wave arrives in phase at a single focal point [221]. The conjugate phase is widely used in classical arrays, and it also can be applied on spatially-fed arrays taking the advantage of avoiding the feeding networks [151]. Both lenses are manufactured with additive fabrication and their focusing properties are compared in terms of their physical dimensions.

The last section presents a multi-focusing solution for transmitarray antennas. A common approach in planar arrays for multi-focusing antennas is the optimization of the amplitude and phase of the excitation of the array elements to radiate the desired pattern [203]. In a multi-target optimization process, the cost function that is minimized must include requirements for all the spots simultaneously. Thus the computational cost significantly increases and hinders the convergence of the algorithm. In Chapter 1, different spatially-fed arrays that generate multiple beam solutions without any optimization of the antenna were reviewed, mainly for space communications. In addition, in [222] a graded-index lens was proposed to obtain a multi-beam pattern by feeding the lens with a multiple-port stacked-patch feed, obtaining four different and independent beams. Hence, spatially-fed arrays can provide multiple beam configurations without needing any optimization process. A straightforward approach is based on a mechanical movable feed to cover different positions, generating a different and independent beam determined by the feed position. Hence, the graded-index planar lens designed in Section 3.3 is used to analyze this concept for a near-field multi-focusing solution at millimeter frequencies. In this case, the graded-index planar lens is illuminated by a cluster of horn antennas. The cluster operates at the same working frequency but each horn antenna uses a shifted carrier concerning the central frequency to obtain independent spots. This section aims to evaluate the graded-index planar lens fed by a multi-feed configuration to evaluate the multi-focusing performance of this approach and apply it to further configurations in Chapter 4. Also, this technique provides an alternative with a low complexity regarding an optimization process, since it is based on a CP design and a proper feed distribution.

The different techniques described in previous sections are sorely based on phase considerations. These solutions provide successful results as it can be found in several published works or throughout this chapter. However, the described approaches are not including different real considerations of an SFA such as the amplitude of the incident field or the behavior of the elements (losses, response within a periodic structure, or response under oblique incidence). These limitations do not enable the control over certain parameters such as SLLs, the depth-of-focus, or the correction of phase aberrations caused by the movement of the feed.

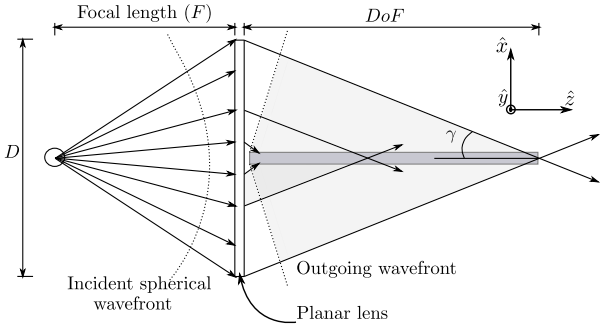

Figure 3.1: *Sketch of the Bessel beam generation through finite aperture antennas using near-field interferences.*

3.2. Bessel beam launcher based on planar lenses at millimetre frequencies

3.2.1. Fundamentals of Bessel beams in finite apertures

The main characteristic of Bessel beams is their propagation through a distance with a constant field intensity without diffraction. An ideal Bessel beam is only generated by an infinite aperture since it carries and infinity energy. Then, the amplitude of this ideal Bessel beam is in the form of

$$\boldsymbol{E}(\rho, z) = E_0 e^{jk_z z} J_0(k_\rho \rho)\hat{\boldsymbol{y}} \tag{3.1}$$

where J_0 is the first-kind zero-order Bessel function, k_ρ and k_z are the radial component and longitudinal component of the free space wave vector, such that $k_0^2 = k_\rho^2 + k_z^2$. The electric field is polarized according to $\hat{\boldsymbol{y}}$.

Admittedly, neither working with infinite nor thousands of λ apertures is physically feasible, purely Bessel beams are not produced but pseudo-Bessel beams are instead. Hence, when working with finite aperture only pseudo-Bessel beams are achievable. These beams are characterized for only having a constant amplitude on a certain propagation distance before rapidly spreading instead of remaining constant through an infinite distance. The beam is produced by the generation of a near-field interference pattern that, basically keeps the field constant within an area. The size of this area is limited by the size of the antenna aperture (D) used.

When this concept is applied to millimeter frequencies antennas and, particularly to an SFA, the working principle is based on the transformation of a spherical incom-

ing wavefront provided by the feed to a plane wave with wave vector lying on a cone, as Figure 3.1 depicts. The outgoing wavefront must generate a near-field interference pattern that behaves as a pseudo-Bessel beam. In Figure 3.1, the extent of the shadowed area is defined by two parameters, D and γ, and it is called depth-of-field (DoF). This area can be easily computed by applying trigonometry according to (3.2) and it corresponds to the theoretical 3 dB contour of the field.

$$\mathrm{DoF} = \frac{D/2}{\tan(\gamma)} \tag{3.2}$$

The theoretical maximum distance achievable is limited to the boundary of the Fresnel region of the antenna (3.3). Conversely, the angle γ must satisfy (3.4), otherwise, the scalar Bessel beam theory previously explained cannot be applied [223].

$$\mathrm{DoF}_{max} = \frac{2D^2}{\lambda} \tag{3.3}$$

$$\sin\gamma \ll 1 \tag{3.4}$$

The design of SFA antennas to radiate a pseudo-Bessel beam can be approached using GO. Let us consider an SFA comprised of a given number of elements regularly distributed on a $N_x \times N_y$ grid. The feed is placed at a focal length F to generate a pseudo-Bessel beam with an angle γ, according to Figure 3.1. The outgoing wavefront must have its wave vector laying on a cone as the wavefront is radiated through the propagation direction $\hat{\boldsymbol{z}}$. This last condition is mandatory to create a proper near-field interference pattern to obtain the desired beam. Then, the elements of the SFA should be properly selected to introduce the required phase-shift to transform the spherical incoming wavefront into the desired one. The phase-shift of each element can be computed using GO since the phase produced by these elements are given by

$$\phi_{SFA}(\rho) = -\phi_{inc}(\rho) - \varphi_{wf} - \frac{2\pi}{\lambda}\rho\tan\gamma \tag{3.5}$$

where φ_{wf} is the phase of the outgoing wavefront, ρ is the axial position of the (m,n) element (3.6), considering the center of the SFA as the center of the circumference, and ϕ_{inc} is the incident phase at the (m,n) element according to (3.7).

$$\rho = \sqrt{x_m^2 + y_n^2} \tag{3.6}$$

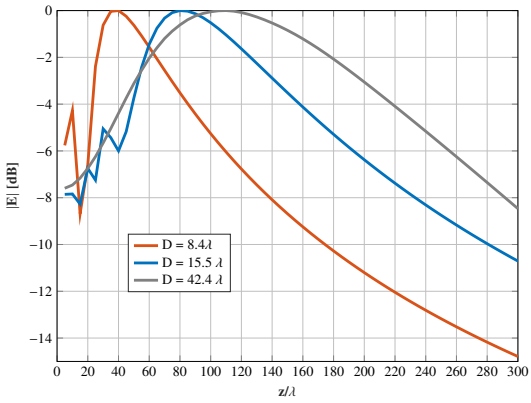

Figure 3.2: *Comparison of different Bessel beams produced with apertures of* $D = 8.4\lambda, 15.5\lambda,$ *and* $, 42.4\lambda$*,* $F = 150$ *mm, and* $5°$ *with a* $\cos^q$ *feed with* $q = 7$*. Normalized patterns.*

$$\phi_{inc}(\rho) = -\frac{2\pi}{\lambda}\sqrt{F^2 + \rho^2} \tag{3.7}$$

Now, different SFA antennas working in transmission have been simulated to analyze the influence of the aperture size on the depth-of-focus achievable on finite apertures. In this case, three different apertures have been used, $D = 8.4\lambda, 15.5\lambda$ and 42.4λ, while keeping γ and F constant and equal to $5°$ and 150 mm, respectively. The feed has been modeled as a $\cos^q$ function with $q = 7$, and the elements have been computed with (3.5). In Figure 3.2 a comparison of the axial intensity of these three pseudo-Bessel beams is shown. As it could be expected, the larger aperture the deeper pseudo-Bessel beam is obtained.

3.2.2. Working principle of graded-index dielectric planar lenses

In this section, the evaluation of a Bessel beam with non-diffraction performances within the near-field region is carried out through the design of a graded-index dielectric planar lens. This graded-index planar lens is equivalent to a transmitarray made up of dielectric-only elements with focusing capabilities. Broadly speaking, a type of transmissive SFA antenna. The concept of a graded-index dielectric planar lens is that the element behaves as an effective index media that introduces a given delay on the transmitted ray. As it occurs in other SFA, the phase-shift of each element may be

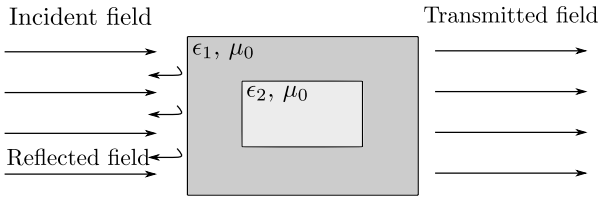

Figure 3.3: *Sketch of a dielectric-only cell based on the combination of two spatially uniform and isotropic materials of dielectric constant ϵ_1 and ϵ_2.*

different depending on its position in the SFA and the required outgoing phase-front. In this case, the effective index media (η_{eff}) of an element of the SFA is related with its effective relative dielectric constant (ϵ_{eff}) through

$$\eta_{eff}^2(\rho) = \epsilon_{eff}(\rho) \tag{3.8}$$

Then, the delay introduced by a cell can be computed using (3.9), and the variation of the effective relative dielectric constant enables to physically control the phase-shift $\phi_{cell}(\rho)$ introduced by an element of the SFA.

$$\phi_{cell}(\rho) = \frac{2\pi f \sqrt{\epsilon_{eff}}}{c_0} \cdot \Delta h \tag{3.9}$$

where f is the operational frequency, c_0 is the speed of light in vacuum and Δh is the thickness of the cell.

One approach to physically implement the dielectric-only cells is the use of dielectric cells based on the combination of two spatially uniform and isotropic materials. Let us assume two spatially uniform materials of dielectric constant ϵ_1 and ϵ_2, respectively. If the first material hosts the second one as Figure 3.3 depicts, the effective dielectric constant of the assembled cell does not depend on the geometry of the cell but on the dielectric constants of both materials and its volume fraction [224–226]. According to [224] the effective dielectric of the cell can be computed using Maxwell-Garnett equation of the form

$$\epsilon_{eff} = \epsilon_1 \frac{2\epsilon_1 + \epsilon_2 + 2P(\epsilon_2 - \epsilon_1)}{2\epsilon_1 + \epsilon_2 - P(\epsilon_2 - \epsilon_1)} \tag{3.10}$$

where P is the volume fraction of the material ϵ_2 over the total volume of the cell.

In this case, the host dielectric material of the proposed cells is the polylactic acid (PLA) which dielectric constant is $\epsilon_1 = 2.85$ and $\tan\delta = 0.0121$ at 40 GHz [227]. Then, if the embedded material is air, only the PLA is needed to accomplish (3.10),

being $\epsilon_2 = \epsilon_0$. Therefore, the cells use PLA as a host material and air ($\epsilon_2 = \epsilon_0$) for the inclusion. The size of these inclusions enables to change the volume fraction P and controls the $\phi_{cell}(\rho)$ introduced in each cell.

It is nevertheless important to note that, in [224], (3.10) provides the effective permittivity of a medium with inclusions of metal spheres and not for two dielectric materials with arbitrary geometry. However, (3.10) does not have any geometrical reference to the inclusions. Therefore, it could be assumed that Maxwell-Garnett could provide the effective permittivity of a dielectric cell with insertions of arbitrary geometry. To validate this assumption and the accuracy of (3.10) for these types of cells, different dielectric cells with different filling factors P have been analyzed. First, the set of cells were simulated in CST Microwave Studio [209] to compute their phase-shift given by the phase of the S-parameter s_{21} (ϕ_{s21}). Then, following the next equations the effective relative dielectric constant according to the phase of the s_{21} can be obtained as

$$\phi_{s21} - (n \cdot 360) = -\beta \cdot \Delta h \tag{3.11}$$

where n is an integer greater than 1, Δh is the thickness of the cell and β is the phase constant expressed as

$$\beta = -\frac{2\pi f}{c_0}\sqrt{\epsilon_{eff}} \tag{3.12}$$

Replacing (3.12) in (3.11), the effective dielectric constant is written as

$$\epsilon_{eff} = \left(\frac{-(\phi_{s21} - n \cdot 360) \cdot c_0}{2\pi f \Delta h}\right)^2 \tag{3.13}$$

The effective permittivity obtained by this method has been compared to the one obtained with (3.10), considering the same filling factor P on both analyses. Then, in CST Microwave Studio different cells of a single dielectric material with the effective permittivity given by (3.10) were simulated to compare their phase-shift with the one obtained previously. The results are shown in Figure 3.4, obtaining a high agreement in both cases. In the light of these results, (3.10) can provide a valid value of the dielectric cells with air gap inclusions. Additionally, [225] shows a validation on the computation of different equivalent dielectric constants of dual-material mixing cells for several geometries of the insertions considering dielectric-only cells.

3.2.3. Definition of cells based on air gaps inserts

In this section, two different types of cells based on air gaps inclusions have been analyzed: a square prism cell and a hexagonal prism. The air gap embedded in the

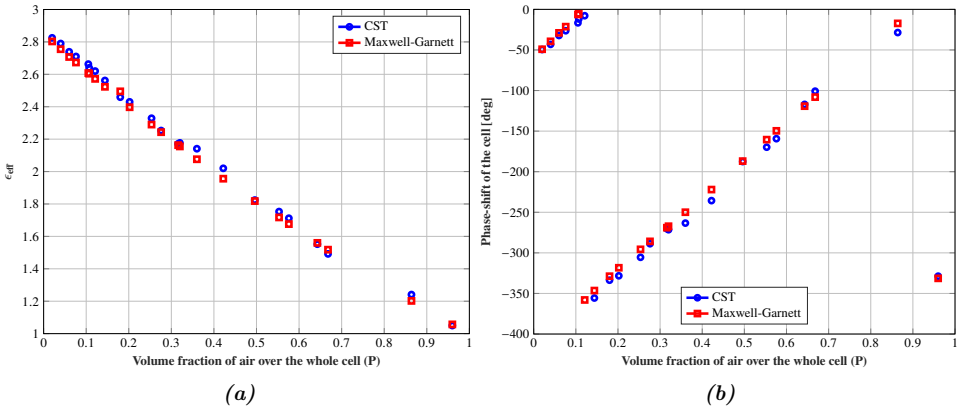

(a) *(b)*

Figure 3.4: *Comparison of (a) the effective dielectric constant and (b) phase-shift computed with CST Microwave Studio and Maxwell-Garnett* (3.10) *for a dielectric cell with air gaps insertions.*

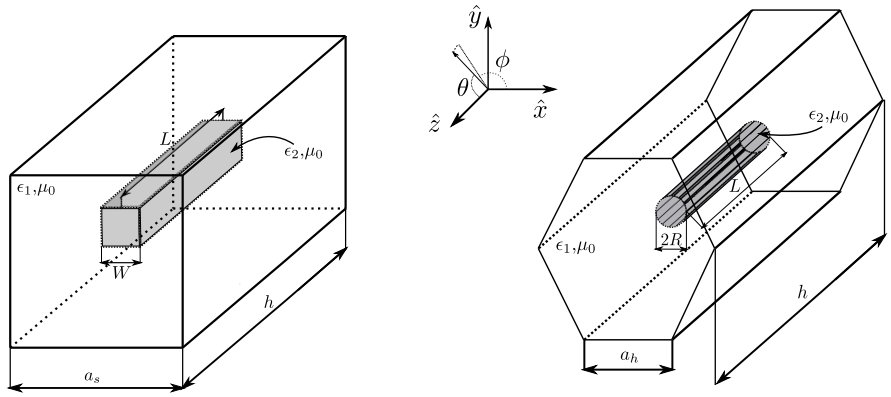

(a) *(b)*

Figure 3.5: *Description of dielectric cells based on air gaps insertions to control the effective dielectric constant (a) square prism with square prism insertions (b) hexagonal prism with cylindrical insertions.*

cell is a square prism and a cylinder respectively. Both cells are depicted on Figure 3.5. Starting from the square prism cell, Figure 3.5(a), the dimensions of the PLA square prism dimensions are $a_s \times a_s \times h$, whilst the second embedded air gap square prism dimensions are $W \times W \times h$. These dimensions are variable to control the infill of the

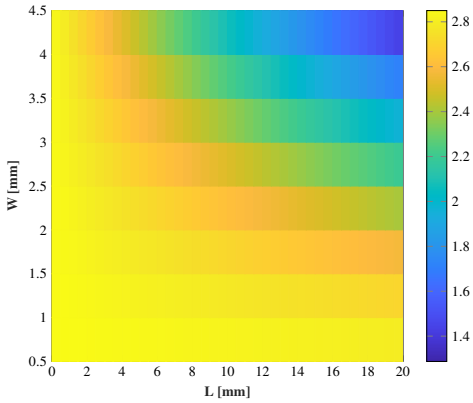

Figure 3.6: *Effective dielectric constant of the square prism cell considering different P factor adjusting the dimensions of the embedded air gap.*

cell. With this geometry, P is defined as

$$P = \frac{V_{airgap}}{V_{prism}} = \frac{W^2 \cdot L}{a_s^2 \cdot h} \tag{3.14}$$

The dimensions of the PLA square prism are $\lambda/2 \times \lambda/2 \times 2\lambda$, whilst the air gap dimension is swept from $W \in (0, \lambda/2)$ and $L \in [0, 2\lambda]$. Thus, both full dielectric cells ($\epsilon_{eff} = 2.85$) and almost air cells ($\epsilon_{eff} = 1.28$) are considered as Figure 3.6 shows. The phase response of each combination of W and L is obtained by a CST Microwave Studio. The cell is analyzed considering periodic boundary conditions in the x- and y- direction and open in z-direction. The cell is illuminated by a normal plane wave propagating in the z-direction with the electric field defined in the y-direction. The analysis is performed at a frequency of 30 GHz. Then, the amplitude and the phase response of the transmission coefficients of the cell (τ_{yy} since the electric vector is defined in the y-direction) are shown in Figure 3.7 for normal incidence. The different combinations of W and L provide a phase-shift range of 360°, enough to fully cover the range to implement $\varphi_{SFA}(\rho)$. Although the $\tan\delta$ of PLA is significantly high compared to other conventional solutions, such as microstrip printed elements, more than 85% of the cells present a transmission loss lower than 1.5 dB.

On the other hand, the hexagonal prism cells with an embedded cylinder air gap, Figure 3.5(b), must have the same response as the square prism cells. Following (3.10), a change in the geometries of the cell does not affect the phase-shift, as long as P is preserved in the new cell. Considering that the height of both cells is the same and

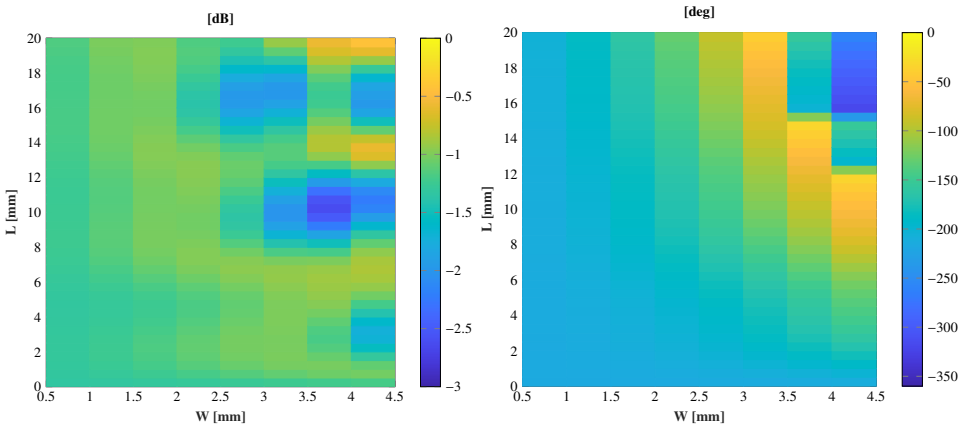

(a) *(b)*

Figure 3.7: *Square prism cell response in function of different P factor adjusting the dimensions of the embedded air gap for normal incidence at 28 GHz. (a) Amplitude (dB) (b) Phase (deg).*

equal to 2λ, the condition to keep the same volume on a single cell is to ensure that the base of both prisms is the same. Using (3.15), which is obtained with the well-known equations to compute the area of a square and a hexagon, it is obtained that the hexagon must have a radius $a_h = 0.31\lambda$ to have the same volume in a single cell regardless of its geometry.

$$a_s^2 = \frac{3}{2\tan(30)} \cdot a_h^2 \tag{3.15}$$

To adjust the cylinder dimensions, the depth of the cylinder remains alike to the depth of the square prism air gap L, while the area of the base of the cylinder must be like the area of the square base of the other air gap. Therefore,

$$R^2 = \frac{W^2}{\pi} \tag{3.16}$$

Now, the analysis carried out with CST Microwave Studio is repeated for different hexagonal prism cells within a bandwidth of 4 GHz, from 26 to 30 GHz, and their equivalent square prism cells according to (3.15) and (3.16). The amplitude and phase of the transmission coefficients τ_{yy} versus frequency is shown in Figure 3.8, which shows a complete agreement between both types of cells. Therefore, the geometry of the cell does not affect the cell response, it is only necessary to control P.

The angular stability of the cell has been also analyzed for different angles of incidence θ and ϕ at 28 GHz. Considering the linear polarization of the incident

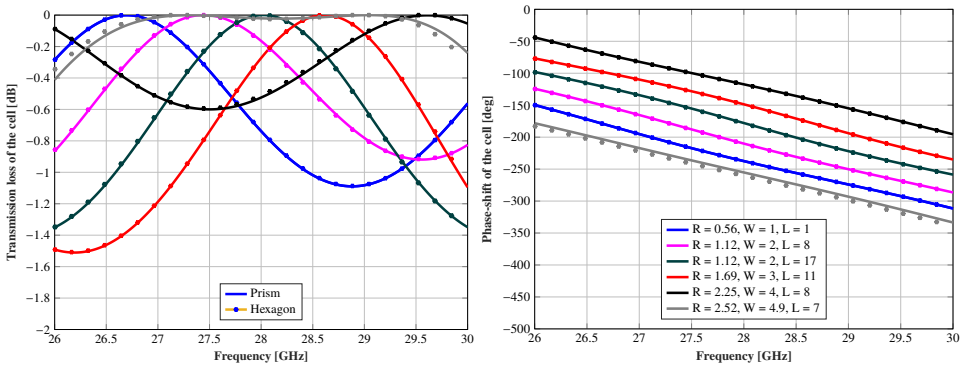

(a) *(b)*

Figure 3.8: *Comparison of the transmission (a) amplitude and (b) phase of different cell (both square and hexagon prism) with the same overall filling factor. The air gap dimensions are in mm.*

field and the angles θ and ϕ defined in Figure 3.5, the analysis has been carried out for $\phi = 0°, 45°$ and $90°$ and $\theta \in [0, 30]^\circ$, being $(\theta, \phi) = (0, 0)^\circ$ normal incidence. In Figure 3.9 the phase response from a set of 6 different cells is shown as a function of θ and ϕ. It should be noted that the angular response has no dependence on ϕ, while θ notably modifies the phase-shift regarding the normal incidence case. This modification is similar to a polynomial response, therefore, it can be approximated by a second-order polynomial of the form

$$\Delta\phi_{cell}(\theta) = p_1 \cdot \theta^2 + p_2 \cdot \theta \tag{3.17}$$

where p_1 and p_2 are the polynomial coefficients. It can be observed in Figure 3.9 that, the curve shape is similar to the phase response obtained with CST Microwave Studio and the one obtained with (3.17), which is common for all the cells with $p_1 = 0.0425$ and $p_2 = 0.7453$. Hence, the phase of the transmission coefficient for each cell, depending on their angle of incidence θ, can be found using (3.18) with a maximum phase error lower than 5° in most of the cases.

$$\phi_{cell}(\theta) = \phi_{cell}(0) + \Delta\phi_{cell}(\theta) \tag{3.18}$$

where $\phi_{cell}(0)$ is the phase response of the cell of normal incidence.

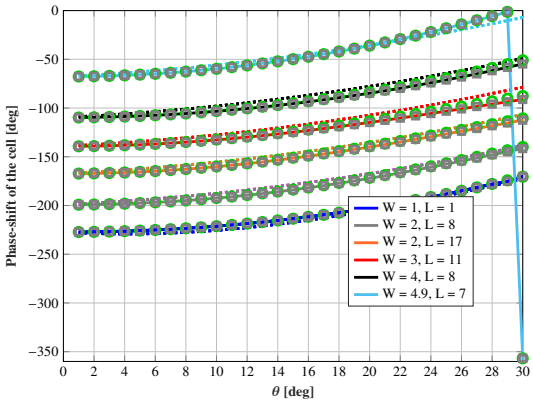

Figure 3.9: *Phase response analyzed for different angles of incidence and the approximation obtained using the polynomial expression for different cells at* 28 *GHz. (Solid line) CST simulations (Dotted line) Approximation. ϕ angles: $\phi = 0^\circ$ (Solid line), $\phi = 45^\circ$ (Grey circle), and $\phi = 90^\circ$ (Green circle). The air gap dimensions are expressed in mm.*

3.2.4. Bessel beam generation by a graded-index planar lens

In this section, the design of a graded-index dielectric planar lens to radiate a Bessel beam is addressed. Particularly, two different designs are made, one for each type of cell. The proposed antenna is a square planar lens made up of 24×24 elements and an equivalent aperture D of 120×120 mm^2. The aperture size does not change due to the cell. However, the distribution of the elements depends on the cell geometry. The square prism is distributed regularly with a periodicity of 5×5 mm^2. Conversely, the hexagonal prism cells are arranged like a honeycomb; thus the cells are placed on an axial distribution. Both configurations are depicted in Figure 3.10. Regardless of the cell geometry, the lenses are fed using a centered configuration as Figure 3.1 depicts, with a focal length $F = 100$ mm, taking the center of the lens as the origin of the system of coordinates. The antenna works at 28 GHz and the Bessel beam should be propagated within a non-diffraction area of 650 mm (DoF). According to (3.2), the beam theoretically behaves as a Bessel beam within the desired range if $\gamma = 5^\circ$.

3.2.4.1. Design procedure of the planar lens

The design of the lenses is based on ray tracing theory according to (3.5) and (3.7). These equations compute the phase of the incident field on the elements of the lens and the phase-shift that should introduce each element to radiate the Bessel beam

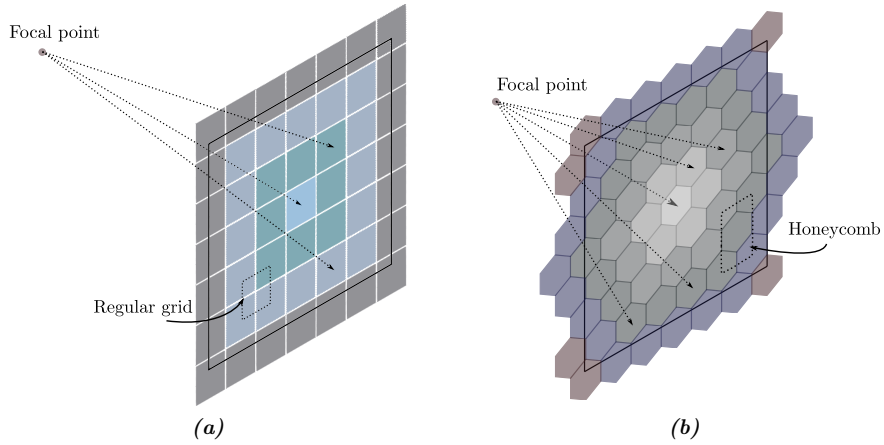

Figure 3.10: *Cell distribution of the lens elements regarding its geometry (a) Square prism cells distributed on a regular grid (b) Hexagon prism cells distributed on a honeycomb.*

previously defined. Therefore, after applying (3.5) to the defined antenna optics, the phase distribution of the transmission coefficients along the surface of the lens is obtained. In Figure 3.11 the phase-shift of each element is shown reminding that their physical distribution is determined by Figure 3.10.

Then, these theoretical phase-shifts have to be physically implemented by an adequate design of the cells. As it was pointing out before, the phase-shift of a cell can be controlled by the variation of its infill, thus by varying P changing the dimensions of the air gap. The designing process is based on the adjustment of the physical dimension to produce the phase-shift of Figure 3.11. When using the square prism cell, the desired phase-shift is achieved with W and L, while in the hexagonal prism cell R and L are needed instead. The phase response of each combination of (W, L) or (R, L) is given by Figure 3.7 and (3.15) and (3.16). However, these results were obtained for normal incidence and (3.5) takes the angle of incidence θ into account. If the phase response of Figure 3.7 was only used to design the cells, an error on the real phase-shift of the cell would be made due to the angle of incidence and, as θ increases the error too. If the phase response of Figure 3.7 is used together with (3.18), the real phase-shift of the cell considering the angle of incident θ will be predicted, minimizing the difference between the phase response of the designed cells and the theoretical ones of Figure 3.11.

Considering the focal length of the lens F and the radius of the center of the cell in the lens ρ, the angle of incidence θ as a function of both parameters is expressed as

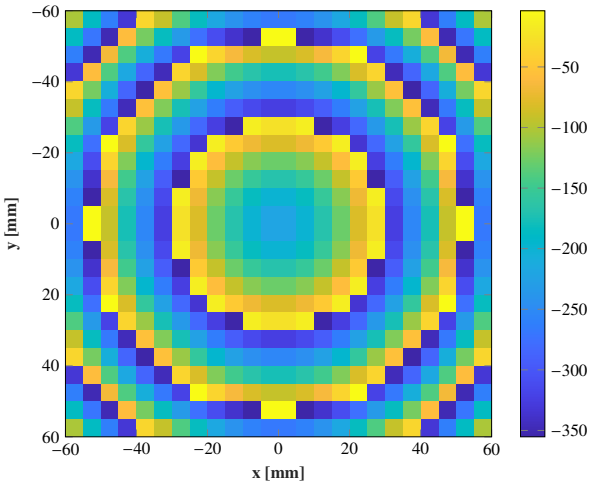

Figure 3.11: *Transmission phase-shift (deg) of the elements of the lens along the surface to radiate the desired Bessel beam according to* (3.5) *for the square prism cells.*

$$\theta = \operatorname{atan}\left(\frac{\rho}{F}\right) \tag{3.19}$$

Then, using (3.19) in (3.17) yields

$$\Delta\phi_{cell}(\rho) = p_1 \cdot \left(\operatorname{atan}\left(\frac{\rho}{F}\right)\right)^2 + p_2 \cdot \left(\operatorname{atan}\left(\frac{\rho}{F}\right)\right) \tag{3.20}$$

and substituting (3.20) in (3.18)

$$\phi_{cell}(\rho) = \phi_{cell}(0) + p_1 \cdot \left(\operatorname{atan}\left(\frac{\rho}{F}\right)\right)^2 + p_2 \cdot \left(\operatorname{atan}\left(\frac{\rho}{F}\right)\right) \tag{3.21}$$

The adjustment of the dimensions of the air gap is done element by element, and the combination of (W, L) or (R, L) selected is the one that minimize the distance from its phase-shift ($\phi_{cell}(\rho)$) and the theoretical phase-shift of (3.5) ($\phi_{SFA}(\rho)$). This process can be written as

$$\phi_{design}(\rho, W, L) = \min\left(|\phi_{cell}(\rho, W, L) - \phi_{SFA}(\rho)|\right), \tag{3.22a}$$

$$\phi_{design}(\rho, R, L) = \min\left(|\phi_{cell}(\rho, R, L) - \phi_{SFA}(\rho)|\right). \tag{3.22b}$$

where $\phi_{cell}(\rho, W, L)$ and $\phi_{cell}(\rho, R, L)$ are the phase-shifts of the whole set of cells analyzed considering the air gap dimensions for a single position of the lens, thus considering the angle of incidence. The resulting layout is made by the cells that

minimize this expression and the amplitude of the cell response is used to discard cells with high losses.

In Figure 3.12(a), the cut $y = 0$ of three different phase-shifts along the lens surface ($\phi_{SFA}(\rho)$, $\phi_{design}(\rho)$ and a hypothetical design considering only the normal incidence response of the cell) are compared. The agreement between the phase-shift of the final layout $\phi_{design}(\rho)$ and the desired one $\phi_{SFA}(\rho)$ is quite good with a very low error, less than 20° in the worst case as Figure 3.12(b) shows. However, when the design is based only on normal incidence the error between the design and $\phi_{SFA}(\rho)$ increases, especially on the edge of the lens where the incidence angle is further from a normal incident obtaining an error higher than 40° and almost 70° in the worst case.

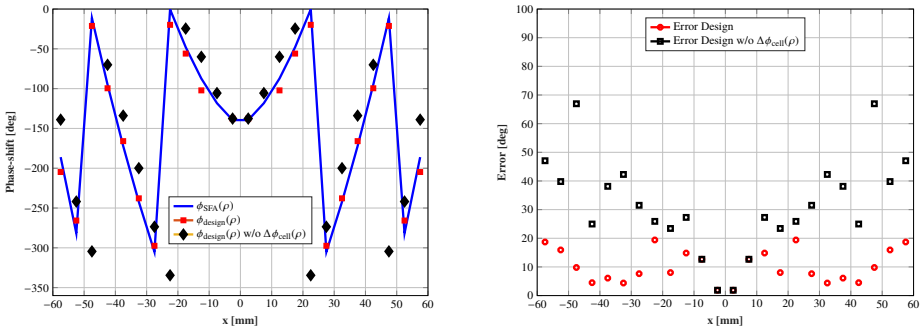

(a) *(b)*

Figure 3.12: *Cut $y = 0$ of $\phi_{SFA}(\rho)$ and $\phi_{design}(\rho)$ considering both the real angle of incident θ ($\Delta\phi_{cell}(\rho)$) and only normal incidence $\phi_{cell}(\rho)$.*

This process is repeated twice to obtain two different layouts, one for each type of cell. In Figure 3.13 the dimensions of the different air gaps are shown. These dimensions are determined by W and L for the square prism cell, and R and L for the hexagon prism cell. Since L is similar in both types of cells and R is computed so that the overall infill is kept in each cell, the effective dielectric constant of both lenses is nearly the same, Figure 3.14. Slight difference in L may be found due to approximations on R.

3.2.4.2. Full-wave simulations

The evaluation of the Bessel beam performances of these two layouts has been made using CST Microwave Studio in a full-wave simulation. The feed is a pyramidal horn antenna of 15 dBi, vertical polarized as Figure 3.15 shows. The distance from the

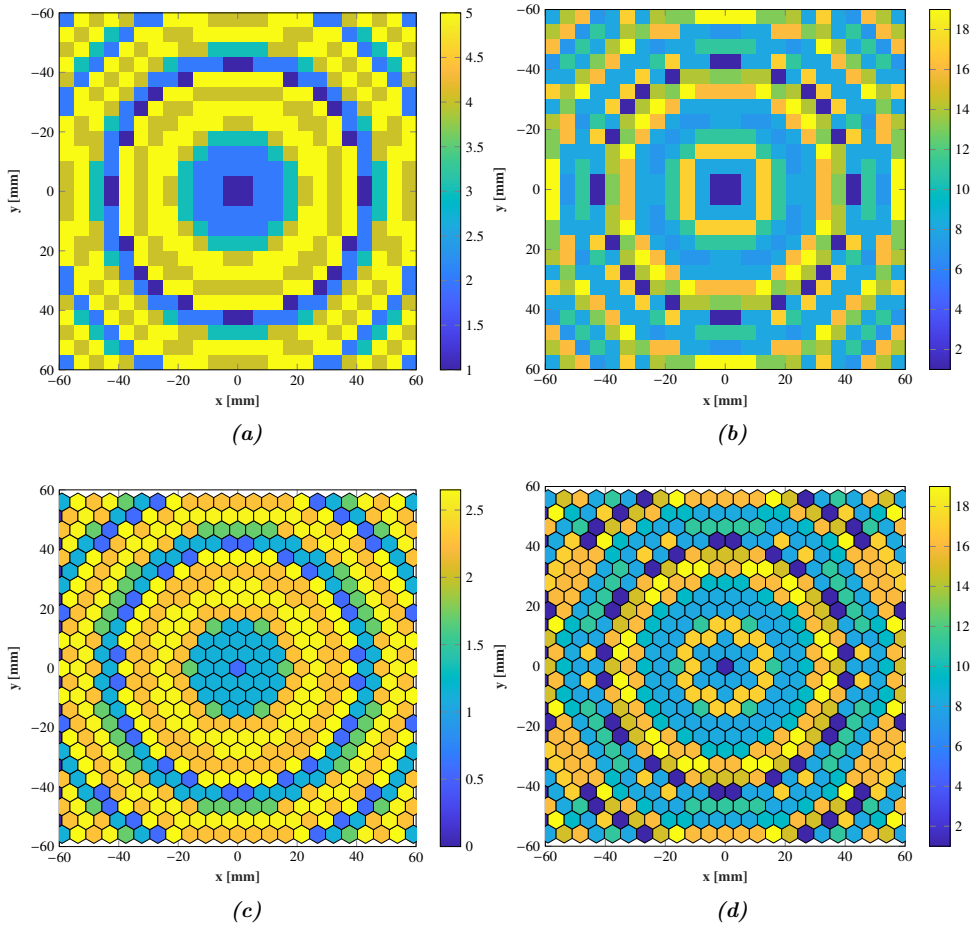

Figure 3.13: *Dimension of the air gaps in the lens made up of square prism cells: (a) W (mm) (b) L (mm). Dimensions of the lens made up of hexagon prism cells: (c) R (mm) and (d) L (mm).*

phase center of the horn and the inner surface of the lens is $F = 100$ mm. Figure 3.16 shows the incident field on the surface of the lens obtained for this configuration, having an illumination taper of nearly -11 dB at the edge of the lens in its main cuts ($x = 0$ and $y = 0$).

The results of the full-wave simulations for the electric field along the *xoz* and *yoz* planes are shown in Figure 3.17 for both layouts at 28 GHz. In both cases, it can be observed the near-field propagating within a nearly non-diffraction area. In Figure 3.18 the cut $x = y = 0$ is detailed for both layouts and the maximum DoF reached by the layout made up of square prism cell is 38.45λ (412 mm) and 44.80λ

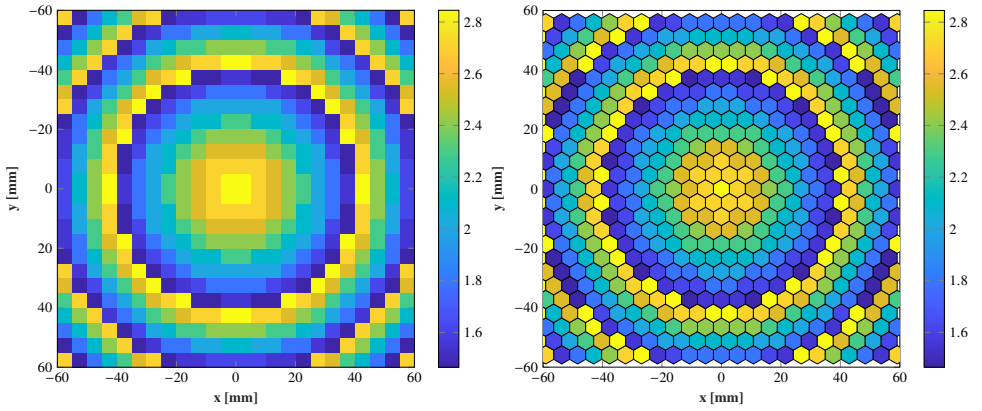

Figure 3.14: *Effective dielectric constant (a) square prism cell (b) hexagon prism cell.*

(480 mm) for the hexagon prism cells. It is important to note that the Bessel lenses were designed using an ideal incident field according to (3.7) and GO. Therefore, when using a real horn antenna other phenomena appear. In this case, the non-symmetry of the horn antenna in its main planes, E- and H- planes, makes the outgoing wavefront is not perfectly formed and the near-field interference pattern is not properly created within the closest area of the antenna, having strong fluctuations on this area. The hexagon cells, probably due to their axial distribution, show a better behavior than the square prism cells, achieving a more stable and confined beam through a larger area. In either of these cases, the Bessel beam reaches a DoF of 60.66λ (650 mm). However, when a horn antenna feeds a Bessel beam generator, it is expected to obtain a shorter DoF than the one computed with (3.2), which is based on GO, and not consider other effects. In addition, these results may be improved using an incident field with axial symmetry, like a Gaussian beam, instead of a pyramidal horn antenna.

3.2.4.3. Experimental validation

The two planar dielectric lenses evaluated in the previous simulations have been manufactured to evaluate the Bessel beam performances in a planar acquisition range. The lenses have been manufactured using Fused Deposition Modeling (FDM), which is a common 3-D printing technique based on the melting and extrusion of a thermoplastic polymer, such as PLA, through a nozzle tip. The material is deposited layer-by-layer onto a platform until the whole piece is completed. This technique is

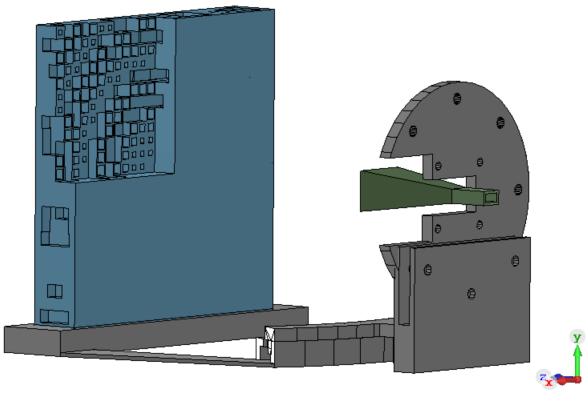

Figure 3.15: *Depicted setup of the full-wave simulation carried out in CST Microwave Studio. A half quarter of the lens has been removed to observe the air gap inclusions.*

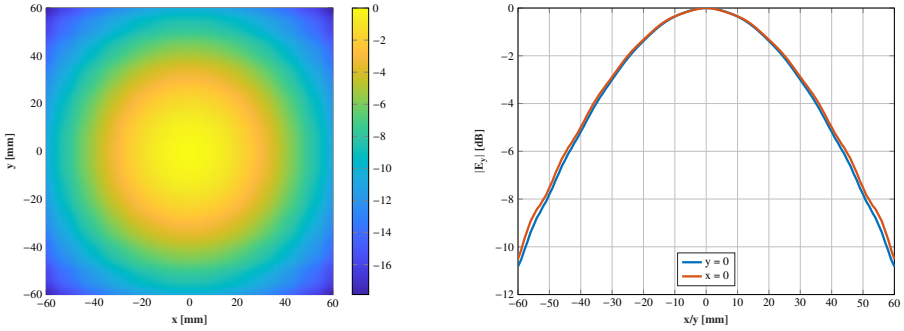

(a) ***(b)***

Figure 3.16: *(a) Illumination taper on the surface of the lens (b) Main cuts $x = 0$ and $y = 0$ of the illumination taper on the surface of the lens using a focal length of* 100 *mm and the pyramidal horn antenna of* 15 *dBi gain.*

widely used in additive manufacturing processes to fabricate prototypes since it offers an easy-manufactured low-cost solution. However, when dealing with accurate designs like these lenses, it is important to set a proper configuration to obtain satisfactory results with high precision. Especially, the thickness wall and the layer height since both control the resolution of the piece. In this case, these parameters were set to 0.4 mm and 0.1 mm respectively, providing a high-resolution printing. It is important to note that using a low-resolution configuration will reduce the printing time. However, it could modify or eliminate the internal walls of low infill cell (cell with a P factor

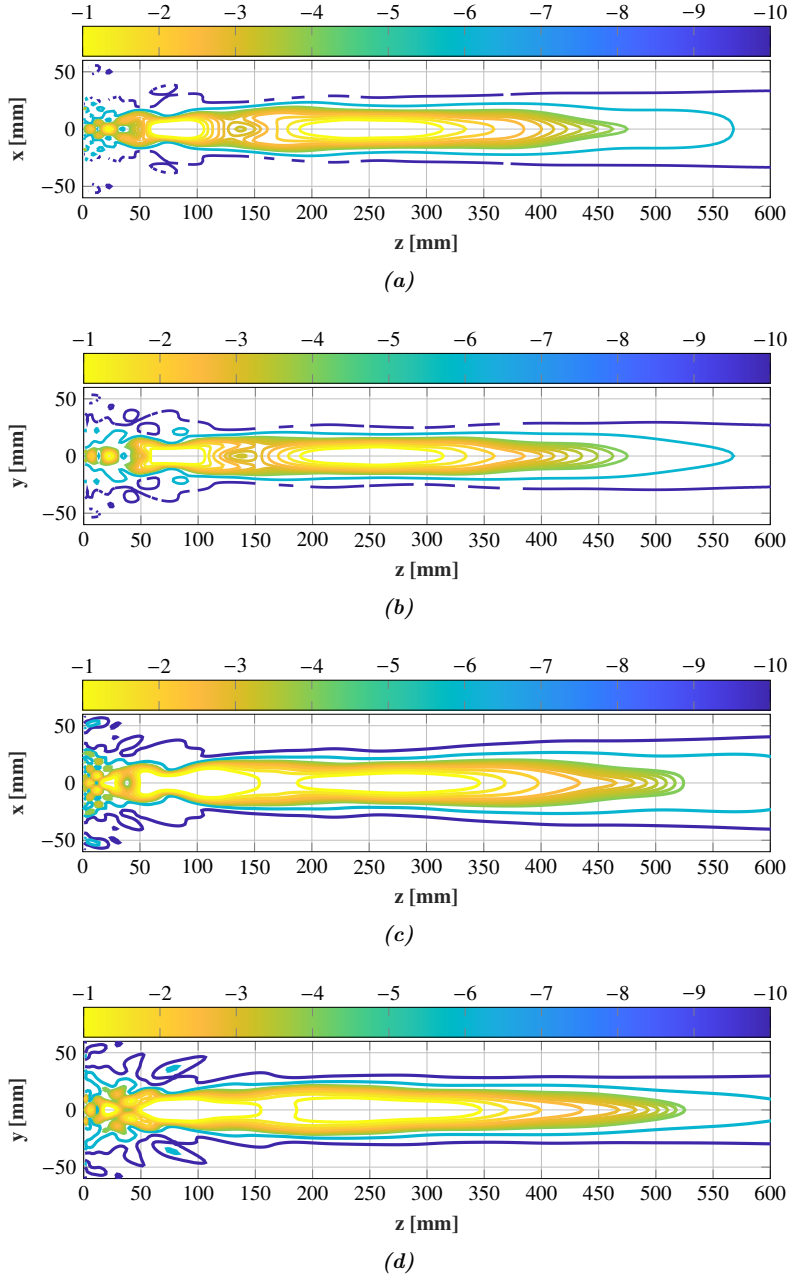

Figure 3.17: *Normalized electric field (dB) for the layout made up of (a)-(b) square prism cells for the xoz and yoz planes, respectively (c)-(d) hexagon prism cells for the xoz and yoz planes, respectively.*

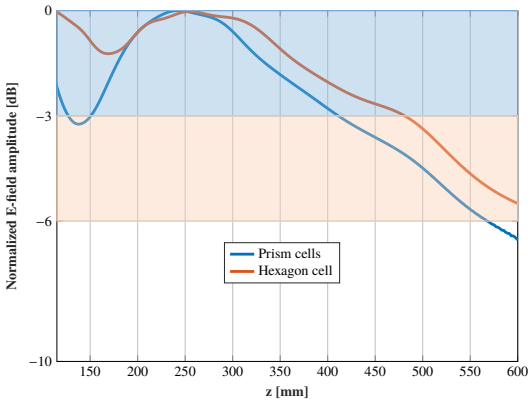

Figure 3.18: *Comparison between the square prism and hexagon prism cells of the normalized amplitude (dB) of the electric field along z-direction and $x = y = 0$ at 28 GHz.*

close to 1) and change the effective dielectric constant and the expected cell response as well. Conversely, a high-resolution configuration inherently increases the printing time to 40 hours for the lens made of square prism cells and up to 48 hours for the hexagonal prism case. Throughout the printing process is highly relevant to keep the same environmental conditions, for instance, a temperature variation could produce air flows and lead to structural deformation on the pieces, such as curvatures on the corners. The humidity is also an important factor since it affects the electromagnetic and printing characteristics of the material. In Figure 3.19(a) the prototype of hexagonal prism cell lens is shown during the manufacturing process, and in Figure 3.19(b) the two manufactured prototypes are shown. In Figure 3.20 the lens of square prism cells can be observed in the setup used to measure the lenses. The lenses were measured in the planar acquisition range at the Universidad of Oviedo. The setup is composed of a vector network analyzer (PNA-X of Keysigth connected to the feeding horn antenna, the pyramidal horn of 15 dBi gain, and a second port to the probe, an open-ended Ka-band waveguide. The lens is placed on a PLA structure aligned to be parallel to the aperture of the probe. The electric field was evaluated within a bandwidth of 4 GHz, from 26 to 30 GHz, at the horizontal xoz plane and different transversal xy planes parallel to the aperture. To alleviate notation, henceforth the square prism lens is referred to as SP and the hexagon prism lens as HP.

The normalized electric field along the propagation direction $\hat{\boldsymbol{z}}$ (see Figure 3.20) is compared to the full-wave simulations in Figure 3.21 for the designing frequency

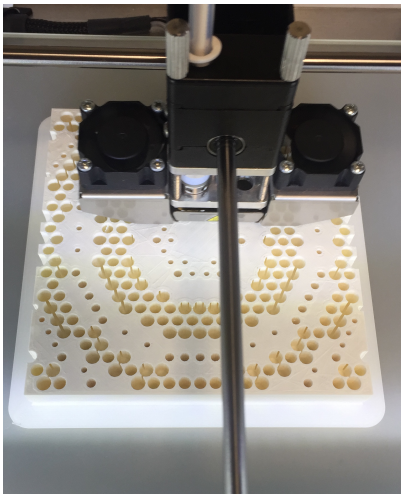

(a)

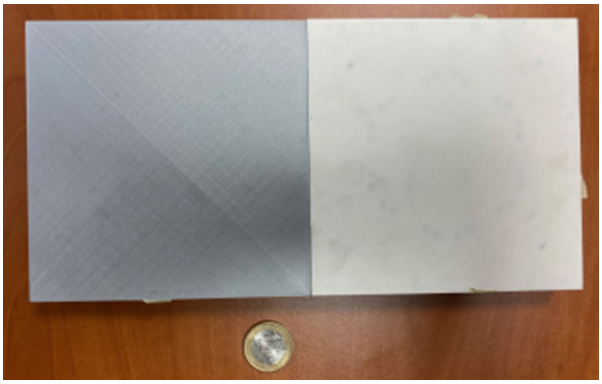

(b)

Figure 3.19: *(a) Manufacturing process of the lens based on hexagonal prism cells of PLA and (b) Manufactured prototypes with 3D additive manufacturing technique. The grey lens on the left is made up of square prism cell while the white one, on the right, is the lens made up of square prism cells.*

of 28 GHz. There is a high agreement between full-wave results and measurements, especially in terms of the achieved DoF and the decay of the Bessel beam. Then, the amplitude of the electric field evaluated at the *xoz* plane for different frequencies is shown in Figure 3.22. The 3 dB decay of the field indicates the limit of the DoF, whose theoretical range according to (3.2) is 650 mm. As it was pointing out in simulations, (3.2) does not consider a real model of the feed or other effects due to the aperture antenna, such as its dimensions or diffractions at the edges of the antenna. Therefore,

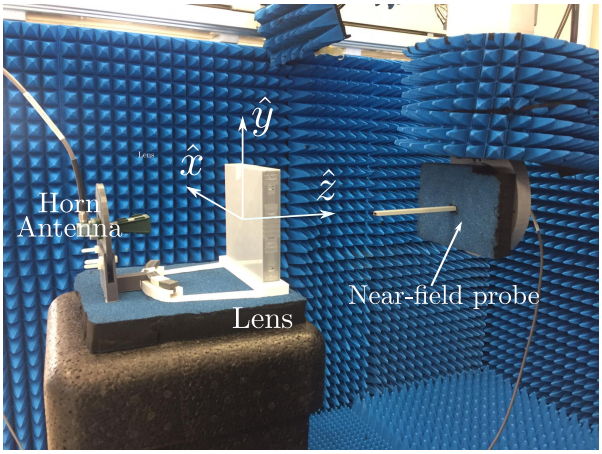

Figure 3.20: *Setup at the planar acquisition range at the Universidad de Oviedo to measure the graded-index planar dielectric lens made up of square prism cells at Ka-band.*

it is expected to reach a shorter DoF in measurements or simulations than with (3.2). Both lenses obtain their best results at the highest frequencies range, from 28 to 30 GHz, reaching a maximum DoF of 43.70λ (437 mm) for the square prism cell lens and 47.50λ (475 mm) at 30 GHz. It is worth noting the hexagon prism lens behavior, which improves the results regarding the square prism cell lens. The in-band response of the HP lens barely changes at the highest frequencies, while the SP lens shows more variations on the Bessel beam performances due to the frequency shifts. Moreover, in the whole measured band, the HP lens reaches a larger non-diffraction area, as well as a more stable Bessel beam through the propagation direction.

The transverse profile in the plane xy parallel to the aperture and at a distance of 250 mm from the lens has been evaluated for three different frequencies: $26.5, 28$ and 29.5 GHz. The measurements are shown in Figure 3.23, obtaining a good axial symmetry with a field distribution similar to the main beam of a Bessel function. The side lobes are hidden because of the antenna. The main cut $y = 0$ of the planes $z = 150$ and 200 and 250 mm, in Figure 3.24 for the whole measured band. These measurements evaluate the beam-waist of the Bessel beam within the non-diffraction range. At the closest plane, $z = 150$ mm, neither the HP lens nor the SP lens properly forms the Bessel beam, whose shape should be like a Bessel distribution. This behavior is reached for the HP lens at the plane $z = 200$ mm, obtaining a Bessel distribution and confining the beam in a spot smaller than 4λ. The main lobe of the SP lens is still flattened at this plane, especially above 28 GHz. In the further plane, $z = 250$

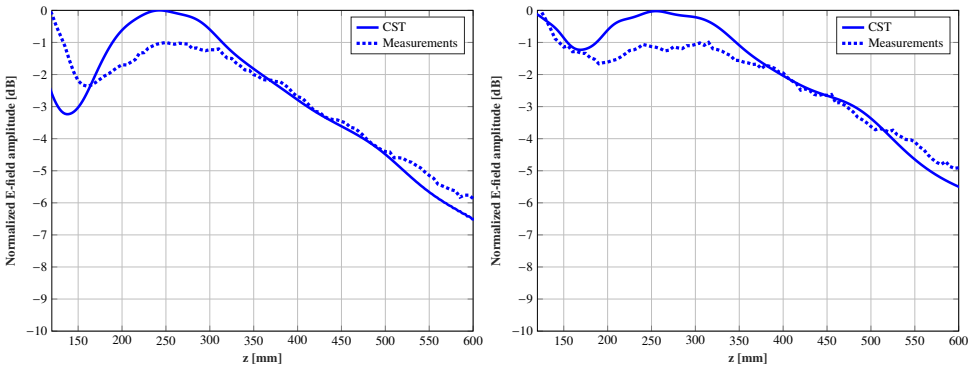

Figure 3.21: *Comparison between full-wave simulations and measurements of the normalized electric field amplitude (dB) along the z-axis and the cut $x = y = 0$ at 28 GHz. Results for the (a) square prism (b) hexagon prism cells lenses.*

mm, the SP lens achieves a behavior more similar to a Bessel function. The HP lens keeps its Bessel behavior contour at this plane as well as within the whole measured range according to the measurements shown in Figure 3.22. Moreover, the unchanged in-band response of the HP lens observed in previous results can also be verified in these transversal xy planes.

The overall performances of the DoF for the two measured prototypes at different frequencies are outlined in Table 3.1. Moreover, the beam-waist at those frequencies is evaluated for the measured plane $z = 250$ mm for its main planes. Particularly, both parameters are evaluated at the design frequency and the upper and lower extreme measured frequencies. As it may be expected, the highest frequency is the largest DoF. This can be expected since the electrical aperture size increases as the frequency does. Conversely, despite showing the HP lens a better behavior than the SP lens in most of the results evaluated, the SP lens at the measured plane at $z = 250$ mm obtains a field confined in a smaller spot than the HP. Additionally, this spot has an almost perfect axial symmetry at the whole band while the spot of the HP lens increases its beams-waist in the vertical direction. However, in both cases the beam-waist is quite good in terms of wavelength, being 2.68λ and 3.1λ at 28 GHz for the SP lens and 2.75λ and 3.57λ for the HP case.

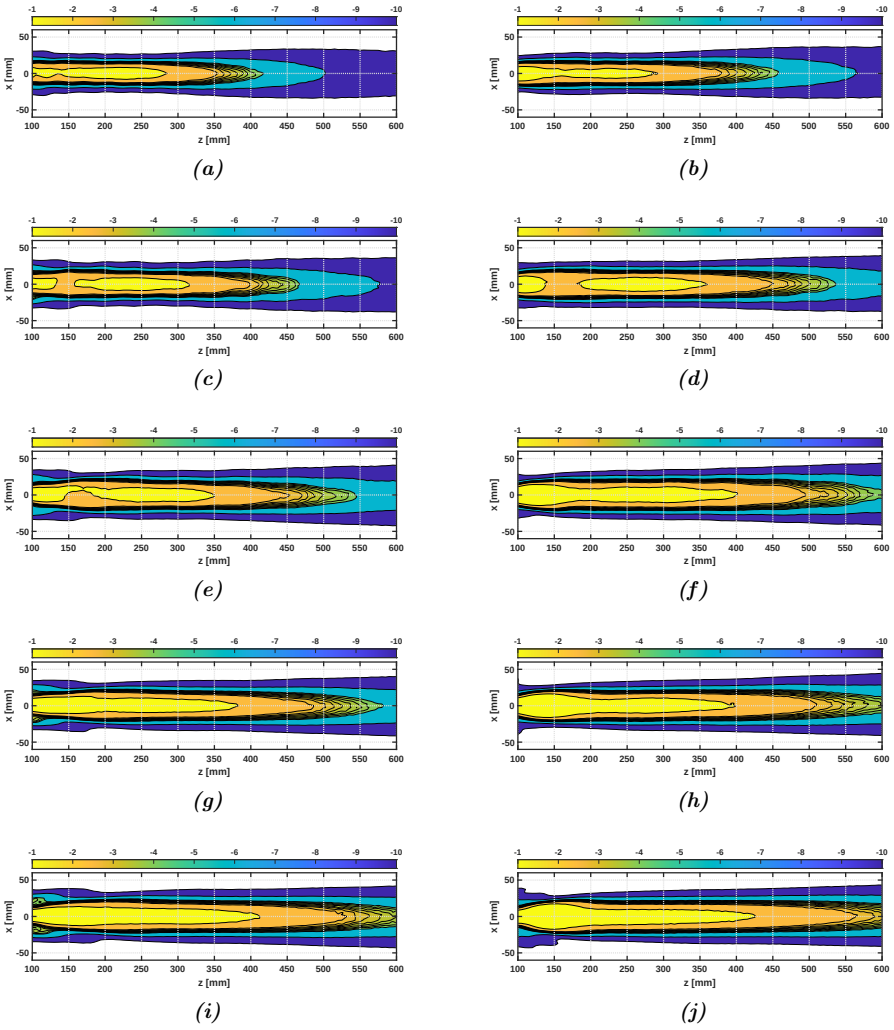

Figure 3.22: *Normalized measured electric field amplitude (dB) at the xoz plane for the lens of square prism cells at (a) 26 GHz (c) 27 GHz (e) 28 GHz (g) 29 GHz (i) 30 GHz and the lens of hexagon prism cells at (b) 26 GHz (d) 27 GHz (f) 28 GHz (h) 29 GHz (j) 30 GHz.*

3.3. Dielectric lenses for near-field focusing

In Section 3.2 it was detailed an approach to obtain a near-field with non-diffraction properties within a certain range in the propagation direction. This means having a near-field that remains constant through this range before rapidly spreading. However,

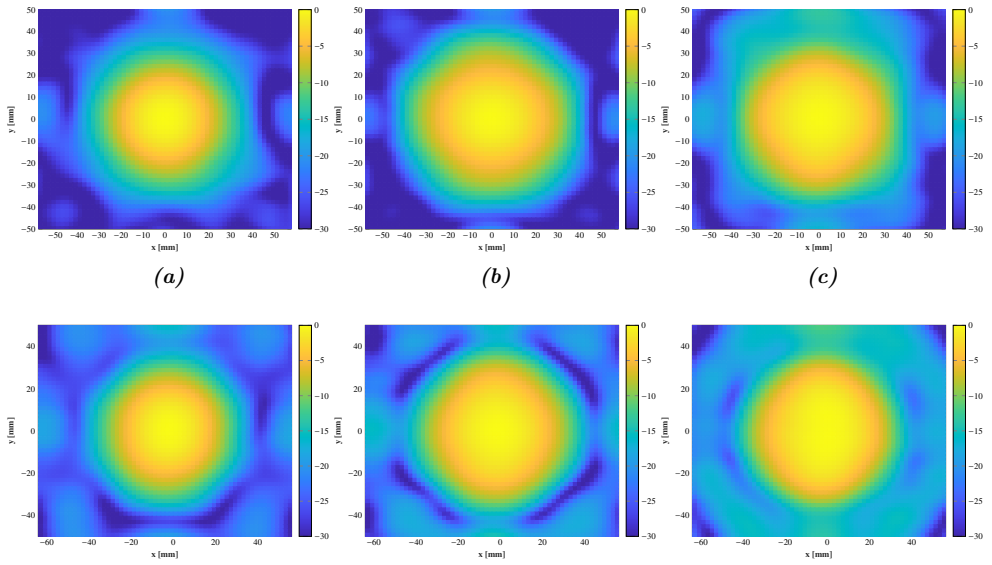

Figure 3.23: *Measured transverse plane at $z = 250$ mm parallel to the antenna aperture for the square prism cell lens at (a) 26.5 GHz (b) 28 GHz and (c) 29.5 GHz and for the hexagon prism cell lens at (d) 26.5 GHz (e) 28 GHz and (f) 29.5 GHz.*

Table 3.1: *Bessel beam performances: DoF and beam-waist for the two measured prototypes. Units expressed in mm*

Frequency (GHz)	Square Prism Cell Lens			Hexagon Prism Cell Lens		
	DoF	Beam-waist		DoF	Beam-waist	
		x-axis	y-axis		x-axis	y-axis
26	246.9	29.3	30.0	276.9	38.4	34
28	379.0	35.8	31	446.8	31.8	41.2
30	504.2	40	38.4	548.0	38.5	43

in some instances, it is from our interest to concentrate the near-field on a small spot, actually, on the smallest spot inasmuch as it is possible. This problem has been typically addressed using antennas with focusing capabilities, especially classical arrays (using feeding networks), lenses or different types of reflective and transmissive SFA antennas. More recent published works extend the list to different types of

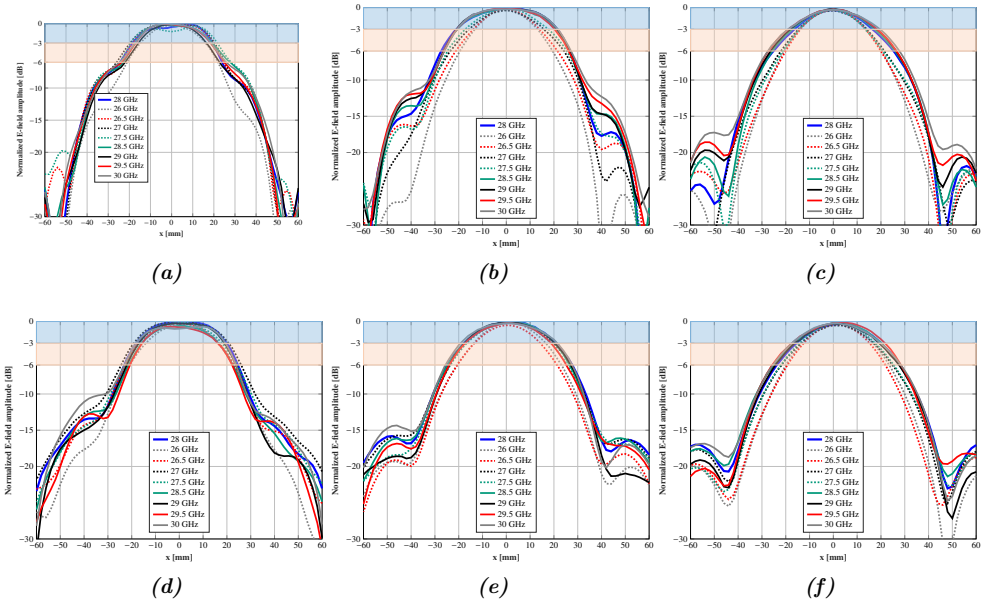

Figure 3.24: *Normalized electric field amplitude (dB) at the xy planes $z = 150$ mm, $z = 200$ mm and and $z = 250$ mm for the (a)-(c) square prism cell and (d)-(e) square prism cell.*

metasurfaces. In this section, a graded-index planar lens is compared with a classical doubly hyperbolic dielectric lens. The aim is to compared the focusing performances of SFA antennas with another classical solution.

The use of a dielectric lens as part of an antenna is a concept that comes from optical lenses. The lens uses its geometry to modify the trajectory of the light while it passes through the lens. On this basis, a dielectric lens can be used to modify the trajectory of an electromagnetic wave while traveling through the lens. In the early stages, the main drawback of lenses lies in the dielectric material to manufacture them, leading to bulky and heavy prototypes. However, the fast advances in millimeter waves technology or the emergence of new materials and manufacturing processes have renewed interest in lens antennas at millimeter bands.

Throughout the last decades, lenses have been used in several applications such as imaging, fixed or mobile broadband communications, or radar applications among others [228, 229]. The lens allows modifying the amplitude, the phase of the primary feed, or both to transform them into a more suitable radiation pattern for the desired application. The working principle of lens antennas is equivalent to the reflector one. However, instead of reflection, the lens is based on the refraction of the electromagnetic

wave at the lens surface or within the lens dielectric material, in the case of isotropic homogeneous lenses or non-uniform refractive index lenses, respectively [230]. A significant advantage over reflectors with regards to the lack of needing a support structure avoiding the block losses. Moreover, large lenses, as reflectors, have an inherent large bandwidth, which is limited only by the feed bandwidth.

Lenses can be classified into several types depending on their physical characteristics: the feed position relative to the lens (integrated or off-body fed), refractive index profile (constant/stepped or non-uniform), or the number of refraction surfaces, among others [230]. In Figure 3.25 two different examples of lenses are depicted. Then, the outgoing radiation pattern of the lenses can be collimated or shaped beam for fixed or scanning beams.

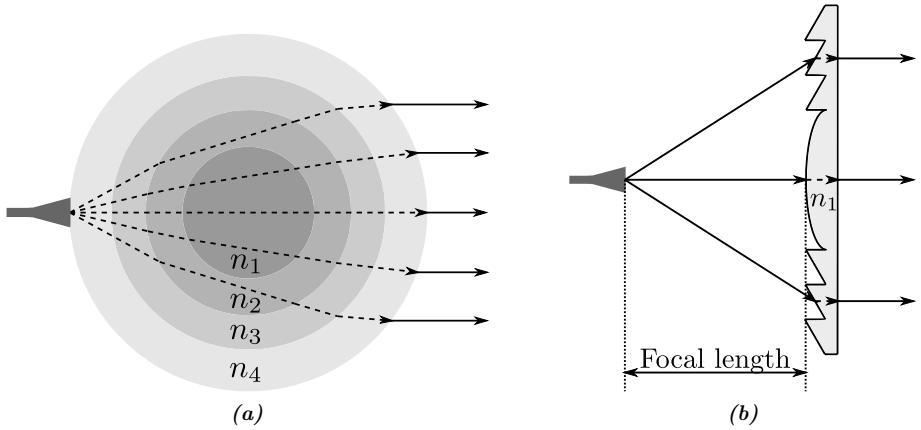

Figure 3.25: *Sketch of two examples of lenses: (a) Integrated lens comprised of multiple refraction (b) Zoning of a hyperbolic lens.*

Early dielectric lens antennas were based on optical lenses, using them to collimate the radiation of a plane wave into the focal point where the feed was placed. Following up on this idea, this section will analyze two different off-body lenses antennas: a doubly hyperbolic lens and a planar lens antenna as in the previous section. This section aims to evaluate the capability of both antennas to focus the near-field of a horn antenna. Then, the performances of both lenses are compared to study the degradation because of the discretization and phase-shift truncation in the planar lenses.

3.3.1. Doubly hyperbolic lens

One of the basic lenses is the hyperbolic lens, which has a single refracting hyperbolic surface. As Figure 3.26 depicts, the refraction occurs in the hyperbolic lens surface, the one closer to the feed, while the planar surface does not refract the rays. The parallel rays of the incident plane wave are refracted at the lens surface in such a way that the output rays intersect a common point, the lens focal point. Considering Fermat's principle, the rays at the focal point have the same electrical path and they arrive in phase, despite having different physical lengths [231]. However, these differences in the physical paths can be compensated by a slower phase velocity in different parts of the lens according to

$$v = \frac{c_0}{n} \tag{3.23}$$

where c_0 is the speed of light in vacuum and n is the index media.

Another option to compensate the physical lengths is with the geometry of the lens so that some rays will pass through a larger dielectric length having a slower velocity than in the air (see Figure 3.26(a)), that is, as a hyperbolic lens works.

Let us assume a hyperbolic lens with a focal length f_1, whose planar surface is joining together to a second planar surface of a second hyperbolic lens with focal point f_2, as Figure 3.26(b) depicts. If the phase center of a feed, for instance, a horn antenna, was placed at F, a spherical wavefront would illuminate the first hyperbolic surface. Due to the geometry of the lens, the incident rays at the hyperbolic surface would be refracted in such a way that at the junction of both lenses all the rays may be in phase. Now, assuming that $n_1 = n_2$ and there is no discontinuity at the junction. The rays would be refracted at the second hyperbolic surface so that the outgoing wavefront would converge to the second focal point F_2. As long as F_2 is within the Fresnel region of the second hyperbolic lens, the doubly hyperbolic lens would focus the near-field on this point.

The design of a doubly hyperbolic lens can be addressed as the design of two single hyperbolic lenses which share the diameter. The design of each lens can be carried out using quasi-optical methods provided that the lens dimensions are large in terms of wavelength. The lens design is based on two principles: the principle of equality of optical paths together with rays between pairs of wavefronts or Snell's law of refraction. On the procedure of a lens design using ray tracing, only the optical paths or rays normal to the wavefront, are considered. The optical path length of a ray in space is just the length of the ray segment, while in a dielectric medium, it is the length times

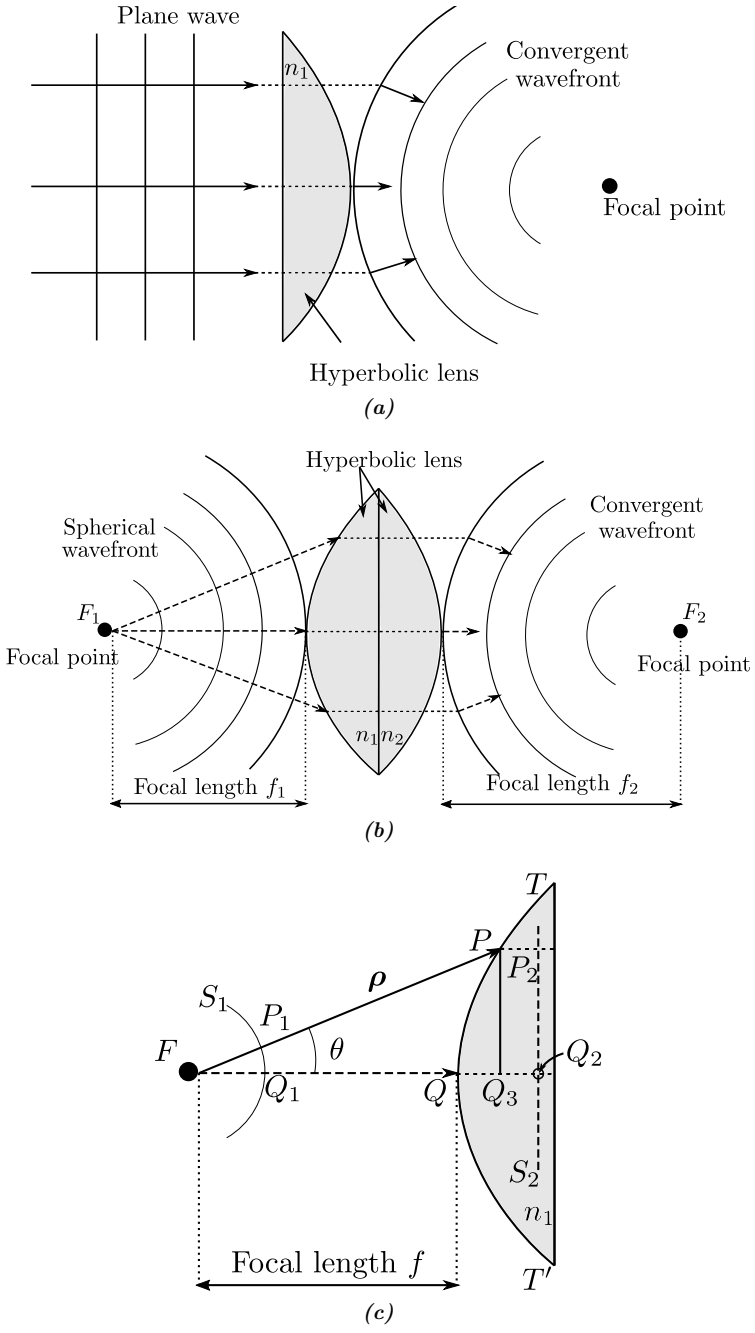

Figure 3.26: *Sketch of the operating principle of (a) hyperbolic lens (b) double hyperbolic lens and (c) parametrization of a hyperbolic lens.*

the index of refraction n, given by

$$n = \sqrt{\epsilon_r \mu_r} \tag{3.24}$$

Henceforth, the procedure of the lens design will be explained according to the geometry of Figure 3.26(c). Then, two important considerations are taken in the design. First, it will be assumed that the lens has an axial-symmetric shape about the optical axis FQ_2. Second, the radiation pattern of the feed is also circularly symmetric. These assumptions enable the removal of the dependence with the φ angle, defined as the angle of rotation about the lens axis of symmetry. Now, the profile TT' is the interface between the air on the left and the dielectric of index refraction n, on the right. This profile is defined so that the phase-front S_1 provided by a source or feed at F is transformed into a plane phase-front S_2 inside the dielectric. Note that, S_2 is parallel to the planar surface of the lens. Applying ray tracing, the equation of the lens surface on an arbitrary point P is derived from the following condition

$$[(P_1P) + n\,(PP_2)] = [(Q_1Q) + n\,(QQ_2)] \tag{3.25}$$

Or, in a more simply expression

$$(FP) = (FQ) + n(QQ_3) \tag{3.26}$$

Considering that $FQ = f$ and the arbitrary point P can be expressed in the polar coordinates (ρ, θ), (3.26) can be written

$$\rho = f + n(r\cos(\theta) - f) \tag{3.27}$$

Now, the equation to generate the hyperbolic surface of the lens can be easily obtained by finding r

$$r = \frac{f\,(n-1)}{(\cos\theta - 1)} \tag{3.28}$$

It must be underlined that the design is sorely based on phase consideration and Snell's law of refraction is not used in deriving (3.28). However, Snell's law of refraction is satisfied at the hyperbolic profile and, likewise at the planar surface since the right-hand interface of the dielectric does not affect the optical paths because it is normal to the outgoing rays [231].

3.3.2. Graded-index planar lens for near-field focusing

Broadly speaking, the main disadvantage of a hyperbolic lens regarding its dimensions, resulting in bulky and heavy antennas. However, graded-index planar lenses have arisen as a potential alternative throughout the last decades. These planar lenses mimic the behavior of classical lenses but obtaining less bulky and lighter antennas with a less complex manufacturing process due to their planar profile. In 3.2, a graded-index planar lens was used to generate a Bessel beam. Now, in this section, a more detailed explanation based on the classical lens concept will be given for a near-field focusing graded-index planar lens.

A hyperbolic dielectric lens defines a geometrical profile, particularly a hyperbola, in such a way that the rays are refracted at this surface, and they pass through a dielectric material to arrive in phase at the outer planar surface of the lens. The distance traveled through the dielectric is not the same for all the rays, it depends on the θ angle and the hyperbolic surface. Thus, the velocity within the dielectric is always the same but the distance changes, enabling to add a larger delay in the rays passing through certain areas, for instance, the center of the lens. Likewise, a planar lens would add either a larger or shorter delay on the ray according to the optical path length traveled by the incident ray. As it can be observed in Figure 3.27, a planar lens has the same thickness h along the whole surface. Thus, the rays would have the same optical path lens within the dielectric. However, according to (3.23) the phase velocity depends on n. Therefore, if the lens had not a single index of diffraction but several, it would be different velocities in the rays passing through the lens as it occurs in the hyperbolic lens because of its profiles.

The design of a planar lens is not based on defining a profile, instead, the lens is discretized in $N_x \times N_y$ cells whose dimensions are $a \times b$, and these cells are the ones designing in this process. The index of refraction n_n of each cell should be selected so that a spherical phase-front S_1 of a source at F_1 is transformed into a phase-front S_2 which converges at F_2. This means, all the rays at F_2 are in phase. Imposing this condition to the path length the rays must satisfy the condition

$$\boldsymbol{r}_1 + n_1 h + \boldsymbol{r}_1' = \cdots = \boldsymbol{r}_3 + n_3 h + \boldsymbol{r}_3' = \cdots = \boldsymbol{r}_n + n_n h + \boldsymbol{r}_n' = l \tag{3.29}$$

where l is an arbitrary phase constant.

A variation of n_n to obtain a slower phase velocity can be also seen as adding a certain delay or phase-shift in the incident field. Both (3.8) and (3.9) relates the index of refraction n of a cell with its phase-shift, simplifying the design of the lens to a design of its cells. According to the condition of (3.29) the phase-shift $\phi_{cell}(\rho)$ of a

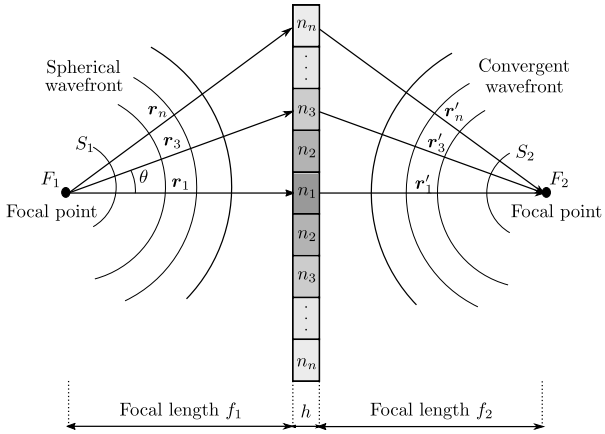

Figure 3.27: *Sketch of the operating principle of a planar dielectric lens to focus the near-field.*

cell has to satisfy

$$\phi_{inc}(\rho) + \phi_{cell}(\rho) + \phi_{out}(\rho) = l \tag{3.30}$$

where $\phi_{inc}(\rho)$ and ρ are the incident phase at the (m, n) element (3.7) and its axial position on the lens (3.6), l is an arbitrary phase constant and $\phi_{out}(\rho)$ is the phase delay from the lens to F_2

$$\phi_{out}(\rho) = -\frac{2\pi}{\lambda}\sqrt{F_2^2 + \rho^2} \tag{3.31}$$

Replacing (3.7) and (3.31) in (3.30), and considering $l = 0$, the phase-shift of a cell is

$$\phi_{cell}(\rho) = -\frac{2\pi}{\lambda}\left(\sqrt{F_1^2 + \rho^2} + \sqrt{F_2^2 + \rho^2}\right) \tag{3.32}$$

The result of applying (3.32) on all the $N_x \times N_y$ elements is the phase of the transmission coefficients τ_{xx} or τ_{yy} which have to introduce each element to radiate the desired focused near-field. Unlike dielectric lenses, the bandwidth of these planar lenses is not limited by the bandwidth of the feed but by the maximum number of phase cycles introduced by the elements of the lens. Therefore, the operative bandwidth of a planar lens is commonly shorter than in a dielectric lens. Finally, it should be noted that classical array theory, (3.32) may be referred to as the CP method [151, 221].

3.3.3. Design process

To completely validate the methodology described throughout this section, two near-field focusing lenses have been designed, manufactured, and measured. First, a doubly hyperbolic dielectric lens has been designed to focus the near-field on a given point. Second, a graded-index planar dielectric lens has also been designed to compare both lenses' performances. The antenna optics and the focused spot performances are the same for both lenses and they are outlined in Table 3.2. It has been chosen a focal distance f_1 of 100 mm, wherein the phase center of the feed is placed. In this case, the feed is a standard horn gain of 15 dBi gain (NARDA V637), which generates an illumination taper of 10 dB at the edge of the lens at 28 GHz, ensuring low diffraction levels. The near-field should be focused at 150 mm from the outer surface of the lens within a beam-waist of 30 mm. The spot beam-waist and the two focal distances f_1 and f_2 determinate the shortest diameter of the lens to achieve these focusing performances. Based on the Gaussian beam equation, which is the type of the outgoing wave expected to have at the lens, it is computed a minimum radius of 120 mm. The electric field of a Gaussian beam assuming polarization in the x-direction and propagation in the z-direction is

$$\boldsymbol{E}(r,z) = E_0 \frac{w_0}{w(z)} e^{\frac{-r^2}{w(z)^2}} e^{-j\left(kz + k\frac{r^2}{2R(z)} - \psi(z)\right)} \hat{\boldsymbol{x}} \tag{3.33}$$

where r is the radial distance from the center axis of the beam, z is the axial distance from the focus of the beam, k is the wavenumber for free-space, $w(z)$ is the radius at which the field decays $1/e$ of their axial values, w_0 is the beam-waist, $R(z)$ is the radius of curvature of the wavefront of the beam at z, and $\psi(z)$ is a phase term at z.

The planar lens is a square lens of 24×24 elements divided in a regular lattice of 5×5 mm^2. The side of the squared lens is 120 mm which is equivalent to the square that inscribes a circumference of the doubly hyperbolic diameter. The material of both dielectric lenses is PLA ($\epsilon_r = 2.95, \tan\delta = 0.0148$), enabling to print the lenses using again the FDM technique with a 3D printer.

The doubly hyperbolic lens is designed according to (3.28) and the geometry of Table 3.2, obtaining the profile shown in Figure 3.28(a). In a first approach to validate the proposed geometry, the lens was simulated with a ray-tracing method with ILASH software [232]. The result of this simulation is shown in Figure 3.28(b), as it can be observed the outgoing rays perfectly converge to a focal point of distance 150 mm (f_2). Then, the doubly hyperbolic lens has been modeled in 3D pieces to carry out a full-wave simulation considering the entire system, horn antenna, and lens, to observe more realistic effects such as the spillover or the diffraction due to the edges. The feed is a horn antenna that provides an illumination taper similar to the NARDA V637

Table 3.2: *Antenna optics and the near-field spot performances.*

Parameter	Doubly hyperbolic lens	Planar Lens
D(mm)	120	169.70
Size	$\varnothing$120(mm)	120×120(mm^2)
f_1(mm)	100	100
f_2(mm)	150	150
$\varnothing_{spot}$(mm)	30	30
Material	PLA	PLA

on single linear polarization at 28 GHz. In Figure 3.29 the setup of the full-wave simulation in CST Microwave Studio is depicted. According to the reference system shown in this figure, the feed is vertical polarized, the electric field is polarized in y-direction, and the results for the planes xoz and yoz are shown in Figure 3.30. Both planes together with the z-axis ($x = y = 0$) (Figure 3.30(c)), verify the results of the ray-tracing simulation, obtaining a doubly hyperbolic lens that properly focusses the near-field at F_2. Moreover, merely a small portion of the incident field is diffracted because of the edge of the lens, this can be observed from the areas of increased field levels in the region beyond the lens. In Figure 3.30 the phase of the xoz plane is shown, observing the transformation of the spherical wavefront of the horn antenna into a converge wavefront due to the doubly hyperbolic lens.

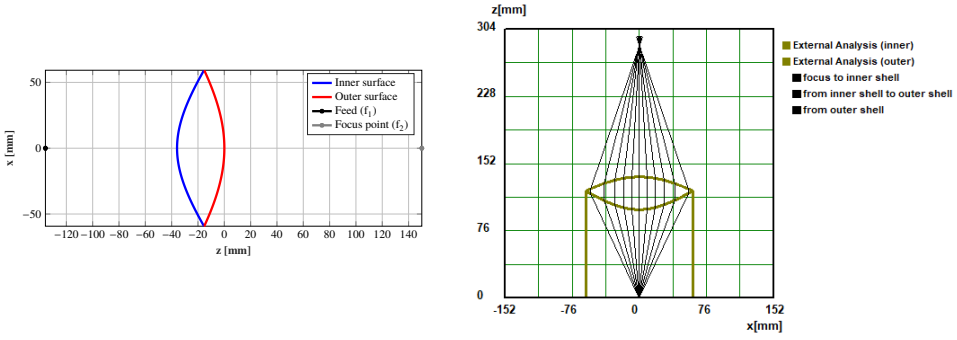

(a) *(b)*

Figure 3.28: *(a) Profile of the doubly hyperbolic lens obtained with* (3.28) *and the defined geometry of Table 3.2 and (b) ray-tracing simulation in the software ILASH.*

On the other hand, the graded-index planar lens has been designed with (3.32) to compute the phase distribution of the transmission coefficients that should introduce

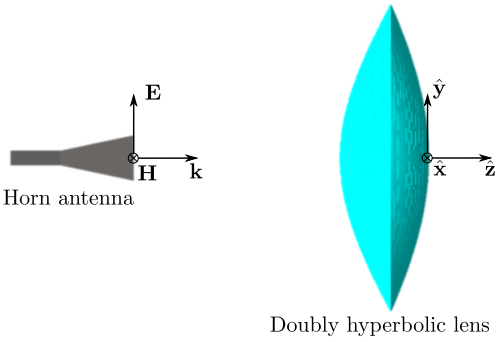

Figure 3.29: *Full-wave simulation of the entire system at 28 GHz using CST Microwave Studio.*

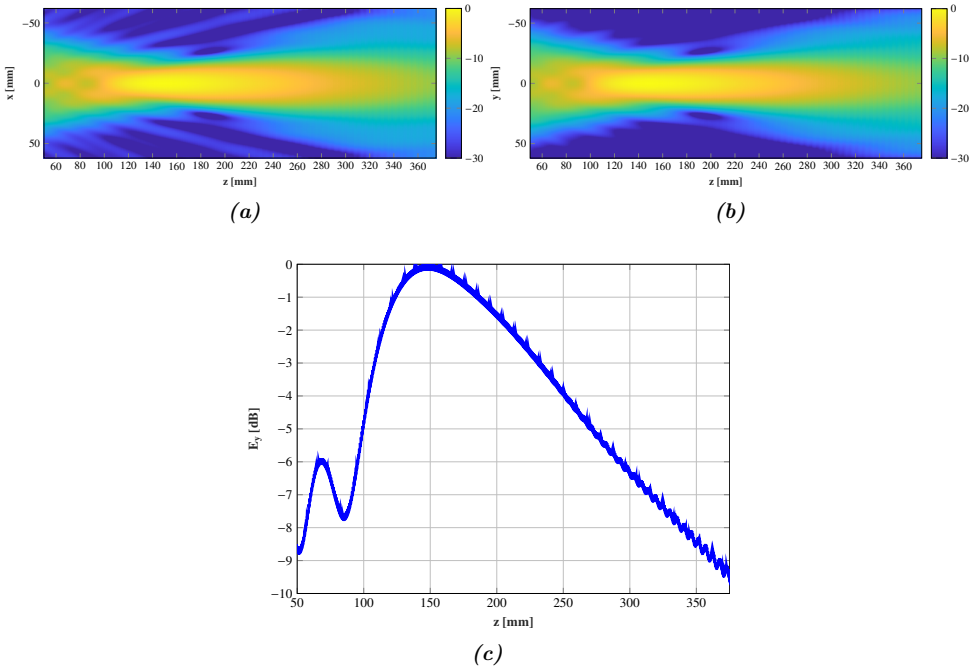

(a) *(b)* *(c)*

Figure 3.30: *Near-field radiated by the doubly hyperbolic dielectric lens (a) xoz plane (b) yoz plane and (c) z-axis ($x = y = 0$).*

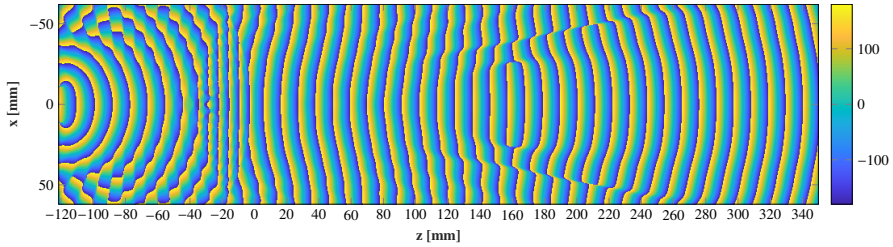

Figure 3.31: *Phase of the spherical wavefront radiated by the horn and its transformation to a convergence wavefront due to the doubly hyperbolic dielectric lens.*

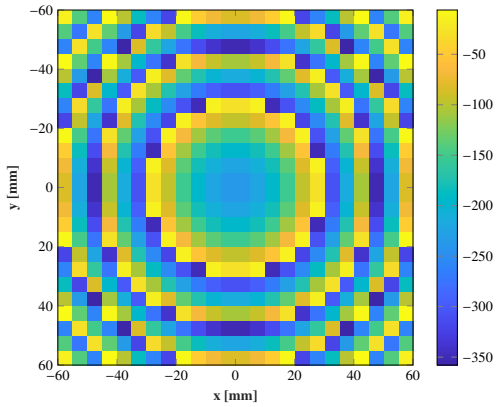

Figure 3.32: *Transmission phase-shift (deg) of the elements of the lens along the surface to radiate the desired focused beam.*

by the elements to focus the radiated beam. As it occurs in the Bessel beam case, the physical implementation of the elements shall be made with a dielectric cell. Particularly, the square prism cell with embedded square prism air gaps of Figure 3.5(a) is chosen, reminding that the variation on the air gap dimensions enables to change the infill of the cell. Thus, a change on the phase-shift and the index of refraction n. In the designing process the dimension W and L of the air gap are adjusted according to (3.22) but using the phase distribution of Figure 3.32. Note that the phase response of the cell is the same as the one of Section 3.2 since this new graded-index planar lens is also designed at 28 GHz. The effective dielectric constant and the index of refraction n of the selected cells are observed in Figure 3.33.

This layout has been evaluated in a full-wave simulation in CST Microwave Studio, using a feed that provides a similar illumination to the one used in the doubly hyperbolic lens. The result for the planes xoz and yoz are shown in Figure 3.34 along with the z-axis ($x = y = 0$). The maximum of the electric field is compressed comparing

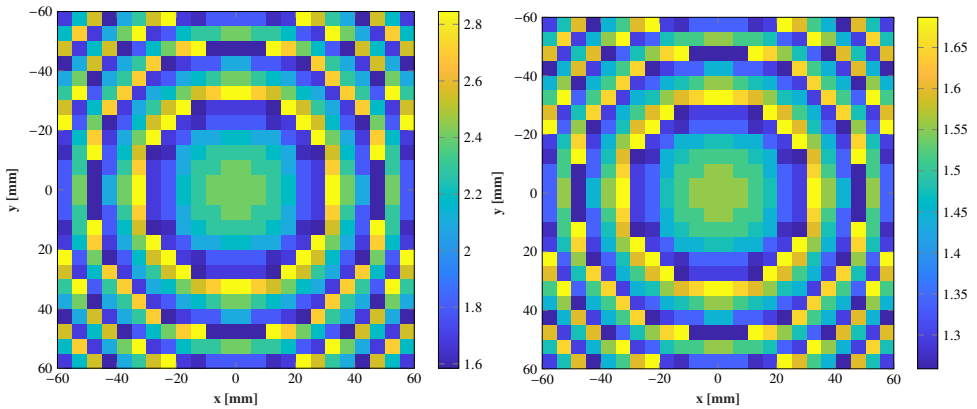

Figure 3.33: *(a) Effective dielectric constant and (b) index of refraction n along the lens surface to produce the focused beam.*

with the doubly hyperbolic lens, particularly a shift of 38 mm from F_2. This effect is not derived from the design but from the CP approach in arrays or SFA antennas [221]. Typically, the maximum of the electric field is not found at the focal point F_2 but closer to the antenna. If it is strictly necessary to obtain the maximum of the electric field at F_2, as it occurs on the doubly hyperbolic lens, the focal length f_2 should be increased to compensate the shift by focusing the field on a further point [221]. However, despite having the maximum of the field at 112 mm, the outgoing wavefront nearly converges to the design focal length, as it can be observed in Figure 3.35. It is worth noting that there is a significant increase in the field diffracted by the planar lens in directions away from the focal point.

3.3.4. Experimental validation

3.3.4.1. Manufacture and planar acquisition range

Both lenses are manufactured taking advantage of the additive manufacturing techniques to obtain low-cost easy-manufacture prototypes, considering that one of the lenses requires to manufacture of two hyperbolic profiles. Once again, the printer Ultimaker 3 is used to print both lenses with an FDM technique using the polylactic acid PLA, which was the dielectric considered in the design. The graded-index planar lens is analogously manufactured to the Bessel lens based on squared prism cells. Particularly, the printer settings are established to have a resolution on the wall thickness of 0.8 mm, 0.1 mm on the layer height, and a 100% of infill. In the light of the different

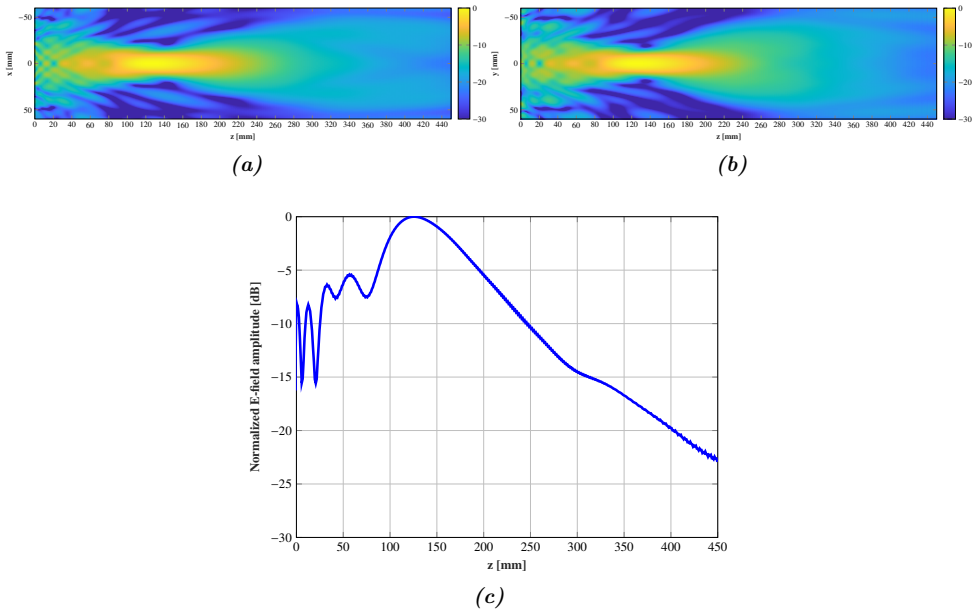

Figure 3.34: *Near-field radiated by the planar dielectric lens (a) xoz plane (b) yoz plane and (c) z-axis ($x = y = 0$).*

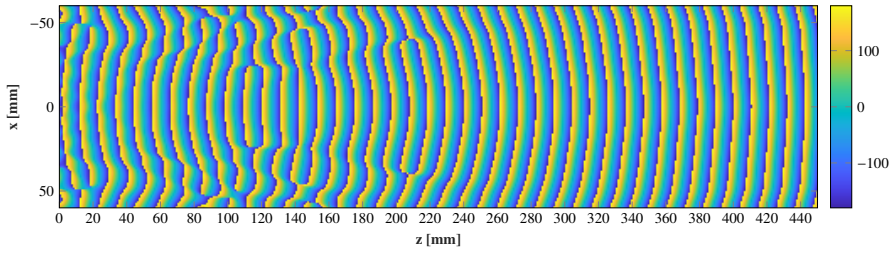

Figure 3.35: *Radiated phase generated by the planar graded-index dielectric lens.*

tests performed these settings enable the print of a high-quality lens, ensuring low errors on the air gaps dimensions, within less than 50 hours to obtain the prototype of Figure 3.37. The nozzle diameter is 0.4.

On the other hand, the doubly hyperbolic lens is also printed with the Ultimaker 3 but using two different materials, PLA and the polyvinyl alcohol (PVA), to ensure a high accuracy on both hyperbolic surfaces. The PVA is a 3D printing material commonly used to create a water-soluble support structure to achieve complex geometries such as the doubly hyperbolic surface. The printer settings are not as critical as in the planar lens since the doubly hyperbolic lens is a solid piece. However, the use of two different materials in the same piece significantly increases the printing time, rising to 30 hours. In Figure 3.36 there is a test of a quarter of the lens, observing the solid PLA block of the lens (grey) and the PVA companion piece (white). The main advantage of using PVA instead of the typical supports made on the same material as the main piece regarding its easy removal since is a water-soluble material. Therefore, once the piece is finished, the double lens is immersed in water to remove the PVA and obtain the final prototype of Figure 3.37

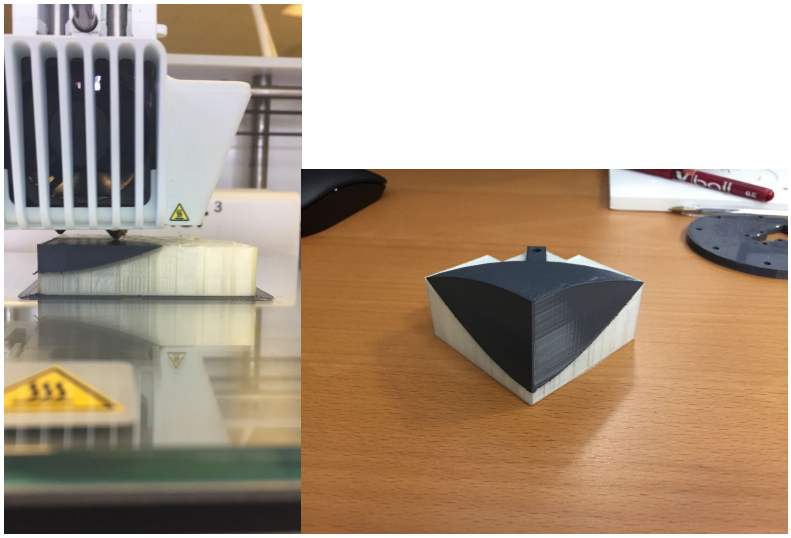

(a) *(b)*

Figure 3.36: *Manufacturing test of the doubly hyperbolic lens in the Ultimaker 3 (a) quarter of the lens while printing it (b) printed quarter lens test.*

The two manufactured prototypes are measured in a near-field planar range at the Universidad de Oviedo, using a similar setup on both cases. This setup is composed of a vector analyzer PNA-X from Keysight whose ports are connected to the feed-

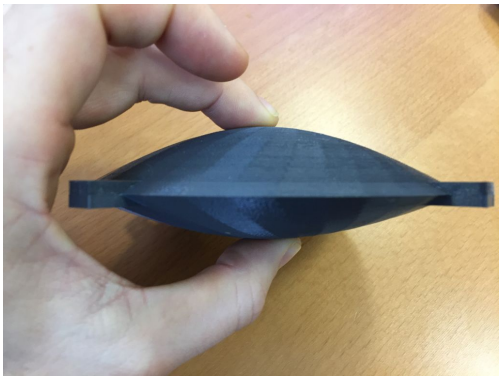

Figure 3.37: *Final prototype of the doubly hyperbolic lens after removing the PVA support.*

ing antenna of the lens and a near-field probe, particularly an open-ended Ka-band waveguide. Owing to availability on the facilities, two different horn antennas have been used to feed the lenses. The doubly hyperbolic lens is fed with the horn antenna of 15 dBi gain NARDA V637, while the Flan 22240-15 of 15 dBi gain is used in the planar lens. Although slight differences are observed in the main cuts of the illumination taper, Figure 3.38, the full-wave simulations considered the real model used in each lens measurement. In addition, neither the doubly hyperbolic lens nor the planar lens takes the amplitude of the incident field into account in their design since they are sorely based on phase considerations. In Figure 3.39(a) the setup is shown while measuring the planar lens and Figure 3.39(b) shows the doubly hyperbolic lens in the support structure along with the NARDA V637.

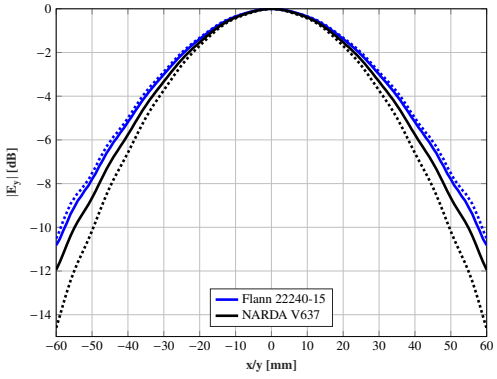

Figure 3.38: *Main cuts $x = 0$ (dotted line) and $y = 0$ (solid line) of the illumination taper on the lens surface for the NARDA V637 and the Flann 22240-15.*

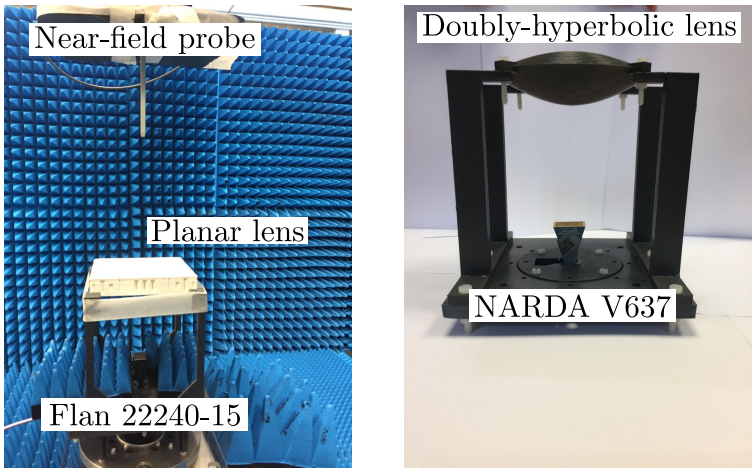

(a) *(b)*

Figure 3.39: *(a) Setup of the near-field planar range of Universidad de Oviedo while measuring the planar lens (b) Doubly hyperbolic lens in its support structure along with the NARDA V637 horn antenna.*

3.3.4.2. Doubly hyperbolic dielectric lens measurements

The near-field radiated by the doubly hyperbolic lens is measured at several planes to evaluate the different focusing parameters. First, the field is measured for the transversal xoz plane in Figure 3.40(a) and the z-axis ($x = y = 0$) in Figure 3.40(b). The figures are normalized to the same value in both cases, which is the near-field magnitude at the focal point. The doubly hyperbolic clearly focuses the near-field within the focal point F_2. Despite having a light magnitude level of the near-field in the proximities of the lens regarding full-wave simulations, the diffraction of the lens is notably low because of the edge of the lens. In Figure 3.40(b) the z-axis is compared to full-wave simulations, having a quite good agreement between both. The focused point on both cases is almost F_2, being 148 and 152 mm in full-wave results and measurements, respectively. Then, the depth-of-focus is 134 mm in simulations and 127 in measurements, defining the depth-of-focus at the 3 dB decay of the field. The beam-waist of the focusing spot is evaluated in the xy plane parallel to the lens aperture in Figure 3.41, obtaining a spot diameter of 18.4 mm or 1.71λ at 28 GHz with an excellent agreement with full-wave results at several levels.

It is assumed that large lenses have an inherent infinite bandwidth only limited by the bandwidth of the feed. Figure 3.42 shows the in-band response of the doubly hyperbolic lens in a bandwidth of 4 GHz, from 26 to 30 GHz. Within this bandwidth

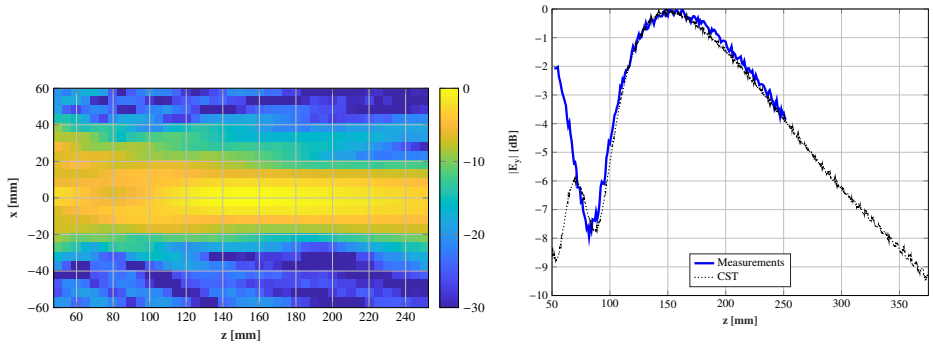

Figure 3.40: *Normalized amplitude (dB) of the near-field radiated by the doubly hyperbolic lens for the (a) transversal xoz plane and (b) the z-axis ($x = y = 0$).*

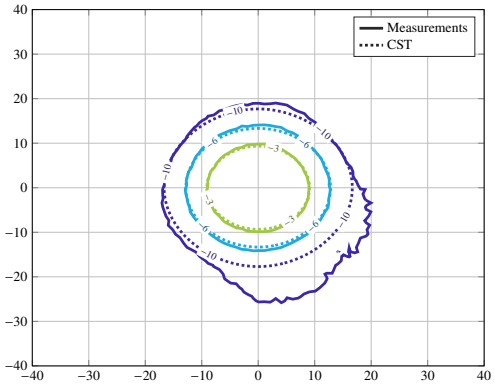

Figure 3.41: *Beam-waist evaluated at the focusing plane for the doubly hyperbolic lens in full-wave simulation and measurements.*

the focused point and the depth-of-focus barely change, showing an excellent in-band response of this lens.

3.3.4.3. Graded-index planar lens measurements

The measurements are also performed for the graded-index planar lens evaluating the near-field at the same planes. The transversal xoz plane of Figure 3.43(a) and the z-axis ($x = y = 0$) of Figure 3.43(b) shows that the lens focuses the near-field magnitude on a closer point than F_2 and the point estimated on full-wave simulations. The diffraction due to the edges is relatively low but higher than in the doubly hyperbolic lens. In the results of the full-wave simulation, the focused point is located at $z = 125$

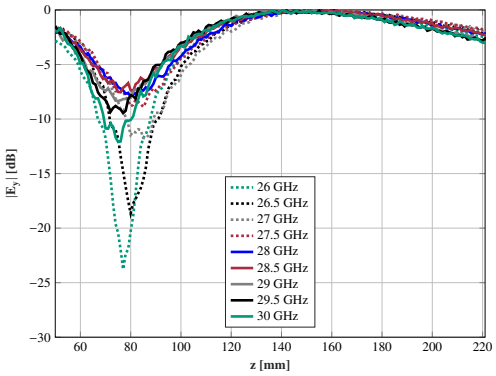

Figure 3.42: *Normalized measured amplitude (dB) of the near-field radiated by the doubly hyperbolic lens for several frequencies, from* 26 *to* 30 *GHz.*

mm while in measurements is at $z = 130$ mm, having a good agreement between both. Then, the depth-of-focus is barely larger in the measurements obtaining 83.7 mm and 79.8 mm in the full-wave results.

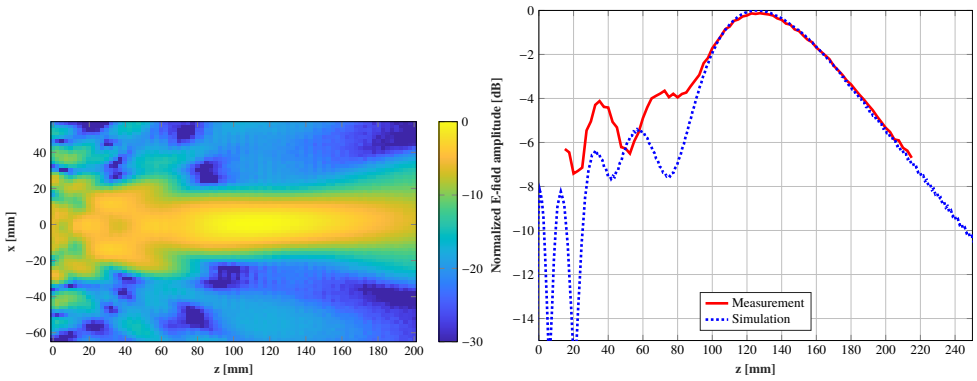

Figure 3.43: *Normalized amplitude (dB) of the near-field radiated by the planar dielectric lens for the (a) transversal xoz plane and (b) z-axis ($x = y = 0$).*

The beam-waist is also evaluated on the parallel plane corresponding to the maximum of the near-field, $z = 130$ mm. In Figure 3.44, both measured and simulated beam-waist are shown. The measured spot is quite similar to the doubly hyperbolic lens with a diameter of 19 mm (1.7λ at 28 GHz). This diameter is slightly larger than expected from the simulations, where the spot diameter is 15 mm (1.4λ at 28 GHz). This disagreement can be also observed at different levels. However, the measured

spot is analogous to the spot generated by the doubly hyperbolic lens.

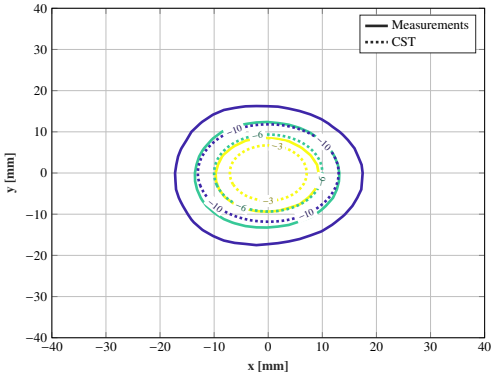

Figure 3.44: *Beam-waist evaluated at the focusing plane for the doubly hyperbolic lens in full-wave simulation and measurements.*

The in-band response of the graded-index planar lens is measured in the same bandwidth as the previous lens, from 26 to 30 GHz. However, the in-band response of this type of lenses is strongly limited by the element response. In Figure 3.45 the z-axis ($x = y = 0$) is shown for several frequencies. The focused point is displaced as the frequency changes. Two effects are associated with this displacement: the element phase response changes at different frequencies and the spatial phase delay of the incident and transmitted fields vary with the frequency. This effect is well known in reflectarray antennas for the incident field but in this case, the impact is deeper since the propagation from f_1 to the lens and from the lens to f_2 contribute to the global variation of the spatial phase delay.

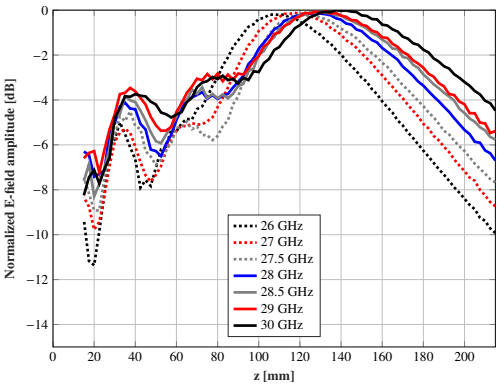

Figure 3.45: *Beam-waist evaluated at the focusing plane for the doubly hyperbolic lens in full-wave simulation and measurements.*

Finally, in Table 3.3 the main physical characteristics of each prototype are detailed. The planar transmitarray allows to save up a 20% of the doubly hyperbolic weight and a 70% of the volume.

Table 3.3: *Electrical and physical performance of the two prototypes manufactured.*

Type	F_2 (mm)	$\varnothing_{\text{spot}}$ (λ)	Thickness (mm)	Volume (mm)	Weight (gr)
Doubly lens	152	1.7	36	961	214
Planar lens	130	1.7	20	288	168

3.4. Multi-feed graded-index planar lens to generate multiple foci in near-field

Throughout this section, a new approach is evaluated to generate a multi-focusing area with several near-field focused spots with a simple design technique, such as CP (3.32), without the need of increasing the complexity of the design. The focusing graded-index planar lens designed in Section 3.3 is used to evaluate the performances and limitations of this approach.

3.4.1. Working principle

The studied approach to generate a near-field multi-focusing area is based on increasing the number of feeds so that each feed is associated with a single focused spot. To understand the concept better, let us suppose that the SFA is a transmissive antenna. The transmitted field on a SFA element according to (2.5) and (2.13) with the $\boldsymbol{A}$ matrix (2.9) particularized for transmission is

$$\boldsymbol{E}_{\text{ap},t}^{X/Y}(x_m, y_n) = \mathbf{T}^{mn} \cdot \boldsymbol{E}_{\text{inc}}^{X/Y}(x_m, y_n) \tag{3.34}$$

If the elements of the SFA are considered ideal phase-shifters, the transmission matrix $\mathbf{T}$ is simplified to

$$\mathbf{T}^{mn} = \begin{pmatrix} e^{j\phi_{xx}^{mn}} & 0 \\ 0 & e^{j\phi_{yy}^{mn}} \end{pmatrix} \tag{3.35}$$

where ϕ_{xx}^{mn} and ϕ_{xx}^{mn} are the phase of the direct coefficients τ_{xx} and τ_{yy}, respectively.

Replacing (3.35) in (3.34), the transmitted field is expressed in the form

$$E^{X}_{\mathrm{ap},t,x} = |E^{X}_{\mathrm{ap},t,x}| \cdot e^{j(\phi^{mn}_{xx}+\phi_{\mathrm{inc},x})}, \tag{3.36a}$$

$$E^{Y}_{\mathrm{ap},t,y} = |E^{Y}_{\mathrm{ap},t,y}| \cdot e^{j\left(\phi^{mn}_{yy}+\phi_{\mathrm{inc},y}\right)}. \tag{3.36b}$$

where $|E^{X}_{\mathrm{inc},x}|$ and $|E^{Y}_{\mathrm{inc},y}|$ are the copolar components of the incident field amplitude at the (m,n) element, considering that the feed is operating in X or Y linear polarization, $\phi_{\mathrm{inc},x}$ and $\phi_{\mathrm{inc},y}$ are the incident phases of the copolar component of the incident field on the (m,n) element. ϕ_{xx} and ϕ_{yy} are the phase responses of the cell for the copolar component of each linear polarization.

Hence, the amplitude of the transmitted field only depends on the amplitude of the incident field, whereas the phase does on two factors: (1) the phase of the incident field and (2) the phase-shift of the SFA element [25]. If the different illuminations on the SFA surface are nearly the same, and the cells are properly designed to ensure good angular stability, only $\phi_{\mathrm{inc},x}$ or $\phi_{\mathrm{inc},y}$ would change from one feed to another. The distance of the radiated field is given by the phase response of the cell and the pointing direction by the phase of the incident field. Thus, if the SFA is designed to focus a single spot and additional feeds are included, whenever the amplitude on the SFA surface is similar, different focused spots will be obtained together with the direction specified by each incident phase. This condition can be easily satisfied if the distance between the SFA and the phase center of the feed is always the same, independently of the physical position of the feed. Assuming that the SFA is designed considering a central feed configuration, the classical feed distribution to ensure the same distance from each phase center to the SFA is a parabolic distribution. This means placing the feeds following a parabolic path. However, in this case, it is used the circular arc path defined by the midpoint of each SFA and the central feed as Figure 3.46 depicts. The error between considering the circular arc path instead of a parabolic path is almost negligible since the parabola and the circular path define almost the same paths for the angles within the angular stability of the cell can be ensured. Note that the feeds are always pointing to the geometric center of the SFA to minimize the differences among the incident field amplitudes.

The minimum angular distance between two adjacent feeds, considering their physical dimension, is given by the angles α and θ for the xoz and yoz plane of the SFA, respectively. Setting the origin of the coordinates at the geometric center of the SFA, the central feed is located at a focal distance equivalent to the radius r of the arc path.

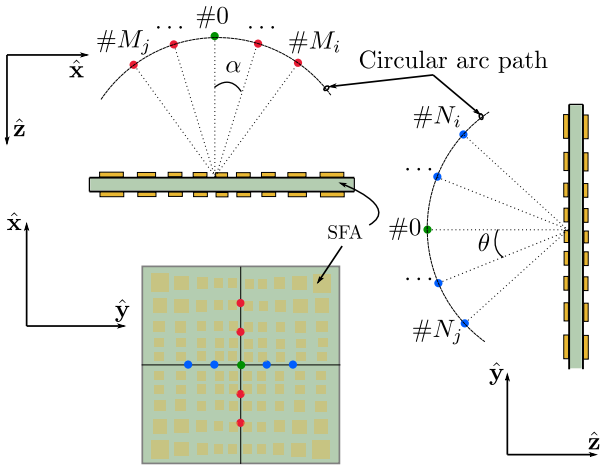

Figure 3.46: *Sketch of the spatial distribution of the feeds along the $\hat{\boldsymbol{x}}$ and $\hat{\boldsymbol{y}}$ axes.*

Therefore, the rest of the feeds are placed at the following positions

$$\begin{aligned}(\hat{\boldsymbol{x}}, \hat{\boldsymbol{y}}, \hat{\boldsymbol{z}}) &= (-r\sin\theta, 0, -r\cos\theta) \text{ for the } xoz \text{ cut} \\ (\hat{\boldsymbol{x}}, \hat{\boldsymbol{y}}, \hat{\boldsymbol{z}}) &= (0, -r\sin\alpha, -r\cos\alpha) \text{ for the } yoz \text{ cut}\end{aligned} \tag{3.37}$$

3.4.2. Multi-focusing performances using a cluster of feeds in a graded-index dielectric lens

3.4.2.1. Antenna and feed cluster definition

As a first approach to evaluate the performances of an SFA focusing on multiples spots, the designed graded-index planar lens of the previous Section 3.3 is simulated with a feeding system based on five horn antennas. The cluster illuminates the lens through a 1D distribution according to the $\hat{\boldsymbol{x}}$-axis with an angular distribution of $\theta = 5°$. According to the antenna definition outlined in Table 3.2, the focal lengths f_1 and f_2 are 100 and 150 mm, respectively. Therefore, the cluster is located on a circumference arc of radius 100 mm (f_1). The phase center location of each feed is easily computed with (3.37), obtaining the positions outlined in Table 3.4. Note that this distribution is not physically achievable because of the physical dimensions of the horn antenna, therefore the simulations will be carried out with a single feed which is moved to cover all the desired positions. Despite not having a cluster on the simulation this first approach will provide information on the degradation of the focusing performances of the antenna due to the angular displacement of the feed.

Table 3.4: *Location of the phase center of each horn antenna of the cluster using a circular arc path configuration (mm).*

	$\theta = 0°$	$\theta = \pm 5°$	$\theta = \pm 10°$	$\theta = \pm 15°$	$\theta = \pm 20°$
$\hat{\boldsymbol{x}}$	0	± 8.71	± 17.36	± 25.88	± 34.22
$\hat{\boldsymbol{y}}$	0	0	0	0	0
$\hat{\boldsymbol{z}}$	-100	-99.61	-98.48	-96.59	-93.97

Let us remind that the graded-index planar lens is made up of 576 elements distributed on a regular lattice of 5×5 mm^2 in the x- and y-direction. The size of the antenna is 120×120 mm^2 with an equivalent aperture of 169.70 mm^2 at the central frequency of 28 GHz. The antenna focuses the field at 150 mm from the outer surface, though the maximum of the electric field is located at 125.64 mm on simulations. The graded-index planar lens is designed using a dielectric-only cell, which uses the variation of the effective index medium to add a phase-shift on the transmitted wave. In this case, the square prism cell with an embedded air gap is used. By adjusting the dimensions of the air gap, the infill of the cell changes, therefore its phase response according to (3.10). Then, the feed is a pyramidal horn antenna of 15 dBi gain that generates an illumination taper of nearly 11 dB at the edge of the lens. Reminding the importance of having similar amplitudes on the incident field at all the positions, the incident field is simulated in a full-wave simulation using CST Microwave Studio. In this simulation, the incident field was evaluated for the central position $\theta = 0°$ and the location at the edge $\theta = 20°$ at the working frequency of 28 GHz. Owing to the symmetric distribution on the circular arc, the maximum differences in the amplitude should be found for these two positions. The results are shown in Figure 3.47, observing that both fields have a similar amplitude, finding only slight differences at the edge of the lens because of the projection of the incident field on the lens surface. However, the difference in an area of radius 50 mm is lower than 1 dB, as Figure 3.48 shows. Conversely, changes in the incident phase are produced since the phase depends only on the phase center location of the feed. Therefore, this variation on the incident phase should move the focused spot to a new position.

The entire antenna (feed and lens) has been analyzed in CST Microwave studio in a full-wave simulation and considering the different positions of the feed, from $\theta = 0°$ to $\theta = \pm 20°$. The electric field for the xoz plane at each position is shown in Figure 3.49, and the 3 dB contour of all the near-field spots are simultaneously compared in Figure 3.50. Both results verify that the planar lens radiates the expected

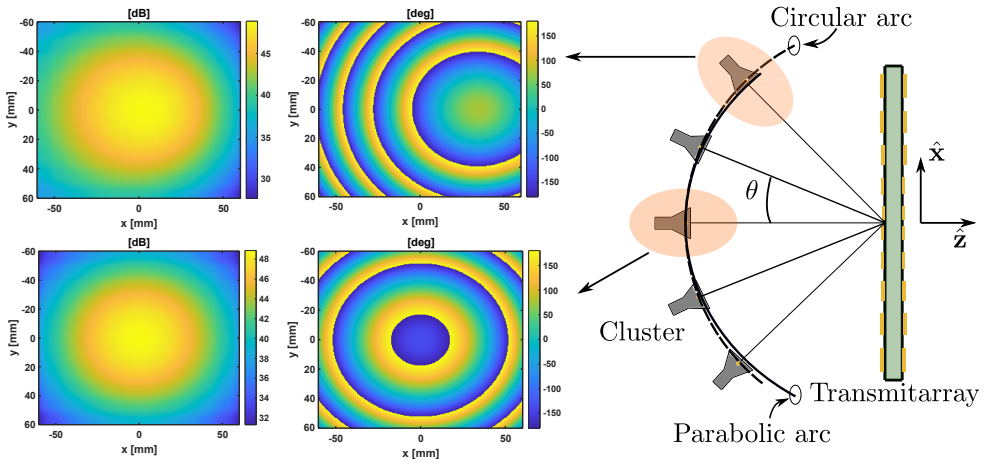

Figure 3.47: *Evaluation of the incident field, amplitude (dB) and phase (deg), for the feed at $\theta = 0°$ and $\theta = 20°$.*

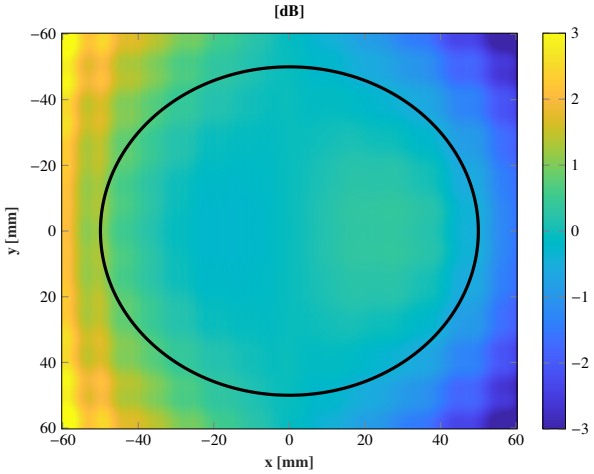

Figure 3.48: *Difference on the incident field amplitude (dB) on the lens surface for the feeds at $\theta = 0°$ and $\theta = 20°$. The error within the solid line is lower than 1 dB of difference.*

spot at the central position, but also a focused spot for each feed position. It is important to underline that the spots follow a similar angular distribution of the feed, but inverting the arc curvature.

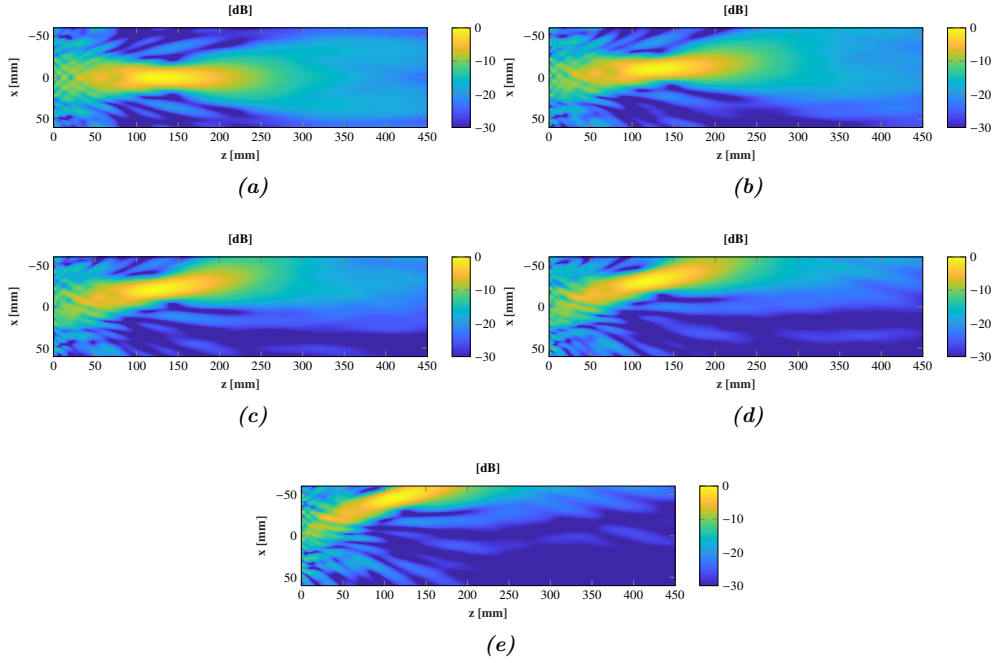

Figure 3.49: *Normalized simulated amplitude electric field at the plane xoz for several positions of the feed.(**a**) $\theta = 0°$, (**b**) $\theta = 5°$, (**c**) $\theta = 10°$, (**d**) $\theta = 15°$ and (**e**) $\theta = 20°$*

In this approach, the horn antennas are intended to work in two different ways. First, the whole cluster works at the same time radiating all the multi-focusing spots as Figure 3.50 shows. However, if all the horn antennas work at the same frequency there will be a strong interference between the focused spots disturbing the desired spot distribution. This problem can be addressed by using the same operational band in the cluster, but each feed must use a shifter carrier concerning the operational frequency. This solution avoids the interferences between the focused spots and provides high isolation among the horn antennas. Second, considering that not all the feeds work at the same time, thus by implementing a switching on the cluster, the focused spots can be alternatively radiated avoiding having two adjacent spots within the same slot. This is a more expensive solution that significantly requires increasing the complexity of the design to control the switching of the cluster. Conversely, the isolation among

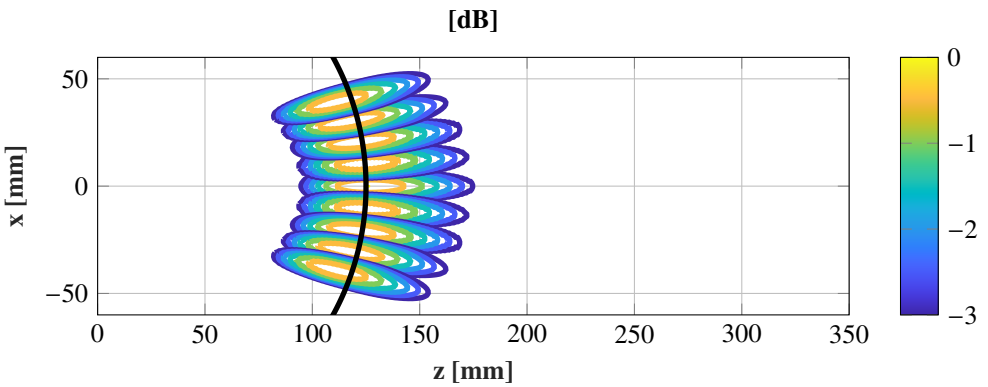

Figure 3.50: *Normalized near-field focused spots comparison for several feed positions,* $\theta \in [0, 20]^\circ$.

the horn antennas is also evaluated assuming the worst case, the same frequency carrier for all the feeds. The setup of Figure 3.51 is simulated in CST Microwave Studio to analyze the S-parameters of the feeds. The setup is composed of the planar lens and three horn antennas at $\theta = 0^\circ$ and $\theta = \pm 15^\circ$. The results of the simulation is shown in Figure 3.51. The three horn antennas are matched in the entire band from 26 to 30 GHz as Figure 3.52(a) shows. The magnitude of the three S-parameters s_{11}, s_{22} and s_{33} is below -15 dB within this band. The magnitude of the s_{21}, s_{31} and s_{32} is shown in Figure 3.52(b), resulting on almost 20 dB of isolation between adjacent horn antennas in the entire band. In this case, the coupling among the horn antennas at the edges is slightly higher because their tilting angle is the same but opposite sign. Therefore, each horn antenna receives the specular reflection on the lens surface by the other horn antenna.

3.4.3. Breadboard manufacture and measurements

In the light of the results obtained in the full-wave simulations, the graded-index lens has been measured again but feeding it with this configuration. The measurements were carried out in a planar acquisition range using the setup shown in Figure 3.53. The feeding horn antenna is the Flann 22240-15 of 15 dBi and it is connected to a port of a vector network analyzed PNA-X from Keysight. A second port is connected to an open-ended Ka-band wave-guide used as a near-field probe. Owing to a limitation on the facilities, only one horn can be used in the measurements. However, the structure that bears the horn antenna enables to move it within an arc of radius 100 mm simulating the different positions of the cluster. The physical dimensions of the horn

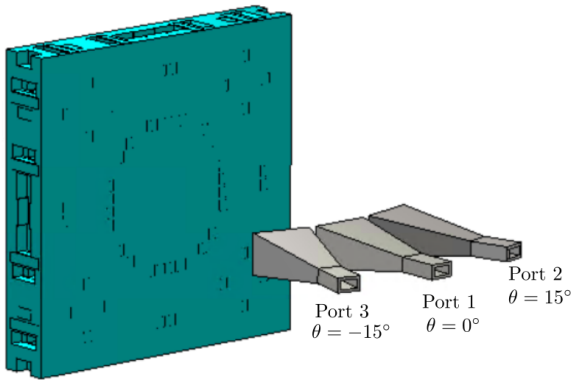

Figure 3.51: *Setup to simulate the S-parameters of the three horn antennas working at the same frequency carrier.*

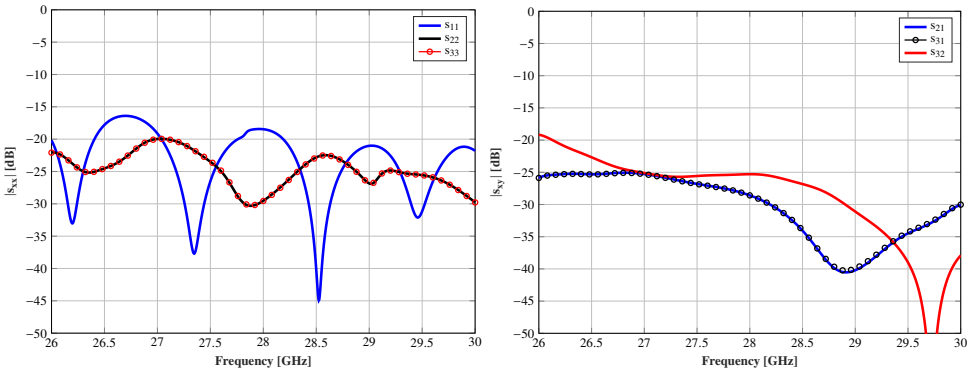

(a) ***(b)***

Figure 3.52: *S-parameters of the horn antennas (a) s_{11}, s_{22} and s_{33} and (b) s_{21}, s_{31} and s_{32} according to the port definition of Figure 3.51.*

antenna aperture limit the number of feeds that can be used on the cluster. Depending on the linear polarization used, this horn antenna can be placed with an angular distribution θ of 10° or 15°. Note that the horn antenna has a pyramidal shape with different apertures dimensions in the E- and H-plane, being the E-plane the shortest aperture. In this case, the measurements were carried out for the angles $\theta = 0°, 15°$ and 20°. These positions allow to evaluate two different configuration of the cluster, considering the feeds on $\theta = 0°$ and $\theta = \pm 15°$ or $\theta = 0°$ and $\theta = \pm 20°$. The measurements are carried only out for the positive θ angles. However, the results can be extended to the negative θ positions due to the antenna symmetry on its $\hat{\boldsymbol{y}}$ main plane. The field is evaluated on the horizontal plane xoz within a bandwidth of

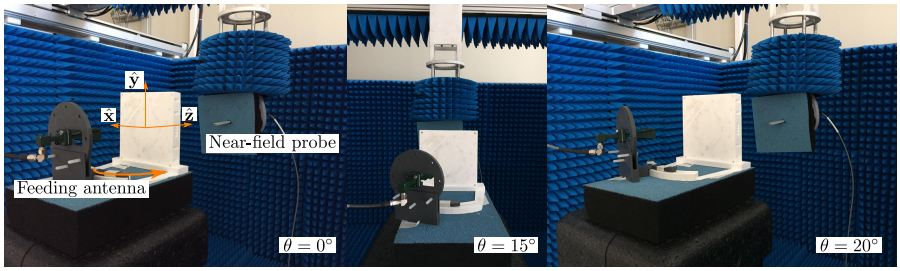

Figure 3.53: *Setup to measure the graded-index planar lens using a multi-feed configuration at the planar acquisition range of the Universidad de Oviedo.*

4 GHz, from 26 GHz to 30 GHz.

The measurements of the electric field in the xoz plane are shown in Figure 3.54 and Table 3.5 outlines the focusing performances of the planar lens at the three positions of the feed. Particularly, it has been established two figures of merit to compare with full-wave simulations: the position of the maximum and the depth-of-focus of the spot. These measurements, as it was observed in the full-wave simulations, verify that a feed distribution according to (3.37) changes the near-field spot direction, keeping its focusing characteristics practically unchanged. The central spot reaches the maximum of the field at a distance of 125.6 mm and a depth-of-focus of 79.9 mm, obtaining a high agreement with simulations. The middle feed ($\theta = 15^{\circ}$) presents a spot that highly agrees with the one obtained in the simulation, in both the direction and size of the spot. Moreover, it is worth noticing that the depth-of-focus of this spot is almost the same as the spot generated by the feed at ($\theta = 15^{\circ}$), showing that this displacement of 15° barely affects the focusing performances. At the widest angular position of the feed ($\theta = 20^{\circ}$), some distortions start to appear on the spot. Mainly, the spot suffers an angular shifter regarding its expected position from the full-wave simulation. Then, the position of the maximum is more compressed than the other two positions. Both effects can be better observed in Figure 3.55 where the 3 dB contour of the three spots are compared. These effects are a consequence of the phase aberrations due to the off-focus feeding.

The in-band response of the planar lens is analyzed from 26 to 30 GHz. Particularly, it has been evaluated the displacement on the spot position because of a variation in the frequency. In Figure 3.56 it has been represented that the distance from the center of the lens to the maximum of the spot for each feed and the different measured frequencies. As it may be expected, when the frequency goes up, the spot goes further and vice versa. Then, it can be observed that the behavior of the spot for $\theta = 0^{\circ}$ and $\theta = 15^{\circ}$ is quite similar in the whole band. In general terms, the graded-index planar

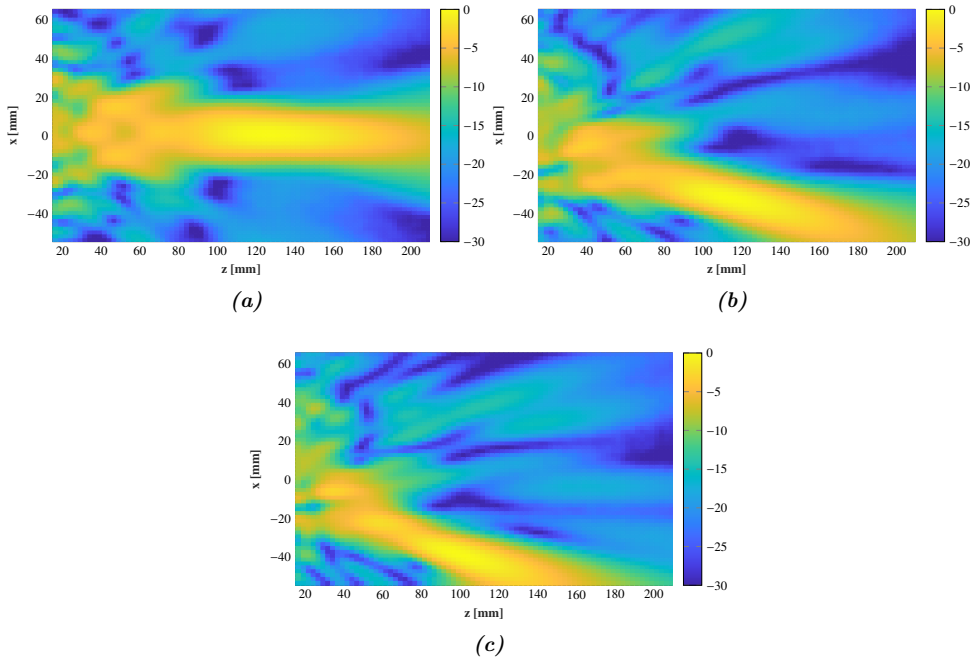

Figure 3.54: *Measured normalized electric field amplitude (dB) for the xoz plane for the three different positions of the feed: (a) $\theta = 0^\circ$ (b) $\theta = 15^\circ$ and (c) $\theta = 20^\circ$.*

Table 3.5: *Electrical feature of the graded-index lens fed by a cluster at three positions. Measurements compared with full-wave simulations.*

θ	Full-wave simulation		Measurement	
	Maximum (mm)	Depth-of-focus (mm)	Maximum (mm)	Depth-focus (mm)
0	(125.6, 0)	79.9	(130,0)	85
15	(116.6,-30)	76.1	(112.5,-32.5)	75.7
20	(110.6,-38.8)	74.2	(97.5,-49.5)	65.6

lens shows good in-band response and a very stable behavior for a displacement of 15°, while for 20° different effects appear because of the spatial phase delay.

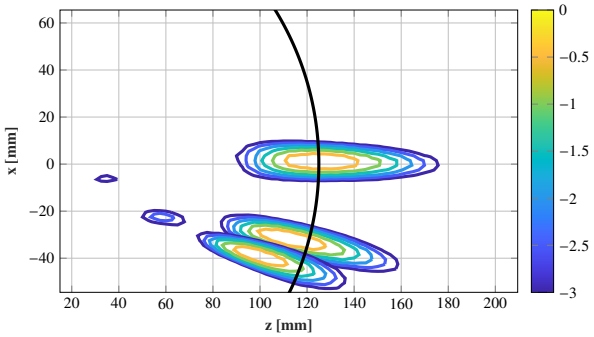

Figure 3.55: *Comparison of the 3 dB contour of the three focused spots.*

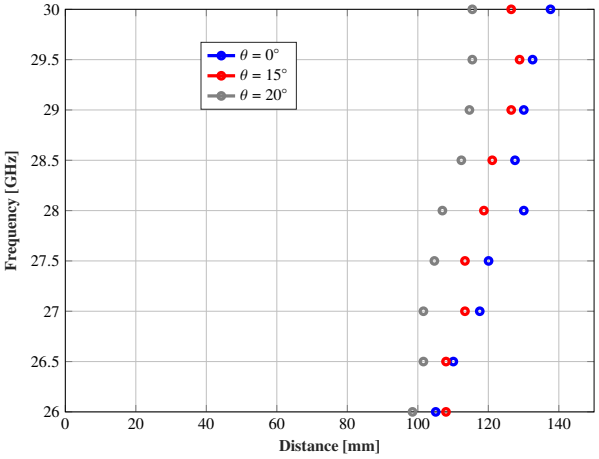

Figure 3.56: *Shift of the focused spot distance to the center of the lens because of the frequency variation.*

3.5. Conclusions

In this chapter, two graded-index planar lenses have been designed and manufactured to evaluate their performances on the generation of Bessel beams in Ka-band. The proposed graded-index planar lenses are comprised of dielectric-only elements. Two different geometries of cells are studied, which are based on a novel approach. The phase of the element is controlled by the insertion of air gaps in the dielectric element. Hence, the overall infill of the cell can be controlled to produce the required phase-shift. The first geometry is a square prism cell with an embedded square air gap prism that allows obtaining a regular distribution of the elements in the antenna surface. The second geometry is a hexagon prism whose air gaps are a cylinder that requires placing the elements on a honeycomb distribution. It has been demonstrated that the geometry of the cell and air gaps does not affect the phase response of the cell, provided that the overall infill of the cell is preserved. Two different layouts, one is based on the square prism and the other on the hexagon prism, are designed and manufactured to produce a Bessel beam within a range of 650 mm. Both layouts were manufactured using a 3D printing technique and measured in a near-field planar range, obtaining a good agreement between full-wave simulations and measurements. Despite having good performance in terms of the non-diffractive range and the beam-waist in both designs, the hexagon prism element exhibits a superior in-band response from 26 to 30 GHz. In light of the obtained results, spatially-fed arrays, in particular graded-index planar lenses, have been demonstrated to be potential candidates to generate Bessel beams at millimeter bands. In addition, graded-index planar lenses are a low-profile antenna with good performance that can take the advantages of 3D additive techniques to reduce the costs.

In the second section, a graded-index planar lens made up of dielectric-only elements is designed and manufactured to compare it with a doubly hyperbolic lens. The elements are based on the square prism cell of previous section. Both lenses focus the near-field obtaining similar performance on the focused spot. The main differences are that the graded-index planar lens delivers the maximum amount of power between the theoretical focal point and the antenna aperture. However, this effect can be mitigated by considering a larger focal distance f_2' on the design to obtain the maximum of the near-field at f_2. Then, the graded-index planar lens is comprised of different dielectric-only elements. Hence, the operational bandwidth of the antenna is limited by the phase response of the element. On the other hand, the working principle of the doubly hyperbolic lens is based on its geometry. The operational bandwidth is ideally infinity and only limited by the feed. Measurements show that the doubly hy-

perbolic lens is very stable within a bandwidth of 4 GHz. Some important drawbacks of curvy lenses are their dimensions and weight, which are significantly higher than in a planar antenna. The use of a graded-index planar lens could be quite useful for applications that require lightweight and compact antennas rather than solutions with large operational bandwidth.

Then, the focused graded-index planar lens is evaluated together with an approach to generate a multiple focus configuration. This approach presents a basic technique to increase the number of focused spots by increasing the number of feeds, leading to the use of a cluster of horn antennas to illuminate the antenna surface. It has been demonstrated that provided a spatial distribution of the feeds so that the different feeds are located in a circular path of radius equivalent to the focal length of the SFA, with the feeds pointing to the geometric center of the SFA, it is feasible to generate different beams whose direction is determined by each position of the feed. The prototype was measured in a near-field planar range, obtaining similar results to full-wave simulations. The graded-index planar lens shows the expected response within an angular range of $\pm 20^{\circ}$ in a bandwidth of 4 GHz, from 26 to 30 GHz, demonstrating that this approach is suitable to achieve these multiple focused patterns. Moreover, the use of dielectric elements instead of resonant elements allows reaching larger bandwidths. While it is true that the angular range is severely restricted by the angular stability of the cell and, the spatial phase delay. This last effect deteriorates the focusing properties of the beam. However, these effects can be minimized if the antenna is designed with more complex techniques than CP, for instance, a bifocal approach.

CHAPTER 4

Design of spatially-fed array antennas for shaping the pattern in near-field region

4.1. Introduction

As it has been detailed in previous chapters the research activity has been developed to achieve antennas with near-field focusing capabilities, either to radiate a constant power density within a limited-size spot or a range. This research activity is strongly tied to wireless technology and its increase in popularity due to the emergence of several applications such as RFID, MWI, or WPT throughout the last years. Latest developments in communications such as the evolution of the Internet of Things (IoT) or the current Fifth Generation 5G of mobile communications have boosted the interest in wireless technologies to their peak. The new generations of mobile communications, namely 5G, beyond 5G (B5G), or the future 6G, have advanced the use of higher frequencies in the millimeter band. Most of these communications are planned to work from Ka-band to 200 GHz, which provide high-speed wireless access in cellular networks [233].

One of the challenges of millimeter-wave communications is related to the signal propagation, which increases its path losses and sensitivity to physical barriers at those frequencies [234]. Hence, an important challenge for the research community is the development of antennas that can satisfy the new requirements imposed by the new wireless applications and technologies. In the framework of IoT and 5G-B5G, the number of devices connected to wireless networks has an exponential increase and the impact of this rise will be more relevant in the millimeter-wave spectrum bandwidth,

which is also known as FR2 (Frequency Range 2). The main frequency bands will be centered in 28, 39, and 60 GHz, which have already been reserved by many administrations to operate this technology at those frequencies. As it was pointed out before, working in FR2 implies an increase in the path losses and a major sensitivity to physical barriers, therefore it is necessary to develop efficient coverages and radio links in these bands and, from the point of view of devices, wireless connectivity through a suitable and proper antenna.

To minimize the path losses and, especially physical barriers, it is quite interesting to place the 5G devices as closely as possible. For instance, in wireless communications to minimize the distance between users and base station as much as possible. The proximity between those devices will place them within the Fresnel region of the antenna devices, particularly in indoor communications. Hence, the deployment of efficient indoor communication operating within the near-field region will be indispensable or even a desired option to support wireless communications on 5G and beyond. Two possible scenarios can be generated with 5G indoor communications. On one hand, specific areas with a lot of devices require total connectivity which implies forgetting extensive coverage areas generated by an external base station in support of small areas wherein the devices are located together with the base station to minimize the path losses. On the other hand, to deploy an indoor base station to cover certain areas which are not covered by an external base station because of physical barriers. In both cases, these scenarios demand the use of antennas with shaped near-field beams similar to communications operating in the far-field region. Although focusing on near-field is still important in many applications, there is a chance to increase the number of applications where the control of the near-field pattern is important not only for focusing but also to develop antennas with near-field shaped beam capabilities.

In this chapter, different scenarios of 5G indoor communication will be addressed to evaluate the potential of spatial-fed arrays in these applications. Similar to other applications which use reflectarray or transmitarray antennas, the chapter is focused on the evaluation of different shaped beams in the near-field. The achievement of these shaped beams is not feasible by analytical expression as occurs in Chapter 2 and it is needed to use other techniques. In this case, the generalized Intersection Approach will be used to imposed specifications on the amplitude of the near-field according to the different scenarios. After performing the phase-only synthesis different solutions based on printed and dielectric-only elements will be evaluated. The goal is both evaluate spatially-fed antennas as a potential candidate to provide coverages on these applications as a low-cost low-profile and high integrability in indoor scenarios due to their planar geometry and test the generalized Intersection Approach to carry out

phase-only synthesis when only imposing arbitrary restriction on the amplitude of the near-field.

In the first section, a single-layer reflectarray is synthesized to generate an indoor femtocell coverage at 28 GHz. The synthesis aims to reach a low ripple amplitude density power area over a desktop within the near-field of the antenna. The synthesis is carried out considering the elements as ideal phase-shifters, therefore using a POS technique. The proposed element is a single-layer dual-polarized patch that does not achieve a full phase cycle but provides a single-layer antenna. The phase limitation of this element is considering in the synthesis process by limiting the degrees of freedom of the optimization variables to the phase-shift range of the cell. The reflectarray is designed and manufactured, obtaining a good agreement between simulations and measurements.

Then, a transmitarray is synthesized to obtain a multi-spot coverage on a dual-linear-polarized configuration at 28 GHz. The coverage is composed of several independent beams to increase the capacity of the systems through the different adjacent spot coverages. As a result, the transmitarray generates a coverage of 20° coverage spot and overall coverage of 50°. The design is carried out with dual-polarized dielectric-only elements to select the most proper polarization in each spot. The measurements show a good agreement with the simulations and requirements.

In the final section, a transmitarray is synthesized to reach indoor coverage in a complex scenario. In this case, the transmitarray is synthesized to achieve a coverage area through the propagation direction, trying to compensate for the inherent effect of the natural behavior of the electromagnetic waves. To achieve this goal, the generalized Intersection Approach employs adaptive masks to define the specifications, which improves the convergence of the synthesis since the near-field itself defines the templates.

4.2. Design, manufacture and test of a reflectarray for indoor femtocell at 28 GHz

4.2.1. Scenario and antenna definition

The definition of the antenna and the scenario are described in several subsections. The first one describes the requirements of the coverage. Then, the antenna optics is defined as well as the feed horn antenna in subsections 4.2.1.1 and 4.2.1.2, respectively.

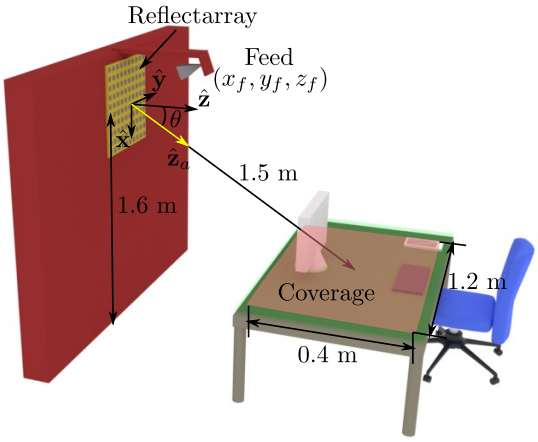

Figure 4.1: *Sketch of the proposed reflectarray behaving as a base station of a femtocell 5G indoor coverage.*

4.2.1.1. Scenario definition

The scenario and the footprint of the chosen femtocell are shown in Figure 4.1. The coordinates are referred to a reflectarray antenna placed on a wall at a height of 1.8 m from the floor, which blends the antenna with the environment. The reflectarray points to the center of a desktop at a height of 1 meters and a distance 1.5 m on the $\hat{\boldsymbol{z}}$ direction, which corresponds to a radiation on a (θ_0, φ_0) direction of $(35^\circ, 0^\circ)$. The coverage area is defined on an yz area of 1.2×0.4 m^2 centered on the pointing direction (solid line contour). The goal is to achieve a constant amplitude distribution within this area with a maximum ripple of 3 dB. Then, there is defined a transition area of 800×150mm^2 to ensure a smooth transition of the field from the area of interest to a second-level restriction area. The maximum level of the near-field outside the coverage and the transition area must be 12 dB lower than the maximum of the coverage area to avoid radiation in non-desired areas and to increase the efficiency of the antenna. These constraints are considered as the required specification level in the later synthesis process at a working frequency of 28 GHz. The reflectarray has to satisfy those condition on the horizontal polarization (H-pol) and the vertical polarization (V-pol) defined by $\hat{\boldsymbol{y}}$ and $\hat{\boldsymbol{x}}$, respectively.

4.2.1.2. Antenna optics

To achieve the defined specifications on the coverage region, it is chosen a reflectarray antenna, particularly a square reflectarray which simplifies the manufacturing com-

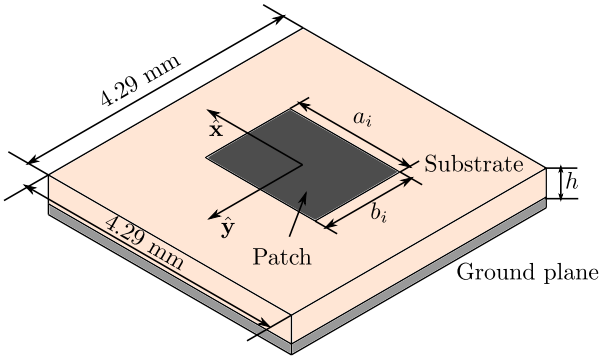

Figure 4.2: *Sketch of the element based on a printed patch. .*

plexity. The reflectarray is made up of 40×40 elements distributed in a regular grid of periodicity of 4.29×4.29 mm^2 ($0.4\lambda_0$ at 28 GHz) in the $\hat{\boldsymbol{x}}$ and $\hat{\boldsymbol{y}}$ direction. The reflectarray breadboard considers a dielectric frame of 8.58 mm to place the screws to joint it to the supporting structure. The total size of the breadboard is 205.92×205.92 mm^2. An important fact is to reach a single-layer reflectarray to provide a high integrable antenna within the indoor scenario. Therefore, the chosen reflectarray element is a single-layer patch cell which provides a good solution between its performances and low-complexity on the design. In Figure 4.2 the patch element is depicted. The dimensions (a_i, b_i) are adjusted to achieve the desired phase-shift on each element and polarization. The patch is printed on a 0.762 mm thickness (h) DiClad 880 substrate ($\epsilon_r = 2.26, tan\delta = 0.0005$) and backed by a ground plane. According to these specifications, the element response about its dimensions is analyzed with a homemade software of the Method of the Moments based on local periodicity (MoM-LP) [235]. Figure 4.3 shows the amplitude and phase response for the normal incident, the working frequency (28 GHz), and the extreme frequency bands of the 5G mm-Wave band at 28 GHz. The phase response at the central frequency presents a soft slope, which minimizes phase-shift errors due to manufacturing tolerance, on the whole, phase-shift range. However, this range is limited to 260° that does not cover a full phase-shift range of 360°. This limitation could reduce the antenna performance, therefore it would be included in the synthesis process. The phase response at different frequencies is very stable and the amplitude response in the worst case is -0.42 dB at 28 GHz, and -0.41 dB and -0.45 dB at 26 and 30 GHz, respectively.

The angular stability is also analyzed through the same procedure and the results are shown in Figure 4.4. The overall performances of the cell at different (θ, ϕ) incident angles are quite good, obtaining a very robust response against variations on the angle

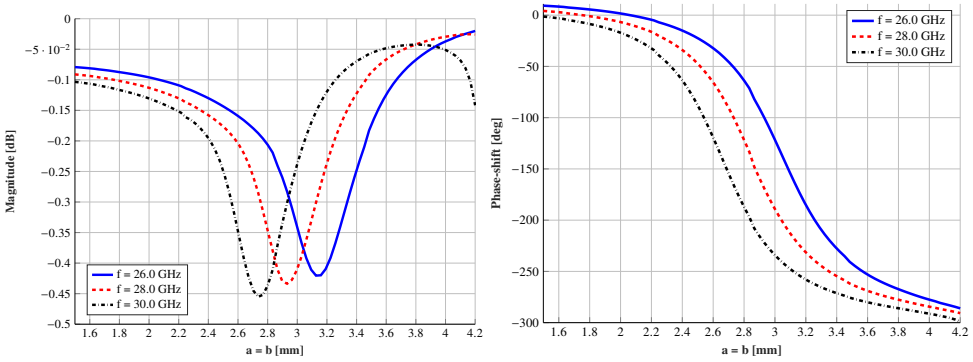

(a) *(b)*

Figure 4.3: *(a) Amplitude (dB) and (b) phase (deg) response of the single-layer patch element at different frequencies and the variation of its dimensions* (a_i, b_i) *at* 28 *GHz under normal incidence.*

of incident. Bearing in mind, that the maximum phase-shift range is 260° for all the cases.

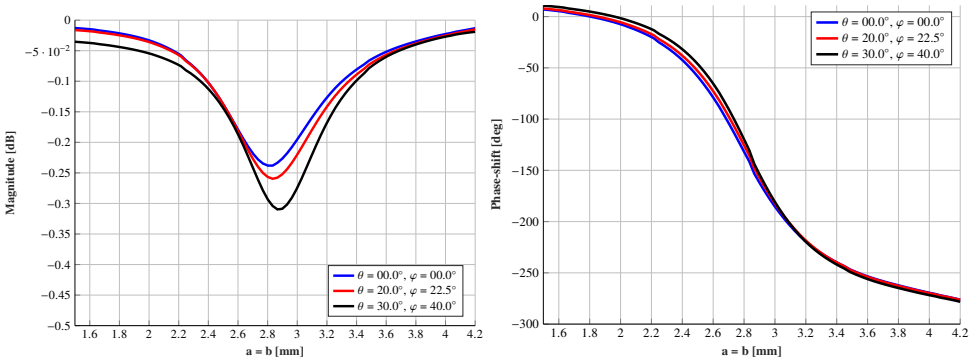

(a) *(b)*

Figure 4.4: *(a) Amplitude (dB) and (a) phase (deg) response of the single-layer patch element for different angles of incidence and the variation of its dimensions* (a_i, b_i) *at* 28 *GHz.*

4.2.1.3. Feed horn antenna

The reflectarray is fed by a horn antenna, working in single linear polarization for H- and V-pol. It is a pyramidal horn antenna (NARDA 665-20) and is shown in Figure 4.5. The gain at the central frequency 28 GHz is 18.6 dBi gain, while at the

extreme frequencies 26 and 30 GHz are 18.1 and 19, respectively. The phase center of the horn antenna is located at the coordinates $(x_f, y_f, z_f) = (-79.3, 0, 200.0)$ mm as it is depicted on Figure 4.5(b). The horn antenna points to $(x_i, y_i) = (-6.4, 0)$ mm and the illumination angle γ is 20˚. According to this geometry the ratio F/D is 0.97.

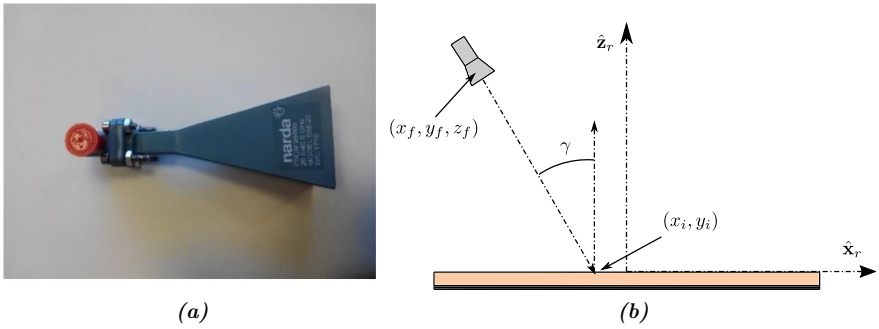

Figure 4.5: *(a) Horn antenna NARDA 665-20 and (b) Lateral view of the breadboard with coordinates of the feed position. The reflectarray coordinate system is on the upper surface.*

The illumination taper is evaluated on the main planes of the reflectarray for both polarization, and it is shown in Figure 4.6. The average taper at the central frequency is 15.8 and 15.7 dB at the edge of the antenna for V- and H-pol.

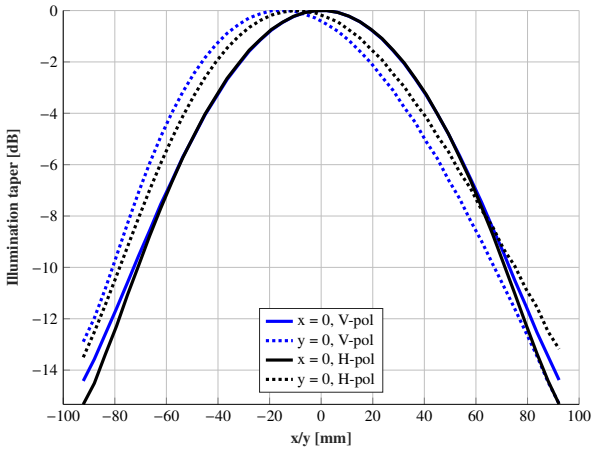

Figure 4.6: *Illumination taper evaluated on the main planes of the reflectarray at* 28 *GHz.*

4.2.2. Near-field pattern synthesis procedure

In this subsection, the pattern synthesis of the sectoral coverage is carried out to obtain a phase distribution of the reflection coefficients on the reflectarray surface that produce the required near-field pattern. Because of the number of elements on the reflectarray, thus the number of optimization variables (1936), and the area wherein the near-field is computed (2×2 m^2) make impractical the use of a direct synthesis method. In this type of synthesis, the optimization variables are the geometrical parameters of the reflectarray element, such as (a_i, b_i), and these dimensions are adjusted to radiate the desired pattern. However, the price to pay is an increase in the complexity of the process since it is needed a full characterization of the cell according to its dimensions in the iterative optimization process. In this case, the obtaining of the reflectarray is addressed in two different and independent steps. First, assuming a fixed amplitude distribution on the reflectarray surface provided by the feed, a phase-only synthesis is applied to obtain the phase of the reflected field in each reflectarray element that radiates the aimed near-field pattern. The output of the phase-only synthesis is the phase of the reflection coefficients (ρ_{xx} or ρ_{yy}) of the $\boldsymbol{R}$ matrix that radiates the desired near-field pattern. Note that, the process is independent for each polarization, therefore the phase-only synthesis is repeated twice to obtain two different phase distributions, one for V-pol (ρ_{xx}) and the other for H-pol (ρ_{yy}). In the second step, which will be discussed in subsection 4.2.4, the dimensions of the patch elements are adjusted, element by element, to produce the phase distribution resulting from the phase-only synthesis for each polarization.

The generalized Intersection Approach for near-field is used to obtain the phase distribution of the reflectarray for the required near-field pattern at the central frequency. In this case, the near-field constraints are only imposed on the magnitude, therefore the cost function of the generalized Intersection Approach is reduced to evaluate the functional d_M instead of d in (2.73).

The convergence of the algorithm into undesired local minima is strongly linked to the starting point used in the synthesis. To overcome these issues, the synthesis is addressed by dividing the problem into different synthesis processes whose requirements are gradually tighter and optimization variables are progressively increased. This means improving the starting point in each stage of the process through obtaining intermediate solutions closer to the final one. In Figure 4.7 a flowchart of this strategy is detailed. Starting for a given phase distribution the phase-only synthesis is carried out with a lighter requirement than the final specifications. Once the algorithm reaches a solution that satisfies these first specifications, a new phase-only

synthesis is carried out but using the phase distribution of the previous synthesis as the starting point. The specifications of the new synthesis are updated to consider tighter requirements. This process is repeated until obtaining a phase distribution that fulfills the final specifications.

To improve the convergence of the algorithm, the number of optimization variables should be reduced, reducing the number of degrees of freedom. As a consequence, the risk of converging to a local minimum becomes lower and the convergence is enhanced. The aim is to carry out a progressive synthesis from the center to the edges, producing a fictitious variation on the number of variables, though the number of elements does not change. This can be carried out by changing the directivity of the feed, thus changing the illumination taper, in such a way that the illumination at the edges is progressively increased from one stage to the next. Starting from a high directivity feed, the field level at the edges is extremely low and the outer elements hardly contribute to the beam shaping because of their low amplitude excitation. However, the elements at the center of the reflectarray contribute significantly to the beam shaping. In each stage, the number of elements considered is progressively increased with the reduction of the directivity of the feed. The number of optimization variables is progressively increased in each step of this strategy, avoiding undesired local minima.

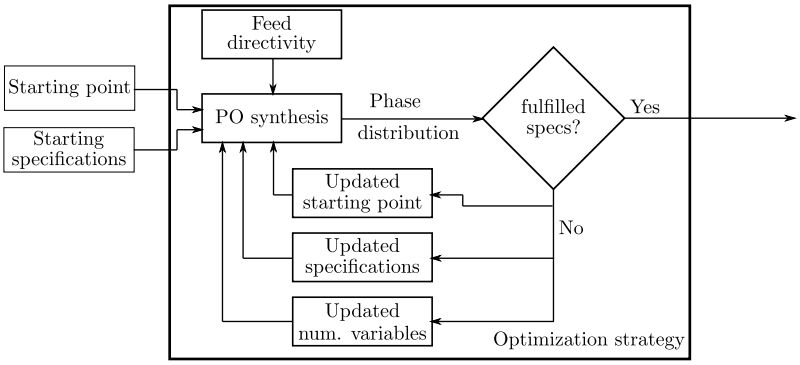

Figure 4.7: *Flowchart of the synthesis strategy followed to avoid non-desired local minima.*

4.2.3. Phase-only synthesis for 5G indoor femtocell coverage

The desired near-field pattern consists of three zones that cover the area of interest onto the desktop and its proximities. The coverage area defined in Figure 4.1 gives the mask requirements in the *yoz* plane shown in Figure 4.8. These specifications should be defined by two masks, corresponding to the maximum and minimum values of each

zone. Within the coverage area (Zone 1) the field should be as flat as possible, having a maximum difference between the maximum and minimum value of the field of 3 dB. Out of this area (Zone 3), the field should be 12 dB lower than the maximum of the coverage area. This value ensures radiating almost most of the power in the desired area and avoids possible interferences with other devices. A transition area (Zone 2) between the coverage and the external area is defined to obtain a smooth decay of the field to ensure a smooth transition between the two coverage zones.

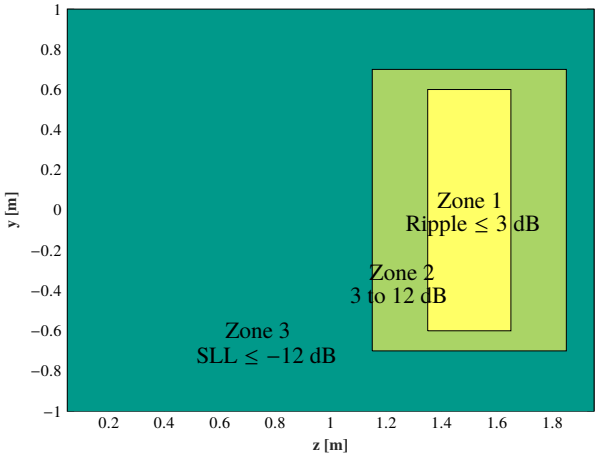

Figure 4.8: *Contoured areas wherein the ripple specifications must be satisfied in the yoz plane expressed in the reflectarray coordinates system.*

The starting point for the first synthesis stage at 28 GHz is the phase distribution of a pencil beam pointing to the center of the coverage ($z = 1.5, y = 0$) m. This phase distribution can be easily computed for either V- or H-pol as

$$\phi_{cell}(x_m, y_n) = k_0 \left(|\boldsymbol{r}_m| - (x_m \cos\varphi_0 + y_m \sin\varphi_0) \sin\theta_0 \right) \tag{4.1}$$

where k_0 is the wave number in vacuum, $\boldsymbol{r}_m$ is the vector from the phase center of the feed to the (m, n)th element defined in the reflectarray coordinate system and (θ_0, φ_0) the pointing direction of the antenna.

The phase distribution provided by (4.1) is evaluated at 28 GHz using a feed modeled as a $\cos^q\theta$ function with a q-factor of 20.56, which generates a similar illumination taper as the horn antenna NARDA 665-20. The obtained near-field pattern is shown in Figure 4.9 superimposed with the contoured mask of minimums for both polarizations. The generalized Intersection Approach is applied following the strategy previously described modifying the masks in each stage of the process to facilitate the convergence

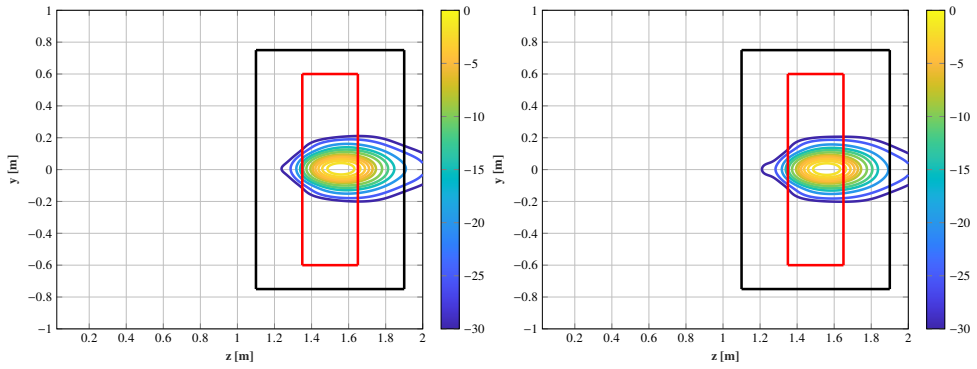

Figure 4.9: *Near-field pattern requirements and the focus pencil beam used as starting point (a) V-polarization (b) H-polarization.*

to a proper solution. The final phase distribution is shown in Figure 4.10. Note that, the solution of the synthesis is restricted to 260°, the same phase-shift achievable using the patch element. The updated solution of an iteration of the Levenberg-Marquardt algorithm (2.88) is now given by the following condition

$$\bar{\phi}_{i+1} = \begin{cases} \bar{\phi}_i + \delta_i, & \text{if} \qquad < 260^\circ \\ 260^\circ, & \text{otherwise} \end{cases} \tag{4.2}$$

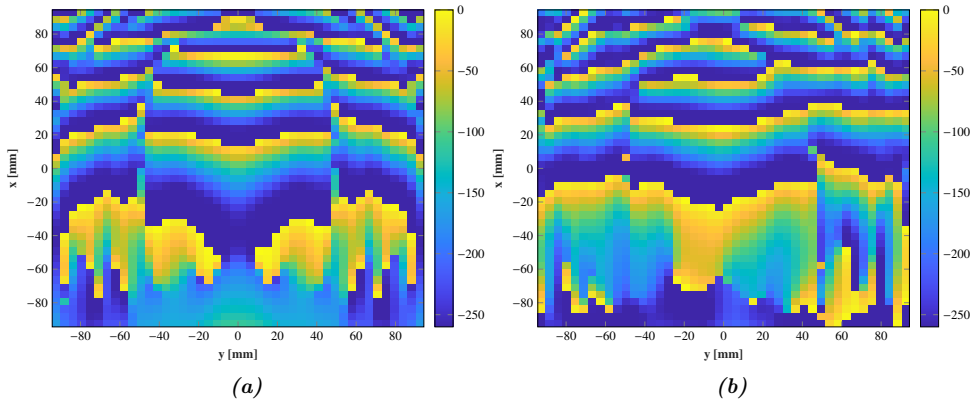

Figure 4.10: *Phase distribution of the reflection coefficients of the element along the reflectarray surface after the phase-only synthesis carried out with the generalized Intersection Approach at 28 GHz (a) V-polarization (b) H-polarization.*

The near-field pattern obtained after the synthesis process practically satisfies the mask requirements on the whole area and both polarizations. The near-field for the V-pol is shown in Figure 4.11 and the H-pol in Figure 4.12. These results are compared with the different zones of requirements, where it can be observed a wide coverage area of 0.36 m^2. Within this area, the field is significantly flat with variations lower than 3 dB on both polarizations. In the zone 3, the field should be 12 dB lower than the maximum of the coverage area. Both horizontal and vertical polarizations completely satisfy this requirement. The field within the transition area smoothly decays, as further you move from the coverage.

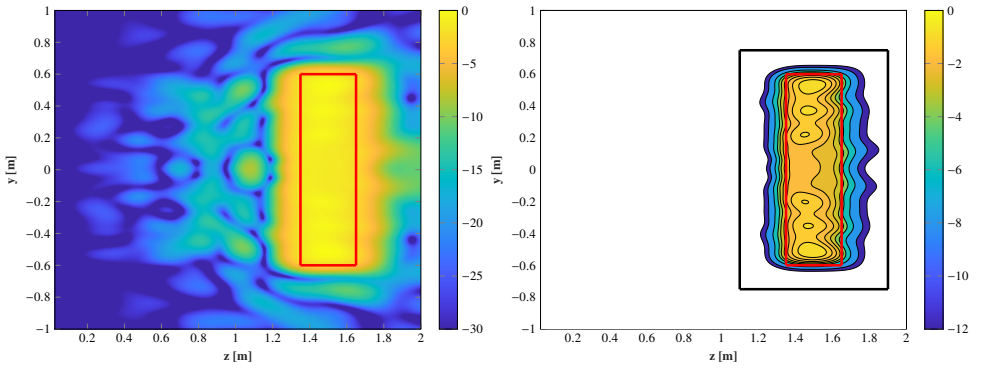

Figure 4.11: *Near-field pattern at the yoz coverage plane radiated by the synthesized phase distribution for V-polarization at* 28 *GHz (a) general and (b) detailed view.*

4.2.4. Synthesis for dual-polarization coverage

Once the synthesis process is finished and the phase distribution that satisfies the requirements is obtained, the dimensions of the elements are adjusted to produce the same response as the required phase distribution. In the designing the patch lengths are adjusted element by element using the MoM-LP and an optimization routine [2], as Figure 4.13 depicts.

In the element characterization, the real angle of incidence from the feed to each reflectarray element is used, improving the accuracy of the analysis facing possibles phase shifts due to the incidence angle. The MoM uses the Floquet theorem to analyze the unit cell, which embeds the element within an infinite array comprised of the same element, therefore considering local periodicity. This analysis enables to take into account mutual couplings between adjacent elements and the reflected field from

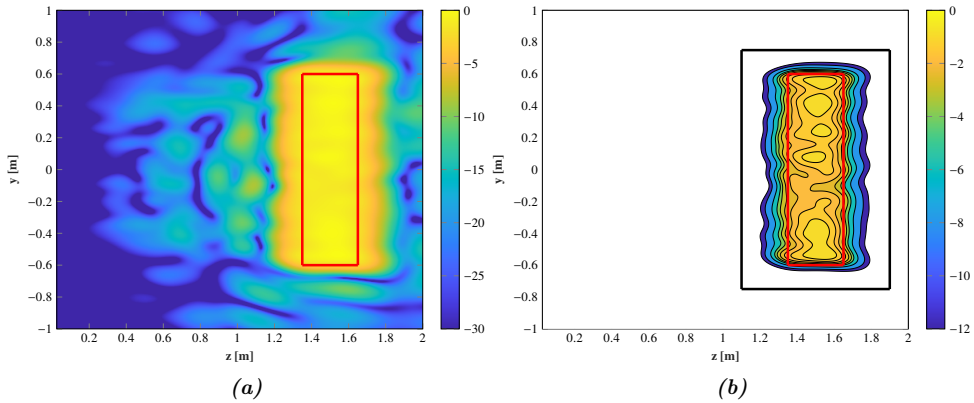

Figure 4.12: *Near-field pattern at the yoz coverage plane radiated by the synthesized phase distribution for H-polarization at 28 GHz.*

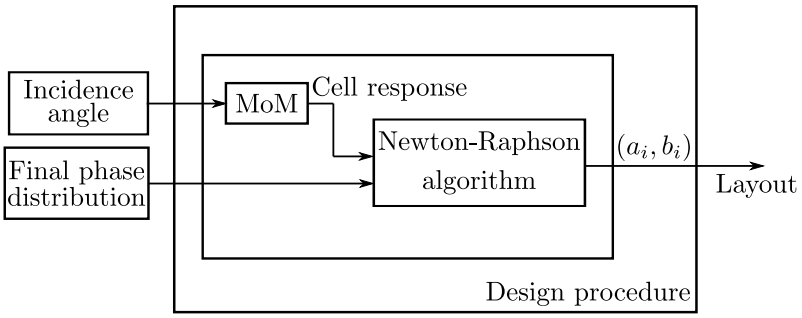

Figure 4.13: *Flowchart of the design strategy followed to obtain the reflectarray design.*

the ground plane. The technique defined in [2], an optimization technique based on the Newton-Raphson algorithm, is used to search the geometrical parameters of the element. The selected element produces the minimum error between the phase-shift of the element and the required phase distribution. This process is carried out element by element and the output is the layout of the reflectarray.

It is important to underline that the patch size variation along the reflectarray surface should be smooth enough to satisfy the local periodicity assumption of the analysis technique. Also, the design does not produce square patches but rectangular, since the reflection coefficients are to some extent different for the two linear polarizations, and the synthesized phase distribution may be slightly different in each polarization.

After applying this process to the phase distributions of Figure 4.10, the patch

dimensions of Figure 4.14 are obtained. In Figure 4.15 the difference between the phase-shift produce by each patch and the require phase-shift is evaluated. In both polarizations, the error is almost 0° with only a few elements with a maximum deviation is 6°.

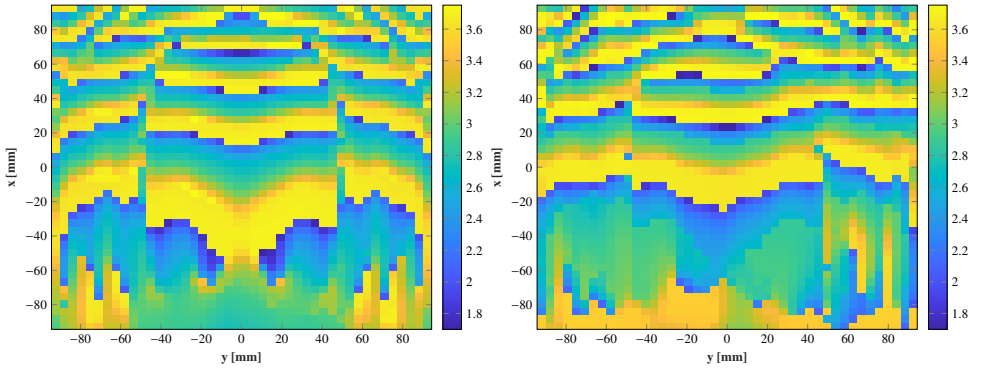

Figure 4.14: *Size of the patch elements to produce the phase-shift of Figure 4.10 (a) Dimensions a_i and (b) b_i of the patch .*

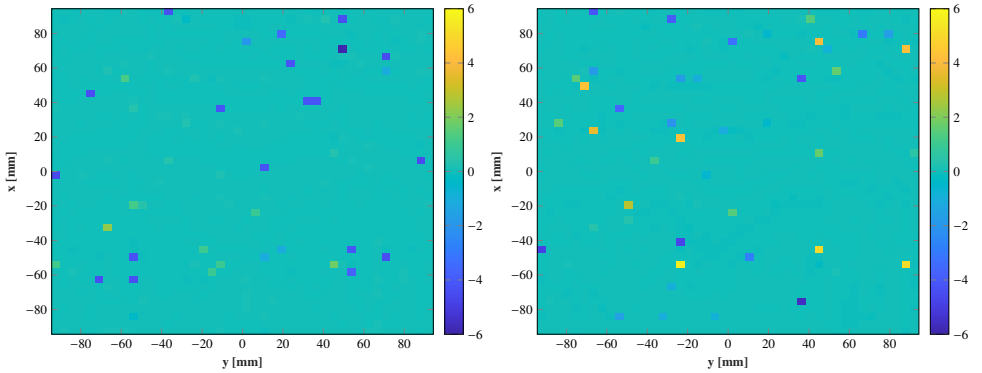

Figure 4.15: *Error produced on the adjustment of the phase-shift of the patches and the required phase-shift of Figure 4.10 (a) V-polarization and (b) H-polarization.*

4.2.5. Analysis of pattern performance in near-field

In Figure 4.16(a) the mask of the layout of the patch dimensions of Figure 4.14 are shown. The prototype is manufactured by a photo-etching technique obtaining the

reflectarray of Figure 4.16(b). The evaluation of the near-field pattern is carried out in two steps. First, the reflectarray antenna is placed in the near-field planar range of Universidad de Oviedo and it is assembled in an aluminum structure tilted 35°, in such a way that a xy plane is parallel to the probe aperture. The probe is an open-ended waveguide at Ka-band and the feed is the horn antenna NARDA 665-20 which phase center is adjusted to the position used in the synthesis process. Because of the dimensions of the facilities is not possible to reproduce the scenario defined. Therefore, the evaluation of the near-field pattern at the desired yoz coverage plane is carried out in two steps. First, the near-field is measured in a xy plane at a distance of 500 mm from the center of the reflectarray. This plane is perpendicular to the propagation direction, and it is large enough to guarantee that most of the radiated power is captured. Then, the near-field at the yoz used in the synthesis is obtained by carrying out a near-field to near-field (NF-NF) transformation using the software GRASP from TICRA [236].

4.2.5.1. Near-field pattern for V-polarization

The next Figure 4.17 shows the near-field pattern in the yoz plane after the NF-NF transformation at 28 GHz. The near-field is normalized to the maximum of the coverage area. It is compared the filled contour of the near-field pattern together with the mask requirements. In Figure 4.17(b) an error map is shown. This map evaluates the difference between the point out of requirements and the masks. More than an 88% is within the mask (white areas) and the mean error of the point out of the boundaries is 0.91 dB, being only a 0.34 dB in more than a 70% (colored areas). As observed in Figure 4.17(b) the majority of the errors are located on the corners of the masks. The use of an axial-symmetric feed makes it difficult to reach a total rectangular contour at the corners of the masks, increasing the errors in these areas. In Figure 4.18 different cut for constant z and y planes are compared with the simulations obtained in the previous subsection. The near-field pattern obtains a high fulfillment on the outer areas, totally satisfying the requirements on the outer Zone 3 and Zone 2 obtains a smooth decay of the field as Figure 4.17 and Figure 4.18 show.

4.2.5.2. Near-field pattern for H-polarization

In Figure 4.19 the filled contour of the near-field pattern is superimposed onto the masks at 28 GHz and the horizontal polarization. Also, it is evaluated the errors of the field points out of the boundaries. The compliance reaches 100% on Zone 3 and almost an 86% on the coverage area. This percentage is slightly lower than the results

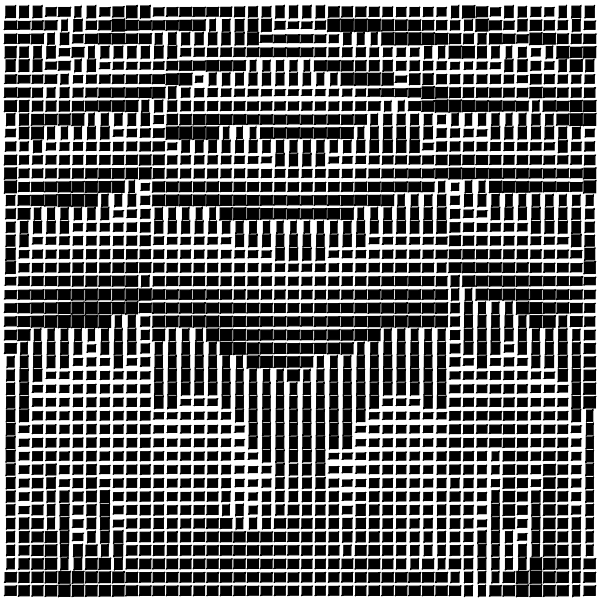

(a)

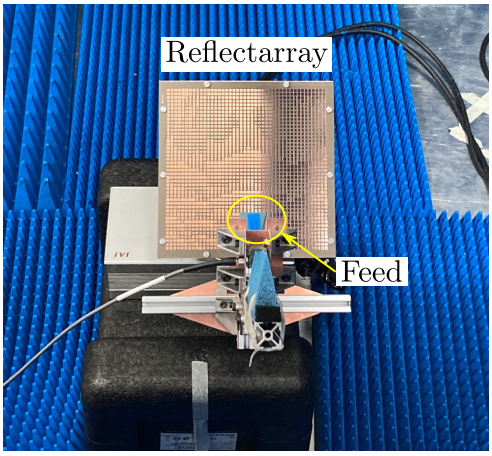

(b)

Figure 4.16: *(a) Mask of the layout used in the manufacture process of the reflectarray (b) Manufactured reflectarray in the near-field planar range of Universidad de Oviedo.*

of the vertical polarization. However, the mean error on the coverage is only a 0.46 dB. In this case, the corners are well-shaped, and the error is focused on particular areas of the coverage. This may be explained due to the projection of the field onto the *yoz* plane. The horizontal component of the field referred to as the reflectarray system is

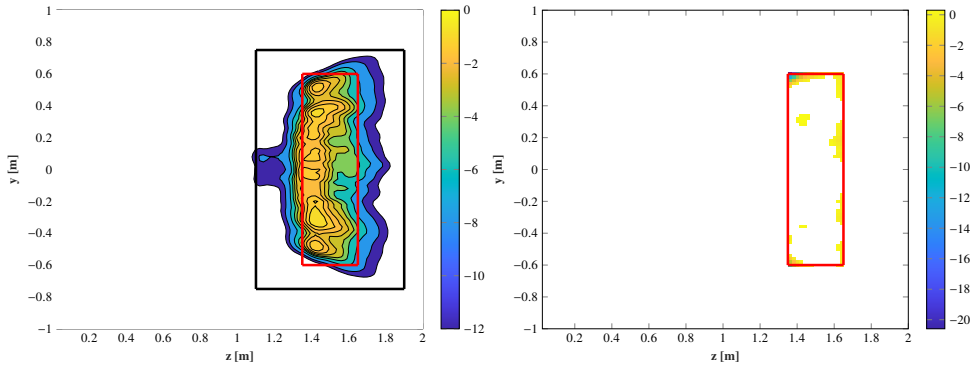

Figure 4.17: *(a) Normalized amplitude (dB) of the measured coverage area at* 28 *GHz (b) Error (dB) on the points out of the boundaries with respect to the maximum and minimum mask values for V-pol*

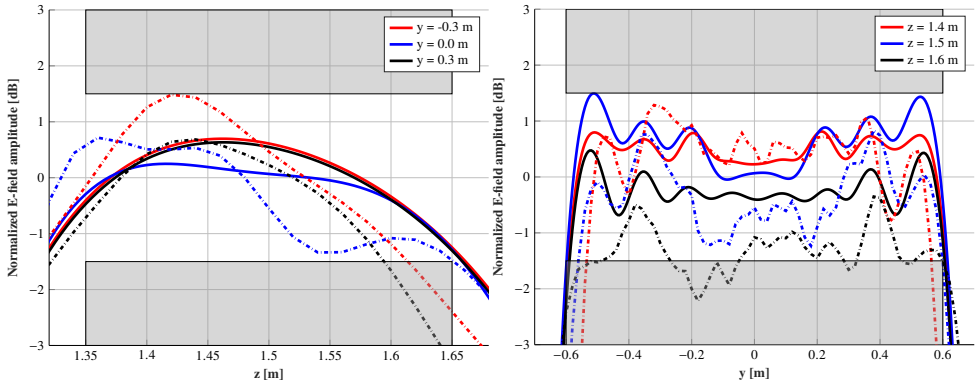

Figure 4.18: *Different cuts of the normalized amplitude of the measured coverage for (a) different y constant planes (b) different z constant planes. (Solid line) Measurements (Dotted line) Simulations at* 28 *GHz and V-pol.*

parallel to the *yoz* plane since the vertical is perpendicular. This fact may lead to a smoother behavior of the field as it can be observed on the cuts of Figure 4.20.

4.2.5.3. In-band response of the reflectarray

In this subsection, the in-band response performances are evaluated in a bandwidth of 4 GHz, from 26 to 30 GHz. In Figure 4.21 the near-field pattern at the extreme

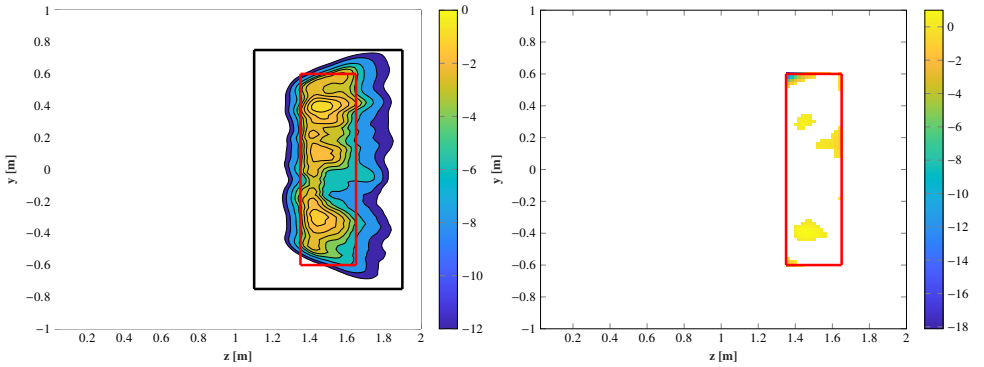

(a) *(b)*

Figure 4.19: *(a) Normalized amplitude (dB) of the measured coverage area at* 28 *GHz (b) Error (dB) on the points out of the boundaries with respect to the maximum and minimum mask values for H-pol.*

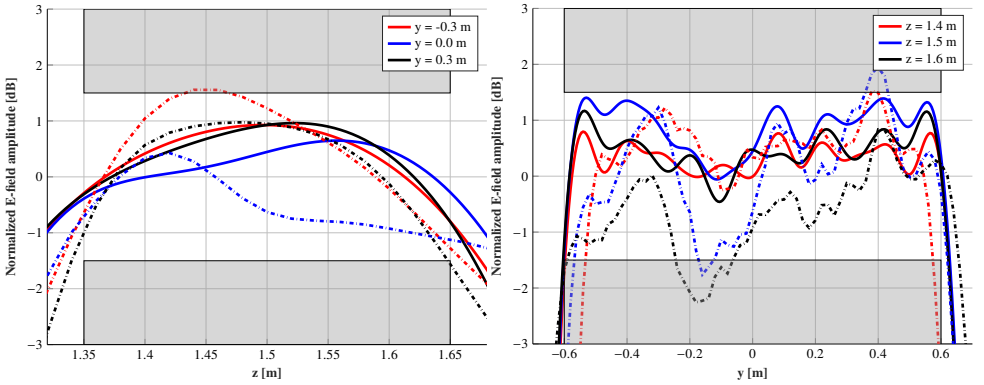

(a) *(b)*

Figure 4.20: *Different cuts of the normalized amplitude of the measured coverage for (a) different y constant planes (b) different z constant planes. (Solid line) Measurements (Dotted line) Simulations at* 28 *GHz and H-pol.*

frequencies is shown. A distortion of the field distribution is observed and therefore an increase of the ripple is found when shifting the frequency. It should be noted that the synthesis process and the design are carried out for a single frequency and the cell is a single-layer structure with a phase limitation of 260˚, thus it is quite challenged to obtain an in-band response. Even though, the percentage of compliance in the horizontal polarization in the worst case is more than a 70% and being an 85.4% at 29 GHz, as it is observed in Table 4.1. Once again, the horizontal polarization has a

better behavior than the vertical polarization, in which the compliance decreases to 52.7% in the worst case. In Zone 3, the field level is not increased and the majority of the near-field is 12 dB lower than the maximum.

Table 4.1: *Compliance of the near-field pattern measured for both polarization and several frequencies.*

	V-pol Requirements		H-pol Requirements	
Frequency (GHz)	Zone 1 3 dB ripple	Zone 3 SLL $\leq$ -12 dB	Zone 1 3 dB ripple	Zone 3 SLL $\leq$ -12 dB
26	64.2%	93.8%	77.1%	94.7%
27	67.1%	94.7%	71.2%	95.2%
28	92.3%	95.2%	87.3%	94.4%
29	69.6%	94.9%	85.4%	93.3%
30	52.7%	94.4%	75.3%	92.5%

4.3. Multi-feed dielectric-only transmitarray for shaped-pattern multi-zone 5G coverage

In this section, an SFA is designed to generate a multi-zone coverage at 28 GHz. Particularly, a transmitarray is proposed to act as a base station on an indoor scenario to generate multiple zones in an alternate polarization configuration, which enables to increase the capacity and performances of a single spot sector coverage. The technique described in Section 3.4 is applied to this transmitarray to generate multiples beams by increasing the number of feeds. Then, this technique is combined with the generalized Intersection Approach to enhance the performances of the spots. The solution of the generalized Intersection Approach is physically implemented with the dielectric-only cells described in Section 3.2, providing a low-cost and easy-manufactured solution that can be manufactured in additive manufacturing.

4.3.1. Scenario and antenna definition

In Figure 4.22 the scenario and the multi-zone coverage is depicted. The base station is composed of a transmitarray and a cluster of 5 horn antennas working in different

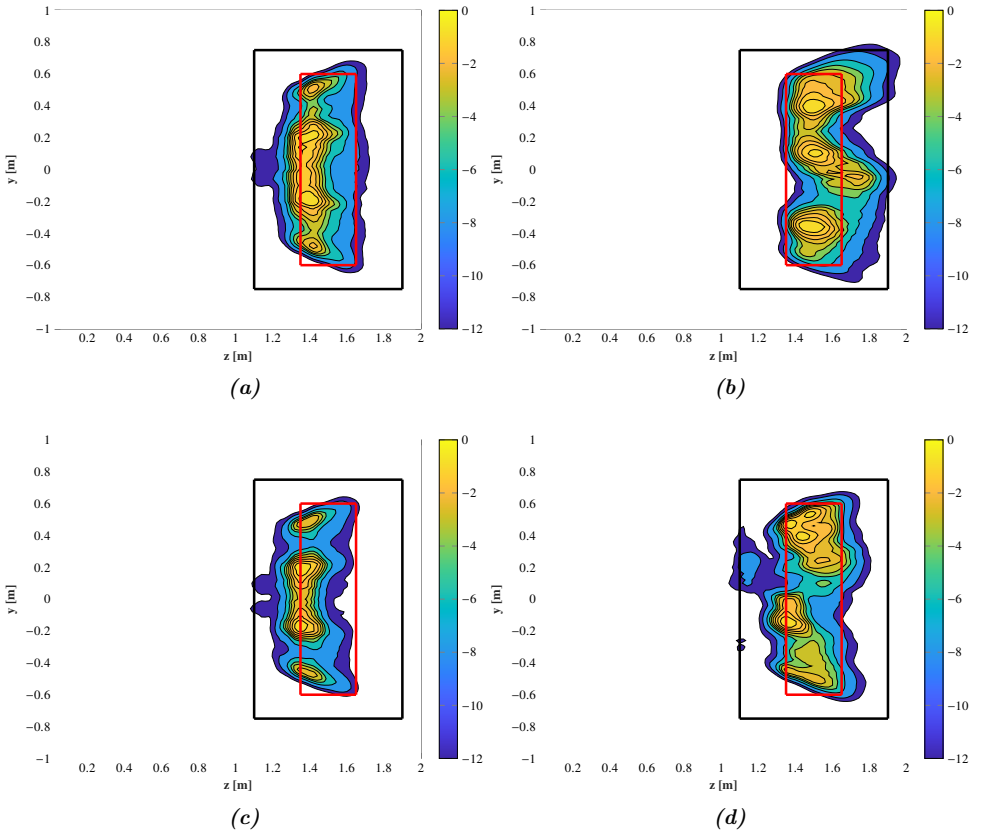

Figure 4.21: *Normalized amplitude of the measured coverage at the extreme frequencies: (a)* 26 *GHz V-pol (b)* 26 *GHz H-pol (c)* 30 *GHz V-pol and (d)* 30 *GHz H-pol* .

linear polarizations and distributed crosswise. The central horn antenna works in the linear polarization defined by the $\hat{\boldsymbol{y}}$-axis (Y-pol), while the 4 lateral horn antennas work in the polarization defined by the $\hat{\boldsymbol{x}}$-axis (X-pol). Therefore, the central spot is polarized in the orthogonal polarization of the other 4 adjacent spots. The coverage area of each spot is defined by the 3 dB decay of the near-field. The coverage of the spots should be wide enough that the external spots area overlapped with the central spot, ensuring a constant near-field power density in the two main planes of the coverage. This configuration may reach a wider area than using a single feed configuration. The interferences between adjacent spots are avoided due to the use of orthogonal codes for each channel. According to the transmitarray coordinates system, the multi-zone coverage is generated on a xy plane at a distance of $z = 1.80$

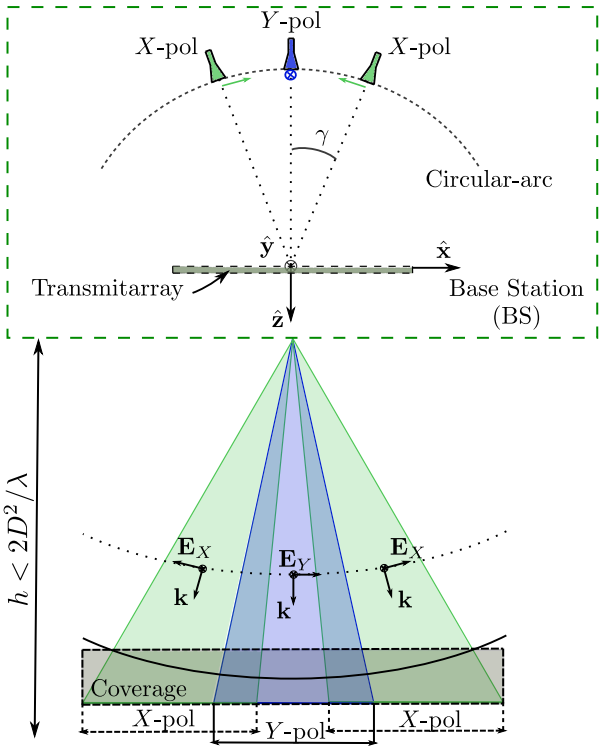

Figure 4.22: *Sketch of the cross-sectional view of the spatial distribution of the feeds in a circular arc path and the multi-zone coverage.*

m.

The transmitarray antenna is made up of 576 elements distributed in a regular grid of 24×24 cells of periodicity 5 mm in each direction. The side of the transmitarray is 120 mm and its equivalent aperture is 169.7 mm. The multi-zone coverage is defined at a distance of 1.8 m from the center of the transmitarray, therefore it is within the Fresnel region of the antenna. The focal distance (f) of the central feed is 100 mm with an f/D of 0.58 which provides a relatively compact structure. The feed is the horn antenna Flann 22240-15 of 15 dBi at 28 GHz and it works in Y-pol. The external feeds are the same horn antenna but working in X-pol at 28 GHz. These feeds are distributed in a 2D circular arc distributed in the main planes of the transmitarray antenna following the distribution

$$\begin{aligned}(\hat{\boldsymbol{x}}, \hat{\boldsymbol{y}}, \hat{\boldsymbol{z}}) &= (-r\sin\gamma, 0, -r\cos\gamma) \text{ for the } xoz \text{ cut} \\ (\hat{\boldsymbol{x}}, \hat{\boldsymbol{y}}, \hat{\boldsymbol{z}}) &= (0, -r\sin\gamma, -r\cos\gamma) \text{ for the } yoz \text{ cut}\end{aligned} \tag{4.3}$$

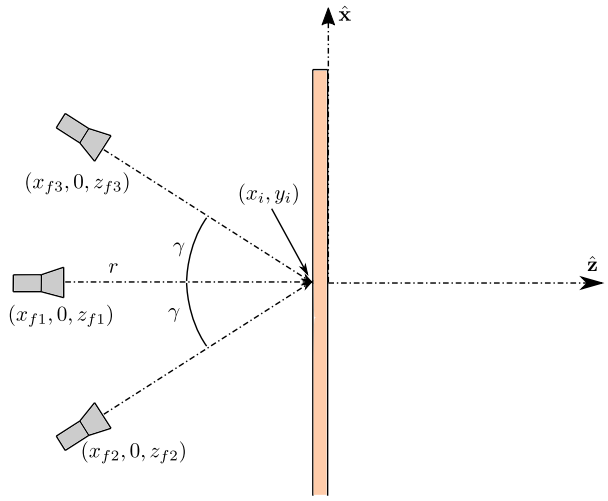

Figure 4.23: *Sketch of the cross sectional view of the spatial distribution of the feeds in the circular xoz arc path. The transmitarray coordinate system is on the outer surface.*

where r is the focal distance f and γ is the angular distribution between the central and an adjacent feed. In this case, γ is $\pm 15^{\circ}$. A further explanation of this equation can be found in Section 3.4 as well as an analysis of the proposed values of γ.

In Figure 4.23 a detailed view of the transmitarray and the horn antenna cluster is shown for the *xoz* plane. In Table 4.2 the position of the phase center of each horn antenna is outlined in accordance with (4.3). As it happens on Section 3.4 the whole cluster point to the center of the transmitarray ($(x_i, y_i) = (0, 0)$) in order to achieve similar amplitude tapers on the different incident fields. In Figure 4.24 the illumination taper at the main cuts is shown, observing a similar illumination lever with a slight shift on the maximum because of the projection of the field onto the transmitarray surface when the feed is displaced.

4.3.2. Near-field phase-only synthesis and transmitarray design

The desired near-field pattern is formed by 5 adjacent spots which are wide enough to achieve a constant field distribution in the main cuts ($x = 0$ and $y = 0$) of the multi-zone coverage. As well as the previous section, a phase-only synthesis with amplitude constraints on the near-field is carried out with the generalized Intersection Approach to obtain a phase distribution of the transmission coefficients that radiates the aimed near-field pattern. The output of the phase-only synthesis is the phase of the τ_{xx} or τ_{yy} of the transmission matrix $\boldsymbol{T}$. Once again, the design of the transmitarray is

Table 4.2: *Phase center placement of the horn antenna.*

	xoz plane			*yoz* plane		
γ (deg)	x (mm)	y (mm)	z (mm)	x (mm)	y (mm)	z (mm)
0°	0	0	0	0	0	0
15°	-25.88	0	-96.59	0	-25.88	-96.59
−15°	25.88	0	-96.59	0	25.88	-96.59

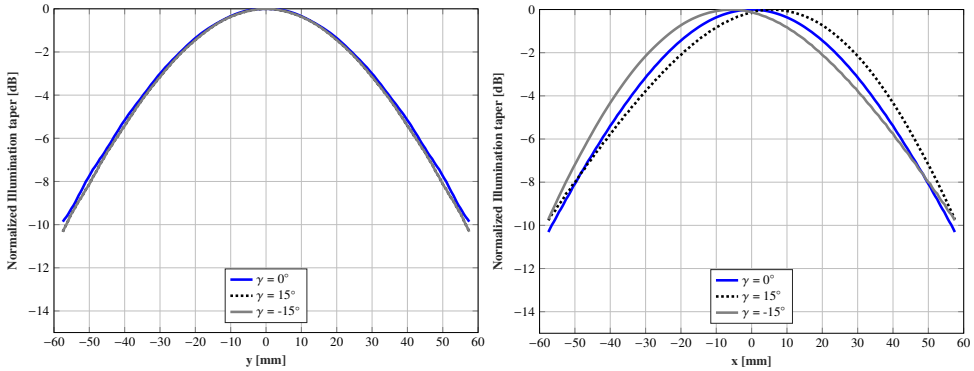

Figure 4.24: *Main cuts of the normalized illumination taper onto the transmitarray surface for the feeds placed on the xoz cut (a) $x = 0$ (b) $y = 0$.*

divided into two steps: the synthesis of the phase of the transmission coefficients and the design of the elements to implement those phase-shifts. The synthesis process is independent of the polarization, obtaining a phase distribution τ_{yy} for the Y-pol and τ_{xx} for the X-pol.

In this scenario, there is a single Y-pol spot whilst there are four different X-pol spots, one spot for each X-pol horn antenna. A feasible alternative to address the synthesis for the X-pol spots is to include a multi-target cost function in the generalized Intersection Approach, which means including four different d_M in the functional (2.73). This solution notably increases the complexity of the synthesis and its convergence to a proper solution. A novel alternative is proposed in this section to address the generation of multi-zone coverages using a multi-feed configuration without increasing the complexity of the phase-only synthesis. In Section 3.4 it was demonstrated that

feeding the antenna with a cluster or multi-feed configuration distributed in a circular arc path and pointing the feeds to the center of the transmitarray, allows achieving a multi-focusing solution on an angular range similar to the angular distribution of the feeds. This solution was applied to focus the near-field. However, if the central spot generates a circular spot instead of focusing the field, the use of feeds on this distribution would generate this circular spot in different angular positions according to the feed position. Therefore, if the phase-only synthesis is applied to obtain a phase distribution for the Y-pol and this solution is extended to the X-pol whose feeds are located according to (4.3), it would be feasible to reach the multi-zone coverage without increasing the complexity of the process.

In a second step, the design is carried out. The phase distribution is physically implemented by the dielectric-only cells described in Section 3.2, particularly the square prism cell which provides a similar response for both linear polarizations. In the designing process, the dimensions of the air gaps are adjusted to minimize the difference between their phase response and the required phase distribution using (3.22).

4.3.2.1. Pattern synthesis for a single spot

The phase-only synthesis aims to search a phase distribution that radiates a near-field according to the specifications of Figure 4.25. These specifications are only given for the central spot (blue circular line) and it must be widened to reach a 3 dB decay in a circular area of radius 400 mm equivalent to an angular range of 25°. This spot corresponds to the central horn antenna which is vertically polarized. The other four adjacent spots should be replicated according to the angular distribution of the feed, having spots at $\gamma = \pm 15°$ in the main planes.

The starting point is a phase distribution of a pencil beam transmitarray pointing in boresight direction ($\theta_0 = 0°, \varphi_0 = 0°$). This phase distribution is computed with (4.1) and its radiated near-field is evaluated at 28 GHz feeding the antenna with the real incident field of the five Flann 22240-15 horn antennas. The 3 dB contour of the five spots is shown in Figure 4.25 along with the mask requirements. The starting point does not reach a uniform amplitude field distribution but shows that it is possible to collimate the spots in nearly the desired angular distribution of ±15°.

The generalized Intersection Approach is applied following the process outlined in Figure 4.7, using tighter requirements in each step. Since the transmitarray size is electrically small ($11.2\lambda \times 11.2\lambda$) it is not necessary to change the directivity of the feed to artificially decrease the transmitarray size. Therefore, the real incident field of the Flann 22240-15 horn antenna is used in the whole process. After the synthesis process the phase distribution of Figure 4.26 is obtained for the Y-pol, which radiates the

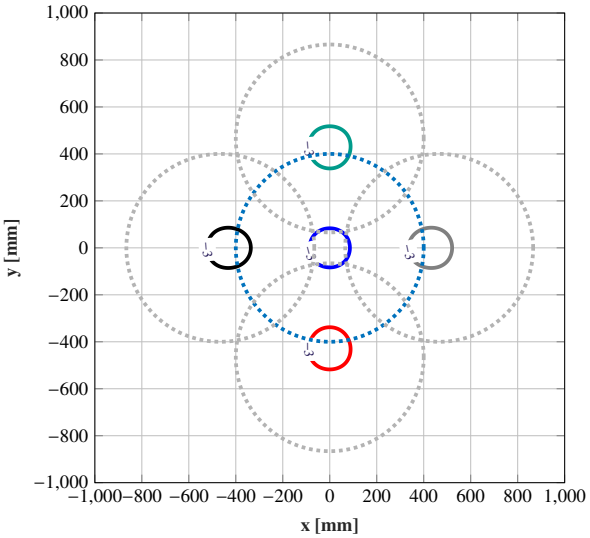

Figure 4.25: *Whole coverage area obtained with the phase distribution computed with* (4.1) *for pencil beam transmitarray antennas and feeding it with the* 5 *horn antennas at* 28 *GHz. The solid black, red, grey and green lines represent the adjacent spot for* X*-pol, while the solid blue line represents the central* Y*-pol spot. The dotted grey lines limit the requirement for the 3 dB decay of each spot.*

near-field of Figure 4.27 . This near-field pattern satisfies the specifications given for the central spot, increasing its size a 457%. Now, this phase distribution is extended to the X-pol and the near-field is evaluated feeding the transmitarray with the cluster working in both polarizations. In Figure 4.28 the 3 dB contour is superimposed with the masks for the 5 spots generated. The different spots are evaluated onto the xy plane parallel to the antenna aperture at a distance of 1.8 m, observing that the lateral spots are shifted following the desired distribution in each main plane. The X-pol spots present a certain distortion not reaching a perfect uniform amplitude distribution within the desired circular area as the central spot.

This effect can be explained since the phase-only synthesis adjusts the phase introduced by the transmitarray elements to obtain a phase on the transmitted field that produces the desired shaped beam in the pointing direction. Then, if the feed is moved from the transmitarray focus, the incident field on the transmitarray surfaces changes, both amplitude, and phase. If the feed position is properly chosen to ensure that the new amplitude of the incident field is similar to the amplitude when the feed is in the transmitarray focus, only the phase of the incident field would change. In this phase, two different effects are combined. First, it is produced a progressive phase on the

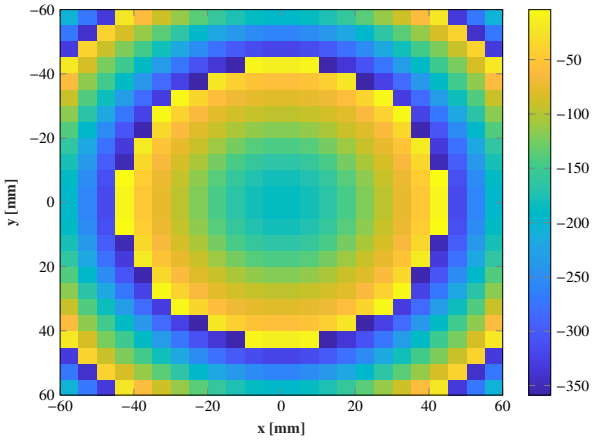

Figure 4.26: *Phase distribution of the Y-pol obtained after the optimization process carried out with the generalized Intersection Approach at 28 GHz.*

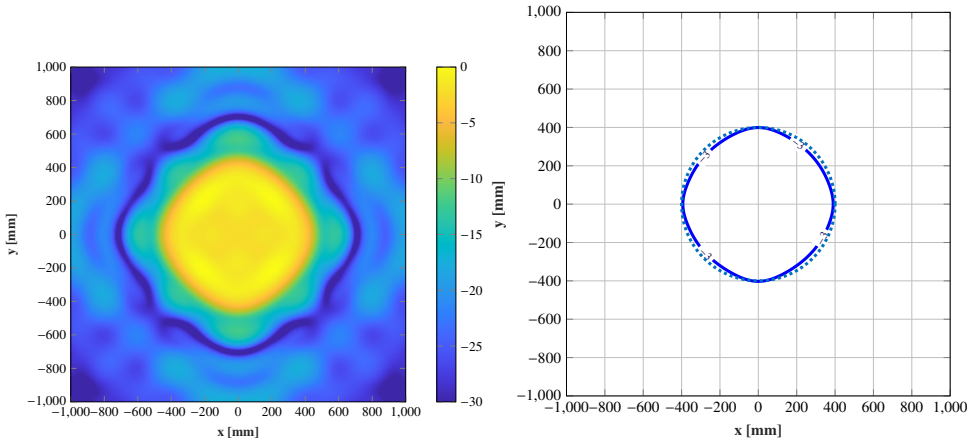

Figure 4.27: *(a) Near-field obtained after applying the generalized Intersection Approach for the central spot at 28 GHz and Y-pol. (b) (blue solid line) 3 dB contour of the central spot after the synthesize (blue dotted line) 3 dB contour requirement for the central spot.*

transmitarray surface about the original illumination due to the displacement of the feed and its pointing direction. Second, the feed radiates a spherical wavefront whilst a pure progressive phase on the transmitarray surface is only reachable whether the incident field is a plane wavefront. Hence, the progressive phase on the transmitarray surface is distorted. Assuming that the cells behave as an ideal phase-shifter (the cell

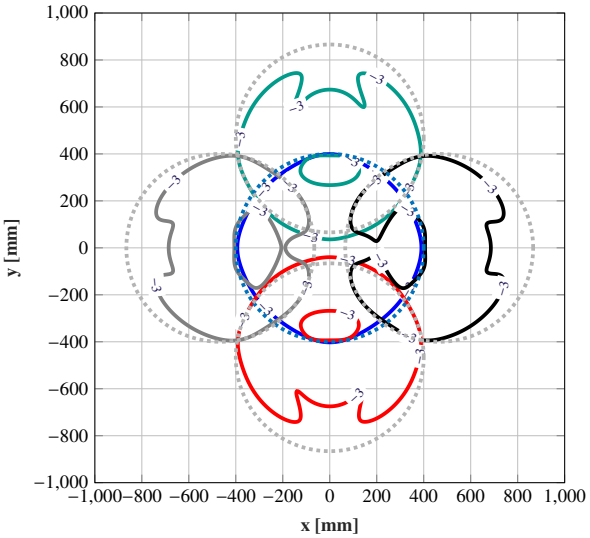

Figure 4.28: *Whole coverage area obtained with the phase distribution of Figure 4.26 and feeding it with the* 5 *horn antennas at* 28 *GHz. The solid black, red, grey and green lines represent the adjacent spot for X-pol, while the solid blue line represents the central Y-pol spot. The dotted grey lines limit the requirement for the 3 dB decay of each spot.*

response does not depend on the incidence angle), the distortion of the progressive phase produces a change in the phase of the transmitted field modifying the shape of the radiated pattern. This effect is minimized in focused or pencil beams since both are more robust than shaped spots or beams, and only slight degradations on the directivity or SLL levels are observed.

4.3.2.2. Design of the transmitarray

The phase distribution of Figure 4.26 is used to carried out a design based on a dielectric-only solution. In this case, the phase distribution is physically implemented by the square prism cells with an embedded square prism air gap (Figure 3.5, Section 3.2). The phase response of this cell is similar to both polarizations, therefore the phase distribution of Y-pol is also applied to X-pol. In the design the dimensions of the air gap (W and L) are adjusted to control the infill of the cell, thus the phase response due to the variation on the dielectric effective constant of the element. The process is carried out element by element, considering a local periodic environment and the real incidence angle according to (3.21). The chosen cell is the one that minimizes the error between its response and the required of Figure 4.26, as (3.22)

defines. After this process the layout of Figure 4.29 is obtained, obtaining the error shown in Figure 4.30. This error is the difference between the implementation phase and the desired one on each cell.

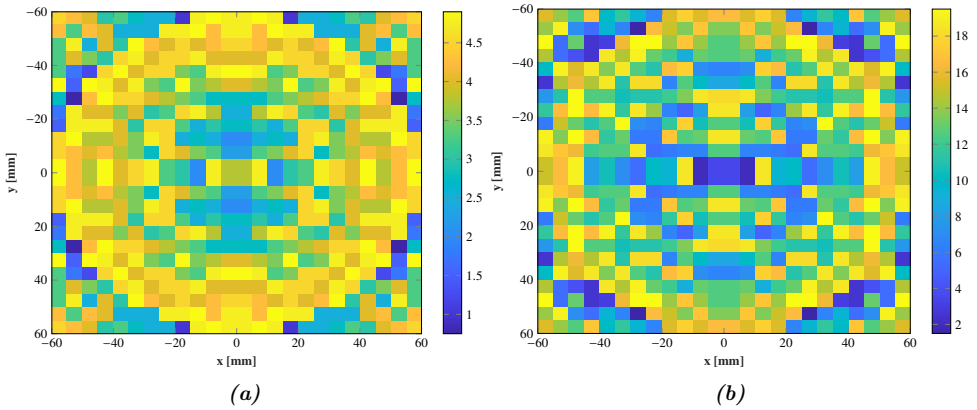

Figure 4.29: *Dimension of the air gaps selected for the layout based on square prism dielectric cells (a) W (mm) (b) L (mm).*

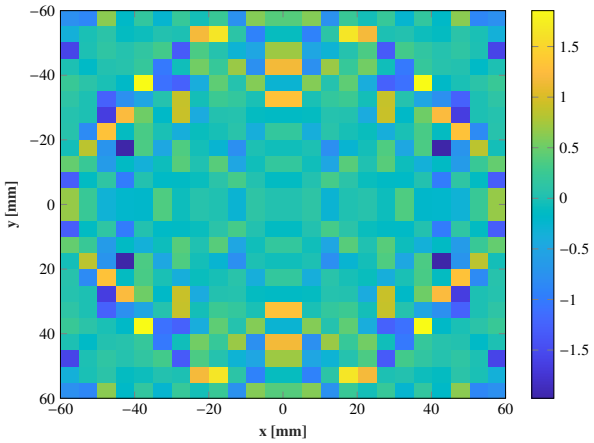

Figure 4.30: *Error (deg) produced on the adjustement of the phase-shift of the dielectric cells and the required phase distribution of Figure 4.26.*

4.3.3. Manufacture and test of the transmitarray

The transmitarray is manufactured using the additive manufacturing technique of FDM and polylactic acid PLA as dielectric, as the dielectric lenses manufactured in

Chapter 3. The 3D printer Ultimaker 3 is set to print with the same resolution as previous cases; a wall thickness of 0.8 mm, a layer height of 0.1 mm, and a 100% of infill. This configuration obtains successful results on transmitarrays or dielectric lens based on these types of cells. The prototype is shown in Figure 4.31(a) during the manufacturing process.

Then, the near-field radiated by this antenna is evaluated in the near-field planar range of Universidad de Oviedo in the setup shown in Figure 4.31(b). The feeding antenna is the Flann 22240-15 horn antenna used in the synthesis and the near-field probe is a Ka-band open-ended waveguide. Since it is not feasible to make use of 5 Flann 22240-15 horn antennas, a PLA structure is design to adjust a single horn antenna to the 5 positions defined in Table 4.2. The dimensions of the near-field planar range are limited to 1.5 m, thus it is not possible to directly measured the multi-zone coverage. Once again, the near-field at the distance of interest is obtained in two steps. A plane parallel to the antenna aperture in a regular grid of 120×120 mm^2 at 100 mm is measured. This plane ensures to measure almost all the radiated power to carry out a NF-NF transformation using GRASP from TICRA. This process is repeated to each feed position changing the feed polarization from horizontal to vertical on the external positions.

The near-field spots are calculated on xy plane and the results are shown in Figure 4.32. These results show a quite good agreement with simulations. The central spot behaves as expected with a total width of 700 mm, practically satisfying the specifications. The lateral spots are distorted such as happened on simulations. Even so, the spots have a total size of more than 550 mm for a 3 dB decay of the field and a total size of more than 1.2 m in the main cuts of the coverage. The difference in the size and shape of the spots between simulations and measurements are mainly due to the design is carried out considering the central spot and the lateral horn antennas change their angle of incidence concerning the central one. Also, in the phase-only synthesis, the element is modeled as an ideal phase-shifter, considering it as a lossless element. However, these elements could have significant high losses because of the dielectric material, affecting the near-field pattern.

The near-field synthesis was carried out on a single plane at a distance of 1.8 m. However, the closest planes should present a similar near-field pattern. The 3 dB contour of different planes is evaluated to observe the near-field pattern not on a single plane but a volume. These results are shown in Figure 4.33. For simplicity, it is only presented the central and lateral spot corresponding to $\gamma = -15^\circ$ in the y-direction. The near-field is evaluated on a volume of 350 mm (1.65, 1.8 and 2 m) wherein the spots keep their pattern, showing a very uniform distribution through the propagation

(a)

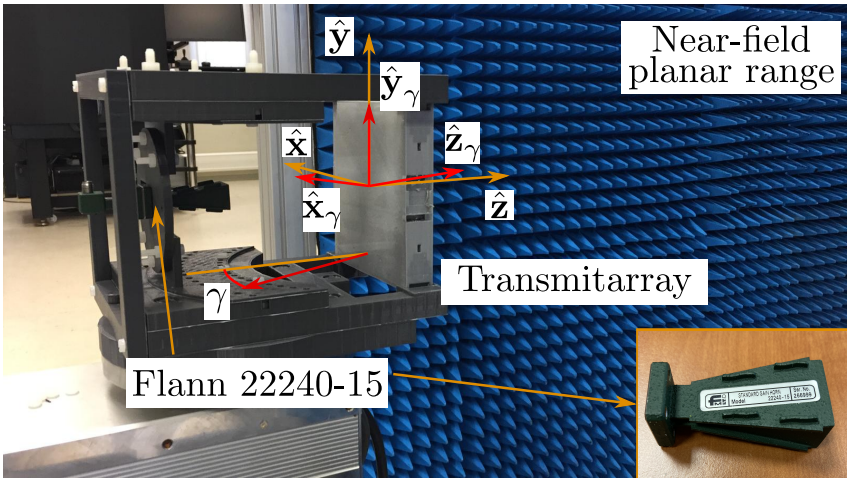

(b)

Figure 4.31: *(a) Prototype during its manufacturing process in the Ultimaker 3 (b) Setup at the near-field planar acquisition range in the Universidad de Oviedo.*

direction $\hat{z}$.

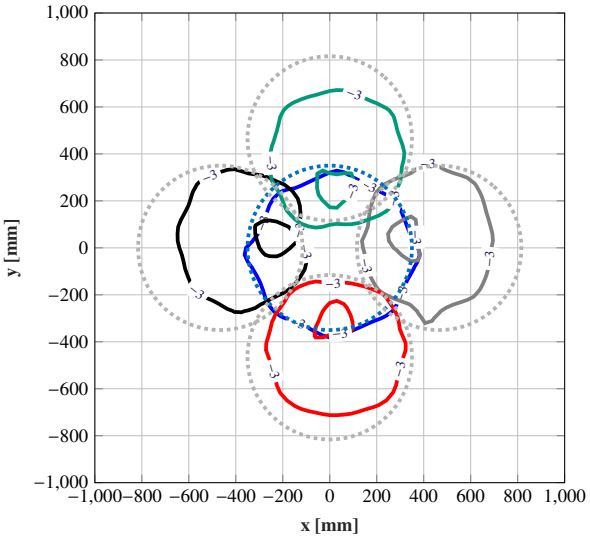

Figure 4.32: *3 dB contour of the whole coverage area obtained after the measurements and the NF-NF transformation feeding the transmitarray with the* 5 *horn antennas at* 28 *GHz. The solid black, red, grey, and green lines represent the adjacent spot for X-pol, while the solid blue line represents the central Y-pol spot. The dotted grey lines limit the requirement for the 3 dB decay of each spot.*

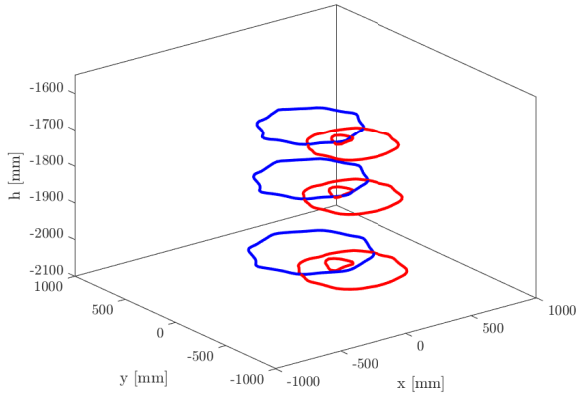

Figure 4.33: *3 dB contour of two spots obtained after the measurements and the NF-NF transformation feeding the transmitarray with the central and one adjacent horn antenna at* 28 *GHz for different heights.*

4.4. Synthesis of a transmitarray for complex and large uniform indoor coverage

In previous sections, it has been demonstrated the efficiency of the generalized Intersection Approach to shape the near-field magnitude of different spatially-fed arrays.

The algorithm was used to obtain coverage on different planes according to certain specifications. In Section 4.2 the near-field amplitude of a reflectarray is synthesized to reach a coverage of 1.2×0.4 mm^2 on a yz plane, while in Section 4.3 it is synthesized to obtain a multi-spot coverage on different xy plane perpendicular to the propagation direction $\hat{\boldsymbol{k}}$.

The different syntheses have been carried out following the strategy detailed in Figure 4.7. Different syntheses are concatenated tightening the requirements but improving the starting point in each new synthesis. The Intersection Approach is a local search algorithm, therefore these new starting points are closer to the goal and the convergence is easier. However, this strategy is endangered by its specifications.

Traditionally, the mask is defined according to the field specifications required on the application. In indoor communications, the interest is to reach a uniform field distribution within a given area by controlling the amplitude ripple or the slopes. A first synthesis could include laxer ripples, a shorter coverage area, or both combined. Then, in consecutive syntheses, the specifications are gradually tightened until finding the desired solutions. Although this strategy works in most cases, it is important to bear in mind that some of the requirements depend on the antenna optics such as the gain or the area wherein the field can be shaped are limited by the antenna aperture. Hence, the specifications always must take these limitations into account to find a solution that can be physically reached by the antenna, otherwise, the algorithm will diverge.

Conversely, it can exist limitations because of the inherent characteristics of electromagnetic waves. It is not the same to synthesize a plane perpendicular to the propagation direction that a plane defined through the propagation direction. Let us assume coverage in a yz plane, being z the propagation direction. The maximum distance on the y-direction is given by the antenna aperture and its projection on the coverage plane, while the maximum range in the z-direction cannot be predicted. Similarly, some issues may appear when the coverage is not defined in a canonical shape. A priori, in these types of scenarios it is hard to define an initial specification compromising the convergence of the synthesis.

In this section, the generalized Intersection Approach algorithm is evolved by the use of adaptive masks on the synthesis process is detailed. Instead of starting from laxer requirements, the mask is defined according to the field pattern. This technique is based on the understanding that the field is similar to a smooth and continuous function, therefore the mask should follow these statements. This fact avoids defining physically infeasible masks with abrupt field changes in complex scenarios. This strategy is particularly useful when synthesizing the field pattern towards the propagation

direction or the near-field phase as it will be seen in Chapter 5. To better understand this concept, a transmitarray antenna based on ideal phase-shifters is synthesized at 39 GHz to obtain a large coverage in a complex scenario defined towards the propagation direction.

4.4.1. Definition of the scenario and the coverage requirements

In Figure 4.34 the scenario proposed to evaluate this novel technique is depicted. The scenario described the circular corridor of the Edificio Polivalente of Universidad de Oviedo. The aim is to generate coverage in the circular corridor using as few antennas as possible at 39 GHz. A feasible configuration of four antennas placed in the positions described in Figure 4.34 (ANT1, ANT2, ANT3, and ANT4). Each antenna must radiate a different coverage that fits with its angular range inside the building.

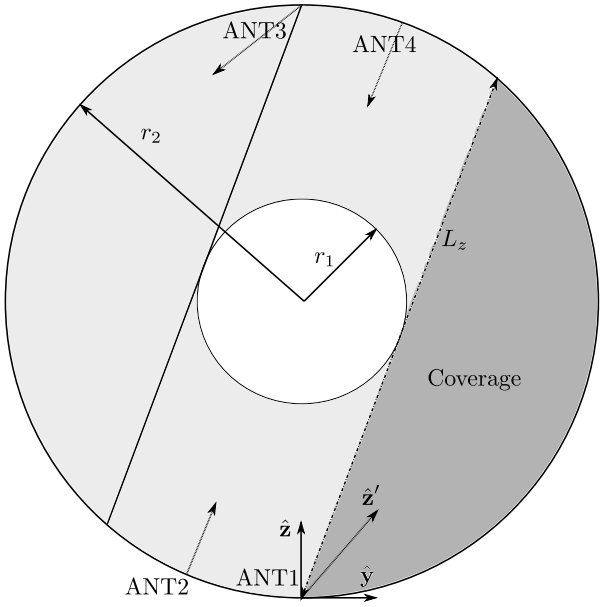

Figure 4.34: *Depicted scenario of the indoor coverage.*

This section is focused on ANT1 and ANT3 since those coverages are the ones with the highest complexity because of their dimensions. The building is modeled as an annulus of radius r_1 and r_2, and the coverage must be radiated only within these two limits. The antenna ANT1 radiates the coverage in the $\hat{\boldsymbol{z}}'$ direction on a yz plane parallel to the floor. As it was seen in the previous section, the planes before and after the synthesized plane are also affected by the improvement, therefore the plane considered in this optimization is defined at a height of 1.5 m ($\hat{\boldsymbol{x}}$ direction), wherein

most of the devices may be found. The synthesis goal is to reach a uniform field distribution within a range larger than 14 m (L_z) on the $\hat{\boldsymbol{z}}'$ direction and adjusted to the variable width of the annulus. It is important to underline that there is an inherent difference in the relative field levels at the closest and furthest point because of the propagation. The synthesis would try to mitigate this effect while the field is also widened in the transverse direction.

4.4.2. Antenna optics

The antenna proposed for this coverage is a transmitarray made up of 1936 elements distributed on a regular grid of periodicity 2.5×2.5 mm^2. The side of the transmitarray is 107.5 mm and the antenna aperture is 152 mm. The transmitarray is fed on a centered configuration with a focal length (f) of 68.5 mm, thus an F/D of 0.45, providing a very compact structure to easily integrate it in the building. The feed is the horn antenna Flann 22240-15 operating on vertical linear polarization (V-pol) or X polarization according to the system shown in Figure 4.34 at 39 GHz.

4.4.3. Near-field phase-only synthesis using adaptive amplitude masks

In this synthesis two different starting points are evaluated: a far- and near-field focused tranmitarray. Both transmitarray antennas are pointing to $(-1.5, 5.25, 5.5)$ m (according to the $(\hat{\boldsymbol{x}}, \hat{\boldsymbol{y}}, \hat{\boldsymbol{z}})$ defined in Figure 4.34) which are the center of the coordinate system. The phase distribution of the far-field tranmitarray is computed with (4.1) and shown in Figure 4.35(a), while in the near-field case (3.32) is generalized for an arbitrary (x, y, z) point as

$$\phi_{cell}(m,n) = -\frac{2\pi}{\lambda}\left(\sqrt{(f_x - x)^2 + (f_y - y)^2 + (fz)^2} - \phi_{inc}(m,n)\right) \tag{4.4}$$

where (m, n) are the coordinates of the (m, n)-th element considering the origin of the coordinates system at the center of the transmitarray; $\phi_{inc}(m, n)$ is the incident field at the (m, n)-th element, and (f_x, f_y, f_z) are the coordinates of the focal point referred to the center of the transmitarray. The resulting phase is shown in Figure 4.35(b).

In Figure 4.36 the near-field radiated by each phase distribution is evaluated onto the coverage area. Although both near-field distributions are very similar the near-field focused transmitarray provides a better starting point for the synthesis since its shape fills better the coverage, Figure 4.36(b). This near-field is computed considering a $\cos^q$ as a feed with a q-factor of 7. In the light of these results, it is quite complex

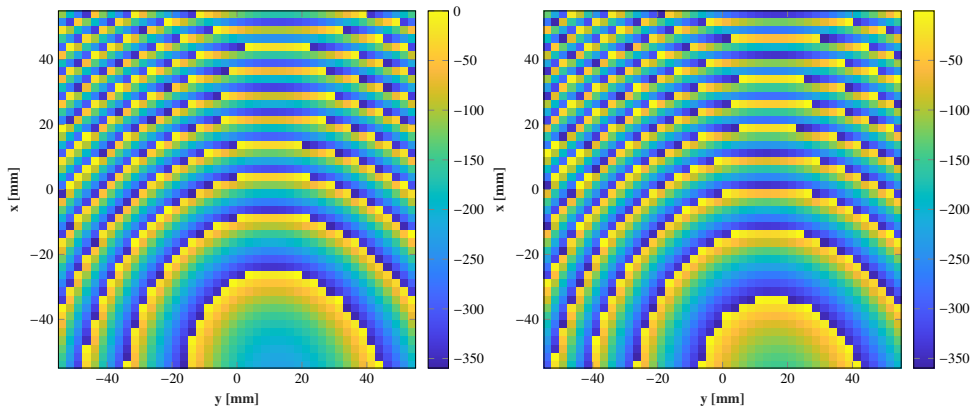

Figure 4.35: *Phase distribution of the X-pol obtained for a (a) far-field and (b) near-field focused transmitarray at* 39 *GHz.*

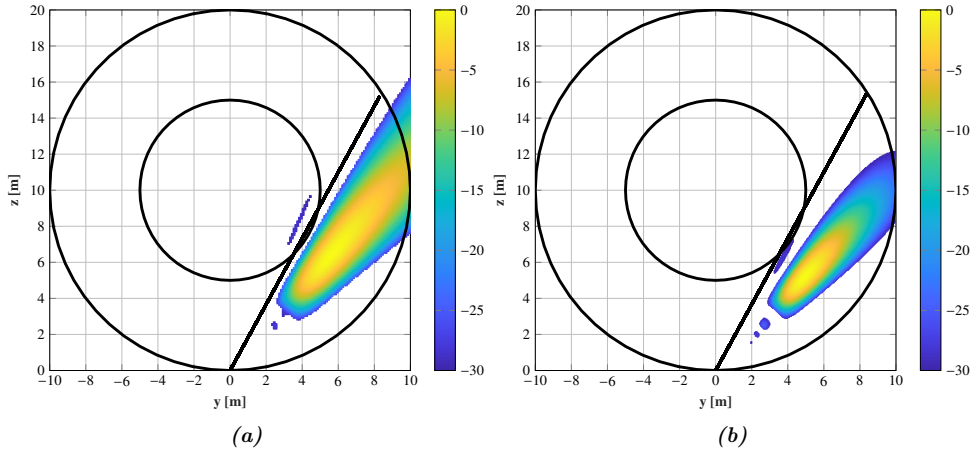

Figure 4.36: *Near-field pattern radiated by the two different phase distribution (a) Far-field focused transmitarray (b) Near-field focused transmitarray at* 39 *GHz.*

to establish the initial mask of requirements. The largest dimension of the coverage is more than 15 meters and there is a difference between relative near-field levels of more than 30 dB in the whole coverage. Here, the use of adaptive masks to the field shape instead of the requirements can ensure to reach a solution that is physically achievable from the antenna.

To explain the definition of these adaptive masks, we take the field of Figure 4.36(b) as reference. This field presents a maximum in a given area and from this point, the

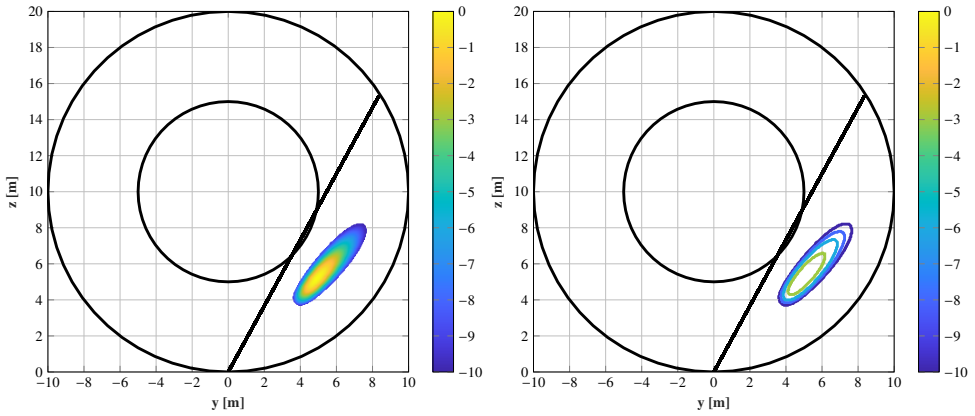

Figure 4.37: *(a)Normalized amplitude (dB) of the near-field within the footprint of the mask (b) Different contoured areas of the adaptive mask for the starting point of the synthesis (dB) at* 39 *GHz.*

field starts to decay in all the directions but different slopes. If the masks are used to modify the slopes, thus the decay of the field, according to the final goal, the synthesis will search for a solution closer to the starting point than defining arbitrary masks only based on the requirements. In Figure 4.37 the contour of the starting point is shown superimposed to the footprint of the coverage. A feasible definition of the mask is outlined in Table 4.3, which leads to the mask shown in Figure 4.37(b). The main difference with other masks is that the limit of each contour is imposed by the field decay, enabling the synthesis to widen the field considering the field pattern in each direction. In each new synthesis, the output near-field defines the new mask requirements, always ensuring that the smooth behavior of the field is preserved. Note that, the $-\infty$ is implemented with a really low value in the mask, typically -140 dB, and the mask of maximums is used to control the SLL avoiding radiations on undesired direction or areas.

4.4.4. Intermediate results of the near-field pattern: evolution of the coverage and masks

After several concatenated syntheses the near-field of Figure 4.38 is obtained. This near-field has been widened following the different decays of the field in each direction. This near-field pattern is almost the same as Figure 4.36 but with different slopes. Once again, the contour of this near-field (Figure 4.39(a)) is used to define the mask

Table 4.3: *Definition of the mask levels regarding the magnitude of the near-field.*

Field contour (dB)	Mask Min. (dB)	Mask Max. (dB)
$-3 \leq \|E\| \leq 0$	-1	0
$-6 \leq \|E\| < -3$	-3	0
$-8 \leq \|E\| < -6$	-6	0
$-10 \leq \|E\| < -8$	-8	0
$-12 \leq \|E\| < -10$	-10	0
$\|E\| \leq -12$	$-\infty$	0

of Figure 4.39(b) used in the next synthesis. The mask is used in the whole synthesis, and it is only modified at the beginning of a new synthesis. In Figure 4.40 it is shown the output near-field after several syntheses of Figure 4.38. It can be observed that the field is widened according to its pattern and considering its natural shape in each direction. This solution significantly improves the initial point filling an important area of the coverage. This near-field defines the next mask, which is shown in Figure 4.41(b).

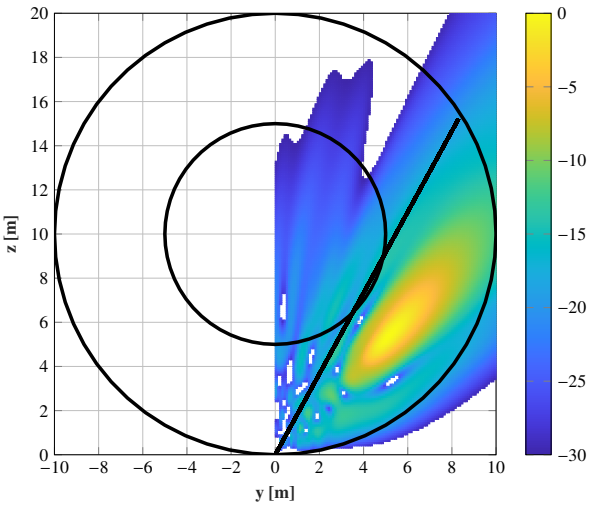

Figure 4.38: *Normalized amplitude (dB) of the near-field after a synthesis using adaptive masks at* 39 *GHz.*

This mask takes into account minimums of the field that can appear in singular areas such as it happens at $(y = 4.3, z = 5)$ m the near-field presents a lower value

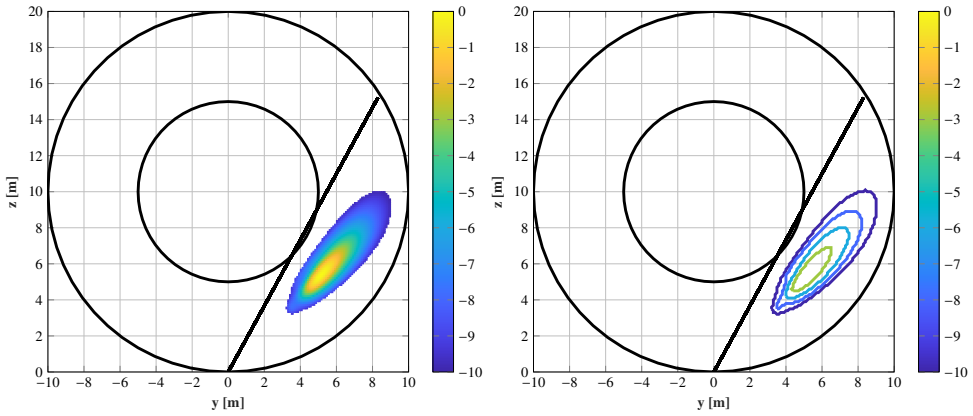

Figure 4.39: *(a)Normalized amplitude (dB) of the near-field within the footprint of the mask (b) Different contoured areas of the adaptive mask for the starting point of the next synthesis (dB) at* 39 *GHz.*

than the adjacent values which level is 2 or 3 dB higher. In this area, the algorithm would try to increase the field level to a value closer to the current field than to its adjacent points. This fact enables the field a gradual increase instead of imposing a condition that the field may not reach. In addition, this gradual change enhances the convergence of the synthesis.

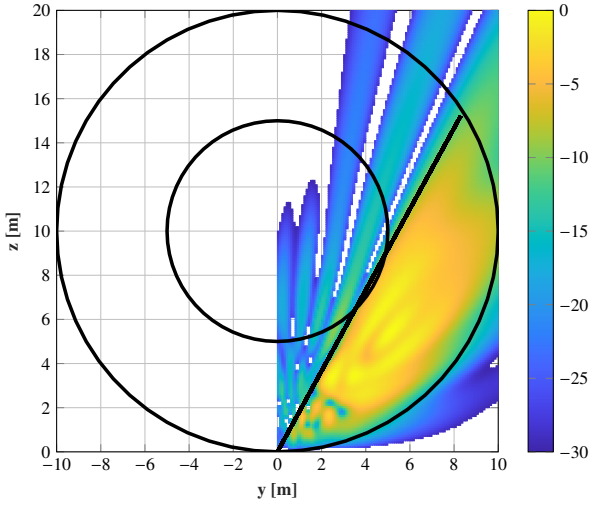

Figure 4.40: *Normalized amplitude (dB) of the near-field after several syntheses using adaptive masks at* 39 *GHz.*

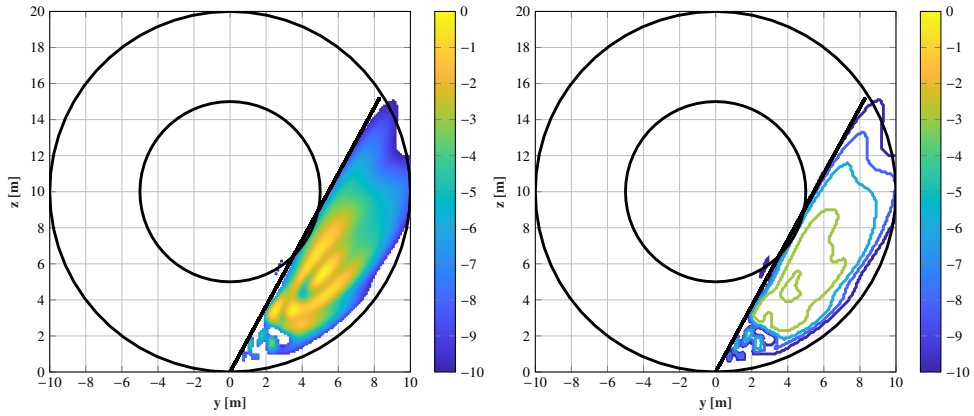

Figure 4.41: *(a)Normalized amplitude (dB) of the near-field within the footprint of the mask (b) Different contoured areas of the adaptive mask for the starting point of the next synthesis (dB) at 39 GHz.*

4.4.5. Final step in the synthesis process

After 27 phase-only syntheses using this adaptive mask technique the phase distribution of Figure 4.42 and the near-field of Figure 4.43 are obtained. This near-field is computed considering the real incident field of the horn antenna Flann 22240-15, which replaced the $\cos^q$ function after 16 iterations. The final near-field reaches a very uniform distribution along the desired area, reducing the relative field levels from more than 30 dB to almost 5 dB within a range of 14 m. In the nearest area to the antenna ($z < 3$ m and $y < 2$ m), the coverage is not properly covered, having a lack of coverage within this area. It may be expected since the starting point does not have a significant level in the area, therefore the adaptive mask does not impose specifications in this range. Two effects can be observed here. First, the starting point is a near-field focused transmitarray whose field pattern presents a deep fluctuation in the area before the maximum, obtaining a hardly shaped field. Second, this mask may be combined with imposing particular requirements in certain areas to enhance the control on the field pattern such as avoiding radiation in certain directions or the SLL level.

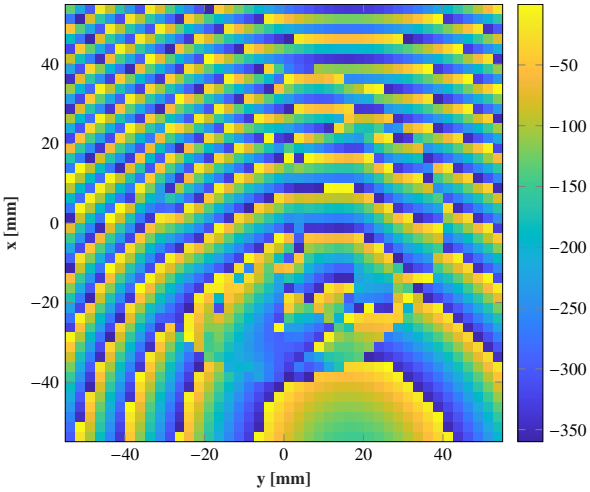

Figure 4.42: *Phase distribution (deg) after the optimization process carried out with the generalized Intersection Approach at* 39 *GHz.*

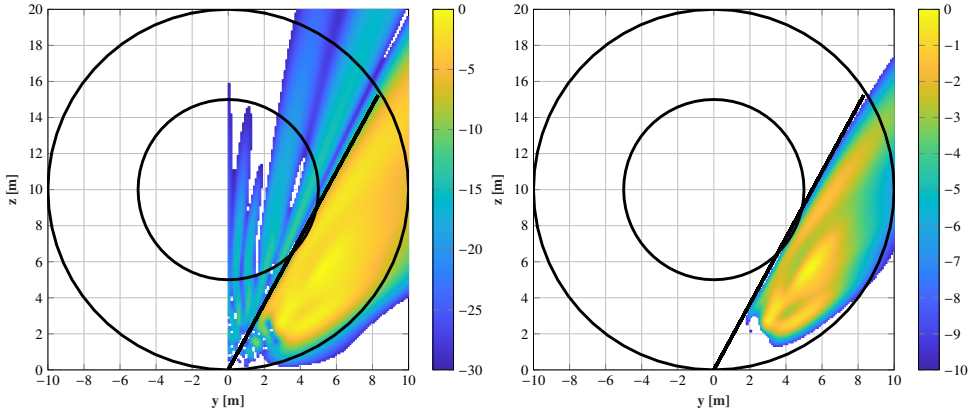

Figure 4.43: *Normalized amplitude (dB) of the near-field after the whole optimization process using the horn antenna Flann 22240-15 as feed. (a) Full and (b) Detailed range at* 39 *GHz.*

4.5. Conclusions

In the first section, the generalized Intersection Approach for near-field has been used to synthesized two spatially-fed arrays, a reflectarray and a transmitarray, to obtain a near-field pattern with amplitude constraints for 5G indoor communications. After the

phase-only synthesis, the reflectarray is designed using a single layer of printed patches that provide an ultra-thin low-profile antenna at the cost of having a maximum phase-shift range of 260°. The reflectarray must radiate a rectangular-shaped pattern on a plane to generate coverage at a central frequency of 28 GHz. Since the patches can control two linear polarizations, the coverage is generated in dual-linear polarization with similar performances. The measurements of the prototype are compared with the near-field obtained in simulations, showing a good agreement between both. Also, the compliance of the requirements is significantly high for both polarizations. These results validate both, the analysis and design technique described in Chapter 2 as well as the use of reflectarray antennas to generate complex-shaped beam patterns.

The second section aims to reach a large coverage within the Fresnel region of the spatially-fed array, particularly a transmitarray at 28 GHz. To increase the dimensions of the coverage area and the capacity of the indoor base station, the coverage is divided into different spots working at the same frequency but different polarizations following the idea presented in Chapter 3. In this case, there are 5 spots generated by 5 different horn antennas generating a multi-zone coverage. Moreover, the central spot works in vertical linear polarization while the other 4 spots on horizontal linear polarization, which avoids near-field interference on the coverage. Once again, the transmitarray is designed with dielectric-only elements. The idea presented in Chapter 3 shows good results on the generation of multiple focused beams, in this section, the same idea is evaluated for multiple shaped near-field beams, since the central spot performance is improved by a phase-only synthesis carried out with the generalized Intersection Approach. After the optimization, the central spot increases its size a 457%, and ideally the other 4 spots should be also improved. However, in the adjacent spots appear a distortion concerning the central spot. This distortion may be appeared due to the progressive phase on the transmitarray surface generated by the feed displacement is also affected by the spherical wavefront radiated by the own feed. This fact distorts the incident progressive phase, thus the transmitted and the near-field too. This effect does not appear in Chapter 3 since focused and pencil beams are more robust. Despite having this unexpected distortion, the total coverage is 1.4 meters in the main planes of the multi-zone coverage. The measurements of the transmitarray highly agree with simulations, obtaining similar spots with similar distortions. The slight difference between simulations and measurements is mainly due to the amplitude response of the cell which is not considered on the phase-only synthesis, as well as the phase response of the cell under oblique incidence.

In the last section, it is presented a novel approach to define the templates when dealing with amplitude constraints within a large area. The synthesis of a transmit-

array antenna, considering ideal phase-shifters, has been carried out to demonstrate that this approach together with the generalized Intersection Approach for near-field is a feasible solution to synthesize the near-field in a plane defined along the propagation direction. Hence, the adaptive mask is an important and useful technique for large complex-shaped patterns and for those patterns that are not easily associated with the antenna optics. As it can be observed in the example, the combination of both techniques achieves a uniform power density over more than 14 meters with a complex shape.

An overall conclusion of this chapter is that the generalized Intersection Approach is a powerful approach to synthesis spatially-fed arrays with amplitude constraints in the radiated near-field. Although this approach does not implement the FFT on the projectors, and the use of an optimization algorithm such as the LM algorithm decreases the efficiency, this approach overcomes the limitation of only synthesizing planes parallel to the antenna aperture, providing a general solution for obtaining complex near-field pattern radiated by spatially-fed arrays.

CHAPTER 5

Demonstration of a reflectarray as a Compact Antenna Test Range probe in mm-Wave frequency band

5.1. Introduction

Throughout Chapter 4, the current issues related to 5G or different wireless communications have been addressed from the point of view of the antenna. However, the development of suitable antennas to satisfy these new technological challenges has inherently entailed the necessity of evolving the antenna measurement systems to validate the designs. Owing to the high number of devices that are expected to be developed in 5G or beyond 5G, measurement Over-The-Air (OTA) systems must be simple, cheap, and compact.

The classical division of antenna measurement systems encompasses far-field ranges (FF-range), near-field scanning range (NF-range), or CATR. A far-field range is characterized by placing the antenna under test (AUT) in the far-field region of the probe, which enables the measurement of the AUT radiation pattern directly. The main drawback of these systems concerns the physical distance between the AUT and the probe to reach the far-field region. It depends on the frequency and the antenna aperture, but these systems typically require large distances and they are a bulky solution.

A NF-range notably reduces the system dimensions since the near-field of the AUT is evaluated instead of the far-field. In this case, the AUT is located within the near-field region of the probe, which provides more compact structures than a FF-range. However, it is not possible to obtain the radiation pattern directly. After measuring the near-field of the AUT it is needed a post-processing stage to carry out a near-field

to far-field (NF-FF) transformation to get the field value. This operation demands a large amount of data, typically the 3D pattern acquisition in dual-polarization, which increases the time of measurements and requires a highly stable system through the whole measurement process.

It is likely that the most popular solution nowadays is a Compact Antenna Test Range. These systems are an attractive alternative to FF- and NF-ranges since they combine the major advantages of both. CATR provides a solution that measures the radiation pattern directly, without carrying out a NF-FF transformation, but placing the AUT within the near-field range of the probe. This is possible due to the existence of an area or volume called the quiet zone (QZ). This QZ is defined as an area within the Fresnel region of the probe wherein the field behaves like a uniform plane wave, which emulates far-field conditions. In addition, since the AUT is placed within the near-field region of the probe, the dimensions can be significantly reduced concerning a FF-range.

As it was stated throughout the different chapters of this thesis, most of the applications related to current and future wireless communications are doing their best on developing efficient systems at (sub)millimeter frequency bands. Particularly, 5G communications in the FR2 frequencies centered in 28 and 39 GHz as well as space communications or other applications such as automotive radars at higher frequencies (e.g., automotive radars at 77 GHz). Going up to these frequencies on antenna measurement systems is not a technological challenge. The true interest arises in the development of new measurement systems with the capacity of performing a fast evaluation of the antenna performance (directivity, pointing direction, operational bandwidth, sidelobe levels, etc) without having a fixed, expensive, and bulky facility to evaluate them. This means developing portable antenna measurement systems which can be carried or deployed in an area of interest such as a laboratory or a manufacturing line. These antenna measurement systems must provide performance similar to a fixed facility to achieve an accurate characterization of the antenna or devices.

Different alternatives have appeared throughout last years [237–239], but most of them require post-processing to finally get the radiation pattern. However, there is a potential alternative that avoids this post-processing stage. A device or antenna testing carried out following the standard OTA ideally aims to characterize the antenna system performance at an infinity distance without a direct connection between the device under test (DUT) and probe. Hence, performing the test in far-field conditions. If the evaluation is performed on devices such as base stations or user terminals at FR2 or higher frequencies, far-field conditions imply a significant electrical and physical distance between the device and the probe. This distance inherently leads to high

free-space attenuation and receiving a significantly attenuated signal. A potential alternative is the development of an SFA antenna that can generate a uniform plane wave. This uniform plane wave emulates far-field conditions, and it thus can be used to evaluate the antenna performances. Moreover, if the uniform plane wave is created near to the aperture, the system would be compact enough to be considered as a portable antenna measuring system, which also decreases the free-space attenuation as well as increases the received power.

In this chapter, the generalized Intersection Approach for near-field is used to synthesize a reflectarray antenna to generate a uniform plane wave over a volume at a close distance. To achieve that, the near-field requirement must be imposed on both amplitude and phase of the radiated near-field, which notably increases the complexity of the synthesis process. First, the phase-only synthesis is carried out to obtain the uniform plane wave for a single linear polarization and the results are validated with a prototype. Then, this technique is applied to extend the design to a dual linear polarization, using a cell of dipoles that allows the control of the two polarizations in a single layer reflectarray. Finally, the first reflectarray is integrated on a homemade CATR setup to measure different antenna patterns in Ka-band. The setup is based on a basic mechanical and control system that validates the concept of a reflectarray-based CATR on a portable and compact structure.

5.2. Review of Compact Antenna Test Range

CATR operational principle is based on a feed, typically a horn antenna, which radiates an impinging wave onto the surface of a parabolic reflector antenna. The reflector collimates the field into a certain direction wherein the quiet zone may be found (see Figure 5.1(a)). The quiet zone is obtained because of the geometrical shape of the parabolic reflector, which produces a plane wave on its reflected field. Then, the uniformity of this plane wave depends on the illumination taper of the incident field onto the reflector surface. Hence, the dimensions of the QZ are associated with the antenna aperture and the illumination taper.

There are two inherent drawbacks to CATR as portable or easily integrated measurement systems. First, the QZ is enhanced by using a large ratio f/D. The larger the focal distance f the lower the illumination taper, at the price of having bulkier structures. Second, lower values of f reduce the system dimensions but increase the illumination taper limiting the QZ size. This last effect can be minimized using a dedicated low directivity feed. However, these feeds increase the field level at the reflector edges and therefore the edge diffraction is increased. The diffraction can

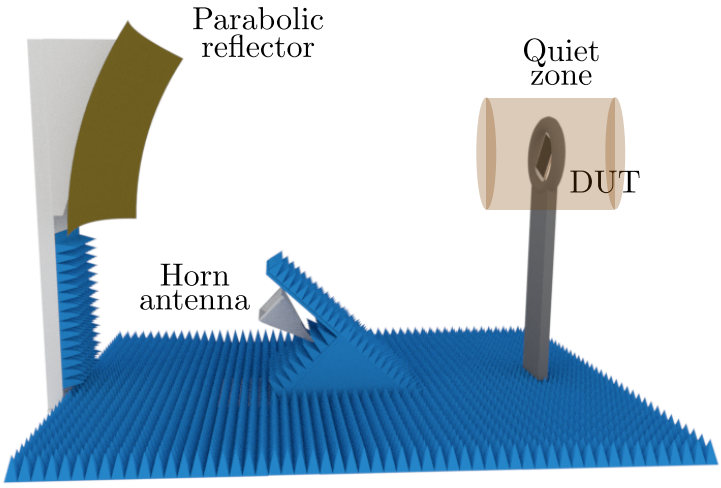

(a)

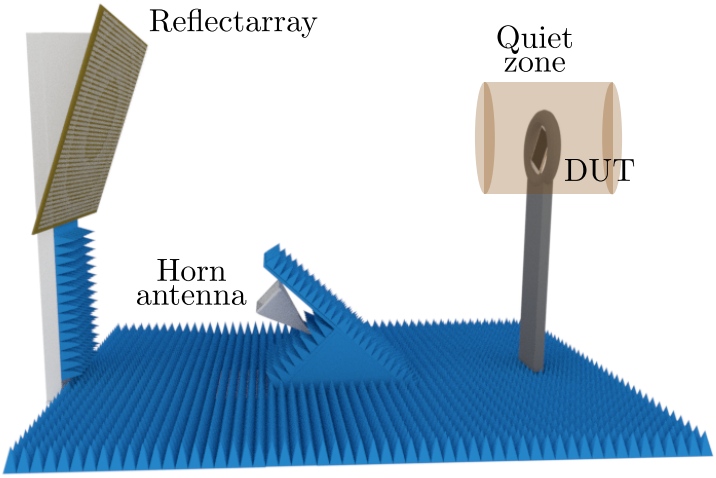

(b)

Figure 5.1: *Sketch of a Compact Antenna Test Range based on a (a) parabolic reflector antenna (b) reflectarray antenna..*

be reduced by using different techniques such as serrated edges or complex geometries in the parabolic reflector surface, which increases the cost and complexity of the manufacturing process.

Different published works have overcome these drawbacks by replacing the parabolic reflector with other antennas. In [240] and [241] a CATR based on a dielectric lens was presented as an alternative. However, the accuracy on the lens surface was not enough to obtain successful results. In [242] a planar hologram is proposed as a low-cost and easy manufacturing solution. The accuracy requirements on a hologram surface are less tight than on a reflector or lens antenna. Also, this hologram-based CATR has demonstrated quite good performances on the measurement of antenna patterns, even when it is compared with a planar near-field scanning range at (sub)millimeter bands [243,244]. However, this concept was developed for a fixed facility. The hologram dimension is more than 1 meter with a large f/D to obtain a very low illumination taper.

In the last years, there is an increasing interest in the development of plane wave generators (PWG) since they are presented as a potential alternative to obtain a uniform plane wave. A PWG is defined as an antenna array that radiates a uniform plane wave over a volume at a close distance. Therefore, it enables far-field conditions to test the devices at a reduced distance minimizing the free-space attenuation and receiving the maximum power from the DUT. Most of the published works are based on preliminary studies using different arrays configurations to obtain the plane wave [207, 208, 245]. In [207], an operational demonstrator of a dual-polarized PWG at millimeter-wave frequencies has been presented, especially in the FR2 band. The proposed PWG reaches a suitable QZ for measuring 5G new radio devices in a relatively compact system. However, the solutions based on arrays require the design of a feeding network, in this case, a beam-forming network, to properly control the excitation on the array elements which increases the complexity of the design.

A natural alternative to parabolic reflectors is reflectarray antennas. This alternative is a low-cost and low-profile solution based on a planar structure and printed elements. This concept was presented in [246] and later in [206]. However, as it occurs with reflector antennas the QZ size is limited by both aperture and illumination taper. An important advantage of a reflectarray over a reflector antenna is that the geometry of the reflectarray elements controls the reflected field performances. Hence, a proper design of the reflectarray elements could overcome or minimize this issue. A sketch of a CATR based on a reflectarray antenna is depicted in Figure 5.1(b).

5.3. Single-linear-polarization Plane Wave Generator based on a reflectarray at mm-Wave

In this section, the capabilities of a reflectarray antenna are evaluated in the generation of a uniform plane wave in a close area to the antenna. The reflectarray works in single

linear polarization at 28 GHz.

5.3.1. Antenna and uniform plane wave characteristics

5.3.1.1. Reflectarray optics

A square reflectarray made up of 44×44 elements is used to generate the uniform plane wave. These 1936 elements are distributed on a regular grid of periodicity 4.29×4.29 mm^2 in the x- and y- direction as Figure 5.2 depicts. The reflectarray is feed using an offset configuration, avoiding the block losses, and its phase center is located at $(x_f, y_f, z_f) = (-79.3, 0, 200)$ mm considering the center of the reflectarray as the origin of the coordinates system. The feed selected is a horn antenna (NARDA 665-20) of 15 dBi gain working at 28 GHz in linear polarization X-pol ($\hat{\boldsymbol{x}}$ axis). The illumination taper on the reflectarray surface is 15.80 dB at the edge of the reflectarray, minimizing the diffraction because of the edges.

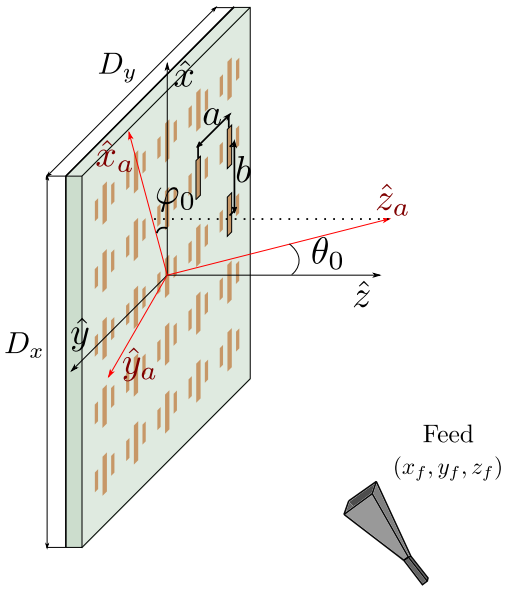

Figure 5.2: *Sketch of an offset configuration reflectarray and its parameters.*

The uniform plane wave is not defined perpendicular to $\hat{\boldsymbol{z}}$ but $\hat{\boldsymbol{z}}_a$. The relation

between both systems are given by

$$\begin{pmatrix} \hat{\boldsymbol{x}}_a \\ \hat{\boldsymbol{y}}_a \\ \hat{\boldsymbol{z}}_a \end{pmatrix} = \begin{pmatrix} \cos\theta\cos^2\varphi + \sin^2\varphi & \cos\varphi\sin\varphi(\cos\theta - 1) & -\sin\theta\cos\varphi \\ \cos\varphi\sin\varphi(\cos\theta - 1) & \cos\theta\sin^2\varphi + \cos^2\varphi & -\sin\theta\sin\varphi \\ \sin\theta\cos\varphi & \sin\theta\sin\varphi & \cos\theta \end{pmatrix} \begin{pmatrix} \hat{\boldsymbol{x}} \\ \hat{\boldsymbol{y}} \\ \hat{\boldsymbol{z}} \end{pmatrix} \quad (5.1)$$

The pointing direction of the reflectarray is $(\theta_0 = 20°, \varphi_0 = 0°)$ which generates an equivalent aperture D of

$$D = D_x \times D_y = 188.76 \text{ mm}\cos\theta_0 \times 188.76 \text{ mm} = 177.36 \times 188.76 \text{ mm}^2 \quad (5.2)$$

where D_x and D_y are the equivalent apertures defined in the vertical $(\hat{\boldsymbol{x}})$ and horizontal $(\hat{\boldsymbol{y}})$ direction, respectively.

5.3.1.2. Unit cell definition

The unit cell selected to design the reflectarray is a cell of three parallel dipoles. In Figure 5.3 the different parameter of the element is depicted. The central dipole is separated from the lateral dipoles at a distance S of 1.43 mm from the central dipole. The dipoles are oriented parallel to the $\hat{\boldsymbol{x}}$-axis and work in single linear polarization. The width of the dipoles is common for all of them ($W = 0.5$ mm), whilst the length of the central dipole is L_1 and the length of the lateral dipoles is L_2. Both lengths are related by a factor of 0.7, being $L_1 = 0.7L_2$.

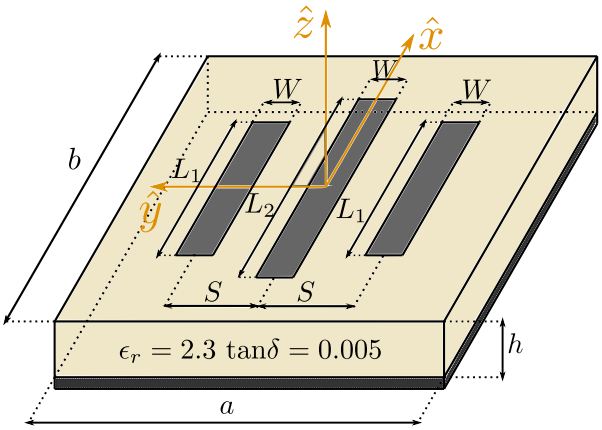

Figure 5.3: *Reflectarray element based on a set of three parallel dipoles for a single polarization.*

The set of dipoles is printed on a single layer of Diclad 880 substrate ($\epsilon_r = 2.3$,

$\tan\delta = 0.005$) of thickness 0.762 mm. The phase response of the cell is controlled by varying the length of the central dipole L_2. In Figure 5.4 the phase and amplitude response are shown for normal incidence at different frequencies. The cell provides a phase-shift larger than 360° and a phase slope smooth enough to minimize the possible phase-shift errors because of manufacturing tolerances. The in-band response of the cell is quite stable within the 2 GHz range and the amplitude losses are always lower than 0.40 dB (> 0.91 of reflection). The angular stability has been also validated and it is shown in Figure 5.5. The cell presents quite good angular stability, especially the phase that barely changes.

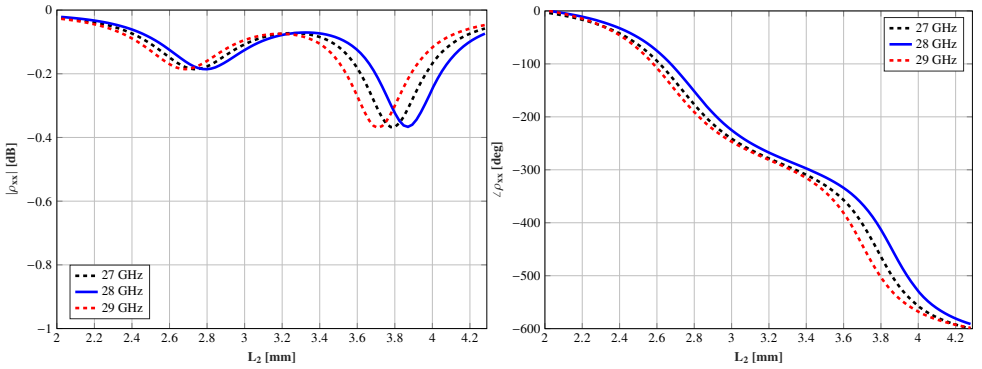

(a) *(b)*

Figure 5.4: *(a) Amplitude (dB) and (b) phase (deg) response of the single-layer three-dipole element for normal incidence.*

5.3.1.3. Uniform plane wave requirements

On the other hand, the uniform plane wave is evaluated on a plane perpendicular to the pointing direction at a distance of 500 mm (46.66λ) from the center of the reflectarray. This configuration provides a very compact structure (reflectarray plus uniform plane wave) but is a major challenge because of the near-field pattern at this distance. Note that, the far-field region for this antenna aperture starts at 12.52 m (1170.40λ).

The uniform plane wave requirements are imposed in a circular area of diameter 100 mm (9.33λ), equivalent to more than the 56% and 53% of the antenna apertures D_x and D_y, respectively. Within this area, the maximum amplitude ripple is 1 dB, whilst 10° in phase, which corresponds to the theoretical definition of a uniform plane

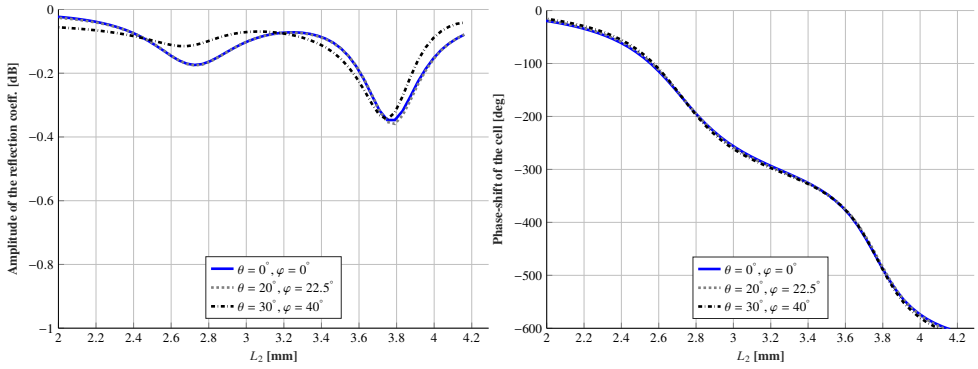

(a) *(b)*

Figure 5.5: *(a) Amplitude (dB) and (b) phase (deg) response of the single-layer three-dipole element for different angles of incidence at 28 GHz.*

wave. It is important to clarify that these ripples establish the maximum difference between two points belonging to uniform plane wave area.

5.3.2. Near-field phase-only synthesis with amplitude and phase constraints

The generalized Intersection Approach is used to synthesize the phase of the reflection coefficients ρ_{xx} of the elements of the reflectarray working in X-pol. Unlike the synthesis carried out in Chapter 4, this synthesis considers constraints on both amplitude and phase of the near-field. Therefore, the cost function is defined by the functional d (5.3) instead of d_M. Ideally, if the synthesis converges, it is assumed that the new phase distribution radiates a near-field closer to the aimed pattern. However, when dealing with amplitude and phase constraints the convergence could not ensure that both are closer to the goal simultaneously. This happens due to d_M evaluates a magnitude difference, while d_P is a phase difference, which is typically much lower than d_M. Therefore, d_M could have a deeper impact on the global cost.

$$d = d_M + d_P = \int_\Omega w_M \left(\left| |\tilde{\boldsymbol{E}}_{NF}|^2 - |\boldsymbol{E}_{NF}^{\mathrm{LMA}}|^2 \right| \right) d\Omega + \int_\Omega w_P \left(\left| \angle\tilde{\boldsymbol{E}}_{NF} - \angle\boldsymbol{E}_{NF}^{\mathrm{LMA}} \right| \right) d\Omega \tag{5.3}$$

Another point to note is that even though d_M and d_P can be mathematically

computed independently, the electric field is a complex magnitude and both amplitude and phase are physically related. Thus, a change in the amplitude leads to a change in the phase. When dealing with a synthesis with requirements only imposed on the amplitude of the near-field, the phase is a degree of freedom and vice versa. However, a synthesis considering specifications on both amplitude and phase simultaneously increases its complexity since the requirements are significantly much tighter and the degrees of freedom are reduced because of the amplitude and phase relation of the electric field.

In the synthesis is quite important to use the functions w_M and w_P (5.3), which weight d_M and d_P, respectively. The functions enable d_M and d_P to have a similar influence on the cost function, leading to a solution that satisfies the amplitude and phase requirements. To make easier the convergence of the synthesis it is divided into two different steps. As it would be seen later, the amplitude of the near-field is further from satisfying the requirements than the phase. Therefore, the first stage is focused on increasing the uniformity of the amplitude while, at least, keeping the phase flatness or improving it. Once the amplitude satisfies the requirements the emphasis is on the phase ripple. Given more importance to the phase or the amplitude, requirements are a matter of properly chosen the values of w_M and w_P.

5.3.2.1. Starting point

The geometry of the reflectarray defined in previous section is used as starting point of the phase-only synthesis of the reflection coefficients ρ_{xx}. The initial phase distribution corresponds to a far-field focused reflectarray computed with (4.1) and pointing to $(\theta_0, \varphi_0) = (20^\circ, 0^\circ)$. The resulting phase distribution is shown in Figure 5.6.

The initial uniform plane wave radiated by this phase distribution is shown in Figure 5.7, both amplitude and phase along with the uniform plane wave boundaries (solid red line). Since the uniform plane wave is found in the pointing direction, the near-field is collimated in this direction and the phase virtually behaves like a plane wavefront. Different x cut along the $\hat{\boldsymbol{x}}$ direction are totally flat while the y cuts increases their phase variation to 22°. This increase of the phase variation is associated with the offset plane of the feed ($y = 0$) and it thus increases the ripple due to the non-symmetry configuration. The amplitude of the near-field has a worse response according to the required specifications. The reflected field depends on the incident field of the feed (2.13), thus whether the amplitude taper at the reflectarray surface is high, the amplitude will increase the ripple in the uniform plane wave. The maximum difference between the highest and lowest field value within the desired area is higher than 8 dB, as shown in Figure 5.7(a).

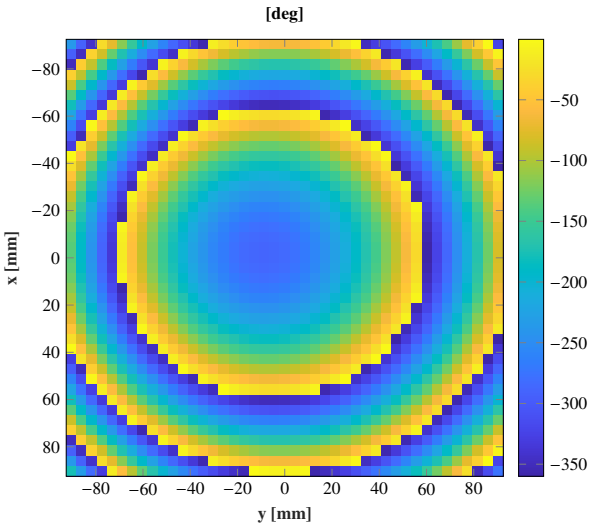

Figure 5.6: *Initial phase distribution (deg) of a far-field focused reflectarray pointed to* $(\theta_0, \varphi_0) = (20^\circ, 0^\circ)$ *at* 28 *GHz.*

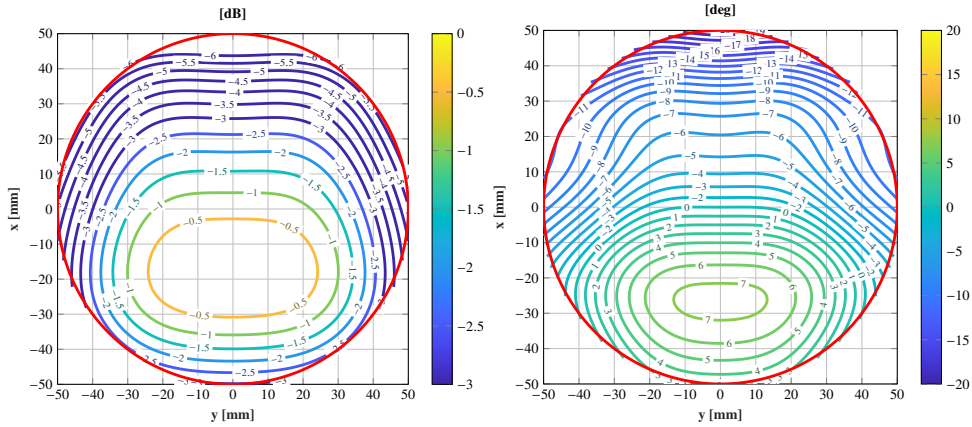

Figure 5.7: *Near-field radiated in the required area by the initial phase distribution used as starting point (a) Normalized amplitude (dB) to the maximum (b) Normalized phase (deg) to the value at the center of the uniform plane wave area at* 28 *GHz.*

5.3.2.2. Synthesis results

The optimization process has followed the scheme of Figure 4.7. A total of eight different stages are needed after reaching the final phase distribution. The specifications

have been gradually tightened from 1.5 dB and 20° to 1 dB and 10° on amplitude and phase, respectively. These last specifications have been reached after a total of 2938 iterations of the generalized Intersection Approach. The resulting phase distribution is shown in Figure 5.8. This phase variation along the reflectarray surface is smooth enough to carry out a proper design.

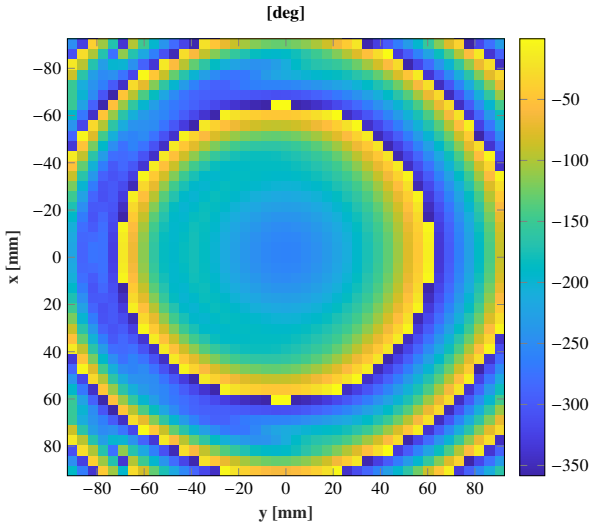

Figure 5.8: *Phase distribution (deg) after the optimization process carried out with the generalized Intersection Approach at* 28 *GHz.*

The uniform plane wave generated by the synthesized phase distribution is shown in Figure 5.9, and Table 5.1 outlines a comparison of the maximum ripples and specification compliance before and after the synthesis process. The improvement of the uniform plane wave, both amplitude, and phase, is quite significant, obtaining a ripple reduction of 7 dB in amplitude ripple and increasing the 1 dB compliance from 25% to nearly 90%. Despite the phase starts from a markedly better point, the resulting phase of the near-field field reduces its ripple to 4.30° in the whole area.

It is from our interest the study of the main cuts of the uniform plane wave ($x = 0$, $y = 0$) since they represent the largest dimension because of its circular shape, and $y = 0$ is the offset plane of the feed. After the synthesis, this cut has been notably improved with an enlargement of 262% and 303% in the size of the desired area in amplitude and phase, respectively. The cut $x = 0$ has been also enlarged in a 209% in amplitude and a 135% in phase. Therefore, the synthesized uniform plane wave has the same size in its main cuts.

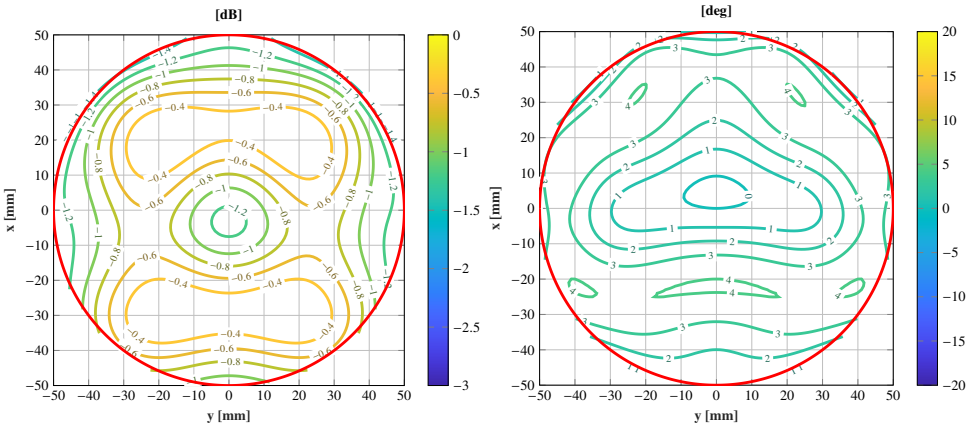

(a) *(b)*

Figure 5.9: *Uniform plane wave radiated by the synthesized phase distribution (a) Normalized amplitude (dB) to the maximum (b) Normalized phase (deg) to the value at the center of the uniform plane wave area at 28 GHz.*

Table 5.1: *Evaluation of the maximum ripple and the specification compliance in the desired area and the cut $y = 0$ for the starting and synthesized point.*

			Starting point		Synthesized point	
		Spec.	Max. ripple	Compliance (%)	Max. ripple	Compliance (%)
Uniform Plane Wave	(dB)	≤ 1	8.01	25.25	1.33	89.42
	(°)	≤ 10	26.82	46.01	4.30	100
Cut $y = 0$	(dB)	≤ 1	8.01	38.83	1.10	83.49
	(°)	≤ 10	26.82	39.80	4.30	100

5.3.3. Reflectarray design

Once the phase distribution of the reflectarray elements has been obtained, the geometry of the elements must be designed. In the design process, the length of the dipoles is adjusted to produce the required phase-shift of Figure 5.8. The process is carried out element by element, considering the real angle of incidence and the real incident field for each cell, following the scheme of Figure 4.13. The technique defined in [2] is applied to adjust the length L_2 of the central dipole to match the phase response of the cell and the phase distribution obtained in the synthesis. The phase response

of the cell is analyzed using homemade software based on the MoM in the spectral domain (MoM-SD) with local periodicity conditions [247]. The output of this process is the 44×44 element layout shown in Figure 5.10 and the maximum error in the phase response is 0.1˚ for an individual element Figure 5.11.

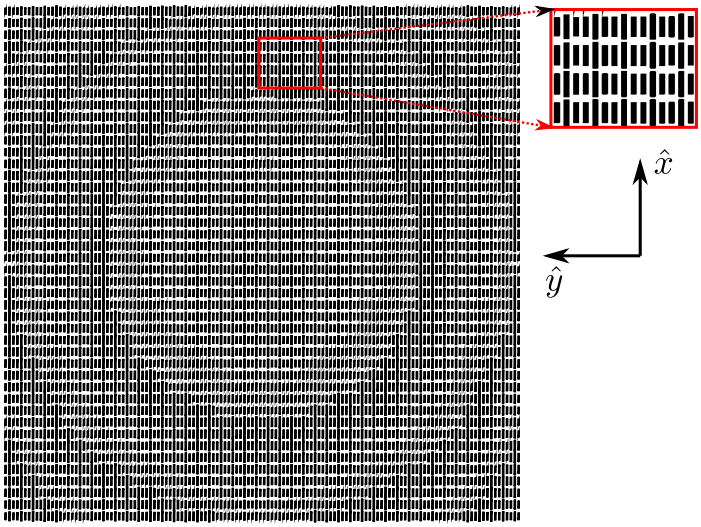

Figure 5.10: *Layout of the* 44×44 *reflectarray.*

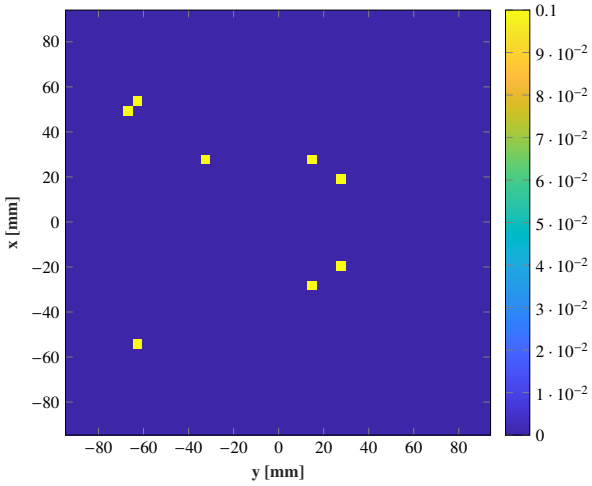

Figure 5.11: *Difference (deg) between the required phase-shift of Figure 5.8 and the phase-shift implemented by the dipoles cell.*

The uniform plane wave radiated by this layout is computed to evaluate its perfor-

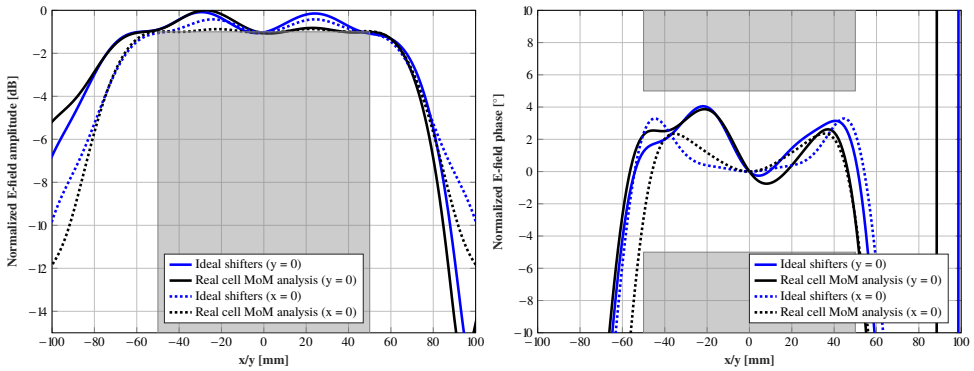

(a) *(b)*

Figure 5.12: *Comparison of the main cuts obtained in the synthesis process and MoM simulations (a) Normalized amplitude (dB) to the maximum (b) Normalized phase (deg) to the value at the center of the uniform plane wave area at* 28 *GHz.*

mance regarding the desired specifications. The main cuts of the uniform plane wave are shown in Figure 5.12, and only slight differences are found between previous results and the layout. These differences are mainly a consequence of the amplitude losses of the cell that are not considered in the phase-only synthesis (the element is modeled as an ideal phase-shift). Despite using this approximation on the phase-only synthesis, the MoM results satisfy the specifications within the desired area boundaries, validating the reflectarray design.

5.3.4. Experimental evaluation of the plane wave generated by the reflectarray

The layout of Figure 5.10 has been manufactured. The prototype is measured in the planar acquisition range of Universidad de Oviedo to evaluate the plane wave performances. The reflectarray is placed on an aluminum structure tilted 20° and the uniform plane wave is generated parallel to the probe aperture (an open-ended Ka-band waveguide). The setup is depicted in Figure 5.13. Four different planes are measured, the synthesized plane at 500 mm and the three planes at 550, 600, and 650 mm. As it occurs in previous results, the nearby planes to the synthesized one are also affected through these planes are not considered on the synthesis. The near-field is measured in a regular grid of 150×150 mm^2 that covers the whole area wherein the uniform plane wave is generated.

In Figure 5.14 the main cuts measured at the different planes are shown in ampli-

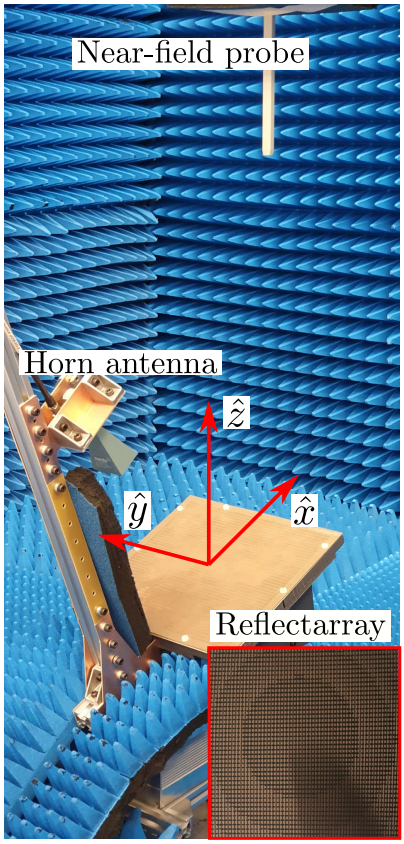

Figure 5.13: *Setup at the near-field planar acquisition range in Universidad de Oviedo and a zoom of the manufactured reflectarray.*

tude and phase. In Figure 5.15 the uniform plane wave for the four planes is evaluated. All these results show a significant improvement in the uniformity of the plane wave in amplitude. The near-field shows a very plane wavefront with a constant behavior within the measured volume. Table 5.2 further details a studio of the maximum peak-to-peak ripples and its percentage of compliance for different specification levels. The peak-to-peak evaluates the maximum difference between the maximum and minimum value of the field.

The synthesized plane at 500 mm presents a maximum peak-to-peak ripple of 2.07 dB in the whole area as Figure 5.15 shows. A 93% of the area is within a 1 to 1.5 dB peak-to-peak ripple, while the main cuts show an amplitude taper lower than 1 dB with a maximum ripple of 1.63 dB in the worst case, the offset plane $y = 0$. The maximum phase deviation in the area is 15.33° and nearly a 90% of the phase is within

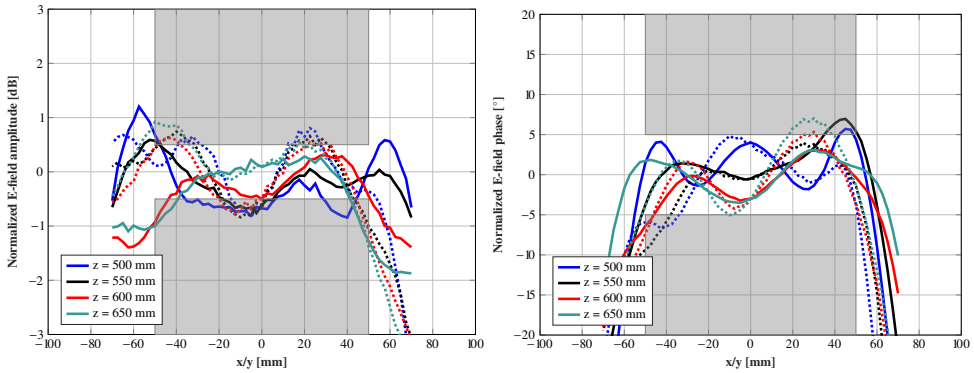

Figure 5.14: *Measurements of the main cuts of the uniform plane wave at* 28 *GHz. (a) Amplitude (dB) normalized to the mean value of the uniform plane wave. (b) Phase (deg) normalized to the mean value of the uniform plane wave area. (Solid line) cut* $y = 0$ *(dotted line) cut* $x = 0$.

a peak-to-peak ripple of 10° (see Figure 5.15(e)). The phase in the main cuts is notably flat having a maximum ripple of 11°. The measurements at the plane of 500 mm show a quite good behavior of the uniform plane wave.

Now, the uniform plane wave performances at the other planes are evaluated. The plane at 550 mm presents a maximum peak-to-peak of 2.15 dB and a 91% of the uniform plane wave is within a peak-to-peak ripple of 1.5 dB, as Figure 5.15(b) shows. As in the previous plane, the amplitude taper evaluated at the main cuts is lower than 1 dB and its maximum ripple of 1.75 dB. The phase at the lower boundary presents a valley on the phase that increases the maximum deviation to 19°. However, the phase in the rest of the area has a smooth variation and a 93% is within a peak-to-peak ripple lower than 15° and a 84% within 10° (see Figure 5.15(f)).

Similar to previous planes, the amplitude at 600 mm has a maximum peak-to-peak ripple of 2.43 dB and nearly the 90% of the uniform plane wave is within a ripple lower than 1.5 dB. The amplitude taper on its main cuts is lower than 1 dB and its maximum ripple of 1.69 dB. The phase is significantly plane like the previous planes, and it only has a maximum phase deviation close to the 15° of the 500 mm plane. More than an 88% of the area is within a ripple of 10° as Figure 5.15(g).

The further plane, $z = 650$ mm, slightly increases the peak-to-peak ripple to 3 dB. This increase is mainly due to the upper area of the uniform plane wave, wherein the field starts to rapidly decay rising the difference with the rest of the area. Despite having an increase in the peak-to-peak an 83% of the area is within a ripple lower

Table 5.2: *Evaluation of the maximum ripple (peak-to-peak in amplitude and deviation in phase) and the specification compliance in the measured uniform plane wave and its main cut $y = 0$.*

		Plane (mm)	Spec. (dB/°)	Max. ripple (dB)	Compliance 1 dB / 10° (%)	Compliance 1.2 dB/15° (%)	Compliance 1.5 dB/20° (%)
Uniform Plane wave	Amplitude (dB)	500	≤ 1	2.07	73.11	83.09	93.22
		550		2.15	71.05	81.34	91.16
		600		2.43	73.35	82.63	89.64
		650		3.02	63.44	71.28	83.01
	Phase (°)	500	≤ 10	15.33	8.88	95.35	100
		550		19.93	84.23	93.67	97.18
		600		15.91	88.04	97.79	100
		650		13.19	88.49	100	100
Cut $y = 0$	Amplitude (dB)	500	≤ 1	1.63	63.41	75.06	92.68
		550		1.75	43.90	63.41	85.36
		600		1.69	58.53	78.04	92.68
		650		2.30	70.73	78.04	78.05
	Phase (°)	500	≤ 10	11.58	82.90	100	100
		550		13.36	82.92	97.56	100
		600		12.70	90.24	100	100
		650		12.05	73.17	100	100

than 1.5 dB (see Figure 5.15(d)). The central area presents a very smooth variation with a ripple lower than 0.8 dB. The amplitude taper on the main cuts is close to 1 dB and the ripple goes up to 2.30 dB. The flatness of the phase is undoubtedly smooth and almost the 90% is within a maximum deviation of 10° and a 100% within a ripple lower than 15°, as Figure 5.15(h) shows.

5.4. Dual-linear-polarization Plane Wave Generator based on a reflectarray at mm-Wave

The geometry described in Section 5.3 is used to design a new reflectarray to generate a uniform plane wave in dual linear polarization at 28 GHz. The feed and the uniform plane wave are the same but extending it to the Y-pol. To include this new requirement, it is necessary to replace the cell of Section 5.3 with a cell that works in dual-linear polarization. In this case, the selected cell is depicted in Figure 5.16. This

cell is based on six dipoles, three operate in X-pol and the other three in Y-pol. The three dipoles of each polarization are similar to the cell of Figure 5.3. The distance from the central to each adjacent dipole is $S = 0.8$ mm. The width W of the dipoles is the same in the six dipoles and equals 0.3 mm. The length of the central dipole is L_{x2} and L_{y2} for the X- and Y-pol, respectively. The lengths of the lateral dipoles are L_{x1} and L_{y1} and each lateral length is related with the central dipole length by a factor of 0.75 (í.e., $L_{x1} = 0.75L_{x2}$). Note that, the lateral dipoles have the same length L_{x1} or L_{y1}.

The proposed cell enables the phase-shift control by the adjustment of each central dipole. An important advantage of this cell is that the dipoles are printed on a single layer obtaining a quite simple topology similar to the reflectarray of previous Section

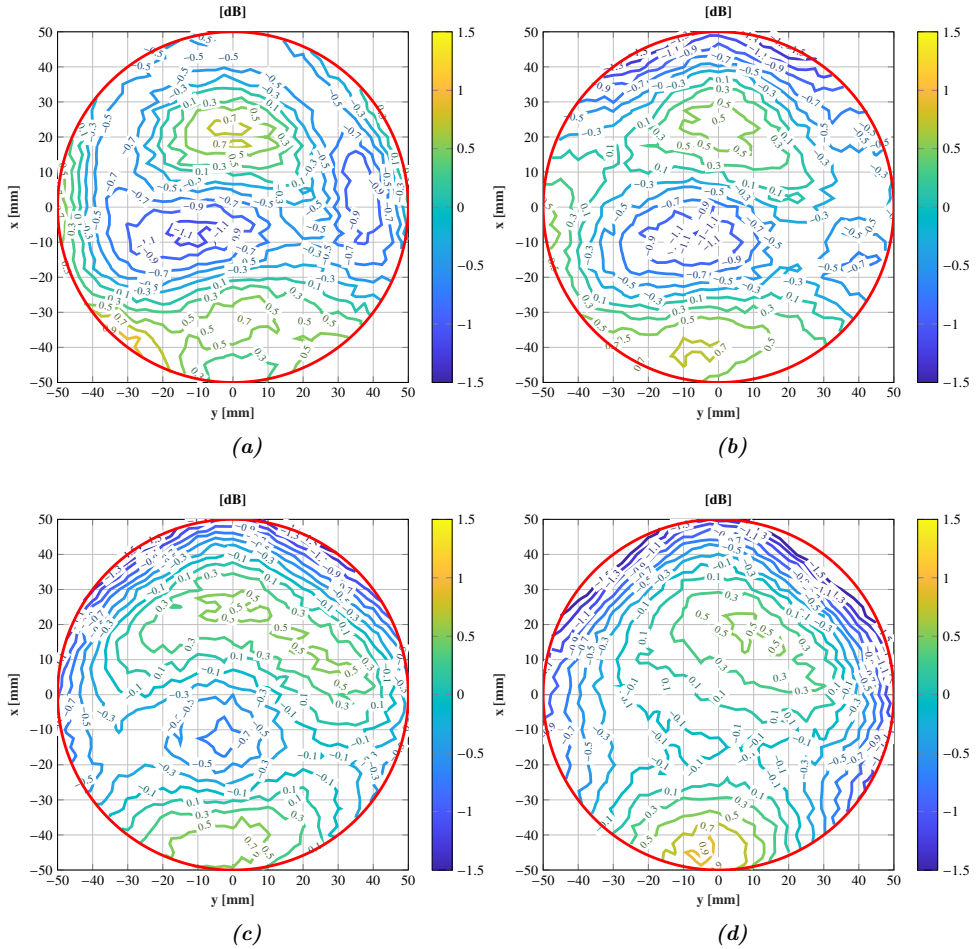

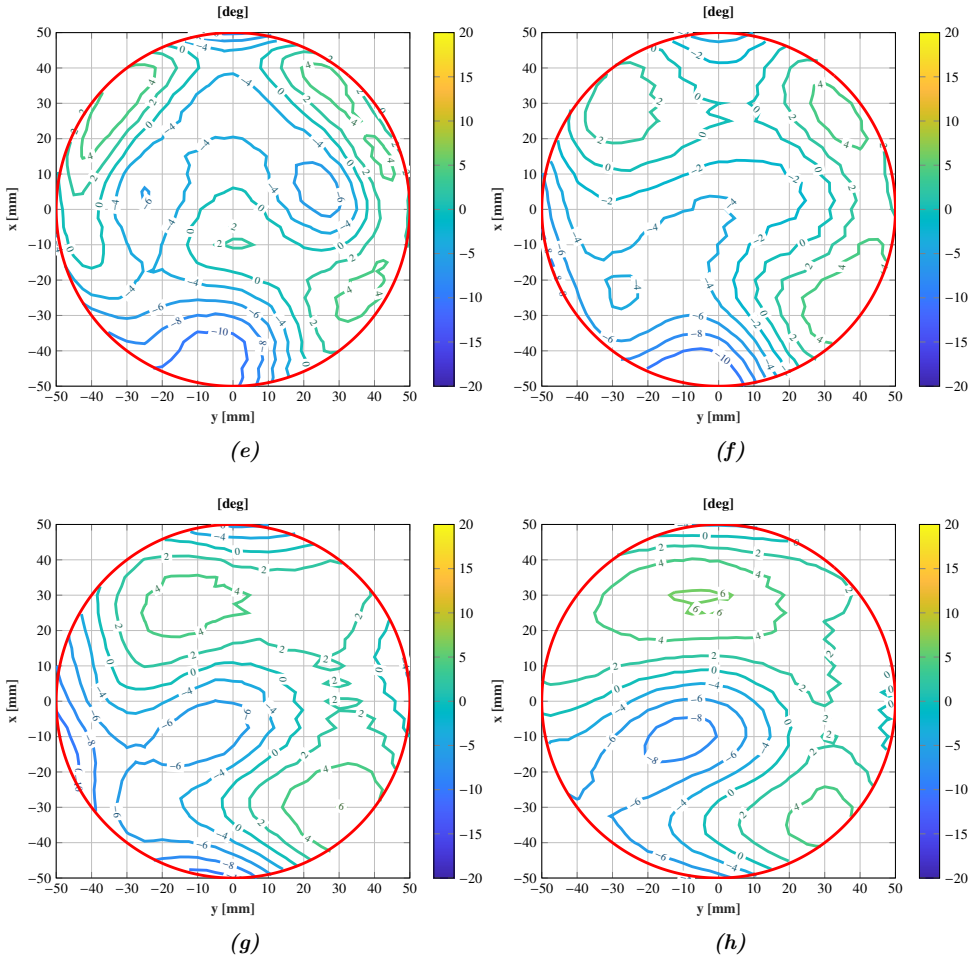

Figure 5.15: *Uniform plane wave measurements at the planes $z = 500$, $z = 550$, $z = 600$ and $z = 650$ mm at 28 GHz. (a) Normalized amplitude (dB) at $z = 500$ mm (b) Normalized amplitude (dB) at $z = 550$ mm (c) Normalized amplitude (dB) at $z = 600$ mm (d) Normalized amplitude (dB) at $z = 650$ mm (e) Normalized phase (deg) at $z = 500$ mm (f) Normalized phase (deg) at $z = 550$ mm (g) Normalized phase (deg) at $z = 600$ mm (h) Normalized phase (deg) at $z = 650$ mm. Both amplitude and phase are normalized to the mean value of each uniform plane wave.*

5.3. This is possible by shifting the elements of each polarization $a/2$ and $b/2$ in each direction, instead of stacking the elements on different layers. The periodicity is 5.3×5.3 mm^2 ($a \times b$). Note that if the periodicity changes the number of elements will change. According to this new periodicity, the number of elements of the reflectarray will be 36×36 instead of 44×44.

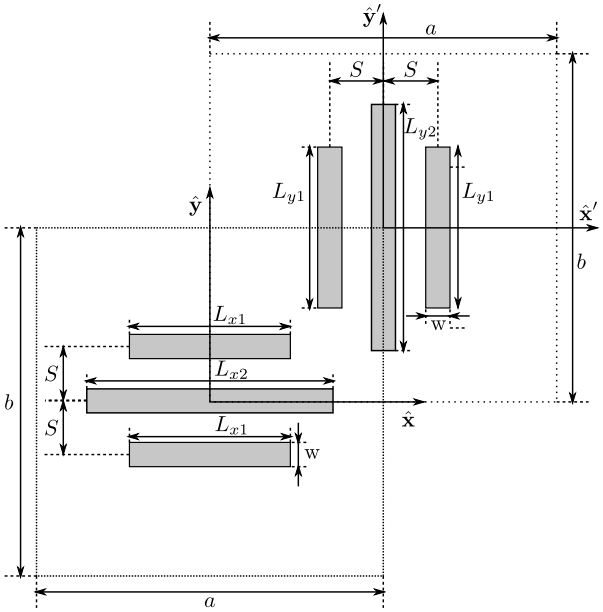

Figure 5.16: *Sketch of the reflectarray cell based on two coplanar sets of three parallel dipoles to operate in dual-linear polarization.*

The substrate is a single layer of Rogers RO4003C substrate ($\epsilon_r = 3.55$, $\tan\delta = 0.0027$) of thickness 0.8128 mm. The phase response of the cell is shown in Figure 5.17 together with the amplitude response for normal incidence at different frequencies (27.5, 28 and 28.5 GHz). Since the set of dipoles of X-pol is the same as the set of Y-pol, the phase-shift of both polarization is the same too. The phase-shift is large enough (400°) with a smooth phase slope to carry out a design. The amplitude losses are 0.40 dB in the worst case.

5.4.1. Near-field synthesis with amplitude and phase constraints

The generalized Intersection Approach is used to synthesize the near-field to obtain a uniform plane wave. In this case, the uniform plane wave must be generated in dual-linear polarization. An important advantage of the proposed reflectarray element is the independent control of the phase response of each polarization. The dipoles of one linear polarization are orthogonal to the dipoles of the other linear polarization, which minimizes the coupling between the two polarization and obtains a low cross-polarization level [102]. But what is more important, the physical implementation of

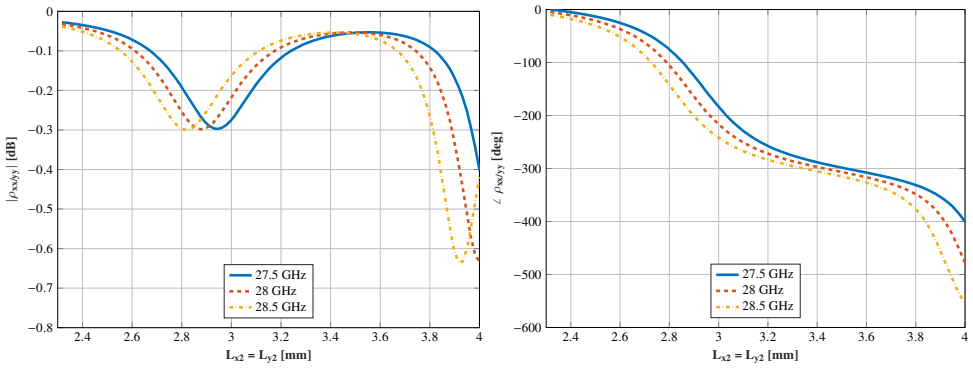

Figure 5.17: *(a) Amplitude (dB) and (b) phase response of the proposed cell based on two sets of three parallel dipoles at different frequencies and normal incidence.*

the X-pol is independent of the phase-shift of the Y-pol. Hence, two different phase-only syntheses can be carried out to obtain a phase distribution for the X-polarized dipoles and other phase distribution for the Y polarized dipoles. Then, the lengths of each set of three dipoles would be independently adjusted but obtaining a layout that radiates the uniform plane wave in dual linear polarization.

Owing to the Y-polarized dipoles are shifted $(a/2, b/2)$ in relation to the $(\hat{\boldsymbol{x}}, \hat{\boldsymbol{y}}, \hat{\boldsymbol{z}})$, this displacements must be taken into account in the computation of the near-field. In Chapter 2 the near-field computation for unit cells with a physical displacement of phase-shifters is discussed and it is applied to the near-field synthesis of the Y-pol. Since it is a phase-only synthesis the cross coefficients ρ_{xy} and ρ_{yx} are canceled as well as ρ_{xx}, the optimization is only carried out for the Y-pol.

5.4.1.1. Starting point

The geometry of Section 5.3 is used as the starting point of the phase-only synthesis of the reflection coefficients ρ_{xx} and ρ_{yy}, only changing the periodicity (5.3×5.3 mm^2) and therefore, the number of elements (36×36). The initial phase distribution is obtained with (4.1) pointing the outgoing beam to $(\theta_0, \varphi_0) = (20°, 0°)$. Although two different phase-only syntheses are carried out, the starting point is the same to obtain the uniform plane wave in the same direction.

The main cuts of the initial uniform plane wave for both polarization are shown in Figure 5.18. As it occurs on the starting point of the previous section, the phase of the uniform plane wave nearly behaves like a plane wavefront while the amplitude is

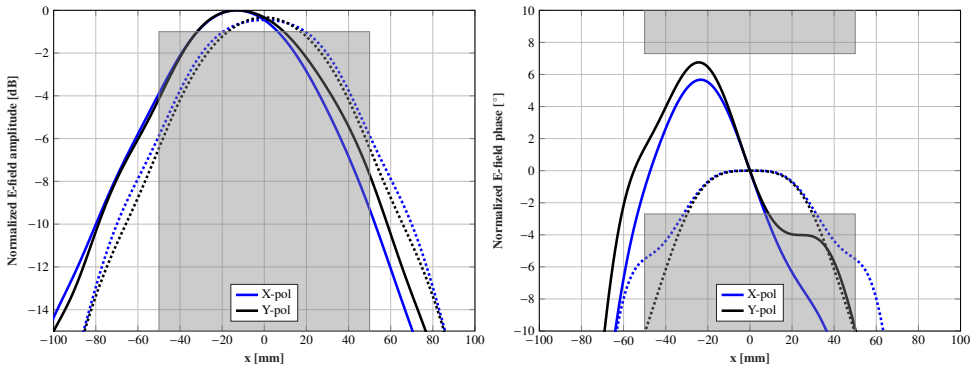

(a) *(b)*

Figure 5.18: *Main cuts of the near-field radiated with the starting phase distribution at* 28 *GHz for both linear polarizations (a) Normalized amplitude (dB) (b) Normalized phase (deg). Dotted line represents the cut* $x = 0$ *and solid line the cut* $y = 0$.

affected by the illumination taper. Also, the cut $y = 0$ increases its ripple because of the non-symmetry configuration of the feed.

5.4.1.2. Synthesis results

The two phase-only syntheses have been carried out following the scheme of Figure 4.7. The X-pol synthesis has required 9 concatenated syntheses while the Y-pol 12 syntheses with a total of more than 4500 iterations in each polarization synthesis. The requirements have been gradually tightened as in Section 5.3. Also, the technique described in Section 4.4 has been used to define the mask of the phase of the uniform plane wave. The resulting phase distribution for each polarization is shown in Figure 5.19. The phase variation along the surface on both results is smooth enough to carry out a design.

The obtained uniform plane wave is shown in Figure 5.20 and Figure 5.21 for X- and Y-pol, respectively. In Table 5.3 a detailed overall of the maximum ripples and specification compliance is summarized, before and after the synthesis. Both amplitude and phase have been significantly improved, reducing the ripple from 9.56 dB to 0.37 dB on the X-pol and from 7.94 dB to 0.44 dB on the Y-pol. The 1 dB compliance is satisfied resulting in a quite uniform amplitude of the uniform plane wave. The phase for the X-pol is within the 10° ripple in a 77%. This percentage seems to be poor. Still, it is increased to an 82% for a 12° ripple and a 92.5% for a 15° ripple evaluation. The areas near the uniform plane wave boundaries, especially at the right

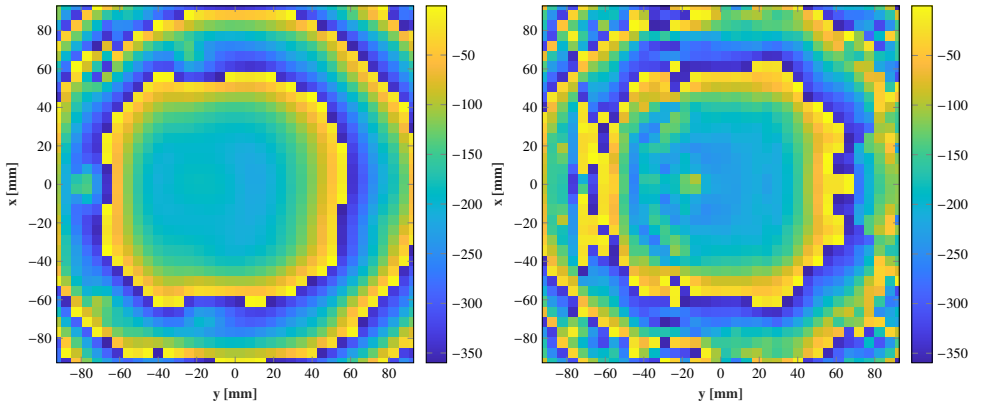

Figure 5.19: *Phase distribution obtained after the synthesis process carried out with the generalized Intersection Approach (a) X-pol (b) Y-pol.*

size, present a strong decay of the phase increasing the phase ripple from 10° to 15° with a maximum deviation of 27° in the whole area. This effect does not appear on the phase of the Y-pol, obtaining that a 90% is within the 10° ripple and a 99.27% within a 15° ripple.

The main cut $y = 0$ is particularly studied since is the largest dimension of the uniform plane wave (the desired area is defined in a circular area) and it is affected by the non-symmetry of the feed location. However, this cut is enlarged a 271% and a 251% in the amplitude of the X- and Y-pol, respectively. The phase presents a better starting point, nonetheless, it is enlarged a 117% on the X-pol and a 163% on the Y-pol.

5.4.2. Reflectarray design in dual-linear-polarization

The two phase distributions obtained after the synthesis process are used to carry out a design. In the design process, the length of the dipoles is adjusted to produce the phase-shift obtained in the synthesis Figure 5.19. As previous results, the design is based on the scheme of Figure 4.13, using both the real angle of incidence and the real incident field to analyze the cell response with a homemade software based on MoM with local periodicity conditions [247]. The technique defined in [2] is applied to adjust the length L_{x1} and L_{y2} which produce the minimum phase error with regard to the phase-shifts of Figure 5.19. Throughout this process is important to avoid the contact between dipoles of different polarizations to avoid the coupling of copolar and

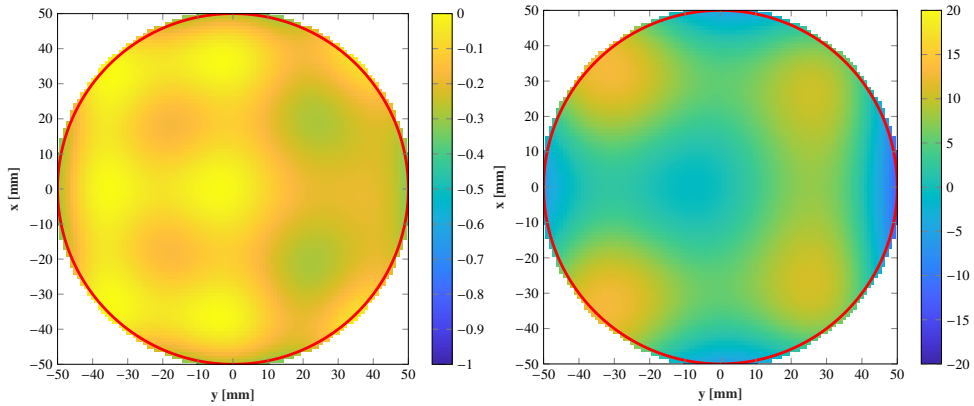

Figure 5.20: *Uniform plane wave radiated by the phase distribution obtained after the synthesis process at 28 GHz for X-pol (a) Normalized amplitude (dB) (b) Normalized phase (deg).*

Table 5.3: *Evaluation of the maximum ripple and the specification compliance in the uniform plane wave and the cut $y = 0$ for the starting and optimized point.*

				Initial		Optimized	
			Spec.	Max. ripple	Comp. (%)	Max. ripple	Comp. (%)
Uniform Plane Wave	X-pol	(dB)	≤ 1	9.56	18.91	0.37	100
		(°)	≤ 10	22.45	58.48	27	77.30
	Y-pol	(dB)	≤ 1	7.94	16.72	0.44	100
		(°)	≤ 10	17.69	69.42	16.77	90.71
$y = 0$	X-pol	(dB)	≤ 1	9.56	36.89	0.57	100
		(°)	≤ 10	22.45	61.16	22.59	73.78
	Y-pol	(dB)	≤ 1	7.94	39.80	0.31	100
		(°)	≤ 10	17.14	61.16	9	100

cross-polar components. The output is the 36×36 element layout shown in Figure 5.22 whose maximum error in the phase response is less than 1° for an individual element in both polarizations, as Figure 5.23 shows.

The layout of Figure 5.22 is analyzed with a MoM analysis and its uniform plane

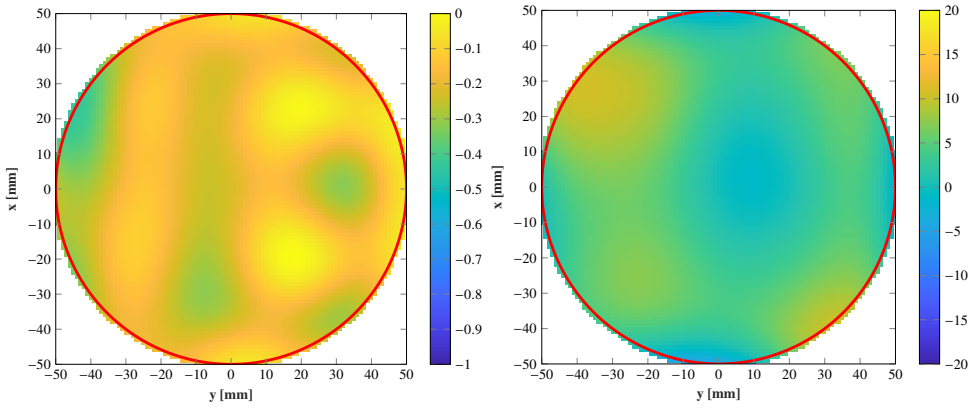

Figure 5.21: *Uniform plane wave radiated by the phase distribution obtained after the synthesis process at 28 GHz for Y-pol (a) Normalized amplitude (dB) (b) Normalized phase (deg).*

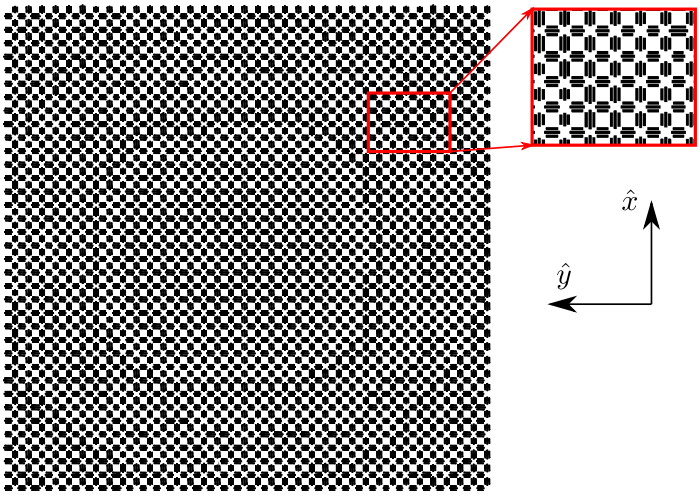

Figure 5.22: *Layout of the dual-polarized reflectarray operating to radiate a uniform plane wave.*

wave is computed to evaluate its performances. In Figure 5.24 and Figure 5.25 the uniform plane waves of the X-pol and Y-pol are shown, respectively. Both uniform plane waves are quite similar to the uniform plane wave of Figure 5.20 and Figure 5.21. The main cuts are shown in Figure 5.26 and compared with the ones of the synthesis results. Since the layout is nearly producing the same phase response, only slight

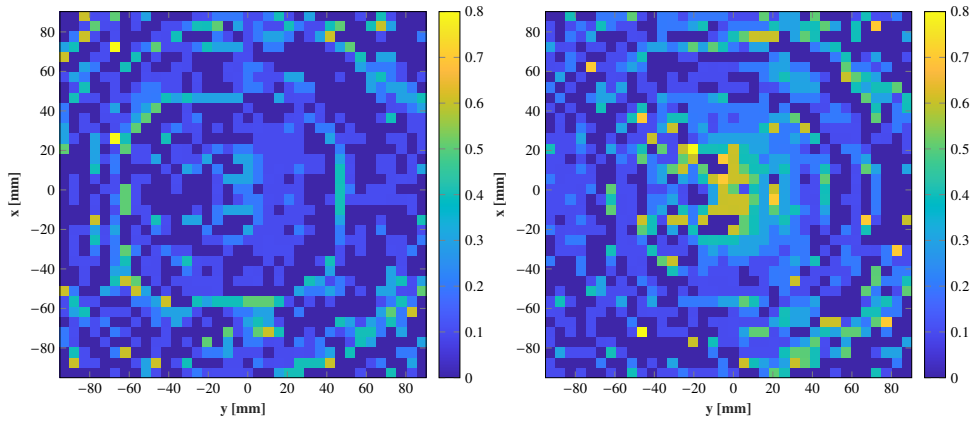

Figure 5.23: *Phase error (deg) on the layout along the reflectarray surface (a) X-pol (b) Y-pol.*

differences are found. The differences are associated with the amplitude losses and possible coupling between adjacent elements. However, despite having these differences, the layout obtains similar results and mostly satisfies the requirements as Table 5.4 shows. Note that, the phase increases the compliance about previous results for the X-pol. This may be explained since the 82% of the phase is within 12° ripple and a 92% within 15°. Therefore, the error is too close to the phase threshold and slight phase changes can significantly improve the phase ripple percentage. In the light of these results, the design is valid for obtaining a uniform plane wave on dual-linear polarization.

Table 5.4: *Evaluation of the maximum ripple and the specification compliance in the uniform plane wave and the cut $y = 0$ for designed layout.*

			X-pol		Y-pol	
		Spec.	Max. ripple	Compliance (%)	Max. ripple	Compliance (%)
Uniform Plane wave	(dB)	≤ 1	0.42	100	0.75	100
	(°)	≤ 10	27	80.14	16.58	93.45
Cut $y = 0$	(dB)	≤ 1	0.42	100	0.63	100
	(°)	≤ 10	23.15	85.43	10.02	99.02

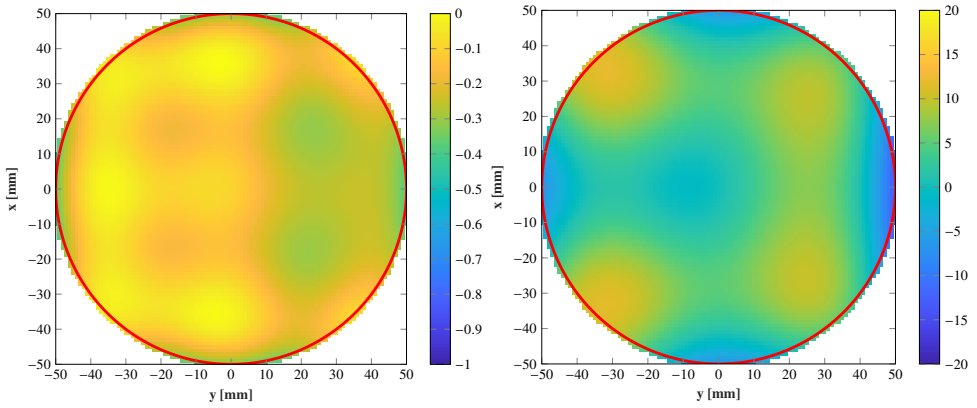

Figure 5.24: *Uniform plane wave radiated by the reflectarray layout at 28 GHz for X-pol (a) Normalized amplitude (dB) (b) Normalized phase (deg).*

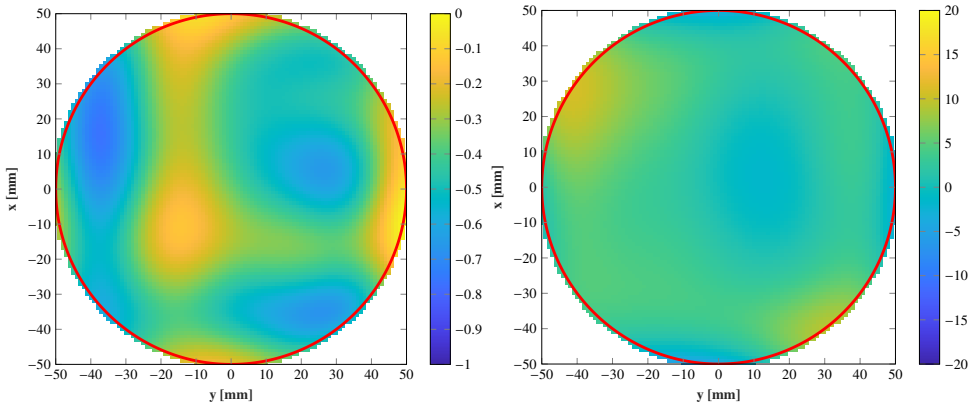

Figure 5.25: *Uniform plane wave radiated by the reflectarray layout at 28 GHz for Y-pol (a) Normalized amplitude (dB) (b) Normalized phase (deg).*

5.5. Demonstration of a Compact Antenna Test Range based on a reflectarray Plane Wave Generator as probe

Section 5.3 describes the near-field synthesis, design, and test of the reflectarray capabilities to generate a uniform plane wave within the Fresnel region to act as a quiet

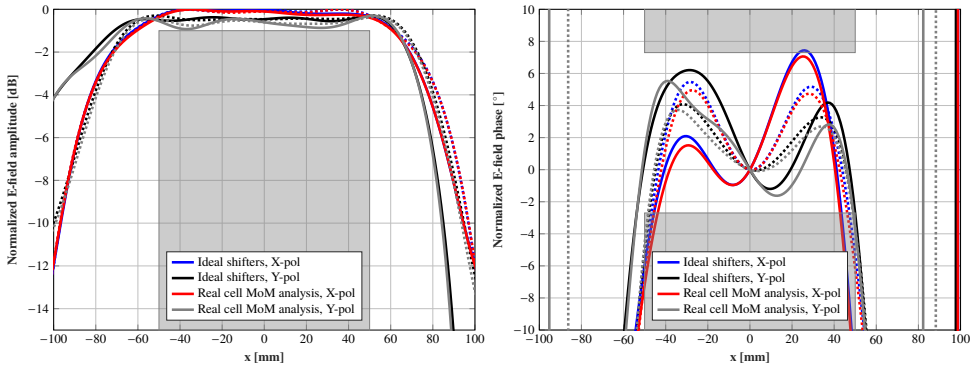

Figure 5.26: *Comparison along the main cuts of the uniform plane wave obtained after the synthesis process and the layout analysis with MoM for both dual-linear polarizations (a) Normalized amplitude (dB) (b) Normalized phase (deg). Dotted line represents the cut $x = 0$ and solid line the cut $y = 0$.*

zone at 28 GHz. The measurements of the uniform plane wave, subsection 5.3.4, show that the measured region satisfies the theoretical requirements to consider that the near-field behaves like a uniform plane wave in most of the measured volume (100 mm × 100 mm × 150 mm). This prototype aimed to validate the capabilities of reflectarray antennas to shape the near-field with both amplitude and phase constraints. Mainly focused on the development of potential alternatives to conventional measurement systems (CATRs and near-field ranges) to measure 5G new radio devices with portable and adaptive measurement systems while keeping their performances.

Once it was demonstrated that reflectarray antennas can radiate a uniform plane wave, therefore to generate a quiet zone, it is necessary to evaluate its capabilities as a probe on a CATR system. To this end, a small CATR has been developed whose probe is the reflectarray designed in Section 5.3. This section aims to validate the concept of reflectarray antennas acting as a CATR system of reducing dimensions at Ka-band, particularly 28 GHz.

5.5.1. Description of the RA-CATR

The developed system is based on the operation scheme of Figure 5.27. The measurement system is composed of the reflectarray working as a probe and the antenna or DUT whose radiation pattern is measured. Both probe and DUT are connected to a Vectorial Network Analyzer (VNA) which enables the measurement of the radiation

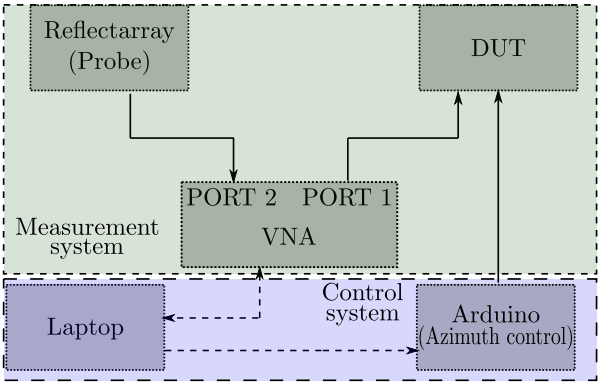

Figure 5.27: *Operational scheme of the reflectarray Compact Antenna Test Range.*

pattern by measuring the s_{21} between the two ports. The DUT is transmitting while the probe is receiving.

The control system is based on a laptop to manage both measurements and control using homemade software developed for this purpose. Simultaneously, the mechanical control of the DUT is done with an ARDUINO ONE and the ADAFRUIT board. The laptop sends the commands to move the AUT while the ARDUINO combined with ADAFRUIT control a motor to rotate the DUT doing and azimuth scan between $[-90°, 90°]$ with a step of $0.36°$. To obtain OTA measurements in a real-time view of the radiation pattern on the VNA, the spam is set to consider ± 90 Hz from 28 GHz.

5.5.2. Demonstration of the measurement of the radiation pattern of an antenna

The reflectarray is integrated on this homemade setup to measure a Ka-band horn antenna, as Figure 5.28 shows. This basic mechanical and control system enables the validation of the reflectarray probe by the measurement of a standard horn antenna (DUT) with a simple CATR configuration. The horn antenna is the A-INFOMW LB-28-10-C-KF of 10 dBi gain that is shown in Figure 5.29. The dimensions of the system are smaller than 1200 mm $\times$ 750 mm $\times$ 750 mm.

As it has been described previously, both DUT and reflectarray are connected to the vector network analyzer whose screen shows the radiation pattern in real-time. In this first approach, only the azimuth can be scanned, measuring the H-plane of the antenna. In Figure 5.30 the measurement of the horn antenna with this reflectarray CATR is compared with the results of a full-wave simulation of the horn antenna on CST Microwave Studio, obtaining a high agreement between both.

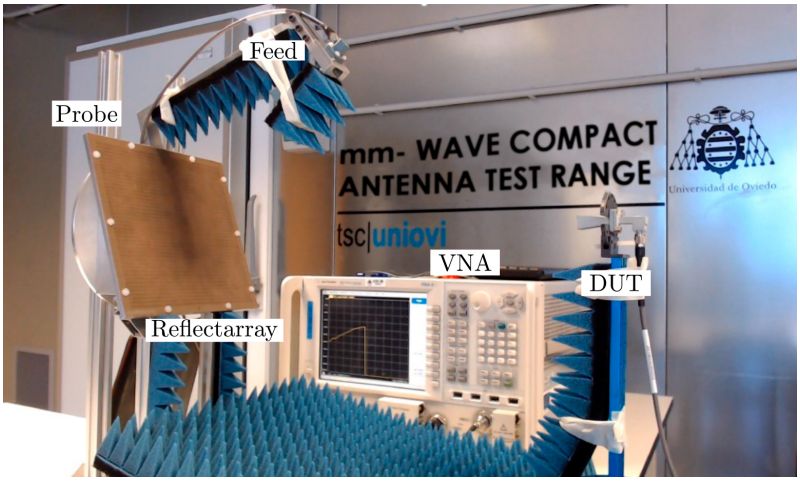

Figure 5.28: *Compact Antenna Test Range based on a reflectarray Plane Wave Generator to validate it in the measurement of devices at* 28 *GHz.*

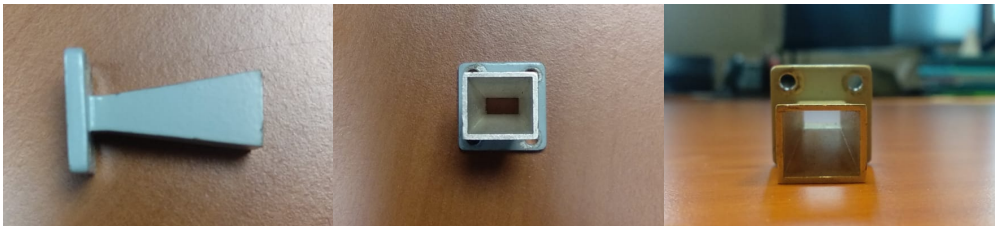

Figure 5.29: *Horn antenna A-INFOMW LB-28-10-C-KF of* 10 *dBi gain.*

Then, the 2 horn antenna array shown in Figure 5.31 is also measured. The array is comprised of two identical horn antennas A-INFOMW LB-28-10-C-KF, as the one shown in Figure 5.29. The separation between the two horn antennas is 50 mm, and the array is designed to radiate a main lobe in the boresight direction and different lobes and nulls within an angular range. The aim is to evaluate the accuracy of the system measuring a radiation pattern with several lobes and nulls. The array is fed with a power divider designed to have similar inputs in both horn antennas at 28 GHz.

The H-plane measured with the proposed system is compared to the one obtained in full-wave simulations in Figure 5.32. The measurement highly agrees with the simulations obtaining a significantly good concordance in the lobes, as well as the nulls, within an angular range of 150°.

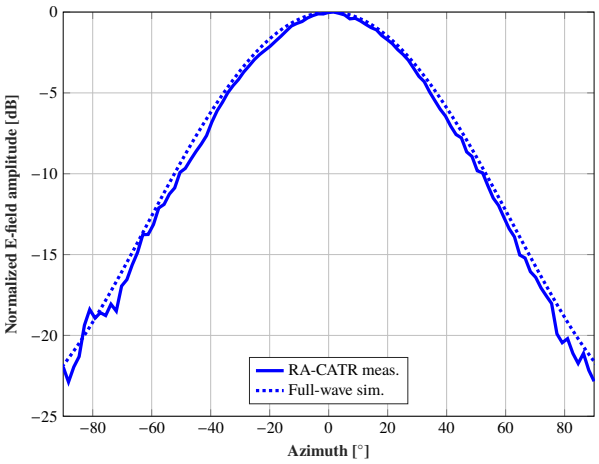

Figure 5.30: *Comparison of the measured and simulated radiation pattern at* 28 *GHz of the horn antenna.*

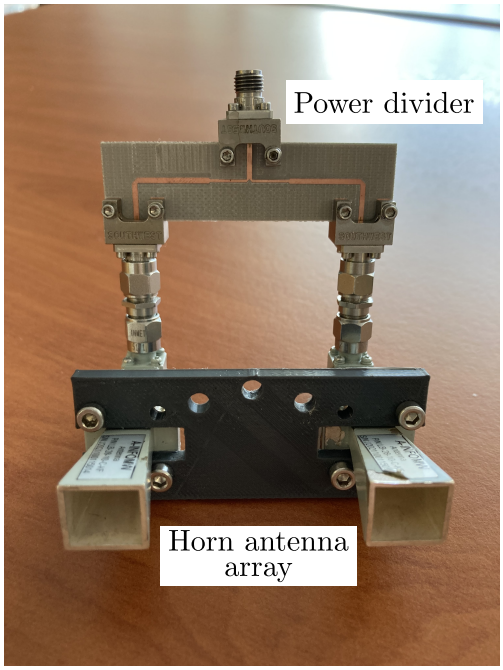

Figure 5.31: *Array comprised of two horn antennas A-INFOMW LB-28-10-C-KF connected through a power divider.*

5.6. Conclusions

Throughout this chapter, the design and evaluation of a reflectarray with amplitude and phase constraints on its radiated near-field has been addressed to obtain a uniform

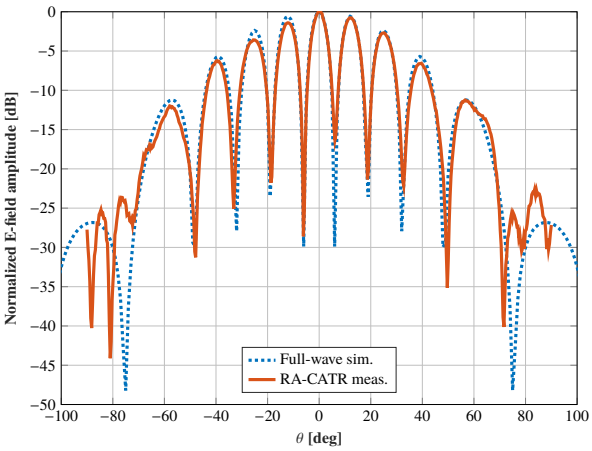

Figure 5.32: *Comparison of the measured and simulated radiation pattern at* 28 *GHz of the* 2×1 *horn antenna array.*

plane wave suitable for working as a CATR probe. First, a phase-only synthesis carried out with the generalized Intersection Approach provides the phase distribution of the reflectarray elements to obtain the required uniform plane wave. The phase-only synthesis synthesized simultaneously the amplitude and the phase of the radiated field. The near-field is synthesis at a distance of 46λ at a central frequency of 28 GHz, and the requirements are 1 dB and 10° of maximum peak-to-peak ripple in the amplitude and phase of the near-field, respectively. The reflectarray is designed using a three parallel dipole element that provides a full phase cycle for a single linear polarization. The measurements show a quite good agreement with simulations, resulting in high compliance of the requirements, both amplitude, and phase. Nearly the 90% of the main cuts at the four different planes are within a 1-1.5 dB peak-to-peak ripple, and a taper lower than 1 dB. The phase of the uniform plane wave is significantly plane through the measured range, and almost a 90% is within 10° of ripple and a 100% within 15°. The uniform plane wave radiated by this prototype practically satisfies the theoretical requirements in a volume of 100mm $\times$ 100mm $\times$ 150mm.

Then, the phase-only synthesis is repeated for two linear polarizations to achieve the same uniform plane wave but dual-polarized. Because of the phase-only considerations is not possible to control both polarizations in the same synthesis, therefore two POS are carried out. In this case, the element is based on two sets of three parallel dipoles printed in the same layer. Hence, it is possible to obtain a dual-polarized reflectarray in a single layer, which provides a low-profile antenna. The final layout is analyzed with a MoM simulation obtaining high compliance of the requirements in

both polarizations, improving the amplitude results of the previous single-polarized reflectarray while keeping the phase behavior.

Finally, the idea of a CATR based on a reflectarray antenna is demonstrated. To evaluate the viability of this concept the reflectarray manufactured in the first section is integrated into a homemade CATR. Two different antenna configurations are measured using the reflectarray as a probe, obtaining a high agreement between the radiation pattern measurements and full-wave simulation of these antenna configurations.

To demonstrate that reflectarray antennas are a potential alternative in the generation of uniform plane wave at millimeter frequencies, as a low-profile low-cost solution for a compact measurement system. The generalized Intersection Approach for near-field has been demonstrated to be powerful in the synthesis of spatially-fed array antennas with complex amplitude and phase patterns.

CHAPTER 6

Conclusions and future research lines

6.1. Final conclusions

This thesis has been devoted to the development of techniques for the analysis and synthesis of spatially-fed array (SFA) antennas for applications within the Fresnel region. A computational model of the near-field radiated by SFA antennas is presented, which is based on the Huygens' Principle and the radiated fields are obtained by superposition. The SFA aperture is sampled accomplishing the Nyquist Theorem and each sample is considered an element modeled as a punctual isotropic source, similar to array theory. The near-field at a point of the space is obtained by the superposition of the radiation of each element. Then, the accuracy was improved by considering each element of the SFA as a small radiating aperture, instead of a punctual isotropic source. This consideration allows us to take the radiated power of the elements into account. The element contribution is computed applying the theory of aperture antennas, which mainly analyses the element with the Equivalence Principle computing the far-field from the tangential fields. When computing the far-field radiated by an aperture antenna, the three Principles of Equivalence can be used, depending on the knowledge of the field in the aperture. It is commonly used the Second Principle of Equivalence since it only requires knowledge of the tangential electric field. The First Principle of Equivalence requires the tangential magnetic field in the aperture, which can be obtained by assuming a locally incident plane wave at the element. This model enables the computation of the field radiated by the SFA at any arbitrary point, provided that the point is within the far-field of a single SFA element. The model is presented together with power analysis, defining different parameters

similar to far-field. Particularly, the power radiated, radiation intensity, link budget, and gain for an SFA antenna are defined and particularized for the Fresnel region.

Concerning the synthesis of SFA antennas, a synthesis technique is introduced to improve the copolar component of SFA near-fields. The Intersection Approach (IA) algorithm for Phase-Only Synthesis (POS) is particularized for the near-field. This algorithm is a very efficient solution that has been extensively used in reflectarray synthesis with great success. Part of its efficiency is due to the FFT used to implement the backward projector. However, when dealing with a near-field implementation the FFT cannot be applied, and the backward projector must be redefined. The Levenberg-Marquardt algorithm (LMA) was chosen to implement the backward projector because of its simplicity and capacity to solve non-linear optimization problems. This leads to obtaining a general optimizing algorithm so-call the generalized Intersection Approach for near-field. The efficiency of the algorithm is significantly decreased about the IA for the synthesis of far-field. However, this approach allows the synthesis of SFA antennas with both amplitude and phase constraints. Also, the efficiency is improved using the finite difference technique in the Jacobian matrix computation.

The rest of the thesis is devoted to the analysis of different SFA antennas to their use in different near-field applications. Some of these applications demand shaped-beam antennas and the generalized Intersection Approach is applied to satisfy the different specifications.

A graded-index planar lens is designed to evaluate its performance to generate Bessel beams at millimeter band, particularly in Ka-band. The antenna is made up of dielectric-only elements, and two novel element topologies are proposed. The phase-shift of the elements is controlled by the insertion of air gaps in the dielectric elements. The air gap insertion modifies the overall infill of the cell and the dielectric constant is modified which also modifies the phase-shift. Although two different topologies are presented, the geometry of both cell and air gap does not affect the phase response of the cell, provided that the overall infill of the cell is kept. The graded-index planar lens is designed to produce a Bessel beam within a range of 650 mm and two different prototypes are manufactured (one for each type of cell). The prototypes are manufactured taking the advantage of 3D printing techniques. The two prototypes are evaluated showing good performances in the generation of Bessel beam within a range from 26 GHz to 30 GHz. Two important conclusions are obtained from these results. First, although Bessel beams are only achievable with infinite apertures, finite apertures and, small apertures as the ones used in this thesis, can also generate Bessel beams within a certain range. Second, SFA antennas are a potential alternative to generate this type of beam at millimeter bands, providing a low-profile antenna with good

performances. A second graded-index planar lens is designed and manufactured to be compared with the focusing capabilities of a doubly hyperbolic lens. Both alternatives achieve focusing the near-field with similar performances, and only two differences are appreciated. The graded-index planar lens does not deliver the maximum power at the theoretical focal point, and its operational bandwidth is limited by the phase response of the elements, while the bandwidth of the doubly-hyperbolic lens is inherently infinity. It is only limited by the bandwidth of the feed. The use of an SFA antenna could be useful for applications that demand light-weighted and compact antennas rather than solutions with large operational bandwidth. Then, the focused graded-index planar lens is evaluated along with an approach to generate a multi-focusing configuration. The approach is based on increasing the number of feeds so that each feed produces a different focused spot. This means using a cluster of horn antennas to illuminate the transmitarray antenna. The cluster must be placed following a circular arc path whose radius is equivalent to the focal distance of the SFA. This distribution ensures obtaining a similar incident field from each feed. Then, if the element has good angular response, the physical displacement of the feed will determine the focus direction of the beam. The prototype was measured following this configuration and the results show an angular spot distribution of $\pm 20^{\circ}$ within a bandwidth of 4 GHz, from 26 to 30 GHz. The use of dielectric-only elements in an SFA antenna enhances the bandwidth response of the antenna regarding resonant elements, reaching larger bandwidths. This approach provides a basic technique to obtain multiples beams. Despite having good results for the angular range evaluated, wider configurations are severely restricted by the angular stability of the cell, the spatial phase delay and the off-focus displacement of the feeds. The feed displacement mainly leads to phase aberrations which deteriorates the focusing properties. The combination of this approach with other phase correction techniques (such as the bifocal approach) would enhance the performances of the antenna for a wide angular configuration of the feeds.

Despite focusing the power within the Fresnel region of the antenna has been the most popular performance demanded on near-field antennas, there is a current interest in extending the range of near-field antenna applications. Some of them requiring shaped-beam patterns similar to far-field. Hence, the generalized Intersection Approach for near-field has been applied to synthesize two SFA antennas, a reflectarray and a transmitarray, to reach a near-field pattern with amplitude constraints. Both syntheses aim to evaluate the performances of SFA antennas working as a base station for 5G indoor communications, as well as the potential of the synthesis technique developed in the thesis. The first antenna is synthesized to radiate a rectangular-shaped beam on a plane to generate coverage over a desktop at a central frequency of 28 GHz.

The reflectarray is designed on a single layer of printed patches to obtain a single-layer low-profile solution, at the cost of having a phase-shift limitation of 260°. This phase limitation was included during the synthesis process. Owing to the patches can control two linear polarizations, the reflectarray operates on dual-polarized configuration and it generates a coverage with similar performances on the two linear polarizations. A prototype is manufactured, and the coverage is measured. The agreement between simulations and measurements is good, and the compliance of the requirements is significantly high for both polarizations. In the light of these results, the analysis, synthesis, and design technique presented through previous chapters, as well as reflectarray antennas, are validated to generated complex shaped-beam near-field patterns. Then, a transmitarray is synthesized to reach a large coverage area within its near-field region at 28 GHz. To increase the dimensions of the coverage and the capacity of the base station, the coverage is divided into several spots generated by different feeds but the same transmitarray. Then, the transmitarray is feed by multiple feeds following the technique proposed in Chapter 3. Particularly, 5 horn antennas are used to generate 5 spots at 28 GHz but working in orthogonal polarizations. As it was observed in Chapter 3, the proposed spatial feed distribution obtains good results on the generation of multiple focused beams. Now, the aim is to evaluate whether this technique is also adequate for shaped-beam patterns. So that, the central spot performances are improved with a phase-only synthesis carried out with the generalized Intersection Approach, and the adjacent spots are also improved due to the spatial feed distribution. The central spot after the synthesis shows an increase of the 457% of its size. However, in the adjacent spots, a certain distortion appears concerning the central spot. The feed displacement generates a progressive phase on the transmitarray surface, which modifies the pointing direction of the beam. However, the feeds also radiated a spherical wavefront that modifies the progressive phase, it thus also modified the transmitted field and the radiated field too. This effect was no appreciated in Chapter 3 since focused and pencil beams are more robust. Despite having this unexpected distortion, the coverage reaches 1.4 m in its main planes. The measured prototype highly agrees with simulations, obtaining similar performances and distortions. The slight differences are mainly because of the amplitude response of the cell, which is not considered during the synthesis since the elements are modeled as ideal phase-shifters. In the topic of shaped-beam patterns with amplitude constraints within the near-field, it is also presented a novel approach to deal with large areas of coverage. In this case, two key points are demonstrated. First, the generalized Intersection Approach can synthesize the near-field in a plane defined along the propagation direction. Second, the proposed technique based on defining the templates

following an adaptive process improves the convergence of the algorithm when dealing with large complex shaped-beam patterns. In the case presented, the combination of both techniques achieves a uniform power density within a range larger than 14 meters with a complex shape. An overall conclusion from the synthesis with SFA with amplitude constraints is that the generalized Intersection Approach is a powerful algorithm to obtain complex shaped-beam patterns in the near-field. Despite not being as efficient as the classical implementation using the FFT on its projectors, the use of the LMA allows overcoming the limitation of only synthesizing planes parallel to the antenna aperture. This approach provides a general solution for the synthesis of SFA antennas with complex and tight requirements on the amplitude of the field radiated.

Then, the generalized Intersection Approach has been used for the synthesis of SFA antennas with both amplitude and phase constraints on their radiated near-field. The aim is to generate a uniform plane wave with a reflectarray, so that these antennas can be used as a CATR probe. The generalized Intersection Approach is used to reach a phase distribution of the reflectarray elements that satisfy the requirement to consider the near-field as a uniform plane wave. The phase-only synthesis must consider the amplitude and phase requirements simultaneously. In this case, the uniform plane wave is generated at a distance of 46λ at an operational frequency of 28 GHz. The near-field must fulfill a maximum ripple of 1 dB on its amplitude and 10° on its phase to be considered as a uniform plane wave. Once the phase distribution is obtained, the reflectarray is designed using a three parallel dipole element for a single linear polarization. The measurements show a quite good agreement with simulations, with a high compliance of the requirements over a volume of 100 mm $\times$ 100 mm $\times$ 150 mm. A nearly 90% of the main cuts within this volume present a ripple lower than 1-1.5 dB (evaluation the peak-to-peak ripple), and a taper lower than 1 dB. The phase is notably plane through the measured range, and almost the 90% is within a ripple of 10° and a 100% within 15°. Then, the POS is repeated for considering the same uniform plane wave but dual-polarized. Owing to the phase-only synthesis limitations is not possible to control both polarization on the same process, thus two different POS are carried out. After these processes, the reflectarray is designed using an element based on two sets of three parallel dipoles printed in the same layer. This topology allows obtaining a dual-polarized reflectarray in a single layer structure, which provides an ultra-thin low-profile antenna. The layout is analyzed with a MoM simulation. The results show high compliance of the requirements on both polarizations, even improving the amplitude results of the previous single-polarized reflectarray. Since the main goal is to evaluate the capability of reflectarray antennas acting as a probe of a CATR system at millimeter frequencies, a reflectarray-based CATR is presented. The

single-polarized reflectarray is integrated into a homemade CATR to evaluate its performance in measuring different antenna radiation patterns. Particularly, two different antennas configurations are measured using this reflectarray as a probe: a single horn antenna and a 2×1 array of horn antennas, both at 28 GHz. The radiation pattern is measured with success, obtaining a high agreement between these measurements and the full-wave simulation of the two different antenna configurations. From these results, two important conclusions can be deduced. Reflectarray antennas are a potential alternative in the generation of uniform plane wave at millimeter frequencies, as a low-profile low-cost solution for compact measurement antenna systems. Then, the generalized Intersection Approach for near-field has been demonstrated to be powerful in the synthesis of SFA antenna. It is worthy to note that this approach cannot only address complex amplitude requirements but also with tight phase constraints simultaneously.

6.2. Original contributions

The following contributions have resulted from the work developed in the present thesis.

- **Development of the near-field model for spatially-fed array antennas**. This model is based on Huygens' Principle together with the Principle of Superposition. The near-field of the whole SFA is computed as the superposition of the far-field contribution of all the elements. Based on Huygens' Principle, the elements are modeled as a punctual isotropic source similar to array near-field models. In this thesis, the accuracy is improved by considering the elements as a small aperture, instead of a punctual isotropic source. The far-field contribution of the element is formulated from the Equivalent Principles, as in a general aperture analysis. The near-field analysis of the SFA is completed with power analysis, defining different parameters such as the radiation intensity or the gain on near-field, which are not defined in the previous works in the literature.

- **Development of the generalized Intersection Approach for near-field** for the first time. The near-field model described in previous point has been included in the Intersection Approach algorithm to synthesize SFA antennas with near-field constraints. Owing to the backward projector cannot be easily implemented to retrieve the field at the antenna apertures, the Levenberg-Marquardt algorithm is used instead. It overcomes the limitations of other approaches found in the literature which only can impose constraints on a plane parallel to the antenna aperture.

- **Application of the generalized Intersection Approach to control the amplitude, and the amplitude and phase of the radiated near-field**. This technique permits to impose of requirements on the amplitude to shape it. In addition, it is feasible to control both amplitude and phase, imposing constraints on both during the synthesis process for the first time, as it was demonstrated in the design of a reflectarray to obtain a uniform plane wave.

- **A novel dual-polarized air gap dielectric-only cell has been proposed to design dielectric-only transmitarrays in millimeter band**. The cell is based on a hosting dielectric material with an embedded air inclusion. This air inclusion allows the modification of the overall infill of the element; therefore the effective dielectric constant is modified too. Since the effective dielectric constant changes, the phase-shift of the element can be adjusted. An important feature of

this concept is that the geometry of the cell and the air inclusion does not affect the phase-shift of the element. Two different topologies have been analyzed obtaining similar results, provided that the overall infill of the cell is kept. An analytical expression has been obtained to characterize the phase response for different angles of incidence. This expression is used to improve the accuracy of the design of the transmitarray.

- **A dielectric-only transmitarray has been designed, manufactured, and tested to experimentally demonstrate the generation of non-diffraction beams in Ka-band with a relatively small aperture**. The transmitarray prototype has been designed to generate a pseudo-Bessel beam within a range of 54.8λ using an aperture of $12\lambda \times 12\lambda$ at 30 GHz. This is the first transmitarray comprised of dielectric cells which are not based on a height adjustment of the cell but air inclusions. The measurements have shown a high agreement with simulations and a good in-band response from 26 to 30 GHz. The overall performances of the obtained Bessel beam are quite good concerning other published works related to 3D printed transmitarray or lenses.

- **A dual-polarized shaped-beam reflectarray has been designed, manufactured, and tested to experimentally provide coverage in indoor femtocells**. The phase distribution has been obtained through a phase-only synthesis carried out with the generalized Intersection Approach with amplitude constraints. Since the elements of the reflectarray are printed patches, a full phase range is not achievable. This phase restriction has been included in the formulation to obtain a phase distribution that can be obtained by the proposed topology. Then, the adjustment of the reflectarray elements has been carried out cell by cell, by means of an efficient homemade routine based on the Method of Moments, assuming local periodicity. The reflectarray generates a dual-polarized uniform power distribution within a rectangular contour of 0.36 mm^2 on a horizontal plane oblique to the propagation direction. The measurements of the reflectarray prototype have proven the proposed phase-only synthesis technique, as well as the near-field model developed in this thesis. The results of the manufactured prototype show a good agreement with simulations.

- **Multiple near-field focused beams are obtained with SFAs fed by a cluster of feeds**. The approach is based on placing the different feeds along an arc path so that each feed generates a different beam. This approach is commonly used on multi-beam antennas in far-field applications. However, only a few works can be found for near-field in the literature. This approach has

been experimentally evaluated to generate multiple focused spots in the Fresnel region of a transmitarray antenna. The concordance between simulations and measurements is quite good, obtaining a basic approach suitable for generating multiple beams in the near-field. Then, this approach was evaluated for a transmitarray that radiates a shaped beam near-field pattern. Also, each feed produces a different beam pointing to a direction defined by the feed position. Despite having a good agreement between simulations and measurements, the displaced beams are slightly distorted. However, the distortion is not caused due to the feed distribution but the designing technique.

- **A novel procedure to define the templates on the phase-only synthesis to achieve successful results on complex near-field scenarios is demonstrated**. For instance, a shaped-beam with uniform power distribution within a large area through the propagation direction, which involves compensating the inherent effect of the natural electromagnetic behavior of the field. The convergence of the synthesis is deeply affected by the templates, and this technique improves the convergence since the radiated near-field itself defines the templates. Instead of defining an arbitrary template according to the desired specifications, the near-field defines the templates according to their shape and the desired specifications. With this approach, the synthesis will search for a solution closer to the starting point than defining a complex template which is unknown whether the antenna can generate it.

- **Demonstrator of the first reflectarray antenna with amplitude and phase constraints to generate a uniform plane wave in a volume close to the antenna aperture in Ka-band**. The reflectarray antenna has been designed using the generalized Intersection Approach with amplitude and phase requirements simultaneously, being the first time that a near-field synthesis is carried out considering both requirements. The reflectarray is designed using a three-dipole cell operating on single linear polarization. The adjustment of the reflectarray elements has been carried out element by element, assuming local periodicity and the real angle of incidence, using an efficient homemade routine based on the Method of Moments. The measurements of the reflectarray have proven the proposed near-field model, as well as the synthesis technique with both amplitude and phase requirements.

- **A novel concept of a reflectarray-based Compact Antenna Test Range for measuring antennas and OTA 5G New Radio Devices in Ka-band**. A reflectarray antenna is proposed to be used as a probe of a reduced and

portable CATR range mainly focused on the antenna measurement of 5G devices. The reflectarray radiates a near-field that satisfies the tight requirements to be considered as a quiet zone wherein the device under test must be placed. Since the quiet zone is created close to the antenna aperture the total structure of the CATR system is significantly reduced, which also minimizes the signal propagation issues associated with those operational frequencies. The reflectarray has been integrated into a homemade CATR, working as a probe, and it has been tested by measuring two antenna configurations. The measured radiation pattern is compared with full-wave simulations, obtaining a high concordance between both. In the light of these results, the reflectarray-based CATR proposed in this thesis is validated for the first time with successful results on the characterization of antennas in Ka-band.

6.3. List of publications related to this work

The original contributions of this thesis have motivated the publication of several papers in international journals and conferences. They are listed below.

6.3.1. International journals

[J1] D. R. Prado, **A. F. Vaquero**, M. Arrebola, M. R. Pino, F. Las-Heras, "General Near Field Synthesis of reflectarray antennas for their use as probes in CATR", *PIER Progress in Electromagnetics Research*, vol. 160, pp. 9-17, 2017.

[J2] D. R. Prado, **A. F. Vaquero**, M. Arrebola, M. R. Pino, F. Las-Heras, "Acceleration of Gradient-Based Algorithm for Near and Far Field Array Antennas Optimization Based on Finite Differences", *IEEE Transactions on Antennas and Propagation*, vol. 66, no. 10, pp. 5239-5248, Oct. 2018.

[J3] **A. F. Vaquero**, M. R. Pino, M. Arrebola, S. A. Matos, J. R. Costa, C. A. Fernandes, "Bessel Beam Generation Using Dielectric Planar Lenses at Millimeter Frequencies", *IEEE Access*, vol. 8, pp. 216185-216196, 2020.

[J4] **A. F. Vaquero**, M. R. Pino, M. Arrebola,S. A. Matos, J. R. Costa, C. A. Fernandes, "Evaluation of a Dielectric-Only Transmitarray for Generating Multi-Focusing Near-Field Spots Using a Cluster of Feeds in the Ka-band", *Sensors*, vol. 21, no. 2, Jan. 2021.

[J5] **A. F. Vaquero**, M. Arrebola, M. R. Pino, R. Florencio, J. A. Encinar, "Demonstration of a Reflectarray with Near-field Amplitude and Phase Constraints as

Compact Antenna Test Range Probe for 5G New Radio Devices", *IEEE Transactions on Antennas and Propagation*, vol. 69, no. 5, pp. 2715-2726, May. 2021.

[J6] **A. F. Vaquero**, M. R. Pino, M. Arrebola,"Dual-Polarized Shaped-Beam Transmitarray to Improve wide-angular 5G femtocell", *IEEE Antennas Wireless Propagation Letters*, (under review).

[J7] B. Imaz-Lueje, **A. F. Vaquero**, D. R. Prado, M. R. Pino, M. Arrebola, "Shaped-Pattern Reflectarray Antennas for mm-wave Networks Using a Simple Cell Topology", *IEEE Access*, (under review).

6.3.2. International conferences

[C1] **A. F. Vaquero**, D. R. Prado, M. Arrebola, M. R. Pino and F. Las-Heras, "Near field synthesis of reflectarray antennas based on Intersection Approach", *11^{th} European Conference on Antennas and Propagation (EuCAP)*, Paris, (France), 19-24/03/2017. (Convened Session).

[C2] **A. F. Vaquero**, M. Arrebola, M. R. Pino, J. R. Costa, S. Matos, and C. A. Fernandes, "Low-Cost Dielectric Flat Lens for Near-Field Focusing", *Proc. of the 2018 IEEE International Symposium on Antennas and Propagation (APS) & USNC/URSI National Radio Science Meeting*, Boston, (USA), 08-13/07/2018.

[C3] **A. F. Vaquero**, D. R. Prado, M. Arrebola, and M. R. Pino, "Reflectarray Antenna for 5-G Indoor Coverage", *Proc. of the 13^{th} European Conference on Antennas and Propagation (EuCAP)*, Krakow, (Poland), 31/03-05/04/2019. (Convened Session).

[C4] **A. F. Vaquero**, M. Arrebola, and M. R. Pino, "Spatially-fed arrays for near-field multiple-spot coverage", *Proc. of the International Conference on Electromagnetic in Advanced Applications and Topical Conference on Antennas and Propagation in Wireless Communications (ICEAA)*, Granada (Spain), 9-13/09/2019. (Special session).

[C5] **A. F. Vaquero**, M. Arrebola, and M. R. Pino, "Near-field multi-focusing transmit-array optimization for multi-position feed", *Proc. of the 41st Annual Meeting & Symposium of the Antenna Measurement Techniques Association (AMTA)*, San Diego, California (USA), 6-11/10/2019.

[C6] **A. F. Vaquero**, M. Arrebola, and M. R. Pino, "Bandwidth response of a reflectarray antenna working as a Compact Antenna Test Range probe", *Proc. of the 41st Annual Meeting & Symposium of the Antenna Measurement Techniques Association (AMTA)*, San Diego, California (USA), 6-11/10/2019.

[C7] **A. F. Vaquero**, M. Arrebola, M. R. Pino, R. Florencio, and J. A. Encinar, "Performance evaluation of near-field plane wave generated by a reflectarray for 5G testing", *Proc. of the 2020 IEEE International Symposium on Antennas and Propagation (APS) & USNC/URSI National Radio Science Meeting*, Boston, (USA), 05-10/07/2020. (Special Session).

[C8] **A. F. Vaquero**, M. Arrebola, M. R. Pino, J. A. Encinar, "Evaluation of a Ka-Band reflectarray Capability to Generate a Uniform Plane Wave in Near Field Region", *Proc. of the 15th European Conference on Antennas and Propagation (EuCAP)*, Düsseldorf (Germany), 22-26/03/2021.

[C9] E. Martinez-de-Rioja, **A. F. Vaquero**, M. Arrebola, E. Carrasco, J. A. Encinar, and M. Achour, "Passive Dual-Polarized Shaped-Beam Reflectarrays to Improve Coverage in Millimeter-Wave 5G Networks", *15th European Conference on Antennas and Propagation (EuCAP)*, Düsseldorf (Germany), 22-26/03/2021.

6.3.3. National conferences

[N1] **A. F. Vaquero**, M. Arrebola, and M. R. Pino, "Reflectarray as plane wave generator for Compact Antenna Test Range in millimeter frequency band", *XXXIV Simposium Nacional de la Unión Científica Internacional de Radio (URSI)*, Málaga (Spain), 04-06/09/2020
Accésit best Young Researcher Paper Award.

[N2] **A. F. Vaquero**, M. R. Pino, and M. Arrebola, "Multi-feed shaped-beam perforated dielectric transmitarray in millimeter-band", *XXXVI Simposium Nacional de la Unión Científica Internacional de Radio (URSI)*, Vigo (Spain), 20-24/09/2021 (Special session).

6.4. Other publications

During the thesis period, and as a result of a short stay at Instituto of Telecomuniçaões, Lisbon, Portugal, under the supervision of Prof. Jorge Rodrigues Costa, a paper is still preparing on the subject of wide-scanning transmitarray in an international journal.

Additionally, as a result of different works developed in parallel to the thesis, two papers were published, and another is still preparing on the subject of printed reflector antennas. Two of them in an international journal and another in an international conference. They are listed below:

[O1] A. Rebollo, **A. F. Vaquero**, M. Arrebola, and M. R. Pino, "3D-Printed Dual-Reflector Antenna With Self-Supported Dielectric Subreflector", *IEEE Access*, vol. 8, pp. 209091-209100, 2020.

[O2] A. Rebollo, **A. F. Vaquero**, M. Arrebola, M. R. Pino, "Experimental validation of a compact 3D-printed subreflector subsystem for Cssegrain antenna in X-band", *Proc. of the 15th European Conference on Antennas and Propagation (EuCAP)*, Düsseldorf (Germany), 22-26/03/2021.

[O3] A. Rebollo, **A. F. Vaquero**, M. R. Pino, and M. Arrebola, "Dual-band mm-Wave Cassegrain Antenna in Additive Manufacturing Technology", *IEEE Antennas Wireless Propagation Letters*, (in preparation).

[O4] **A. F. Vaquero**, S. A. Matos, M. Arrebola, J. R. Costa, C. A. Fernandes, "Wide-scanning 3D-printed transmit-array for SATCOM in Ka-band", *IEEE Transactions on Antennas and Propagation*, (in preparation).

6.5. Projects related to this work

Part of the work of the present thesis has contributed to the development of several research projects. The listed main researchers belong to the institution where the thesis work was developed.

[P1] **"Development of a European-based Collaborative Network to Accelerate Technological, Clinical and Commercialisation Progress in the Area of Medical Microwave Imaging"** , Code: TD1301, Funding: ESF/COST, Term: 01/11/2013–01/11/2017. Main researcher: Jorge Manuel Lopes Leal Rodrigues da Costa.

[P2] **"Reflectarray Antennas with Improved Performances And Design Techniques (RAIPAD)"** , Code: 1-7064/12/NL/MH, Funding: European Space Agency (ESA), Term: 01/09/2012–31/03/2014. Main researcher: Manuel Arrebola.

[P3] **"Antenas Reconfigurables para Transferencia Eficiente de Información y Energía a múltiples usuarios en femtoceldas/Reconfigurable Antennas for a Multi-User Efficient Information and Energy Transfer in femtocells (ARTEINE)"**, Code: MINECO-18-TEC2017-R, Funding: Ministerio de Economía y Competividad (Spanish Goverment), Term: 01/01/2018–31/12/2020. Main researcher: Marcos Rodríguez Pino and Germán León.

[P4] **"Ayudas a organismos públicos de investigación para apoyar la actividad que desarrollen sus grupos de investigación en el Principado de Asturias en el periodo 2018-2020"**, Code: FC-GRUPIN-IDI/2018/000191, Funding: Principado de Asturias, Term: 01/01/2018–31/12/2020. Main researcher: Fernando Las-Heras Andrés.

[P5] **"RFID shoplifting Gateway in UHF band"**, Code: FUO-20-124, Funding: University of Pisa, Term: 01/04/2020–30/04/2020. Main researcher: Marcos Rodríguez Pino.

[P6] **"Synthesis and design of reflect-arrays for improving coverage of 5G base station antennas at mm-waves"**, Code: FUO-221-20, Funding: METAWAVE CORPORATION., Term: 01/09/2020– 01/08/2021. Main researcher: Manuel Arrebola.

6.6. Future research lines

The work presented in this thesis has opened several research lines of interest that could not be pursued. They are listed below, grouped whether they are aimed to improve either the near-field model or the synthesis, or near-field applications.

6.6.1. Related to near-field modeling and synthesis

- **Enhancement of near-field modeling for spatially-fed array antennas**. On one hand, different approaches can be applied to speed up the computation of the radiated field as well as obtaining a more efficient computation. On the other hand, different approaches can be used to improve the accuracy of the near-field model, which include the cross-polar components and other effects associated with the antenna such as diffraction at edges or the radiation of the primary feed.
    - Ddifferent approaches can be implemented to speed up and increase the efficiency of the near-field computation of an SFA antenna. Firstly, the

FFT can be applied to the tangential field at the aperture of the SFA to obtain the radiated field, similar to the approaches used on the far-field computation of reflectarray and transmitarray antennas. Secondly, another alternative is based on the use of the Plane Wave Spectrum, which provides a more efficient computation than the model presented in this thesis. Both methods speed up and increase the efficiency of the near-field model. However, they are strongly limited to the condition of computing the near-field in planes parallels to the aperture of the SFA antenna, obtaining a faster and more efficient calculation at the cost of reducing the volume wherein the near-field can be computed.

- The model presented in this thesis improves its accuracy by considering the SFA elements as a small aperture instead of a punctual isotropic source, as it occurs on array models. However, it is assumed that the tangential field at the element surface is constant. Different alternatives could enhance the accuracy of the model such as modeling the field at the element as cosine, cosine squared, or a Gaussian. Another alternative is increasing the sampling on the SFA surface so that the tangential field is computed at several positions within the element surface. This last approach would take the phase variation through the cell into account.

- As a result of applying the previous point on the model presented in this thesis, the accuracy of the near-field computation would be improved. However, the accuracy of the cross-polar component deeply depends on having an accurate and full characterization of the matrix $\boldsymbol{A}$. This analysis can be included in the near-field model, which would allow obtaining a quite accurate computation of all radiated components. Through the different chapters, the characterization of the cell has been obtained using CST Microwave Studio or a dedicated MoM software. However, these solutions significantly increase the computational cost of the model since they must be applied to each element of the SFA to compute the tangential fields. A potential alternative is the use of surrogate models together with different Artificial Intelligence (IA) techniques, such as Artificial Neural Networks (ANN), Support Vector Machines (SVM), or kriging. Another alternative is the modeling of the SFA elements with equivalent circuits. These different alternatives allow obtaining an efficient full characterization of the matrix $\boldsymbol{A}$ concerning a dedicated MoM software or CST Microwave Studio.

- The diffraction effects because of the edge of the SFA antenna can be mini-

mized by imposing a high illumination taper level. However, it is not always possible to achieve that. The illuminations taper is mainly imposed by the primary feed and the f/D rate. Including a diffraction model in the analysis would improve the characterization of the radiated field, especially when dealing with near-field shaped beams close to the antenna aperture. Other effects can be also included in the SFA analysis, such as the radiation of the primary feed or evanescent modes. The first effect may have a deep impact when the distance at which the near-field is computed is very close to the antenna aperture and the primary feed has secondary lobes pointing to the same direction as the SFA does. Second, the evanescent modes are negligible in the far-field analysis. However, these modes can play an important role in the near-field analysis. It could be especially interesting to include the high order evanescent Floquet modes in the near-field model and characterize their influence in the radiated field when the near-field is computed very close to the SFA aperture.

- **Extend the formulation of the near-field model from linear polarized to circular polarized SFA antennas**. The current formulation has been developed and validated for linear polarized SFA antennas, though the model can be extended to considered circular polarization. This new formulation would require manufacturing different SFA prototypes to validate the new formulation with measurements.

- **The synthesis technique can be extended to directly optimize the layout of an SFA antenna in near-field applications**. The presented POS technique allows achieving very complex shaped beams. However, since it only works with the phase of the direct coefficients, there is no control over different parameters such as the bandwidth or the cross-polar during the synthesis process.

    - A direct optimization of the layout implies optimizing one or several parameters of the SFA element geometry. Therefore, it is necessary to include a method to analyze the SFA element response during the optimization process. This fact would significantly reduce the efficiency of the algorithm. A key factor is to develop an efficient characterization of the matrix $\boldsymbol{A}$ on the optimization process. As it was pointed out before different IA techniques can be used, such as SVM, kriging, equivalent circuit models, or even a dedicated MoM analysis for a given geometry.

- A direct optimization would allow to obtain purely polarized beams in the near-field region.
- A direct optimization of the layout would enable bandwidth optimizations or even considering a multi-feed configuration during the optimization process. This type of optimization needs to consider the real angle of incidence of the different feeds in each element since the element response would change from one incident field to the other. This effect is similar to a multi-band optimization. The element response would change from one frequency to the others and the element response must be included in the optimization.

6.6.2. Related to near-field applications

- Concerning **near-field focusing SFA antennas**, the next points could be evaluated to have a further analysis of SFA antennas with these capabilities.
  - Development SFA antennas with near-field focusing capabilities based on additive manufacturing techniques using ultra-thin elements. The SFA antennas manufactured on these technologies typically use dielectric-only elements, whose phase-shift is obtained by the variation of their effective dielectric constant. The use of materials with a high dielectric constant compatible with additive manufacturing techniques would allow a reduction of the size of the SFA elements, to reach thinner topologies similar to printed SFA antennas.
  - Evaluate focusing SFA antennas and their performances in a real system. Particularly, whether the use of non-diffraction beams improves the performances of different systems such as near-field radars for detection or imaging, or WPT systems.
  - Development of reconfigurable SFA antennas with scanning capabilities of the near-field focus. This characteristic would have a particular interest in detection application since different points of a surface can be scanned without a displacement of the antenna or the object under observation. In addition, the reconfigurability of the spot would allow changing the pointing direction of the antenna to be focused wherein the devices or objects are located. This fact would increase the efficiency of WPT or minimize the undesired scattering on MWI. Also, spot reconfigurability can be applied

to correct the spot deviation because of frequency variations on wideband near-field radars.

- The extension of the algorithm to address a direct optimization of the SFA layout would allow enhancing the **SFA** performances **for wireless communication coverages**.

  - This optimization may reach complex near-field shaped-beam patterns with bandwidth requirements or multi-band coverage configurations with a single SFA antenna since the different frequencies can be considered during the optimization process.

  - Likewise, the optimization of the layout would consider multi-feed configurations, which would increase the capacity of the base stations based on SFA antennas. Similar to space communications, the SFA can generate a spot by each feed, with orthogonal polarization, and obtaining coverage with high-pure-polarized spots.

  - The point discussed previously can be applied to circular polarized SFA antenna.

- The development of **compact antenna measuring systems**, with a reduced distance between the probe and the device under test, would allow to minimize the propagation loss, which can be notably important at high frequencies (millimeter, sub-millimeter o terahertz bands). The reflectarray-based Compact Antenna Test Range proposed in this thesis can be a potential alternative to be used at higher frequencies, such as the sub-millimeter band, for the next B5G or 6G communications. Conversely, the main drawback of reflectarray antennas is their narrow-band response, which can be overcome with a direct optimization of the layout with bandwidth requirements.

- General to the different near-field applications, it is a key factor **to study the capabilities of SFA antennas at higher frequencies**, making a special emphasis on popular bands such as V-band. This increase in the operational frequency would require to also analyze new manufacturing process more adequate to those frequencies. For instance, printed or dielectric-only elements could present significantly high losses, while metal-only elements may reduce them, becoming a more suitable solution.

- **Using conformal SFA surfaces, such as multi-faceted, curved, or spherical domes**, may enhance the performances of SFA antennas on several applications. Mainly, reducing the spill-over or increasing the bandwidth of the SFA.
- **Development of sensing systems** based on near-field SFA antennas **for the characterization of other devices or materials**.

References

[1] D. G. Berry, R. G. Malech, and W. A. Kennedy, "The reflectarray antenna," *IEEE Trans. Antennas Propag.*, vol. 11, no. 6, pp. 645–651, Nov. 1963.

[2] J. Huang and J. A. Encinar, *Reflectarray Antennas*. Hoboken, NJ, USA: John Wiley & Sons, 2008.

[3] J. Huang, "Bandwidth study of microstrip reflectarray and a novel phased reflectarray concept," in *Antennas and Propagation Society International Symposium*, vol. 1, Newport Beach, California, USA, Jun. 18–23, 1995, pp. 582–585.

[4] D. M. Pozar, "Bandwidth of reflectarrays," *Electron. Lett.*, vol. 39, no. 21, pp. 1490–1491, Oct. 2003.

[5] J. A. Encinar and J. A. Zornoza, "Broadband design of three-layer printed reflectarrays," *IEEE Trans. Antennas Propag.*, vol. 51, no. 7, pp. 1662–1664, Jul. 2003.

[6] N. Misran, R. Cahill, and V. Fusco, "Design optimisation of ring elements for broadband reflectarray antenna," *IEE Proc. Microw. Antennas Propag.*, vol. 150, no. 6, pp. 440–444, Dec. 2003.

[7] A. Massaccesi, P. Pirinoli, V. Bertana, G. Scordo, S. L. Marasso, M. Cocuzza, and G. Dassano, "3d-printable dielectric transmitarray with enhanced bandwidth at millimeter-waves," *IEEE Access*, vol. 6, pp. 46 407–46 418, 2018.

[8] E. Carrasco, J. A. Encinar, and M. Barba, "Bandwidth improvement in large reflectarrays by using true-time delay," *IEEE Trans. Antennas Propag.*, vol. 56, no. 8, pp. 2496–2503, Aug. 2008.

[9] M. Zhou, S. B. Sørensen, Y. Brand, and G. Toso, "Doubly curved reflectarray for dual-band multiple spot beam communication satellites," *IEEE Transactions on Antennas and Propagation*, vol. 68, no. 3, pp. 2087–2096, 2020.

[10] H. Legay, D. Bresciani, E. Labiole, R. Chiniard, and R. Gillard, "A multi facets composite panel reflectarray antenna for a space contoured beam antenna in Ku band," *Progr. Electromagn. Res. B*, vol. 54, pp. 1–26, Aug. 2013.

[11] M. Zhou, S. B. Sørensen, P. Meincke, and E. Jørgensen, "Design and optimization of multi-faceted reflectarrays for satellite applications," in *The 8^{th} European Conference on Antennas and Propagation (EUCAP)*, The Hague, The Netherlands, Apr. 6–11, 2014, pp. 1423–1427.

[12] D. M. Pozar, S. D. Targonski, and R. Pokuls, "A shaped-beam microstrip patch reflectarray," *IEEE Trans. Antennas Propag.*, vol. 47, no. 7, pp. 1167–1173, Jul. 1999.

[13] J. A. Encinar, L. S. Datashvili, J. A. Zornoza, M. Arrebola, M. Sierra-Castaner, J. L. Besada-Sanmartin, H. Baier, and H. Legay, "Dual-polarization dual-coverage reflectarray for space applications," *IEEE Trans. Antennas Propag.*, vol. 54, no. 10, pp. 2827–2837, Oct. 2006.

[14] H. Hasani, J. S. Silva, S. Capdevila, M. García-Vigueras, and J. R. Mosig, "Dual-band circularly polarized transmitarray antenna for satellite communications at (20, 30) ghz," *IEEE Transactions on Antennas and Propagation*, vol. 67, no. 8, pp. 5325–5333, 2019.

[15] P. Naseri, S. A. Matos, J. R. Costa, C. A. Fernandes, and N. J. G. Fonseca, "Dual-band dual-linear-to-circular polarization converter in transmission mode application to k/ka -band satellite communications," *IEEE Transactions on Antennas and Propagation*, vol. 66, no. 12, pp. 7128–7137, 2018.

[16] H. R. Phelan, "Spiralphase reflectarray for multitarget radar," *Microwave Journal*, vol. 20, no. 1, pp. 67–77, Jul. 1977.

[17] H. Kamoda, T. Iwasaki, J. Tsumochi, T. Kuki, and O. Hashimoto, "60-ghz electronically reconfigurable large reflectarray using single-bit phase shifters," *IEEE Transactions on Antennas and Propagation*, vol. 59, no. 7, pp. 2524–2531, 2011.

[18] O. Bayraktar, O. A. Civi, and T. Akin, "Beam switching reflectarray monolithically integrated with rf mems switches," *IEEE Transactions on Antennas and Propagation*, vol. 60, no. 2, pp. 854–862, 2012.

[19] M. Barba, E. Carrasco, J. E. Page, and J. A. Encinar, "Electronic controllable reflectarray elements in x band," *Frequenz*, vol. 61, no. 9-10, pp. 203–206, 2007.

[20] H. Legay, B. Salome, E. Girard, S. Ramongassie, J. Encinar, and G. Toso, "Reflectarrays antennas for sar missions," in *11th International Symposium on Antenna Technology and Applied Electromagnetics [ANTEM 2005]*, 2005, pp. 1–4.

[21] J. Wang, V. Manohar, and Y. Rahmat-Samii, "Beam steerable reflectarray enabling cubesat internet of space: Conceptualization and design (invited paper)," in *2020 14th European Conference on Antennas and Propagation (EuCAP)*, 2020, pp. 1–4.

[22] Y.-S. Chen, Y.-H. Wu, and C.-C. Chung, "Solar-powered active integrated antennas backed by a transparent reflectarray for cubesat applications," *IEEE Access*, vol. 8, pp. 137 934–137 946, 2020.

[23] S. R. Rengarajan, "Reflectarrays of rectangular microstrip patches for dual-polarization dual-beam radar interferometers," *Progr. Electromagn. Res.*, vol. 133, pp. 1–15, 2013.

[24] J. A. Encinar and J. A. Zornoza, "Three-layer printed reflectarrays for contoured beam space applications," *IEEE Trans. Antennas Propag.*, vol. 52, no. 5, pp. 1138–1148, May 2004.

[25] M. Arrebola, J. A. Encinar, and M. Barba, "Multifed printed reflectarray with three simultaneous shaped beams for LMDS central station antenna," *IEEE Trans. Antennas Propag.*, vol. 56, no. 6, pp. 1518–1527, Jun. 2008.

[26] P. Robustillo, J. Zapata, J. A. Encinar, and M. Arrebola, "Design of a contoured-beam reflectarray for a eutelsat european coverage using a stacked-patch element characterized by an artificial neural network," *IEEE Antennas Wireless Propag. Lett.*, vol. 11, pp. 977–980, 2012.

[27] M. Zhou, S. B. Sørensen, Y. Brand, and G. Toso, "Doubly curved reflectarray for dual-band multiple spot beam communication satellites," *IEEE Transactions on Antennas and Propagation*, vol. 68, no. 3, pp. 2087–2096, 2020.

[28] M. Zhou, O. Borries, and E. Jørgensen, "Design and optimization of a single-layer planar transmit-receive contoured beam reflectarray with enhanced performance," *IEEE Transactions on Antennas and Propagation*, vol. 63, no. 4, pp. 1247–1254, 2015.

[29] D. R. Prado and M. Arrebola, "Effective xpd and xpi optimization in reflectarrays for satellite missions," *IEEE Antennas and Wireless Propagation Letters*, vol. 17, no. 10, pp. 1856–1860, 2018.

[30] D. R. Prado, M. Arrebola, M. R. Pino, and F. Las-Heras, "Complex reflection coefficient synthesis applied to dual-polarized reflectarrays with cross-polar requirements," *IEEE Transactions on Antennas and Propagation*, vol. 63, no. 9, pp. 3897–3907, 2015.

[31] D. R. Prado, J. A. López-Fernández, M. Arrebola, M. R. Pino, and G. Goussetis, "Wideband shaped-beam reflectarray design using support vector regression analysis," *IEEE Antennas and Wireless Propagation Letters*, vol. 18, no. 11, pp. 2287–2291, 2019.

[32] W. Hu, M. Arrebola, R. Cahill, J. A. Encinar, V. Fusco, H. S. Gamble, Y. Álvarez, and F. Las-Heras, "94 GHz dual-reflector antenna with reflectarray subreflector," *IEEE Trans. Antennas Propag.*, vol. 57, no. 10, pp. 3043–3050, Oct. 2009.

[33] C. Tienda, J. A. Encinar, M. Arrebola, M. Barba, and E. Carrasco, "Design, manufacturing and test of a dual-reflectarray antenna with improved bandwidth and reduced cross-polarization," *IEEE Transactions on Antennas and Propagation*, vol. 61, no. 3, pp. 1180–1190, 2013.

[34] M. Abdollahvand, K. Forooraghi, J. A. Encinar, Z. Atlasbaf, and E. Martinez-de Rioja, "A 20/30 ghz reflectarray backed by fss for shared aperture ku/ka-band satellite communication antennas," *IEEE Antennas and Wireless Propagation Letters*, vol. 19, no. 4, pp. 566–570, 2020.

[35] E. Martinez-de Rioja, J. A. Encinar, M. Barba, R. Florencio, R. R. Boix, and V. Losada, "Dual polarized reflectarray transmit antenna for operation in ku- and ka-bands with independent feeds," *IEEE Transactions on Antennas and Propagation*, vol. 65, no. 6, pp. 3241–3246, 2017.

[36] D. R. Prado, M. Arrebola, M. R. Pino, and G. Goussetis, "Contoured-beam dual-band dual-linear polarized reflectarray design using a multiobjective multistage optimization," *IEEE Transactions on Antennas and Propagation*, vol. 68, no. 11, pp. 7682–7687, 2020.

[37] D. Martinez-de Rioja, R. Florencio, E. Martinez-de Rioja, M. Arrebola, J. A. Encinar, and R. R. Boix, "Dual-band reflectarray to generate two spaced beams

in orthogonal circular polarization by variable rotation technique," *IEEE Transactions on Antennas and Propagation*, vol. 68, no. 6, pp. 4617–4626, 2020.

[38] S. Mener, R. Gillard, R. Sauleau, A. Bellion, and P. Potier, "Dual circularly polarized reflectarray with independent control of polarizations," *IEEE Transactions on Antennas and Propagation*, vol. 63, no. 4, pp. 1877–1881, 2015.

[39] J. Lanteri, C. Migliaccio, J. Ala-Laurinaho, M. Vaaja, J. Mallat, and A. V. Raisanen, "Four-beam reflect-array antenna for mm-waves: Design and tests in far-field and near-field ranges," in *2009 3rd European Conference on Antennas and Propagation*, 2009, pp. 2532–2535.

[40] D. Martinez-De-Rioja, E. Martinez-De-Rioja, J. A. Encinar, R. Florencio, and G. Toso, "Reflectarray to generate four adjacent beams per feed for multispot satellite antennas," *IEEE Transactions on Antennas and Propagation*, vol. 67, no. 2, pp. 1265–1269, 2019.

[41] E. Martinez-de Rioja, J. A. Encinar, A. G. Pino, B. Gonzalez-Valdes, S. V. Hum, and C. Tienda Herrero, "Bifocal design procedure for dual-reflectarray antennas in offset configurations," *IEEE Antennas and Wireless Propagation Letters*, vol. 17, no. 8, pp. 1421–1425, 2018.

[42] E. Martinez-de Rioja, J. A. Encinar, R. Florencio, and C. Tienda, "3-d bifocal design method for dual-reflectarray configurations with application to multibeam satellite antennas in ka-band," *IEEE Transactions on Antennas and Propagation*, vol. 67, no. 1, pp. 450–460, 2019.

[43] D. Martinez-de Rioja, E. Martinez-de Rioja, Y. Rodriguez-Vaqueiro, J. A. Encinar, A. Pino, M. Arias, and G. Toso, "Transmit–receive parabolic reflectarray to generate two beams per feed for multispot satellite antennas in ka-band," *IEEE Transactions on Antennas and Propagation*, vol. 69, no. 5, pp. 2673–2685, 2021.

[44] M. Zhou, S. B. Sørensen, P. Meincke, and E. Jørgensen, "Design and optimization of multi-faceted reflectarrays for satellite applications," in *The 8th European Conference on Antennas and Propagation (EuCAP 2014)*, 2014, pp. 1423–1427.

[45] V. Patel, P. Mevada, D. Pujara, S. Chakrabarty, and M. Mahajan, "Analysis of multi-faceted reflectarray antenna for spatial bandwidth improvement," in *2020 IEEE International Symposium on Antennas and Propagation and North American Radio Science Meeting*, 2020, pp. 359–360.

[46] D. McGrath, "Planar three-dimensional constrained lenses," *IEEE Transactions on Antennas and Propagation*, vol. 34, no. 1, pp. 46–50, 1986.

[47] A. Aziz, X. Zhang, F. Yang, S. Xu, and M. Li, "A dual-band orthogonally polarized contour beam transmitarray design," *IEEE Transactions on Antennas and Propagation*, pp. 1–1, 2021.

[48] C. C. Cruz, C. A. Fernandes, S. A. Matos, and J. R. Costa, "Synthesis of shaped-beam radiation patterns at millimeter-waves using transmit arrays," *IEEE Transactions on Antennas and Propagation*, vol. 66, no. 8, pp. 4017–4024, 2018.

[49] M. Frank, F. Lurz, R. Weigel, and A. Koelpin, "Electronically reconfigurable 6 × 6 element transmitarray at k-band based on unit cells with continuous phase range," *IEEE Antennas and Wireless Propagation Letters*, vol. 18, no. 4, pp. 796–800, 2019.

[50] J. Y. Lau and S. V. Hum, "Reconfigurable transmitarray design approaches for beamforming applications," *IEEE Transactions on Antennas and Propagation*, vol. 60, no. 12, pp. 5679–5689, 2012.

[51] M. Maasch, M. Roig, C. Damm, and R. Jakoby, "Voltage-tunable artificial gradient-index lens based on a liquid crystal loaded fishnet metamaterial," *IEEE Antennas and Wireless Propagation Letters*, vol. 13, pp. 1581–1584, 2014.

[52] T. K. Pham, L. Guang, D. González-Ovejero, and R. Sauleau, "Dual-band transmitarray with low scan loss for satcom applications," *IEEE Transactions on Antennas and Propagation*, vol. 69, no. 3, pp. 1775–1780, 2021.

[53] E. B. Lima, S. A. Matos, J. R. Costa, C. A. Fernandes, and N. J. G. Fonseca, "Circular polarization wide-angle beam steering at ka-band by in-plane translation of a plate lens antenna," *IEEE Transactions on Antennas and Propagation*, vol. 63, no. 12, pp. 5443–5455, 2015.

[54] E. Martinez-de Rioja, J. A. Encinar, A. Pino, B. Gonzalez-Valdes, S. V. Hum, C. Tienda, and G. Toso, "Bifocal technique applied to dual transmitarray antennas," in *12th European Conference on Antennas and Propagation (EuCAP 2018)*, 2018, pp. 1–5.

[55] M. J. Veljovic and A. K. Skrivervik, "Circularly polarized transmitarray antenna for cubesat intersatellite links in k-band," *IEEE Antennas and Wireless Propagation Letters*, vol. 19, no. 10, pp. 1749–1753, 2020.

[56] O. M. Bucci, G. D'Elia, G. Mazzarella, and G. Panariello, "Antenna pattern synthesis: a new general approach," *Proc. IEEE*, vol. 82, no. 3, pp. 358–371, Mar. 1994.

[57] P. Woodward, "A method of calculating the field over a plane aperture required to produce a given polar diagram," *Journal of the Institution of Electrical Engineers - Part IIIA: Radiolocation*, vol. 93, pp. 1554–1558(4), January 1946.

[58] A. Chakraborty, B. N. Das, and G. S. Sanyal, "Beam shaping using nonlinear phase distribution in a uniformly spaced array," *IEEE Trans. Antennas Propag.*, vol. 30, no. 5, pp. 1031–1034, Sep. 1982.

[59] J. Perini and M. Idselis, "Note on antenna pattern synthesis using numerical iterative methods," *IEEE Trans. Antennas Propag.*, vol. 19, no. 2, pp. 284–286, Mar. 1971.

[60] T. S. Fong and R. A. Birgenheier, "Method of conjugate gradients for antenna pattern synthesis," *Radio Sci.*, vol. 6, no. 12, pp. 1123–1130, Dec. 1971.

[61] T. H. Ismail, D. I. Abu-Al-Nadi, and M. J. Mismar, "Phase-only control for antenna pattern synthesis of linear arrays using the Levenberg-Marquardt algorithm," *Electromagnetics*, vol. 24, no. 7, pp. 555–564, 2004.

[62] J. Álvarez, M. Arrebola, R. G. Ayestarán, and F. Las-Heras, "Systematic framework for reflectarray synthesis based on phase optimization," *Int. J. Antennas Propag.*, vol. 2012, pp. 1–9, Jun. 2012.

[63] O. M. Bucci, G. Franceschetti, G. Mazzarella, and G. Panariello, "Intersection approach to array pattern synthesis," *IEE Proc. Microw. Antennas Propag.*, vol. 137, no. 6, pp. 349–357, Dec. 1990.

[64] J. A. Zornoza and J. A. Encinar, "Efficient phase-only synthesis of contoured-beam patterns for very large reflectarrays," *Int. J. RF Microw. Comput. Eng.*, vol. 14, no. 5, pp. 415–423, Sep. 2004.

[65] J. M. Johnson and Y. Rahmat-Samii, "Genetic algorithm optimization and its application to antenna design," in *Antennas and Propagation Society International Symposium*, vol. 1, Seattle, Washington, USA, Jun. 20–24, 1994, pp. 326–329.

[66] P. Nayeri, F. Yang, and A. Z. Elsherbeni, "Design of single-feed reflectarray antennas with asymmetric multiple beams using the particle swarm optimization

method," *IEEE Trans. Antennas Propag.*, vol. 61, no. 9, pp. 4598–4605, Sep. 2013.

[67] D. W. Boeringer and D. H. Werner, "Particle swarm optimization versus genetic algorithms for phased array synthesis," *IEEE Trans. Antennas Propag.*, vol. 52, no. 3, pp. 771–779, Mar. 2004.

[68] I. López, J. R. Pérez, and J. Basterrechea, "An approach for the design of reflectarrays using CG-FFT and PSO," in *Proceedings of the Fourth European Conference on Antennas and Propagation (EuCAP)*, Barcelona, Spain, Apr. 12–16, 2010, pp. 1–5.

[69] J. Nocedal and S. J. Wright, *Numerical Optimization*, 2nd ed. New York, NY, USA: Springer, 2006.

[70] G. A. F. Seber and C. J. Wild, *Nonlinear Regression*. Hoboken, NJ, USA: John Wiley & Sons, 2003.

[71] D. R. Prado, A. F. Vaquero, M. Arrebola, M. R. Pino, and F. Las-Heras, "General near-field synthesis of reflectarray antennas for their use as probes in catr," *Progress In Electromagnetics Research*, vol. 160, pp. 9–17, 2017.

[72] J. A. Encinar, M. Arrebola, L. F. de la Fuente, and G. Toso, "A transmit-receive reflectarray antenna for direct broadcast satellite applications," *IEEE Trans. Antennas Propag.*, vol. 59, no. 9, pp. 3255–3264, Sep. 2011.

[73] O. M. Bucci, G. D'Elia, and G. Romito, "Power synthesis of conformal arrays by a generalised projection method," *IEE Proc. Microw. Antennas Propag.*, vol. 142, no. 6, pp. 467–471, Dec. 1995.

[74] D. R. Prado, M. Arrebola, M. R. Pino, R. Florencio, R. R. Boix, J. A. Encinar, and F. Las-Heras, "Efficient crosspolar optimization of shaped-beam dual-polarized reflectarrays using full-wave analysis for the antenna element characterization," *IEEE Trans. Antennas Propag.*, vol. 65, no. 2, pp. 623–635, Feb. 2017.

[75] M. Ettorre, M. Casaletti, G. Valerio, R. Sauleau, L. Le Coq, S. C. Pavone, and M. Albani, "On the near-field shaping and focusing capability of a radial line slot array," *IEEE Transactions on Antennas and Propagation*, vol. 62, no. 4, pp. 1991–1999, 2014.

[76] Y. Wu, J. Wu, and Z. Li, "Plane wave synthesis using near field wave spectrum transform embedded into intersection approach," in *2018 International Conference on Microwave and Millimeter Wave Technology (ICMMT)*, 2018, pp. 1–3.

[77] S. Loredo, G. León, and E. G. Plaza, "A fast approach to near-field synthesis of transmitarrays," *IEEE Antennas and Wireless Propagation Letters*, vol. 20, no. 5, pp. 648–652, 2021.

[78] J. Huang, "Microstrip reflectarray," in *Antennas and Propagation Society International Symposium*, vol. 2, London, Ontario, Canada, Jun. 24–28, 1991, pp. 612–615.

[79] D.-C. Chang and M.-C. Huang, "Multiple-polarization microstrip reflectarray antenna with high efficiency and low cross-polarization," *IEEE Trans. Antennas Propag.*, vol. 43, no. 8, pp. 829–834, Aug. 1995.

[80] M. E. Cooley, J. F. Walker, D. G. Gonzalez, and G. E. Pollon, "Novel reflectarray element with variable phase characteristics," *IEE Proc. Microw. Antennas Propag.*, vol. 144, no. 2, pp. 149–151, Apr. 1997.

[81] H. Deguchi, N. Takagi, M. Tsuji, and H. Shigesawa, "Microstrip reflectarray with offset feed for improving effective aperture area," in *IEEE Antennas and Propagation Society International Symposium*, vol. 3, Columbus, Ohio, USA, Jun. 22–27 2003, pp. 290–293.

[82] D. M. Pozar and S. D. Targonski, "A microstrip reflectarray using crossed dipoles," in *IEEE Antennas and Propagation Society International Symposium*, vol. 2, Atlanta, Georgia, USA, Jun. 21–26, 1998, pp. 1008–1011.

[83] J. A. Zornoza and M. E. Bialkowski, "Australia and new zealand satellite coverage using a microstrip patch reflectarray," *Microwave and Optical Technology Letters*, vol. 37, no. 5, pp. 321–325, 2003.

[84] D. M. Pozar and T. A. Metzler, "Analysis of a reflectarray antenna using microstrip patches of variable size," *Electron. Lett.*, vol. 29, no. 8, pp. 657–658, Apr. 1993.

[85] D. M. Pozar, S. D. Targonski, and H. D. Syrigos, "Design of millimeter wave microstrip reflectarrays," *IEEE Trans. Antennas Propag.*, vol. 45, no. 2, pp. 287–296, Feb. 1997.

[86] E. Carrasco, M. Barba, and J. A. Encinar, "Aperture-coupled reflectarray element with wide range of phase delay," *Electron. Lett.*, vol. 42, no. 12, pp. 667–668, Jun. 2006.

[87] J. Huang and R. J. Pogorzelski, "A Ka-band microstrip reflectarray with elements having variable rotation angles," *IEEE Trans. Antennas Propag.*, vol. 46, no. 5, pp. 650–656, 1998.

[88] Y. Guo and S. Barton, "Phase correcting zonal reflector incorporating rings," *IEEE Trans. Antennas Propag.*, vol. 43, no. 4, pp. 350–355, Apr. 1995.

[89] C. G. M. Ryan, J. R. Bray, Y. Antar, M. Chaharmir, J. Shaker, and A. Ittipiboon, "A broadband transmitarray using double square ring elements," in *2009 13th International Symposium on Antenna Technology and Applied Electromagnetics and the Canadian Radio Science Meeting*, 2009, pp. 1–4.

[90] C. G. M. Ryan, M. R. Chaharmir, J. Shaker, J. R. Bray, Y. M. M. Antar, and A. Ittipiboon, "A wideband transmitarray using dual-resonant double square rings," *IEEE Trans. Antennas Propag.*, vol. 58, no. 5, pp. 1486–1493, 2010.

[91] A. H. Abdelrahman, A. Z. Elsherbeni, and F. Yang, "High-gain and broadband transmitarray antenna using triple-layer spiral dipole elements," *IEEE Antennas Wireless Propag. Lett.*, vol. 13, pp. 1288–1291, 2014.

[92] M. Niroo Jazi, M. R. Chaharmir, J. Shaker, and A. R. Sebak, "Broadband transmitarray antenna design using polarization-insensitive frequency selective surfaces," *IEEE Trans. Antennas Propag.*, vol. 64, no. 1, pp. 99–108, 2016.

[93] C.-Y. Hsu, L.-T. Hwang, T.-S. Horng, S.-M. Wang, F.-S. Chang, and C. N. Dorny, "Transmitarray design with enhanced aperture efficiency using small frequency selective surface cells and discrete jones matrix analysis," *IEEE Trans. Antennas Propag.*, vol. 66, no. 8, pp. 3983–3994, 2018.

[94] J. A. Encinar, "Design of two-layer printed reflectarrays using patches of variable size," *IEEE Trans. Antennas Propag.*, vol. 49, no. 10, pp. 1403–1410, Oct. 2001.

[95] F.-C. E. Tsai and M. E. Bialkowski, "Designing a 161-element Ku-band microstrip reflectarray of variable size patches using an equivalent unit cell waveguide approach," *IEEE Trans. Antennas Propag.*, vol. 51, no. 10, pp. 2953–2962, Oct. 2003.

[96] E. B. Lima, S. A. Matos, J. R. Costa, C. A. Fernandes, and N. J. G. Fonseca, "Circular polarization wide-angle beam steering at ka-band by in-plane translation of a plate lens antenna," *IEEE Trans. Antennas Propag.*, vol. 63, no. 12, pp. 5443–5455, 2015.

[97] M. E. Bialkowski and H. J. Song, "Dual linearly polarized reflectarray using aperture coupled microstrip patches," in *IEEE Antennas and Propagation Society International Symposium*, vol. 3, Boston, Massachusetts, USA, Jul. 8–13, 2001, pp. 486–489.

[98] S. Costanzo, F. Venneri, and G. D. Massa, "Bandwidth enhancement of aperture-coupled reflectarrays," *Electron. Lett.*, vol. 42, no. 23, pp. 1320–1321, Nov. 2006.

[99] B. D. Nguyen, K. T. Pham, V.-S. Tran, L. Mai, and N. Yonemoto, "Reflectarray element using cut-ring patch coupled to delay line," *IEEE Antennas Wireless Propag. Lett.*, vol. 14, pp. 571–574, 2015.

[100] L. Li, Q. Chen, Q. Yuan, K. Sawaya, T. Maruyama, T. Furuno, and S. Uebayashi, "Novel broadband planar reflectarray with parasitic dipoles for wireless communication applications," *IEEE Antennas Wireless Propag. Lett.*, vol. 8, pp. 881–885, 2009.

[101] J. H. Yoon, Y. J. Yoon, W.-S. Lee, and J.-H. So, "Broadband microstrip reflectarray with five parallel dipole elements," *IEEE Antennas Wireless Propag. Lett.*, vol. 14, pp. 1109–1112, 2015.

[102] R. Florencio, J. Encinar, R. R. Boix, and G. Perez-Palomino, "Dual-polarisation reflectarray made of cells with two orthogonal sets of parallel dipoles for bandwidth and cross-polarisation improvement," *IET Microw. Antennas Propag.*, vol. 8, no. 15, pp. 1389–1397, Aug. 2014.

[103] R. Florencio, J. A. Encinar, R. R. Boix, V. Losada, and G. Toso, "Reflectarray antennas for dual polarization and broadband telecom satellite applications," *IEEE Trans. Antennas Propag.*, vol. 63, no. 4, pp. 1234–1246, Apr. 2015.

[104] E. Martinez-de Rioja, J. A. Encinar, M. Barba, R. Florencio, R. R. Boix, and V. Losada, "Dual polarized reflectarray transmit antenna for operation in ku- and ka-bands with independent feeds," *IEEE Trans. Antennas Propag.*, vol. 65, no. 6, pp. 3241–3246, 2017.

[105] D. R. Prado, J. A. López-Fernández, M. Arrebola, and G. Goussetis, "Support vector regression to accelerate design and crosspolar optimization of shaped-beam reflectarray antennas for space applications," *IEEE Trans. Antennas Propag.*, vol. 67, no. 3, pp. 1659–1668, 2019.

[106] D. R. Prado, M. Arrebola, M. R. Pino, and G. Goussetis, "Broadband reflectarray with high polarization purity for 4k and 8k uhdtv dvb-s2," *IEEE Access*, vol. 8, pp. 100 712–100 720, 2020.

[107] J. A. Ortiz-Fuentes, J. Silva-Montero, J. I. Martinez-Lopez, J. Rodriguez-Cuevas, and A. E. Martynyuk, "Dual-frequency reflectarray based on split-ring slots," *IEEE Antennas Wireless Propag. Lett.*, vol. 16, pp. 952–955, 2017.

[108] C. Sabah, "Multiband metamaterials based on multiple concentric open-ring resonators topology," *IEEE J. Sel. Topics Quantum Electron.*, vol. 19, no. 1, pp. 8 500 808–8 500 808, 2013.

[109] R. Florencio, R. R. Boix, and J. A. Encinar, "Efficient spectral domain mom for the design of circularly polarized reflectarray antennas made of split rings," *IEEE Trans. Antennas Propag.*, vol. 67, no. 3, pp. 1760–1771, 2019.

[110] L. Moustafa, R. Gillard, F. Peris, R. Loison, H. Legay, and E. Girard, "The phoenix cell: A new reflectarray cell with large bandwidth and rebirth capabilities," *IEEE Antennas Wireless Propag. Lett.*, vol. 10, pp. 71–74, 2011.

[111] S. Adel and H. Hammad, "Modified phoenix cell for microstrip reflectarray antennas," in *Middle East Conference on Antennas and Propagation (MECAP)*, Cairo, Egypt, Dec. 29–31, 2012, pp. 1–3.

[112] S. A. Ibrahim and H. F. Hammad, "Modified phoenix cell for microstrip reflectarray antennas," in *IEEE Antennas and Propagation Society International Symposium (APSURSI)*, Orlando, Florida, USA, Jul. 7–13, 2013, pp. 1562–1563.

[113] I. Derafshi, N. Komjani, and M. Mohammadirad, "A single-layer broadband reflectarray antenna by using quasi-spiral phase delay line," *IEEE Antennas Wireless Propag. Lett.*, vol. 14, pp. 84–87, 2015.

[114] M. R. Chaharmir, J. Shaker, M. Cuhaci, and A. Ittipiboon, "A broadband reflectarray antenna with double square rings as the cell elements," in *First European Conference on Antennas and Propagation (EuCAP)*, Nice, France, Nov. 6–10, 2006, pp. 1–4.

[115] M. K. Arshad, F. A. Tahir, and A. Rashid, "Design of a single layer reflectarray unit cells based on hexagonal ring for wideband operation," in *IEEE Antennas and Propagation Society International Symposium (APSURSI)*, Memphis, Tennessee, USA, Jul. 6–11, 2014, pp. 815–816.

[116] R. S. Malfajani and Z. Atlasbaf, "Design and implementation of a broadband single-layer reflectarray antenna with large-range linear phase elements," *IEEE Antennas Wireless Propag. Lett.*, vol. 11, pp. 1442–1445, 2012.

[117] D. Headland, T. Niu, E. Carrasco, D. Abbott, S. Sriram, M. Bhaskaran, C. Fumeaux, and W. Withayachumnankul, "Terahertz reflectarrays and nonuniform metasurfaces," *IEEE J. Sel. Topics Quantum Electron.*, vol. 23, no. 4, 2017.

[118] S. H. Zainud-Deen, S. M. Gaber, and K. H. Awadalla, "B11. rectangular dielectric resonator transmitarrays," in *2012 29th National Radio Science Conference (NRSC)*, 2012, pp. 89–95.

[119] X. Liu, L. Peng, Y.-f. Liu, W.-s. Yu, Q.-x. Zhao, X. Jiang, S.-M. Li, and C. Ruan, "Ultrabroadband all-dielectric transmitarray designing based on genetic algorithm optimization and 3-d print technology," *IEEE Trans. Antennas Propag.*, vol. 69, no. 4, pp. 2003–2012, 2021.

[120] S. Long, M. McAllister, and L. Shen, "The resonant cylindrical dielectric cavity antenna," *IEEE Trans. Antennas Propag.*, vol. 31, no. 3, pp. 406–412, 1983.

[121] Y. Liu, H. Wang, and X. Dong, "Design of a double-layer dielectric-only transmitarray antenna for thz application," in *2018 IEEE International Symposium on Antennas and Propagation USNC/URSI National Radio Science Meeting*, 2018, pp. 1191–1192.

[122] A. Petosa and A. Ittipiboon, "Design and performance of a perforated dielectric fresnel lens," *IEE Proceedings - Microwaves, Antennas and Propagation*, vol. 150, pp. 309–314(5), October 2003.

[123] A. M. G. S. H. Zainud-Deen and K. H. Awadalla, "Transmitarray using perforated dielectric material for wideband applications," *Progress In Electromagnetics Research M*, vol. 24, pp. 1–13, 2012.

[124] M. K. T. Al-Nuaimi and W. Hong, "Discrete dielectric reflectarray and lens for e-band with different feed," *IEEE Antennas Wireless Propag. Lett.*, vol. 13, pp. 947–950, 2014.

[125] A. Massaccesi, M. Beccaria, and P. Pirinoli, "3d-printable perforated dielectric reflectarray in ka-band," in *2019 IEEE International Symposium on Antennas and Propagation and USNC-URSI Radio Science Meeting*, 2019, pp. 295–296.

[126] A.-E. Mahmoud, W. Hong, Y. Zhang, and A. Kishk, "W-band mutlilayer perforated dielectric substrate lens," *IEEE Antennas Wireless Propag. Lett.*, vol. 13, pp. 734–737, 2014.

[127] M. Wang, S. Xu, F. Yang, and M. Li, "Design of a ku-band triple-layer perforated dielectric transmitarray antenna," in *2016 IEEE International Symposium on Antennas and Propagation (APSURSI)*, 2016, pp. 1381–1382.

[128] S. Loredo and G. León, "Synthesis algorithm for "quasi-planar" dielectric lenses," in *2019 13th European Conference on Antennas and Propagation (EuCAP)*, 2019, pp. 1–4.

[129] H. Yi, S.-W. Qu, K.-B. Ng, C. H. Chan, and X. Bai, "3-d printed millimeter-wave and terahertz lenses with fixed and frequency scanned beam," *IEEE Trans. Antennas Propag.*, vol. 64, no. 2, pp. 442–449, 2016.

[130] A. Massaccesi, G. Dassano, and P. Pirinoli, "Beam scanning capabilities of a 3d-printed perforated dielectric transmitarray," *Electronics*, vol. 8, no. 4, 2019.

[131] A. H. Abdelrahman, A. Z. Elsherbeni, and F. Yang, "Transmission phase limit of multilayer frequency-selective surfaces for transmitarray designs," *IEEE Trans. Antennas Propag.*, vol. 62, no. 2, pp. 690–697, 2014.

[132] ——, "Transmitarray antenna design using cross-slot elements with no dielectric substrate," *IEEE Antennas Wireless Propag. Lett.*, vol. 13, pp. 177–180, 2014.

[133] R. Y. Wu, Y. B. Li, W. Wu, C. B. Shi, and T. J. Cui, "High-gain dual-band transmitarray," *IEEE Trans. Antennas Propag.*, vol. 65, no. 7, pp. 3481–3488, 2017.

[134] G. Liu, H.-j. Wang, J.-s. Jiang, F. Xue, and M. Yi, "A high-efficiency transmitarray antenna using double split ring slot elements," *IEEE Trans. Antennas Propag.*, vol. 14, pp. 1415–1418, 2015.

[135] X. Zhao, C. Yuan, L. Liu, S. Peng, Q. Zhang, and H. Zhou, "All-metal transmitarray for circular polarization design using rotated cross-slot elements for high-power microwave applications," *IEEE Trans. Antennas Propag.*, vol. 65, no. 6, pp. 3253–3256, 2017.

[136] E. Carrasco and J. Perruisseau-Carrier, "Reflectarray antenna at terahertz using graphene," *IEEE Antennas Wireless Propag. Lett.*, vol. 12, pp. 253–256, 2013.

[137] Z. Chang, B. You, L.-S. Wu, M. Tang, Y.-P. Zhang, and J.-F. Mao, "A reconfigurable graphene reflectarray for generation of vortex thz waves," *IEEE Antennas and Wireless Propagation Letters*, vol. 15, pp. 1537–1540, 2016.

[138] L. Shi, Q. Zhang, S. Zhang, G. Liu, and C. Yi, "Accurate characterization of graphene reconfigurable reflectarray antenna element by svr," *IEEE Journal on Multiscale and Multiphysics Computational Techniques*, vol. 6, pp. 50–55, 2021.

[139] M. Tamagnone and J. R. Mosig, "Theoretical limits on the efficiency of reconfigurable and nonreciprocal graphene antennas," *IEEE Antennas and Wireless Propagation Letters*, vol. 15, pp. 1549–1552, 2016.

[140] A. Moessinger, R. Marin, J. Freese, S. Mueller, A. Manabe, and R. Jakoby, "Investigations on 77 ghz tunable reflectarray unit cells with liquid crystal," in *2006 First European Conference on Antennas and Propagation*, 2006, pp. 1–4.

[141] R. Marin, A. Moessinger, F. Goelden, S. Mueller, and R. Jakoby, "77 ghz reconfigurable reflectarray with nematic liquid crystal," in *The Second European Conference on Antennas and Propagation, EuCAP 2007*, 2007, pp. 1–5.

[142] S. Bildik, S. Dieter, C. Fritzsch, M. Frei, C. Fischer, W. Menzel, and R. Jakoby, "Reconfigurable liquid crystal reflectarray with extended tunable phase range," in *2011 41st European Microwave Conference*, 2011, pp. 1292–1295.

[143] G. Perez-Palomino, M. Barba, J. A. Encinar, R. Cahill, R. Dickie, P. Baine, and M. Bain, "Design and demonstration of an electronically scanned reflectarray antenna at 100 ghz using multiresonant cells based on liquid crystals," *IEEE Transactions on Antennas and Propagation*, vol. 63, no. 8, pp. 3722–3727, 2015.

[144] W. Hu, R. Cahill, J. A. Encinar, R. Dickie, H. Gamble, V. Fusco, and N. Grant, "Design and measurement of reconfigurable millimeter wave reflectarray cells with nematic liquid crystal," *IEEE Transactions on Antennas and Propagation*, vol. 56, no. 10, pp. 3112–3117, 2008.

[145] X. Li, Y. Wan, J. Liu, D. Jiang, T. Bai, K. Zhu, J. Zhuang, and W.-Q. Wang, "Broadband electronically scanned reflectarray antenna with liquid crystals," *IEEE Antennas and Wireless Propagation Letters*, vol. 20, no. 3, pp. 396–400, 2021.

[146] J. Y. Lau and S. V. Hum, "A wideband reconfigurable transmitarray element," *IEEE Transactions on Antennas and Propagation*, vol. 60, no. 3, pp. 1303–1311, 2012.

[147] F. Diaby, A. Clemente, L. Di Palma, L. Dussopt, K. Pham, E. Fourn, and R. Sauleau, "Design of a 2-bit unit-cell for electronically reconfigurable transmitarrays at ka-band," in *2017 47th European Microwave Conference (EuMC)*, 2017, pp. 1321–1324.

[148] A. Clemente, F. Diaby, L. D. Palma, L. Dussopt, and R. Sauleau, "Experimental validation of a 2-bit reconfigurable unit-cell for transmitarrays at ka-band," *IEEE Access*, vol. 8, pp. 114 991–114 997, 2020.

[149] E. Carrasco, M. Barba, and J. A. Encinar, "Electronically switchable-beam reflectarray antenna," in *Proceedings of the Fourth European Conference on Antennas and Propagation*, 2010, pp. 1–5.

[150] C.-C. Cheng, B. Lakshminarayanan, and A. Abbaspour-Tamijani, "A programmable lens-array antenna with monolithically integrated mems switches," *IEEE Transactions on Microwave Theory and Techniques*, vol. 57, no. 8, pp. 1874–1884, 2009.

[151] P. Nepa and A. Buffi, "Near-field-focused microwave antennas: Near-field shaping and implementation." *IEEE Antennas and Propagation Magazine*, vol. 59, no. 3, pp. 42–53, 2017.

[152] J. Sherman, "Properties of focused apertures in the fresnel region," *IRE Transactions on Antennas and Propagation*, vol. 10, no. 4, pp. 399–408, 1962.

[153] M. Bogosanovic and A. G. Williamson, "Microstrip antenna array with a beam focused in the near-field zone for application in noncontact microwave industrial inspection," *IEEE Transactions on Instrumentation and Measurement*, vol. 56, no. 6, pp. 2186–2195, 2007.

[154] S. Karimkashi and A. A. Kishk, "Focused microstrip array antenna using a dolph-chebyshev near-field design," *IEEE Transactions on Antennas and Propagation*, vol. 57, no. 12, pp. 3813–3820, 2009.

[155] H.-W. Liu, C.-H. Weng, C.-F. Yang, Y.-S. Lin, F.-S. Chen, Y.-C. Huang, and C.-W. Hsu, "Design of rfid near-field focusing circular patch array antenna at 2.4ghz with applications," in *2010 Internet of Things (IOT)*, 2010, pp. 1–4.

[156] H.-T. Chou, M. R. Pino, P. Nepa, and C.-Y. Liu, "Near-field focused subarrays in a multi-panel configuration," *IEEE Access*, vol. 7, pp. 143 097–143 108, 2019.

[157] H.-T. Chou, H.-T. Cheng, S.-J. Chou, L.-R. Kuo, A. Buffi, and P. Nepa, "Dome-shaped ellipsoidal reflector antenna for uhf-rfid readers with confined near-field detection region," *IEEE Antennas and Wireless Propagation Letters*, vol. 16, pp. 2505–2508, 2017.

[158] S. Adibelli, P. Juyal, C.-L. Cheng, and A. Zajic, "Terahertz near-field focusing using a 3-d printed cassegrain configuration for backscattered side-channel detection," *IEEE Transactions on Antennas and Propagation*, vol. 67, no. 10, pp. 6627–6638, 2019.

[159] D. R. Reid and G. S. Smith, "A comparison of the focusing properties of a fresnel zone plate with a doubly-hyperbolic lens for application in a free-space, focused-beam measurement system," *IEEE Transactions on Antennas and Propagation*, vol. 57, no. 2, pp. 499–507, 2009.

[160] S. Karimkashi and A. A. Kishk, "Focusing properties of fresnel zone plate lens antennas in the near-field region," *IEEE Transactions on Antennas and Propagation*, vol. 59, no. 5, pp. 1481–1487, 2011.

[161] M. Ettorre, M. Casaletti, G. Valerio, R. Sauleau, L. Le Coq, S. C. Pavone, and M. Albani, "On the near-field shaping and focusing capability of a radial line slot array," *IEEE Transactions on Antennas and Propagation*, vol. 62, no. 4, pp. 1991–1999, 2014.

[162] M. Ettorre, M. Casaletti, G. Valerio, L. Le Coq, R. Sauleau, S. C. Pavone, and M. Albani, "A radial line slot array focusing in the near field: Analysis and design," in *The 8th European Conference on Antennas and Propagation (EuCAP 2014)*, 2014, pp. 1222–1226.

[163] Y. Monnai and H. Shinoda, "Focus-scanning leaky-wave antenna with electronically pattern-tunable scatterers," *IEEE Transactions on Antennas and Propagation*, vol. 59, no. 6, pp. 2070–2077, 2011.

[164] D. Blanco, J. L. Gómez-Tornero, E. Rajo-Iglesias, and N. Llombart, "Radially polarized annular-slot leaky-wave antenna for three-dimensional near-field microwave focusing," *IEEE Antennas and Wireless Propagation Letters*, vol. 13, pp. 583–586, 2014.

[165] Y. F. Wu, Y. J. Cheng, and Z. X. Huang, "Ka-band near-field-focused 2-d steering antenna array with a focused rotman lens," *IEEE Transactions on Antennas and Propagation*, vol. 66, no. 10, pp. 5204–5213, 2018.

[166] S.-C. Chang, H.-T. Chou, and H.-J. Huang, "2-d luneburg lens beamforming network for planar phased array of antennas to radiate near-field focused multibeams," *IEEE Transactions on Antennas and Propagation*, vol. 68, no. 8, pp. 5904–5915, 2020.

[167] H.-T. Chou and Z.-C. Tsai, "Near-field focus radiation of multibeam phased array of antennas realized by using modified rotman lens beamformer," *IEEE Transactions on Antennas and Propagation*, vol. 66, no. 12, pp. 6618–6628, 2018.

[168] S. L. Liu, X. Q. Lin, and Z. B. Zhu, "Ka-band multi-focus and pattern manipulation in near-field based on three-dimensional printed transmit-array antenna," *IET Microw. Antennas Propag.*, vol. 14, pp. 510–514(4), May 2020.

[169] J. Durnin, "Exact solutions for nondiffracting beams. i. the scalar theory," *J. Opt. Soc. Am. A*, vol. 4, no. 4, pp. 651–654, Apr 1987.

[170] J. Durnin, J. J. Miceli, and J. H. Eberly, "Diffraction-free beams," *Phys. Rev. Lett.*, vol. 58, pp. 1499–1501, Apr 1987.

[171] D. Mcgloin and K. Dholakia, "Bessel beams: Diffraction in a new light," *Contemporary Physics*, vol. 46, no. 1, pp. 15–28, Jan. 2005.

[172] J. Arlt and K. Dholakia, "Generation of high-order bessel beams by use of an axicon," *Optics Communications*, vol. 177, no. 1, pp. 297–301, 2000.

[173] Y. Yu and W. Dou, "Production of thz pseudo-bessel beams with uniform axial intensity using irregular binary axicons," *IET Optoelectronics*, vol. 4, pp. 195–200(5), October 2010.

[174] M. F. Imani and A. Grbic, "Generating evanescent bessel beams using near-field plates," *IEEE Transactions on Antennas and Propagation*, vol. 60, no. 7, pp. 3155–3164, 2012.

[175] M. Ettorre and A. Grbic, "Generation of propagating bessel beams using leaky-wave modes," *IEEE Transactions on Antennas and Propagation*, vol. 60, no. 8, pp. 3605–3613, 2012.

[176] M. Ettorre, S. M. Rudolph, and A. Grbic, "Generation of propagating bessel beams using leaky-wave modes: Experimental validation," *IEEE Transactions on Antennas and Propagation*, vol. 60, no. 6, pp. 2645–2653, 2012.

[177] W. Fuscaldo, G. Valerio, A. Galli, R. Sauleau, A. Grbic, and M. Ettorre, "Higher-order leaky-mode bessel-beam launcher," *IEEE Transactions on Antennas and Propagation*, vol. 64, no. 3, pp. 904–913, 2016.

[178] M. Qing Qi, W. X. Tang, and T. J. Cui, "A broadband bessel beam launcher using metamaterial lens," *Scientific Reports*, vol. 5, no. 1, p. 11732, Jun 2015.

[179] M. Ettorre, S. C. Pavone, M. Casaletti, and M. Albani, "Experimental validation of bessel beam generation using an inward hankel aperture distribution," *IEEE Transactions on Antennas and Propagation*, vol. 63, no. 6, pp. 2539–2544, 2015.

[180] D. Comite, G. Valerio, M. Albani, A. Galli, M. Casaletti, and M. Ettorre, "Exciting vorticity through higher order bessel beams with a radial-line slot-array antenna," *IEEE Transactions on Antennas and Propagation*, vol. 65, no. 4, pp. 2123–2128, 2017.

[181] M. Albani and S. C. Pavone, "Optimization of a rlsa bessel beam launcher for a microwaves near-field link," in *2019 International Conference on Electromagnetics in Advanced Applications (ICEAA)*, 2019, pp. 1329–1329.

[182] S. C. Pavone, M. Ettorre, M. Casaletti, and M. Albani, "Analysis and design of bessel beam launchers: Transverse polarization," *IEEE Transactions on Antennas and Propagation*, pp. 1–1, 2021.

[183] S. C. Pavone, M. Ettorre, and M. Albani, "Analysis and design of bessel beam launchers: Longitudinal polarization," *IEEE Transactions on Antennas and Propagation*, vol. 64, no. 6, pp. 2311–2318, 2016.

[184] H.-T. Chou, T.-M. Hung, N.-N. Wang, H.-H. Chou, C. Tung, and P. Nepa, "Design of a near-field focused reflectarray antenna for 2.4 ghz rfid reader applications," *IEEE Transactions on Antennas and Propagation*, vol. 59, no. 3, pp. 1013–1018, 2011.

[185] S. Yu, N. Kou, Z. Ding, and Z. Zhang, "Design of dual-polarized reflectarray for near-field shaped focusing," *IEEE Antennas and Wireless Propagation Letters*, vol. 20, no. 5, pp. 803–807, 2021.

[186] E. G. Plaza, G. León, S. Loredo, A. Arboleya, F. Las-Heras, C. M. S. Álvarez, and M. Rodriguez-Pino, "An ultrathin 2-bit near-field transmitarray lens," *IEEE Antennas and Wireless Propagation Letters*, vol. 16, pp. 1784–1787, 2017.

[187] L. Dussopt, K. Medrar, and L. Marnat, "Millimeter-wave gaussian-beam transmitarray antennas for quasi-optical s -parameter characterization," *IEEE Transactions on Antennas and Propagation*, vol. 68, no. 2, pp. 850–858, 2020.

[188] P. Zhang, L. Li, X. Zhang, H. Liu, and Y. Shi, "Design, measurement and analysis of near-field focusing reflective metasurface for dual-polarization and multi-focus wireless power transfer," *IEEE Access*, vol. 7, pp. 110 387–110 399, 2019.

[189] Y. C. Zhong and Y. J. Cheng, "Ka-band wideband large depth-of-field beam generation through a phase shifting surface antenna," *IEEE Transactions on Antennas and Propagation*, vol. 64, no. 12, pp. 5038–5045, 2016.

[190] Q.-S. Jia, S. Ding, H.-B. Dong, X. Han, Z.-J. Zhu, B.-Z. Wang, Y. M. Huang, and M. Bozzi, "Synthesis of bessel beam using time-reversal method incorporating metasurface," *IEEE Access*, vol. 9, pp. 30 677–30 686, 2021.

[191] N. Bayat and P. Mojabi, "On the use of focused incident near-field beams in microwave imaging," *Sensors*, vol. 18, no. 9, 2018.

[192] P.-F. Li, S.-W. Qu, and S. Yang, "Two-dimensional imaging based on near-field focused array antenna," *IEEE Antennas and Wireless Propagation Letters*, vol. 18, no. 2, pp. 274–278, 2019.

[193] P.-F. Li, S.-W. Qu, S. Yang, and Z.-P. Nie, "Microstrip array antenna with 2-d steerable focus in near-field region," *IEEE Transactions on Antennas and Propagation*, vol. 65, no. 9, pp. 4607–4617, 2017.

[194] J. M. Felício, J. M. Bioucas-Dias, J. R. Costa, and C. A. Fernandes, "Antenna design and near-field characterization for medical microwave imaging applications," *IEEE Transactions on Antennas and Propagation*, vol. 67, no. 7, pp. 4811–4824, 2019.

[195] J. Loane and S.-W. Lee, "Gain optimization of a near-field focusing array for hyperthermia applications," *IEEE Transactions on Microwave Theory and Techniques*, vol. 37, no. 10, pp. 1629–1635, 1989.

[196] H. Underwood, A. Peterson, and R. Magin, "Electric-field distribution near rectangular microstrip radiators for hyperthermia heating: theory versus experiment in water," *IEEE Transactions on Biomedical Engineering*, vol. 39, no. 2, pp. 146–153, 1992.

[197] K. D. Stephan, J. B. Mead, D. M. Pozar, L. Wang, and J. A. Pearce, "A near field focused microstrip array for a radiometric temperature sensor," *IEEE Transactions on Antennas and Propagation*, vol. 55, no. 4, pp. 1199–1203, 2007.

[198] W.-T. Hung, J.-J. Tung, and S.-Y. Chen, "A focusing reflectarray and its application in microwave virus sanitizer," *Radio Science*, vol. 49, no. 10, pp. 890–898, 2014.

[199] D. Oloumi and K. Rambabu, "Metal-cased oil well inspection using near-field uwb radar imaging," *IEEE Transactions on Geoscience and Remote Sensing*, vol. 56, no. 10, pp. 5884–5892, 2018.

[200] A. Mazzinghi, M. Balma, D. Devona, G. Guarnieri, G. Mauriello, M. Albani, and A. Freni, "Large depth of field pseudo-bessel beam generation with a rlsa antenna," *IEEE Transactions on Antennas and Propagation*, vol. 62, no. 8, pp. 3911–3919, 2014.

[201] H.-T. Chou, N.-N. Wang, H.-H. Chou, and J.-H. Qiu, "An effective synthesis of planar array antennas for producing near-field contoured patterns," *IEEE Transactions on Antennas and Propagation*, vol. 59, no. 9, pp. 3224–3233, 2011.

[202] A. Buffi, A. A. Serra, P. Nepa, H.-T. Chou, and G. Manara, "A focused planar microstrip array for 2.4 ghz rfid readers," *IEEE Transactions on Antennas and Propagation*, vol. 58, no. 5, pp. 1536–1544, 2010.

[203] R. González Ayestarán, G. León, M. R. Pino, and P. Nepa, "Wireless power transfer through simultaneous near-field focusing and far-field synthesis," *IEEE Transactions on Antennas and Propagation*, vol. 67, no. 8, pp. 5623–5633, 2019.

[204] D. R. Prado, M. Arrebola, M. R. Pino, and F. Las-Heras, "Evaluation of the quiet zone generated by a reflectarray antenna," in *2012 International Conference on Electromagnetics in Advanced Applications*, 2012, pp. 702–705.

[205] A. F. Vaquero, D. R. Prado, M. Arrebola, M. R. Pino, and F. Las-Heras, "Reflectarray probe optimization at millimeter frequencies," in *2016 10th European Conference on Antennas and Propagation (EuCAP)*, 2016, pp. 1–4.

[206] C. Granet, M. Zhou, S. B. Sørensen, K. W. Smart, J. S. Kot, and J. Ness, "Reflectarray compact antenna test range concept," in *2019 13th European Conference on Antennas and Propagation (EuCAP)*, 2019, pp. 1–5.

[207] F. Scattone, D. Sekuljica, A. Giacomini, F. Saccardi, A. Scannavini, E. Kaverine, S. Anwar, N. Gross, P. O. Iversen, and L. J. Foged, "Towards testing of 5g millimeter wave devices using plane wave generators," in *2021 15th European Conference on Antennas and Propagation (EuCAP)*, 2021, pp. 1–4.

[208] Y. Zhang, Z. Wang, X. Sun, Z. Qiao, W. Fan, and J. Miao, "Design and implementation of a wideband dual-polarized plane wave generator with tapered feeding nonuniform array," *IEEE Antennas and Wireless Propagation Letters*, vol. 19, no. 11, pp. 1988–1992, 2020.

[209] "CST," Computer Simulation Technology AG, Darmstadt, Germany.

[210] "HFSS," Ansys Inc., Pittsburgh, Pennsylvania, USA.

[211] D. R. Prado, "Advanced techniques for the analysis and synthesis of reflectarray antennas with applications in near and far fields," Ph.D. dissertation, Universidad de Oviedo, Nov. 2016.

[212] C. A. Balanis, *Antenna theory: analysis and design*. Wiley-Interscience, 2005.

[213] R. F. Díaz, "Contribución el análisis eficiente y a la mejora de prestaciones de antenas reflectarray," Ph.D. dissertation, Universidad Politécnica de Madrid, 2015.

[214] M. Arrebola, "Contribution to the analysis and design of shaped-beam printed reflectarrays in complex configurations," Ph.D. dissertation, Universidad Politécnica de Madrid, 2008.

[215] D. R. Prado, M. Arrebola, M. R. Pino, and F. Las-Heras, "An efficient calculation of the far field radiated by non-uniformly sampled planar fields complying Nyquist theorem," *IEEE Trans. Antennas Propag.*, vol. 63, no. 2, pp. 862–865, Feb. 2015.

[216] W. L. Stutzman and G. A. Thiele, *Antenna Theory and Design*, 3rd ed. Hoboken, NJ, USA: John Wiley & Sons, 2012.

[217] J. Álvarez, R. G. Ayestarán, G. León, L. F. Herrán, A. Arboleya, J. A. López-Fernández, and F. Las-Heras, "Near field multifocusing on antenna arrays via

non-convex optimisation," *IET Microw. Antennas Propag.*, vol. 8, no. 10, pp. 754–764, Jul. 2014.

[218] Y. Gan, H. Meng, Y. Chen, X. Zhang, and W. Dou, "Generation of bessel beams with 3d-printed lens," *International Journal of RF and Microwave Computer-Aided Engineering*, vol. 30, no. 4, p. e22029, 2020.

[219] Y. L. Fan, X. Q. Lin, and S. L. Liu, "Ka-band quasi-nondiffraction beam generation through a broadband bessel lens antenna," in *2019 IEEE Asia-Pacific Microwave Conference (APMC)*, 2019, pp. 1223–1225.

[220] ——, "Ka-band quasi-nondiffraction beam generation through a broadband bessel lens antenna," in *2019 IEEE Asia-Pacific Microwave Conference (APMC)*, 2019, pp. 1223–1225.

[221] A. Buffi, P. Nepa, and G. Manara, "Design criteria for near-field-focused planar arrays," *IEEE Antennas Propag. Mag.*, vol. 54, no. 1, pp. 40–50, Jun. 2012.

[222] E. Garcia-Marin, D. S. Filipovic, J. L. Masa-Campos, and P. Sanchez-Olivares, "Low-cost lens antenna for 5g multi-beam communication," *Microwave and Optical Technology Letters*, vol. 62, no. 11, pp. 3611–3622, 2020.

[223] S. Mishra, "A vector wave analysis of a bessel beam," *Optics Communications*, vol. 85, no. 2, pp. 159–161, 1991.

[224] J. C. M. Garnett and J. Larmor, "Xii. colours in metal glasses and in metallic films," *Philosophical Transactions of the Royal Society of London. Series A, Containing Papers of a Mathematical or Physical Character*, vol. 203, no. 359-371, pp. 385–420, 1904.

[225] B. Sareni, L. Krähenbühl, A. Beroual, and C. Brosseau, "Effective dielectric constant of periodic composite materials," *Journal of Applied Physics*, vol. 80, no. 3, pp. 1688–1696, 1996.

[226] A. Sihvola and J. Kong, "Effective permittivity of dielectric mixtures," *IEEE Transactions on Geoscience and Remote Sensing*, vol. 26, no. 4, pp. 420–429, 1988.

[227] J. M. Felício, C. A. Fernandes, and J. R. Costa, "Complex permittivity and anisotropy measurement of 3d-printed pla at microwaves and millimeter-waves," in *2016 22nd International Conference on Applied Electromagnetics and Communications (ICECOM)*, 2016, pp. 1–6.

[228] J. R. Costa, E. B. Lima, and C. A. Fernandes, "Compact beam-steerable lens antenna for 60-ghz wireless communications," *IEEE Transactions on Antennas and Propagation*, vol. 57, no. 10, pp. 2926–2933, 2009.

[229] C. A. Fernandes, E. B. Lima, and J. R. Costa, "Broadband integrated lens for illuminating reflector antenna with constant aperture efficiency," *IEEE Transactions on Antennas and Propagation*, vol. 58, no. 12, pp. 3805–3813, 2010.

[230] ——, *Dielectric Lens Antennas*. Singapore: Springer Singapore, 2016, pp. 1001–1064.

[231] S. SILVER, *Microwave Antenna Theory and Design. Edited by S. Silver, Etc*, ser. [Massachusetts Institute of Technology. Radiation Laboratory Series. no. 12.]. McGraw-Hill Book Company, 1949. [Online]. Available: https://books.google.es/books?id=Fi42MwEACAAJ

[232] E. Lima, J. R. Costa, M. G. Silveirinha, and C. A. Fernandes, "Ilash - software tool for the design of integrated lens antennas," in *2008 IEEE Antennas and Propagation Society International Symposium*, 2008, pp. 1–4.

[233] Y. Wang, J. Li, L. Huang, Y. Jing, A. Georgakopoulos, and P. Demestichas, "5g mobile: Spectrum broadening to higher-frequency bands to support high data rates," *IEEE Vehicular Technology Magazine*, vol. 9, no. 3, pp. 39–46, 2014.

[234] S. Salous, V. Degli Esposti, F. Fuschini, R. S. Thomae, R. Mueller, D. Dupleich, K. Haneda, J.-M. Molina Garcia-Pardo, J. Pascual Garcia, D. P. Gaillot, S. Hur, and M. Nekovee, "Millimeter-wave propagation: Characterization and modeling toward fifth-generation systems. [wireless corner]," *IEEE Antennas and Propagation Magazine*, vol. 58, no. 6, pp. 115–127, 2016.

[235] C. Wan and J. A. Encinar, "Efficient computation of generalized scattering matrix for analyzing multilayered periodic structures," *IEEE Trans. Antennas Propag.*, vol. 43, no. 11, pp. 1233–1242, Nov. 1995.

[236] "Grasp v9," TICRA, Copenhagen, Denmark.

[237] M. García-Fernández, Y. Álvarez López, A. Arboleya, B. González-Valdés, Y. Rodríguez-Vaqueiro, M. E. De Cos Gómez, and F. Las-Heras Andrés, "Antenna diagnostics and characterization using unmanned aerial vehicles," *IEEE Access*, vol. 5, pp. 23 563–23 575, 2017.

[238] Y. l. López, M. García-Fernández, and F. Las-Heras, "A portable cost-effective amplitude and phase antenna measurement system," *IEEE Transactions on Instrumentation and Measurement*, vol. 69, no. 9, pp. 7240–7251, 2020.

[239] G. Álvarez Narciandi, J. Laviada, Y. Álvarez López, and F. Las-Heras, "Portable freehand system for real-time antenna diagnosis and characterization," *IEEE Transactions on Antennas and Propagation*, vol. 68, no. 7, pp. 5636–5645, 2020.

[240] T. Hirvonen, J. Tuovinen, and A. Raisanen, "Lens-type compact antenna test range at mm-waves," in *1991 21st European Microwave Conference*, vol. 2, 1991, pp. 1079–1083.

[241] A. D. Olver and A. A. Saleeb, "Lens-type compact antenna test range," *Electronics Letters*, vol. 15, pp. 409–410(1), July 1979.

[242] J. Tuovinen, A. Vasara, and A. Raiisainen, "A new type of compact antenna test range," in *1992 22nd European Microwave Conference*, vol. 1, 1992, pp. 503–508.

[243] T. Sehm, J. Ala-Laurinaho, T. Hirvonen, and A. V. Räisänen, "Antenna measurements using a hologram catr," *Electronics Letters*, vol. 35, pp. 757–758(1), May 1999.

[244] J. Ala-Laurinaho, T. Hirvonen, P. Piironen, A. Lehto, J. Tuovinen, A. Raisanen, and U. Frisk, "Measurement of the odin telescope at 119 ghz with a hologram-type catr," *IEEE Transactions on Antennas and Propagation*, vol. 49, no. 9, pp. 1264–1270, 2001.

[245] F. Scattone, D. Sekuljica, A. Giacomini, F. Saccardi, A. Scannavini, E. Kaverine, S. Anwar, N. Gross, P. O. Iversen, and L. J. Foged, "Preliminary assesment of millimeter wave plane wave generator for 5g device testing," in *2021 15th European Conference on Antennas and Propagation (EuCAP)*, 2021, pp. 1–5.

[246] D. R. Prado, M. Arrebola, M. R. Pino, and F. Las-Heras, "Evaluation of the quiet zone generated by a reflectarray antenna," in *International Conference on Electromagnetics in Advanced Applications (ICEAA)*, Cape Town, South Africa, Sep. 2–7, 2012, pp. 702–705.

[247] R. Florencio, R. R. Boix, E. Carrasco, J. A. Encinar, and V. Losada, "Efficient numerical tool for the analysis and design of reflectarrays based on cells with three parallel dipoles," *Microwave and Optical Technology Letters*, vol. 55, no. 6, pp. 1212–1216, 2013.